

UNIVERSIDADE DE LISBOA
INSTITUTO SUPERIOR TÉCNICO

**Transverse Momentum Dependent Parton
Distribution Functions through SIDIS and Drell-Yan
at COMPASS**

Márcia Margarida Varanda Quaresma

Supervisor: Doctor Maria Paula Frazão Bordalo e Sá

Co-supervisors: Doctor Sérgio Eduardo de Campos Costa Ramos
Doctor Catarina Marques Quintans

**Thesis approved in public session to obtain the PhD Degree in
Physics**

Jury final classification: Pass with Distinction and Honour

Jury

Chairperson: Chairman of the IST Scientific Board

Members of the Committee:

Doctor Maria Paula Frazão Bordalo e Sá

Doctor João Carlos Carvalho de Sá Seixas

Doctor Luís Miguel Faria Pereira Lopes da Silva

Doctor Michela Chiosso

Doctor Celso Filipe Correia Franco

2016

UNIVERSIDADE DE LISBOA
INSTITUTO SUPERIOR TÉCNICO

**Transverse Momentum Dependent Parton
Distribution Functions through SIDIS and Drell-Yan
at COMPASS**

Márcia Margarida Varanda Quaresma

Supervisor: Doctor Maria Paula Frazão Bordalo e Sá

Co-supervisors: Doctor Sérgio Eduardo de Campos Costa Ramos
Doctor Catarina Marques Quintans

**Thesis approved in public session to obtain the PhD Degree in
Physics**

Jury final classification: Pass with Distinction and Honour

Jury

Chairperson: Chairman of the IST Scientific Board

Members of the Committee:

Doctor Maria Paula Frazão Bordalo e Sá, Professora Associada (com Agregação)
Aposentada do Instituto Superior Técnico da Universidade de Lisboa

Doctor João Carlos Carvalho de Sá Seixas, Professor Associado (com Agregação)
do Instituto Superior Técnico da Universidade de Lisboa

Doctor Luís Miguel Faria Pereira Lopes da Silva, Professor Auxiliar Convidado
do Instituto Superior Técnico da Universidade de Lisboa

Doctor Michela Chiosso, Ricercatore, Università degli Studi di Torino - Diparti-
mento di Fisica, Itália

Doctor Celso Filipe Correia Franco, Investigador Pos-Doc, Laboratório de Instru-
mentação e Física Experimental de Partículas (LIP), Lisboa

Funding Institution:

Grant SFRH/BD/72769/2010
from FCT - Fundação para a Ciência e Tecnologia

Host Institution:

LIP - Laboratório de Instrumentação
e física experimental de Partículas

To my father

Acknowledgements

First I would like to thank my supervisor Professor Paula Bordalo and my co-supervisor Professor Sérgio Ramos for all the support. They always cared about me and tried to help as much as they could in everything.

A special thanks goes to Doctor Catarina Quintans, also my co-supervisor, with whom I have shared the same room during all my stay at LIP, and since we were just few meters apart I used to think out loud and share all my doubts with her and she was always very concerned with me and my work.

I thank the COMPASS collaboration because without all of them my thesis would not exist. A special thank goes to the Drell-Yan group where I was involved since I started. For Doctor Michela Chiosso, who was part of my jury, a very big thank. I was very pleased to have her in my defense. For Doctor Takahiro Sawada with whom I have cross-checked various analyses and who was always very available to help me. For my friend Ricardo Longo with whom I have shared very pleasant times and knowledge.

I wish to thank my friend Doctor Bakur Parsamyan with whom I have done and cross-check many analyses and who was a constant support for me, mainly during the last part of my PhD.

I also would like to thank all my colleagues from LIP, specially the COMPASS group at LIP, Celso Franco, Luís Silva, Ana Sofia Nunes, Marcin Stolarski and Christophe Pires.

Finally I thank my family and my friends. My pillars: my mother, my brother and my boyfriend. They always push me and support me, without their love I would not succeed.

Resumo

A estrutura de spin do nucleão tem sido estudada pela experiência COMPASS no CERN. A medição da difusão inelástica profunda semi-inclusiva (SIDIS) tem sido uma ferramenta poderosa no acesso às funções de distribuição partónicas (PDFs) e às funções de distribuição partónicas dependentes do momento transversal (TMD PDFs). O alvo polarizado de COMPASS oferece a possibilidade de medir as modulações azimutais dependentes da orientação de spin e a extração das assimetrias de spin transversal, que são convoluções de TMD PDFs e Funções de Fragmentação (FF) do nucleão. A análise destes dados é feita em várias regiões cinemáticas, o que fornece uma vasta informação para a teoria, que assim podem extrair as TMDs e as FFs e a sua dependência cinemática. As TMD PDFs são também acessíveis através da medição do processo de Drell-Yan (DY) polarizado; neste caso as assimetrias de spin transversal são convoluções de duas TMD PDFs, uma que corresponde ao quark proveniente do hadrão do feixe e a outra ao quark do hadrão do alvo. Em COMPASS, um feixe de píões negativos e um alvo de prótons polarizados da amónia permitem a medição do processo de DY.

Em 2010 a tomada de dados de COMPASS foi dedicada à medição do processo de SIDIS, com múons positivos naturalmente polarizados longitudinalmente difundidos no alvo de prótons polarizados transversalmente. A medição do múon difundido e dos hádrons no estado final dão acesso às modulações angulares. As três células do alvo são transversalmente polarizadas, as duas exteriores com polarização oposta à polarização da interior, e esta configuração troca a cada duas semanas. Os eventos são combinados entre dois períodos seguidos, o que permite um melhor controlo de eventuais erros sistemáticos. A análise destes dados em intervalos de Q^2 , x , p_{Th} , z , y e W é apresentada nesta tese. Em 2015 a tomada de dados de COMPASS foi dedicada à medição do DY polarizado. Como a experiência COMPASS foi desenhada e desenvolvida para a medição de DIS, esta teve que sofrer modificações para a medição de DY. O processo de DY tem uma secção eficaz muito baixa, pelo que é essencial um feixe de elevada intensidade. Um absorvedor de hádrons foi adicionado imediatamente a jusante do alvo para parar os hádrons secundários, permitindo a passagem dos múons. O absorvedor também protege os detetores de possíveis danos devido ao excesso de radiação enquanto mantém o fundo combinatório a um nível razoável. Em 2009 fez-se uma curta tomada de dados exploratória dedicada a DY, na qual se usou um protótipo de absorvedor de hádrons. A análise destes dados é apresentada nesta tese. A tomada de dados de 2015 foi precedida por uma tomada de dados piloto no final de 2014, com a maioria do dispositivo experimental nas mesmas condições de 2015 mas ainda sem polarização do alvo. A análise preliminar destes dados é apresentada. Assim como a análise preliminar de parte dos dados de 2015 que já foram reconstruídos. COMPASS tem a oportunidade de aceder às TMD PDFs através de dois processos independentes e selecionando o mesmo espaço de fases. Estes resultados são muito promissores para a comunidade de TMD PDFs, a previsão de que a TMD Sivers deve mudar de sinal quando acedida através de DY ou de SIDIS será verificada com estes dados.

Palavras-chave: Drell-Yan, SIDIS, TMDs, COMPASS, Spin

Abstract

The spin structure of the nucleon has been studied at the COMPASS experiment at CERN. The Semi-Inclusive Deep Inelastic Scattering (SIDIS) measurements are a powerful tool to access the Parton Distribution Functions (PDFs) and the Transverse Momentum Dependent Parton Distribution Functions (TMD PDFs). The COMPASS polarised target gives the opportunity to measure the azimuthal modulations depending on the spin orientation and the extraction of the transverse spin asymmetries, which are convolutions of TMD PDFs of the nucleon and Fragmentation Functions (FF). The analysis of these data is done in several kinematic bins, which provides a vast input for the theoreticians to extract the TMDs and the FFs and their kinematic dependence. The TMD PDFs are also accessible through the measurement of the Drell-Yan process, in this case the transverse spin asymmetries are convolutions of two TMD PDFs, one corresponding to the annihilating quark from the beam hadron and the other to the annihilating quark from the target hadron. In COMPASS a negative pion beam and the polarised protons from ammonia target allow the measurement of the polarised DY process.

In 2010 the COMPASS data taking was dedicated to the measurement of the SIDIS process, the naturally polarised positive muons scattering off a transversely polarised proton target. The detection of the scattering muon and the final state hadrons give access to the angular modulations. The three target cells are transversely polarised, the two outer ones oppositely to the inner one, and this configuration changes every two weeks. The events are combined between the two sub-periods with opposite polarisation, which allows to better control possible systematic effects. The analysis of these data in bins of Q^2 , x , p_{Th} , z , y and W is presented. The 2015 COMPASS data taking was dedicated to the polarised DY measurement. As the COMPASS experiment was designed and developed for DIS and spectroscopy measurements, it had to suffer modifications for the DY measurement. The DY process has a very low cross-section, thus a high intensity beam is mandatory. A hadron absorber has been added just downstream of the target to stop the secondary hadrons allowing only the passage of the muon pairs. This protects the detectors from possible radiation damage while keeping the combinatorial background at a reasonable level. A short DY beam test run, using a hadron absorber prototype, was performed in 2009. The analysis of these data is presented in this thesis. The 2015 DY run was preceded by a pilot run in 2014, with the majority of the 2015 setup already set up, but still with no target polarisation. The analysis of these data is also presented in this thesis, as well as the analysis of some preliminary reconstructed 2015 data. COMPASS has the opportunity to access the TMD PDFs from two independent processes and selecting the same phase space coverage. These results are very promising for the TMD PDFs community, since the theoretical prediction that the Sivers TMD must change sign when accessed through the DY or the SIDIS processes should be verified with these data.

Key-words: Drell-Yan, SIDIS, TMDs, COMPASS, Spin

Contents

Acknowledgements	vii
Resumo	ix
Abstract	xi
Contents	xiii
List of Tables	xvii
List of Figures	xix
1 Experimental and Theoretical Overview	1
1.1 Structure Functions and Parton Distribution Functions	1
1.2 Longitudinal Nucleon Structure - Experimental Contributions	3
1.3 Transverse Nucleon Structure	5
1.3.1 The Sivers Distribution	7
1.3.2 The Boer-Mulders Distribution	10
1.3.3 The Transversity Distribution and the Collins Fragmentation Function	11
1.3.4 Breakthroughs on TMDs	14
1.4 Recent and future projects	14
1.5 The SIDIS Cross Section	15
1.5.1 Cross Section in Terms of the Asymmetries	17
1.6 The DY Cross Section	19
1.6.1 Cross Section in Terms of the Asymmetries	20
2 The COMPASS Experiment	23
2.1 The Beam	25
2.2 The Target	27
2.3 Tracking Detectors	30

2.3.1	Very Small Angle Trackers	30
2.3.2	Small Angle Trackers	30
2.3.3	Large Angle Trackers	31
2.4	Particle Identification	33
2.5	Trigger	35
2.6	Data Acquisition	36
2.7	Data Production	37
3	Spectrometer Alignment	39
3.1	Alignment Procedure	39
3.1.1	Alignment Parameters	40
3.1.2	Alignment Program	40
3.1.3	Quality Criteria	43
3.1.4	Results	43
4	Extraction of Transverse Spin Asymmetries from SIDIS	47
4.1	The 2010 Data Taking	47
4.2	Data Quality Tests	48
4.3	Events Selection	49
4.4	Binning	58
4.5	Asymmetry Extraction Methods	58
4.5.1	1D Binned Method - Double Ratio	58
4.5.2	1D Binned Method - Quadruple Ratio	61
4.5.3	Unbinned Maximum Likelihood Method	62
4.6	Systematic Effects	63
4.6.1	Azimuthal Stability	64
4.6.2	Compatibility of Results between Different Data Taking Periods	69
4.6.3	Compatibility between Different Extraction Methods	70
4.6.4	False Asymmetries	70
4.6.5	Summary of Systematic Studies	74
4.7	Transverse Spin Asymmetries	75
4.8	Selection of a Different z Range	83
4.8.1	Systematic Effects	84
4.8.2	Transverse Spin Asymmetries for $0.1 < z < 0.2$ and $z > 0.2$	94

5	The 2009 Drell-Yan Beam Test	103
5.1	Data Taking Conditions	103
5.2	Data Production	104
5.3	Event Selection	105
5.4	Dimuon Mass Distribution	106
5.5	Distribution of Events by Trigger	109
5.6	Trigger Purity	111
5.7	Double Triggers Efficiency	111
5.8	Kinematic Distributions	111
5.9	Contributions for the Measured J/ψ Yields	114
5.10	Combinatorial Background Studies	115
5.11	J/ψ Monte-Carlo	116
5.11.1	Geometrical Acceptance	116
5.11.2	Reconstruction Efficiency	117
5.11.3	Z Vertex Resolution and Cells Contamination	117
5.11.4	Mass and Momentum Resolutions	118
5.11.5	Kinematic Distributions	120
6	The 2014 Drell-Yan Pilot Run	125
6.1	Data Taking Conditions	125
6.2	Data Production	126
6.3	Event Selection	126
6.4	Z vertex distribution	127
6.5	Dimuon Mass Distribution and the Impact of the Trigger Validation	132
6.6	Combinatorial Background Estimation	132
6.7	Dimuon mass distributions by trigger	134
6.8	Kinematic Distributions	134
7	The 2015 Polarised Drell-Yan Run	139
7.1	Event Selection	139
7.2	Z Vertex Distribution	144
7.3	Dimuon Mass Distribution and the Impact of the Trigger Validation	144
7.4	Combinatorial Background Estimation	145
7.5	Dimuon Mass Distributions by Trigger	147

7.6 Kinematic Distributions	147
7.7 Asymmetries Extraction	149
8 Conclusion	153
A Combinatorial background evaluation	157
Bibliography	159

List of Tables

1.1	First moments for valence and sea quarks from SMC, HERMES and COMPASS. . .	4
1.2	Results for the gluon polarisation from DIS experiments.	5
1.3	Results on TMDs from COMPASS, HERMES and JLab experiments.	7
2.1	Detectors used in 2010 SIDIS run and in 2009, 2014 and 2015 DY runs.	26
2.2	Beam parameters.	27
3.1	Detectors used in 2014 alignment.	45
4.1	2010 data taking organization.	48
4.2	Statistics reduction due to quality tests.	50
4.3	Impact of the selection cuts on the number of events.	52
4.4	Impact of the selection cuts on the number of hadrons.	52
4.5	Distribution of the hadrons by the 4 Q^2 kinematic ranges.	53
4.6	x bins to be used in the analysis, for each Q^2 bin.	58
4.7	p_{Th} , z , y and W bins to be used in the analysis.	58
4.8	Systematic uncertainty in units of statistical one for each asymmetry.	75
4.9	Final number of hadrons depending on the z range selected.	84
4.10	Distribution of the hadrons by the 4 Q^2 ranges and for $0.1 < z < 0.2$ and $z > 0.2$. . .	84
4.11	z bins to be used in analysis for for $0.1 < z < 0.2$ and $z > 0.2$	84
4.12	Systematic uncertainty for each asymmetry and for $0.1 < z < 0.2$ and $z > 0.2$	87
5.1	The impact of each selection criterion in the statistics.	107
5.2	Statistics divided by trigger.	110
5.3	Triggers efficiency.	112
5.4	Geometrical acceptance.	117
5.5	Reconstruction efficiency.	118

6.1	The impact of each selection criterion in the statistics.	130
6.2	Statistics divided by trigger.	135
7.1	2015 data taking organization.	140
7.2	The impact of each selection criterion in the statistics.	140
7.3	Statistics divided by trigger.	147
7.4	Preliminary values for the mean target polarisation and relaxation time.	152

List of Figures

1.1	The quark helicity distributions at $Q^2 = 3 \text{ (GeV}/c^2)^2$	5
1.2	Parton distribution functions organised according to the nucleon polarisation and the quarks polarisation.	6
1.3	The Sivers asymmetries for pions and kaons from COMPASS.	8
1.4	The Sivers asymmetries for pions and kaons from COMPASS and HERMES.	9
1.5	Comparison between the Sivers asymmetries for pions and three different global fits.	9
1.6	Sivers functions of the u -quark and the d -quark.	10
1.7	Azimuthal modulations from DY cross-section measured by the NA10.	11
1.8	Boer-Mulders functions for u , d , \bar{u} and \bar{d} quarks for $Q^2 = 1 \text{ (GeV}/c^2)^2$	12
1.9	$A_{\cos(2\phi_h)}^{UU}$ asymmetry for charged hadrons.	12
1.10	The Collins asymmetries for pions and kaons from COMPASS.	13
1.11	Transversity distributions for u and d quarks and the favored and unfavored Collins functions.	14
1.12	Diagram of the SIDIS process.	15
1.13	Definition of the azimuthal angles on the target rest frame.	16
1.14	Diagram of the DY process.	19
1.15	Definition of the azimuthal angles on the Collins Soper frame.	20
1.16	Definition of the azimuthal angles on the target rest frame.	20
2.1	2010 COMPASS setup for the SIDIS measurement.	24
2.2	2014 COMPASS setup for the DY measurement.	24
2.3	BMS schematic drawing.	27
2.4	μ^+ beam polarisation as a function of its momentum.	27
2.5	Target device.	28
2.6	Dilution factor.	29
2.7	MicroMegas principle of operation.	31

2.8	GEMs principle of operation.	31
2.9	DCs principle of operation.	32
2.10	MDT module.	32
2.11	Schematic view of a COMPASS straw detector.	33
2.12	Principle of operation of the RICH detector and its schematic view.	34
2.13	Schematic view of MW1.	34
2.14	Schematic view of the hodoscopes positions.	35
2.15	Principle of veto signals.	36
2.16	Trigger concept to select low Q^2 SIDIS events.	37
2.17	Schematic of the DAQ system in COMPASS.	38
3.1	Alignment control distributions for DC00X1 plane.	46
4.1	Distribution of the vertex position along the beam direction.	53
4.2	Q^2 versus x distribution.	53
4.3	Mass distribution of the final hadronic state.	54
4.4	Distribution of the fractional energy of the virtual photon.	54
4.5	Distribution of the momentum fraction carried by the struck quark from proton.	54
4.6	Distribution of the transverse momentum of the hadrons.	54
4.7	Distribution of the fraction of the photon energy transferred to the hadron.	55
4.8	Distribution of ϕ_S azimuthal angle.	55
4.9	Distribution of ϕ_h azimuthal angle.	56
4.10	Distribution of W , for different Q^2 ranges.	56
4.11	Distribution of the fractional energy of the virtual photon for each Q^2 bin.	56
4.12	Distribution of x for each Q^2 bin.	57
4.13	Hadrons transverse momentum distribution for each Q^2 bin.	57
4.14	Fraction of the photon energy transferred to the hadron for each Q^2 bin.	57
4.15	Mean values of Q^2 , x , p_{Th} , z , y and W for each kinematic bin in x , p_{Th} , z , y and W	59
4.16	Cells numeration in double ratio method.	60
4.17	Cells numeration in quadruple ratio method.	61
4.18	R-test results for the z range $z > 0.1$	65
4.19	T-test results for the z range $z > 0.1$	66
4.20	RA-test results for the z range $z > 0.1$	68
4.21	RA-T-test results for the z range $z > 0.1$	69

4.22	Compatibility between the results from different data taking periods.	71
4.23	Comparison between the asymmetries from the QR and the UL methods.	72
4.24	Comparison between the asymmetry errors from the QR and the UL methods. . . .	73
4.25	Evaluation of the systematic error from the false asymmetries, for the z range $z > 0.1$.	74
4.26	$A_{UT}^{\sin(\phi_h - \phi_S)}$ asymmetry, Siverts asymmetry, in bins of x, p_{Th}, z, y, W and Q^2	76
4.27	$A_{UT}^{\sin(\phi_h + \phi_S - \pi)}$ asymmetry, Collins asymmetry, in bins of x, p_{Th}, z, y, W and Q^2	77
4.28	$A_{UT}^{\sin(3\phi_h - \phi_S)}$ asymmetry in bins of x, p_{Th}, z, y, W and Q^2	78
4.29	$A_{LT}^{\cos(\phi_h - \phi_S)}$ asymmetry in bins of x, p_{Th}, z, y, W and Q^2	79
4.30	$A_{UT}^{\sin(\phi_S)}$ asymmetry in bins of x, p_{Th}, z, y, W and Q^2	80
4.31	$A_{UT}^{\sin(2\phi_h - \phi_S)}$ asymmetry in bins of x, p_{Th}, z, y, W and Q^2	81
4.32	$A_{LT}^{\cos(\phi_S)}$ asymmetry in bins of x, p_{Th}, z, y, W and Q^2	82
4.33	$A_{LT}^{\cos(2\phi_h - \phi_S)}$ asymmetry in bins of x, p_{Th}, z, y, W and Q^2	83
4.34	R-test results for the z ranges $0.1 < z < 0.2$ and $z > 0.2$	85
4.35	T-test results for the z ranges $0.1 < z < 0.2$ and $z > 0.2$	86
4.36	RA-test results for the z ranges $0.1 < z < 0.2$ and $z > 0.2$	88
4.37	RA-T-test results for the z ranges $0.1 < z < 0.2$ and $z > 0.2$	89
4.38	Compatibility between the results from different data taking periods for the z ranges $0.1 < z < 0.2$ and $z > 0.2$	90
4.39	Comparison between the asymmetries from the QR and the UL methods, for the z ranges $0.1 < z < 0.2$ and $z > 0.2$	91
4.40	Comparison between the asymmetry errors from the QR and the UL methods, for the z ranges $0.1 < z < 0.2$ and $z > 0.2$	92
4.41	Evaluation of the systematic error from the false asymmetries, for the z ranges $0.1 <$ $z < 0.2$ and $z > 0.2$	93
4.42	$A_{UT}^{\sin(\phi_h - \phi_S)}$ asymmetry, Siverts asymmetry, in bins of x, p_{Th}, z, y, W and Q^2 , for $0.1 < z < 0.2$ and $z > 0.2$	95
4.43	$A_{UT}^{\sin(\phi_h + \phi_S - \pi)}$ asymmetry, Collins asymmetry, in bins of x, p_{Th}, z, y, W and Q^2 , for $0.1 < z < 0.2$ and $z > 0.2$	96
4.44	$A_{UT}^{\sin(3\phi_h - \phi_S)}$ asymmetry in bins of x, p_{Th}, z, y, W and Q^2 , for $0.1 < z < 0.2$ and $z > 0.2$	97
4.45	$A_{LT}^{\cos(\phi_h - \phi_S)}$ asymmetry in bins of x, p_{Th}, z, y, W and Q^2 , for $0.1 < z < 0.2$ and $z > 0.2$	98
4.46	$A_{UT}^{\sin(\phi_S)}$ asymmetry in bins of x, p_{Th}, z, y, W and Q^2 , for $0.1 < z < 0.2$ and $z > 0.2$.	99

4.47	$A_{UT}^{\sin(2\phi_h-\phi_S)}$ asymmetry in bins of x, p_{Th}, z, y, W and Q^2 , for $0.1 < z < 0.2$ and $z > 0.2$.	100
4.48	$A_{LT}^{\cos(\phi_S)}$ asymmetry in bins of x, p_{Th}, z, y, W and Q^2 , for $0.1 < z < 0.2$ and $z > 0.2$.	101
4.49	$A_{LT}^{\cos(2\phi_h-\phi_S)}$ asymmetry in bins of x, p_{Th}, z, y, W and Q^2 , for $0.1 < z < 0.2$ and $z > 0.2$.	102
5.1	Z_{vtx} distribution.	106
5.2	Transverse position of the vertex.	106
5.3	Momenta of muons before the selection of $p_{\mu^-} < 100$ GeV/ c .	107
5.4	Momenta of muons after the selection of $p_{\mu^-} < 100$ GeV/ c .	107
5.5	Momenta of muons before the selection of $p_{\mu^-} < 100$ GeV/ c and for double 1 trigger.	107
5.6	Momenta of muons before the selection of $p_{\mu^-} < 100$ GeV/ c and for double 2 trigger.	107
5.7	The impact of the selection criteria in the dimuon mass distribution.	108
5.8	Dimuon mass distribution.	108
5.9	Dimuon mass distribution after the selection criteria but without PID requirement.	109
5.10	Dimuon mass distribution as a function of the Z_{vtx} position.	109
5.11	Trigger double 1, one muon in HCAL1 and one muon in Middle.	110
5.12	Trigger double 1, one muon in HCAL1 and one muon in Ladder.	110
5.13	Trigger double 1, one muon in HCAL1 and one muon in Outer.	110
5.14	Trigger double 1, one muon in HCAL1 and one muon in one SAS hodoscope system.	110
5.15	Trigger double 2, two muons in HCAL1.	111
5.16	Dimuon momentum distribution for all masses and for $M_{\mu\mu} > 2.5$ GeV/ c^2 .	112
5.17	Dimuon transverse momentum distribution for all masses and for $M_{\mu\mu} > 2.5$ GeV/ c^2 .	112
5.18	x_F distribution for all masses and for $M_{\mu\mu} > 2.5$ GeV/ c^2 .	112
5.19	x_2 versus x_1 distribution for $M_{\mu\mu} > 2.5$ GeV/ c^2 .	112
5.20	Momentum distribution of each muon for $M_{\mu\mu} > 2.5$ GeV/ c^2 and double trigger.	113
5.21	Momentum distribution of each muon for $M_{\mu\mu} > 2.5$ GeV/ c^2 and double 1 trigger.	113
5.22	Momentum distribution of each muon for $M_{\mu\mu} > 2.5$ GeV/ c^2 and double 2 trigger.	113
5.23	The $\mu^+\mu^-$ mass distribution, the $\mu^+\mu^+$ and the $\mu^-\mu^-$ mass distributions.	115
5.24	The $\mu^+\mu^-$ mass distribution, the $\mu^+\mu^+$ and the $\mu^-\mu^-$ mass distributions after applying the image cut.	115
5.25	The dimuon mass distribution together with the combinatorial background evaluation.	116
5.26	The accepted dimuon momentum distributions per zone (MC truth).	117
5.27	The reconstructed MC dimuon momentum distributions per zone.	118

5.28	Z vertex resolution.	119
5.29	Z vertex distributions of the accepted and the reconstructed events.	119
5.30	Z vertex resolution for the upstream cell.	119
5.31	Z vertex resolution for the downstream cell.	119
5.32	Mass resolution.	120
5.33	Dimuon transverse momentum resolution.	120
5.34	Momentum resolution of negative muons.	120
5.35	Momentum resolution of positive muons.	120
5.36	Comparison of dimuon masses between data and MC.	121
5.37	Comparison of dimuon momentum between data and MC.	121
5.38	Comparison of dimuon transverse momentum distributions between data and MC.	122
5.39	Comparison of x_F distributions between data and MC.	122
5.40	x_2 versus x_1 distribution for data.	122
5.41	x_2 versus x_1 distribution for MC.	122
5.42	Comparison of negative muons momentum distributions between data and MC.	123
5.43	Comparison of positive muons momentum distributions between data and MC.	123
5.44	Comparison of the μ^- momentum distributions between data and MC, rejecting outer from trigger.	123
5.45	Comparison of the μ^+ momentum distributions between data and MC, rejecting outer from trigger.	123
5.46	Comparison of the radiation lengths crossed by the negative muons in the absorber between data and MC.	124
5.47	Comparison of the radiation lengths crossed by the positive muons in the absorber between data and MC.	124
5.48	Comparison of μ^- energy loss in the absorber between data and MC.	124
5.49	Comparison of μ^+ energy loss in the absorber between data and MC.	124
6.1	Muons momentum distribution before the selection $p_{\mu^-} < 100 \text{ GeV}/c$ or $\theta_{\mu^-} > 12$ mrad.	127
6.2	Muons momentum distribution after the selection $p_{\mu^-} < 100 \text{ GeV}/c$ or $\theta_{\mu^-} > 12$ mrad.	127
6.3	Z_{vtx} distributions with the whole selection criteria apart from the Z_{vtx} selection.	128
6.4	Y_{vtx} versus X_{vtx} distribution. The red circumference indicate the cut to be applied.	128
6.5	X_{vtx} position. In red is the distribution for the selected vertices.	128
6.6	Y_{vtx} position. In red is the distribution for the selected vertices.	128

6.7	Last measured point of each muon.	129
6.8	First measured point of each muon.	129
6.9	Time difference between the muons.	129
6.10	Mean time of the negative muons.	130
6.11	Mean time of the positive muons.	130
6.12	The impact of the selection criteria in the dimuon mass distribution.	131
6.13	Z_{vtx} distributions, with the whole selection criteria apart from the Z_{vtx} selection, for high mass events.	131
6.14	Dimuon mass distribution, without the trigger validation and the image cut.	133
6.15	Dimuon mass distribution, after the trigger validation is applied, but without the image cut.	133
6.16	The $\mu^+\mu^-$ mass distribution, the $\mu^+\mu^+$ and the $\mu^-\mu^-$ mass distributions.	133
6.17	The $\mu^+\mu^-$ mass distribution, the $\mu^+\mu^+$ and the $\mu^-\mu^-$ mass distributions after ap- plying the image cut.	133
6.18	Dimuon mass distribution together with the combinatorial background evaluated.	134
6.19	Mass distribution for all double triggers.	135
6.20	Mass distribution for LAS-LAS double trigger.	135
6.21	Mass distribution for LAS-Middle double trigger.	135
6.22	Mass distribution for LAS-Outer double trigger.	135
6.23	Dimuon momentum distribution for $M_{\mu\mu} > 4 \text{ GeV}/c^2$	136
6.24	Feynman x distribution for $M_{\mu\mu} > 4 \text{ GeV}/c^2$	136
6.25	Dimuon transverse momentum distribution for $M_{\mu\mu} > 4 \text{ GeV}/c^2$	136
6.26	x_2 versus x_1 distribution for $M_{\mu\mu} > 4 \text{ GeV}/c^2$	136
6.27	Distribution of the $\cos(\theta_{CS})$	137
6.28	Distribution of the ϕ_{CS}	137
7.1	The impact of the selection criteria in the dimuon mass distribution.	141
7.2	Muons momentum distribution before the selection $p_{\mu^-} < 100 \text{ GeV}/c$ or $\theta_{\mu^-} > 12$ mrad.	141
7.3	Muons momentum distribution after the selection $p_{\mu^-} < 100 \text{ GeV}/c$ or $\theta_{\mu^-} > 12$ mrad.	141
7.4	Z_{vtx} distributions with the whole selection criteria apart from the Z_{vtx} selection.	142
7.5	Y_{vtx} versus X_{vtx} distribution. The red circumference indicate the cut to be applied.	142
7.6	X_{vtx} position. In red is the distribution for the selected vertices.	142
7.7	Y_{vtx} position. In red is the distribution for the selected vertices.	142

7.8	Last measured point of each muon.	143
7.9	First measured point of each muon.	143
7.10	Time difference between the muons.	143
7.11	Mean time of the negative muons.	144
7.12	Mean time of the positive muons.	144
7.13	Z_{vtx} distributions with the whole selection criteria apart from the Z_{vtx} selection for high mass events.	145
7.14	Ratio between the Z_{vtx} distributions with and without the image cut for high mass events.	145
7.15	Dimuon mass distribution without the trigger validation and the image cut are applied.	146
7.16	Dimuon mass distribution with the trigger validation and the image cut applied. . .	146
7.17	Ratio between the fit function and the mass distribution presented in Fig. 7.16. . . .	146
7.18	The $\mu^+\mu^-$ mass distribution, the $\mu^+\mu^+$ and the $\mu^-\mu^-$ mass distributions.	147
7.19	The $\mu^+\mu^-$ mass distribution, the $\mu^+\mu^+$ and the $\mu^-\mu^-$ mass distributions after applying the image cut.	147
7.20	Dimuon mass distribution together with the combinatorial background evaluated. . .	148
7.21	Mass distribution for LAS-LAS double trigger.	148
7.22	Mass distribution for LAS-Middle double trigger.	148
7.23	Mass distribution for LAS-Outer double trigger.	148
7.24	Dimuon momentum distribution for $M_{\mu\mu} > 4 \text{ GeV}/c^2$	149
7.25	Feynman x distribution for $M_{\mu\mu} > 4 \text{ GeV}/c^2$	149
7.26	Dimuon transverse momentum distribution for $M_{\mu\mu} > 4 \text{ GeV}/c^2$	150
7.27	x_2 versus x_1 distribution for $M_{\mu\mu} > 4 \text{ GeV}/c^2$	150
7.28	x_1 distribution for $M_{\mu\mu} > 4 \text{ GeV}/c^2$	150
7.29	x_2 distribution for $M_{\mu\mu} > 4 \text{ GeV}/c^2$	150
7.30	Distribution of the $\cos(\theta_{CS})$	151
7.31	Distribution of the ϕ_{CS}	151
7.32	Distribution of the ϕ_S	151
8.1	Sivers asymmetry for different x bins in bins of Q^2	154
8.2	Sivers asymmetry for $16 < Q^2 < 81 \text{ (GeV}/c^2)^2$ and in several bins of x , p_{Th} , z , y and W	154
8.3	Sivers asymmetry for the three different z ranges in bins of Q^2	155

8.4	Sivers asymmetry predictions. The prediction on the right hand side [72] consider $x_F = x_\pi - x_p$ and has a cut on $p_T < 2 \text{ GeV}/c$. The prediction on the left hand side [73] consider $x_F = x_p - x_\pi$ and has a cut on $p_T < 1 \text{ GeV}/c$	155
-----	--	-----

Experimental and Theoretical Overview

The internal spin structure of the nucleon is being studied since the '70s. Its study was strongly motivated by the results published by the European Muon Collaboration (EMC) in 1988 [1], suggesting that the contribution from the quarks spin to the nucleon spin was very small. This result has induced new experiments and theoretical developments. In a first stage it was important to cross-check the EMC result and, in case of success, to continue the studies to understand the spin structure of the nucleon. Nowadays the contribution from the quark's spin to the nucleon's spin, denominated by $\Delta\Sigma$, is expected to be around 60% in the relativistic quark model. The measured value, for a fixed Q^2 (the photon virtuality), is $\Delta\Sigma(Q^2 = 3 \text{ (GeV}/c^2)^2) = 0.30 \pm 0.01(stat) \pm 0.02(evol)$ [2].

The different possible contributions for the nucleon's spin structure became a subject of study and several experiments have dedicated their efforts to contribute to this knowledge. The gluon contribution has become an important measurement. Also, the significant transverse spin asymmetries that have been measured in proton-proton and in lepton-nucleon collisions suggested that the intrinsic transverse momentum and the orbital angular momentum (OAM) may have an important role in the description of the nucleon's spin structure.

There is still a huge work and progress to be done in this field. Several experiments are ongoing and others are being prepared to give their contribution, the COMMon Muon Proton Apparatus for Structure and Spectroscopy (COMPASS) experiment being one of them.

1.1 Structure Functions and Parton Distribution Functions

Both the polarised deep inelastic scattering (DIS) and the polarised proton-proton collisions have been contributing to the understanding of the spin structure of the nucleon. The DIS measurements were performed at the Stanford Linear Accelerator Center (SLAC) and at the Jefferson Laboratory (JLab) using electron beams, at the Deutsches Elektronen-Synchrotron (DESY) using electron and positron beams and at the European Organization for Nuclear Research (CERN) using muon beams. All of these experiments have a fixed target, so they involve the scattering of a lepton beam off a longitudinal or transversely polarised nucleon. The proton-proton scattering measurements were performed at the Relativistic Heavy Ion Collider (RHIC).

The measurements with longitudinal polarisation allow the access to the helicity distributions of partons in the nucleon, which can be seen as the probability difference of finding a parton with longitudinal polarisation parallel or anti-parallel to that of the nucleon. On the other hand, the measurements with transverse polarisation allow the access to the transversity distributions of

partons in the nucleon, the probability difference of finding a parton with transverse polarisation parallel or anti-parallel to that of the nucleon.

The study of the internal spin structure of the nucleon started with the measurement of the proton spin structure function, $g_1(x, Q^2)$, x being the nucleon momentum fraction carried by the interacting quark. The polarised DIS differential cross-section can be written in terms of the unpolarised structure functions, $F_1(x, Q^2)$ and $F_2(x, Q^2)$, and the polarised ones, $g_1(x, Q^2)$ and $g_2(x, Q^2)$,

$$\frac{d^2\sigma}{dx dy} = \frac{8\pi\alpha^2}{Q^2} \left[\frac{y}{2} F_1(x, Q^2) + \frac{1}{2xy} \left(1 - y - \frac{y^2\gamma^2}{4} \right) F_2(x, Q^2) + c_1 g_1(x, Q^2) + c_2 g_2(x, Q^2) \right] \quad (1.1)$$

where the constants c_1 and c_2 depend on y and $\gamma = Q^2/\nu^2 = 4M^2x^2/Q^2$ and are different for a different nucleon polarisation. y represents the beam momentum fraction carried by the virtual photon and ν is the energy of the virtual photon.

Considering the nucleon longitudinal polarisation, the spin structure function $g_1(x, Q^2)$ can be written in the parton model as

$$g_1(x, Q^2) = \frac{1}{2} \sum_q e_q^2 \Delta q(x, Q^2) \quad (1.2)$$

where $\Delta q(x, Q^2)$, the spin dependent Parton Distribution Function (PDF), also so-called helicity distribution, is given by

$$\Delta q(x, Q^2) = (q^{\rightarrow} + \bar{q}^{\rightarrow})(x, Q^2) - (q^{\leftarrow} + \bar{q}^{\leftarrow})(x, Q^2) \quad . \quad (1.3)$$

When integrated over x ,

$$\Delta q(Q^2) = \int_0^1 \Delta q(x, Q^2) dx \quad (1.4)$$

is the fraction of the spin of the nucleon carried by quarks and anti-quarks of flavour q . Summing over quark flavours it gives the contribution from the quark's spin to the nucleon's spin.

Analogous to the helicity distributions measured with longitudinal polarisation, the transversity distributions, $h_1^q(x, Q^2)$, introduced in 1979 by Ralston and Soper [3] are measured with the transverse polarisation of the nucleon,

$$h_1^q(x, Q^2) = (q^{\uparrow} + \bar{q}^{\uparrow})(x, Q^2) - (q^{\downarrow} + \bar{q}^{\downarrow})(x, Q^2) \quad (1.5)$$

and describe the density of transversely polarised quarks inside a transversely polarised nucleon. The transversity distribution can be accessed through Semi-Inclusive Deep Inelastic Scattering (SIDIS) processes, measuring in the final state not only the scattered muon but also one or more of the resulting hadrons.

In the '70 Cahn has pointed out the importance of the azimuthal dependences arising from a non zero intrinsic transverse momentum (k_T) of the partons [4]. In the following years, along with the pQCD parton model framework, a set of Transverse Momentum Dependent Parton Distribution Functions (TMD PDFs), Fragmentation Functions (FFs) and their factorization scheme has been established [5–7]. The generalised parton distributions (GPDs) were introduced in the '90s [8], allowing the description of the radial position distributions of partons at a specific longitudinal momentum within the nucleon. Both TMD PDFs and GPDs can be related to the orbital angular momentum contributions of quarks and gluons to the nucleon spin.

1.2 Longitudinal Nucleon Structure - Experimental Contributions

Since the '70s there have been several experiments contributing to the understanding of the nucleon's spin structure. They are mainly polarised deep inelastic lepton-nucleon scattering and proton-proton scattering experiments. In 2015 COMPASS performed a polarised Drell-Yan (DY) experiment using pion-proton interactions.

The first high energy polarised proton beams were achieved at the Zero-Gradient Synchrotron (ZGS) at the Argonne National Laboratory (ANL) in 1973. The results from the experiments at ANL showed large Single Spin Asymmetries (SSA) in polarised proton-proton scattering [9, 10].

The SLAC experiments were pioneers in the spin physics field measuring the lepton-nucleon scattering. The first measurements of the nucleon spin structure were performed in the late '70s by the experiments E80 [11, 12] and E130 [13, 14]. A sequence of new experiments, E142 [15], E143 [16], E154 [17] and E155 [18, 19] were performed with higher precision also at SLAC.

In parallel with the SLAC experiments, CERN experiments also started taking data in the '80s. The first CERN experiment contributing to the spin physics studies was the European Muon Collaboration (EMC). The results from the EMC were very puzzling, suggesting that the naive parton picture that the contribution from the spin of the quarks to the spin of the nucleon is dominant, is actually very small [1, 20]. In the beginning of the '90s the Spin Muon Collaboration (SMC) appeared as a successor of the EMC. It has performed the first determination of the individual quark distributions for different flavours, through the SIDIS process [21, 22], measuring the hadrons in the final state in coincidence with the scattered lepton. These hadrons, namely the pions and kaons, carry the information about the struck quark or anti-quark from the nucleon.

In the '90s, at the Fermi National Accelerator Laboratory (FNAL or FermiLab), a fixed target experiment using polarised proton beams at 200 GeV/c performed a proton-proton scattering experiment with 20 times higher energy than at ANL.

All these experiments completed their data taking and analyses in the last decade. But the investment in this field did not finish. It was important to understand the small value of the contribution from the spin of the quarks to the spin of the nucleon. This motivated several more experiments. In 1995 the HERMES experiment at DESY started, which has been vastly contributing for the knowledge of the nucleon spin structure. It has published results for the proton, neutron and deuteron structure functions as well as the quark flavour contribution to them [23, 24]. The COMPASS experiment at CERN has started to take data in 2002 and finished its first stage in 2012. Its data also contributed for the knowledge of the spin dependent structure functions of deuterons [2] and protons [25], as well as the quark flavour contribution [26]. The JLab experiments started to take data in 1999 in three dedicated halls, the HALL A [27], the HALL B, also known as Continuous Electron Beam Accelerator Facility (CEBAF) Large Acceptance Spectrometer (CLAS) [28], and the HALL C.

In 2002, the Relativistic Heavy Ion Collider (RHIC) at the Brookhaven National Laboratory (BNL) started functioning, being the first collider with the capability to collide polarised protons. Three experiments at RHIC were dedicated to polarisation studies. The BRAHMS experiment studied only transversely polarised proton collisions and finished data taking in 2006. PHENIX and STAR continue taking data with longitudinally and transversely polarised proton beams.

JLab was upgraded, increasing the available energy to 12 GeV and in addition to the HALLS A, B and C, a new HALL D, smaller in acceptance, has been created.

Experiment	x	Q^2 [(GeV/c ²) ²]	Δu	Δd	$\Delta \bar{u}$	$\Delta \bar{d}$
SMC	0.003 – 0.7	10	$0.72 \pm 0.11 \pm 0.06$	$-0.45 \pm 0.30 \pm 0.25$	$0.01 \pm 0.05 \pm 0.01$	$0.01 \pm 0.14 \pm 0.12$
HERMES	0.023 – 0.6	2.5	$0.60 \pm 0.07 \pm 0.04$	$-0.17 \pm 0.07 \pm 0.05$	$0.00 \pm 0.04 \pm 0.02$	$-0.05 \pm 0.03 \pm 0.01$
COMPASS	0.004 – 0.7	3	$0.67 \pm 0.03 \pm 0.03$	$-0.28 \pm 0.06 \pm 0.03$	$0.02 \pm 0.02 \pm 0.01$	$-0.05 \pm 0.03 \pm 0.02$
			Δs			
HERMES	0.02 – 0.6	2.5	$0.037 \pm 0.019 \pm 0.027$			
COMPASS	0.004 – 0.7	3	$-0.01 \pm 0.01 \pm 0.01$			

Table 1.1: First moments for valence and sea quarks, u , d and s , from SMC [22], HERMES [24, 29] and COMPASS [26]. The values were obtained in the measured x range, quoted in the second column. For the sea quarks the values were obtained from data up to $x = 0.3$. The extractions were done for the Q^2 quoted in the third column.

All these experiments have contributed to improve the knowledge about the spin structure of the nucleon. Nowadays the proton spin puzzle is still unsolved. The data is well in agreement among all experiments. But there are still a lot of questions to answer, such as: how is the spin 1/2 of the proton built up from the spin and orbital angular momentum of the quarks and gluons; why is the quark’s spin contribution so small; is the proton spin a valence quark effect, a sea quark effect or a gluon effect; can we extract information about the quark and gluon orbital angular momentum from experiments with minimal model dependence.

The three experiments SMC [22], HERMES [29] and COMPASS [26] contributed to the extraction of the flavour dependent polarised quark distributions for valence and sea quarks, through the SIDIS process. They measured asymmetries between polarised and unpolarised distributions, which are described as convolutions of PDFs and FFs, the probability of a quark with a certain flavour to fragment in a specific hadron. Their results are shown in Table 1.1. Both HERMES [24] and COMPASS [26] have contributed to the strangeness measurement. The COMPASS results are shown in Fig. 1.1 together with the predictions from the DSSV global analysis calculated at NLO [30]; the FFs were extracted from a global fit from the DeFlorian-Stratmann-Sassot (DSS) group [31]. The distributions for sea quarks, u , d and s are very small, compatible with zero.

The gluon polarisation was measured for the first time by the FNAL E581/704 collaboration in a very indirect way, using a polarised proton beam and a polarised proton target. Their result [32] suggested that the gluon contribution is not very large in the region $0.05 \lesssim x_g \lesssim 0.35$. Also HERMES [33] and SMC [34] have contributed to the gluon polarisation measurements, performing high- p_T analyses. COMPASS has contributed to this measurement with two different analyses. The high- p_T analysis [35] and the open charm analysis [36], [37]. The most recent results on gluon polarisation belong to HERMES [38] and COMPASS [39]. The results from these experiments are summarized in Table 1.2. The gluon polarisation is very small and with large uncertainties, it is compatible with zero in some cases, in the measured range. However, the integral is positive and could be significant if the RHIC data is taken into account in a global analysis [40]. This result suggests a significant contribution of the gluon spin to the proton spin, being a key ingredient for the spin puzzle. Therefore, the gluon helicity may limit the amount of orbital angular momentum required to balance the proton spin.

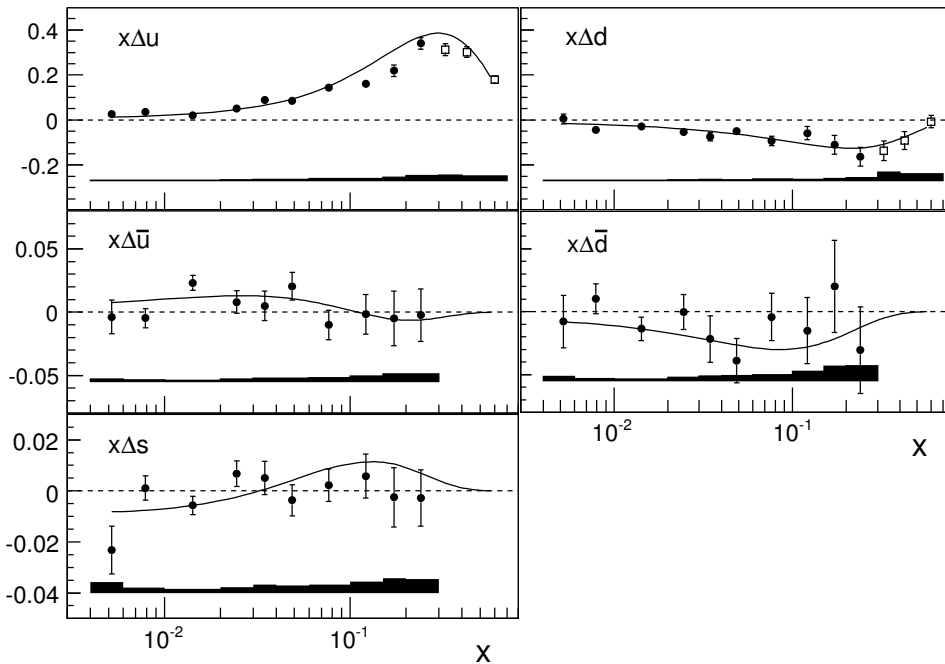


Figure 1.1: The quark helicity distributions at $Q^2 = 3 \text{ (GeV}/c^2)^2$. The values for $x < 0.3$ are derived at LO from the COMPASS spin asymmetries using the DSS fragmentation functions [31]. Those at $x > 0.3$ are derived assuming $\Delta\bar{q} = 0$, see [26] for more details. The curves show the predictions of the DSSV fit calculated at NLO [30].

Experiment	$\langle x_g \rangle$	$\langle \mu^2 \rangle \text{ (GeV}/c)^2$	$\Delta g/g$
HERMES	0.17	2	$0.41 \pm 0.18 \pm 0.03$
HERMES	0.22	1.35	$0.049 \pm 0.034 \pm 0.010^{+0.126}_{-0.099}$
SMC	0.07	3	$-0.20 \pm 0.28 \pm 0.10$
COMPASS (high- p_T - LO)	0.095	3	$0.024 \pm 0.089 \pm 0.057$
COMPASS (all- p_T - LO)	0.09	3	$0.125 \pm 0.060 \pm 0.063$
COMPASS (open charm - LO)	0.11	13	$-0.06 \pm 0.21 \pm 0.08$
COMPASS (open charm - NLO)	0.20	13	$-0.13 \pm 0.15 \pm 0.15$

Table 1.2: Results for the gluon polarisation from DIS experiments.

1.3 Transverse Nucleon Structure

After the quarks and gluon polarisation studies have been performed, the next possible contribution to be addressed is the orbital angular momentum. This motivated new theoretical and experimental investigations of the three dimensional structure of the nucleon. Deep-Virtual Compton Scattering (DVCS) allows the access to the GPDs and the study of the three dimensional structure of the nucleon in the position space. HERMES and JLab experiments were pioneers in the study of the GPDs. The correlations between the intrinsic transverse momentum of the partons, their spin and the spin of the nucleon can be accessed measuring the spin asymmetries from lepton-nucleon and hadron-hadron scatterings. These asymmetries are proportional to convolutions of TMD PDFs and FFs or just to TMD PDFs in the case of the DY process. The TMD PDFs describe the three dimensional structure of the nucleon in the momentum space; they depend on x , Q^2 and k_T . The FFs describe the probability of a given

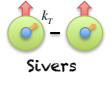
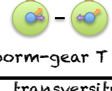
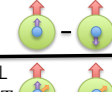
		Nucleon		
		unpolarised	longitudinally polarised	transversely polarised
Quark	unpolarised	f_1  unpolarised PDF		f_{1T}^\perp  Sivers
	longitudinally polarised		g_1  helicity	g_{1T}^\perp  worm-gear T
	transversely polarised	h_1^\perp  Boer-Mulders	h_{1L}^\perp  worm-gear L	h_1 transversity  h_{1T}^\perp pretzelosity 

Figure 1.2: Parton distribution functions organised according to the nucleon polarisation and the quarks polarisation.

quark to fragment into a specific hadron with a certain energy fraction. COMPASS, HERMES, JLab and RHIC contributed for the study of the TMD PDFs.

As mentioned before, high transverse asymmetries associated with spin-momentum correlations were observed by the first time in the '70s at ANL and these measurements were confirmed by subsequent experiments. However, only in the '90s a theoretical framework was developed to describe them.

In Quantum ChromoDynamics (QCD) eight quark TMD PDFs are needed to describe the nucleon structure at leading twist [41, 42]. They are grouped in Fig. 1.2. Three distributions survive the integration over the intrinsic transverse momentum k_T of quarks inside the nucleon. They are the unpolarised PDF $f_1(x)$, the helicity distribution $g_1(x)$ and the transversity distribution $h_1(x)$. The other five distributions do not survive the integration over k_T , they describe correlations between the quark's transverse momentum, its spin and the spin of the nucleon. The distribution $h_1^\perp(x, k_T)$ is called the Boer-Mulders function; $f_{1T}^\perp(x, k_T)$ is the Sivers function; $h_{1T}^\perp(x, k_T)$ is the pretzelosity function; and $h_{1L}^\perp(x, k_T)$ and $g_{1T}^\perp(x, k_T)$ are the worm-gear functions, which link two perpendicular spin directions.

The three distributions describing transversely polarised quarks, denoted by h , are chiral-odd. Measurable quantities are chiral-even. In order to be able to access them experimentally, they have to appear convoluted with other chiral-odd distribution. This is possible in the DY process, where two chiral-odd PDFs appear convoluted, and in SIDIS where a chiral-odd PDF appears convoluted with the Collins FF.

Experimental data on the TMD PDFs have been mostly obtained from SIDIS, measuring asymmetries which are related to the convolution of TMD PDFs with the unpolarised fragmentation function $D(z, p_T)$ or, in the case of chiral-odd TMD PDFs, with a chiral-odd Collins FF $H_{1T}^\perp(z, p_T)$.

COMPASS, HERMES and JLab experiments have obtained results on TMDs, from proton, deuteron and neutron data. These results are listed in Table 1.3.

Modulation	TMD \otimes FF	Collaboration	Data	\sqrt{s}	Target	Final state hadrons
$A_{UT}^{\sin(\phi+\phi_S)}$	$h_1 \otimes H_1^\perp$ transversity \otimes Collins FF	COMPASS HERMES JLab - HALL A	2002 – 2004 2007, 2010 2002 – 2003 2002 – 2005 2008 – 2009	18 7.4 3.5	${}^6\text{LiD}$ NH ₃ H ${}^3\text{He}$	h^\pm [43], π^\pm, K^\pm, K^0 [44] h^\pm [45, 46] π^\pm, K^\pm, K^0 [47] π^\pm [48] π^\pm, π^0, K^\pm [49] π^\pm [50]
$A_{UT}^{\sin(\phi-\phi_S)}$	$f_{1T}^\perp \otimes D$ Sivers \otimes unpol. FF	COMPASS HERMES JLab - HALL A	2002 – 2004 2007, 2010 2002 – 2003 2002 – 2005 2008 – 2009	18 7.4 3.5	${}^6\text{LiD}$ NH ₃ H ${}^3\text{He}$	h^\pm [43], π^\pm, K^\pm, K^0 [44] h^\pm [45, 51] π^\pm, K^\pm, K^0 [47] π^\pm [48] π^\pm, π^0, K^\pm [52] π^\pm [50]
$A_{UU}^{\cos(2\phi)}$	$h_1^\perp \otimes H_1^\perp$ Boer-Mulders \otimes Collins FF	COMPASS HERMES JLab - CLAS	2002 – 2006 2000 – 2007 2001 – 2002	18 7.4 3.5	${}^6\text{LiD}$ H, D H	h^\pm [53] h^\pm, π^\pm, K^\pm [54] π^+ [55]
$A_{UT}^{\sin(3\phi-\phi_S)}$	$h_{1T}^\perp \otimes H_1^\perp$ pretzelosity \otimes Collins FF	COMPASS HERMES	2002 – 2004 2007, 2010 2002 – 2005	18 7.4	${}^6\text{LiD}$ NH ₃ H	h^\pm [56] h^\pm [57, 58] π^\pm, π^0, K^\pm [59]
$A_{UL}^{\sin(2\phi)}$	$h_{1L}^\perp \otimes H_1^\perp$ worm-gear 1 \otimes Collins FF	COMPASS HERMES JLab - CLAS	2002 – 2004 1996 – 1997 1998 – 2000 2001	18 7.4 3.5	${}^6\text{LiD}$ H D NH ₃	h^\pm [60] π^\pm [61] π^0 [62] π^\pm, π^0, K^+ [63] π^\pm, π^0 [64]
$A_{LT}^{\cos(\phi-\phi_S)}$	$g_{1T}^\perp \otimes D$ worm-gear 2 \otimes unpol. FF	COMPASS HERMES JLab - HALL A	2002 – 2004 2007, 2010 2003 – 2005 2008 – 2009	18 7.4 3.5	${}^6\text{LiD}$ NH ₃ H ${}^3\text{He}$	h^\pm [56] h^\pm [57, 58] π^\pm, π^0, K^\pm [65] π^\pm [66]

Table 1.3: Results on TMDs from COMPASS, HERMES and JLab experiments.

1.3.1 The Sivers Distribution

The Sivers distribution was proposed for the first time by Sivers in 1990 [67] as an attempt to explain the large single-spin asymmetries observed in the '70s [9], [10].

The Sivers distribution describes the correlation between the intrinsic transverse momentum k_T of the quark, the spin S and the momentum p of its parent nucleon, $S \cdot (k_T \times \hat{p})$. The k_T dependence is related to the non-zero parton orbital angular momentum in the nucleon.

The Sivers distribution is odd under time reversal and because of this property it was believed for more than a decade that this correlation would be forbidden. But in 2002 Brodsky and colleagues showed that the Sivers effect could be present in SIDIS [68] and in DY [69]. In SIDIS because of the final-state interactions resulting from the gluon exchange between the outgoing quark and the target spectator system. In DY because of the initial-state interactions resulting from the gluon exchange between the incoming quark and the target spectator system. In the same year Collins demonstrated that the Sivers distribution is reversed in sign in hadron induced hard processes, such as DY in comparison with SIDIS, which violates the naive universality of the TMD PDFs [70].

The SIDIS measurements showed Sivers asymmetries at the level of 5% for the proton target. The COMPASS results are shown in Fig. 1.3 for charged pions and kaons, and also for neutral kaons. Since in the proton (uud) the scattering of the u quarks dominates (8:1, due to the e_q^2 factor), the positive Sivers amplitude for π^+ ($u\bar{d}$) suggests a positive Sivers function for u quarks. The vanishing amplitude for π^- ($\bar{u}d$) requires cancellation effects, which are supported by the deuteron data. The magnitude of the Sivers asymmetry of the proton for K^+ ($u\bar{s}$) is higher than for π^+ , while naively they were expected to be similar since both have a valence u quark. This difference points to a significant role of the sea quarks. The JLab measurements favor a

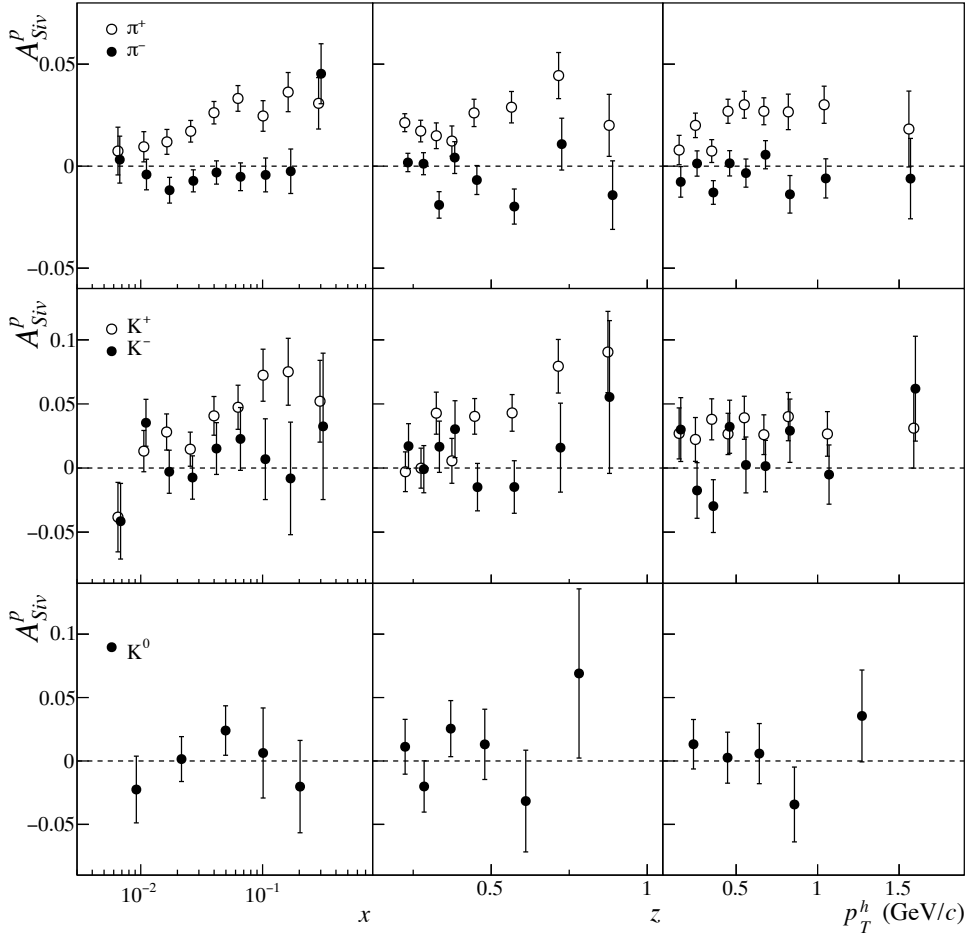


Figure 1.3: The Siverts asymmetries for charged pions (top), charged kaons (middle) and neutral kaons (bottom) as a function of x , z and p_T^h from COMPASS [47].

negative amplitude for π^+ from neutron (udd), but still compatible with zero, and an asymmetry compatible with zero for π^- . The Siverts asymmetries from deuteron were all compatible with zero for charged hadrons, both pions and kaons and neutral kaons. This also supports a negative d -quark Siverts distribution.

The comparison between COMPASS and HERMES results for proton are in Fig. 1.4. A smaller Siverts amplitude is found for COMPASS, which has a higher Q^2 coverage, 2 to 3 times larger than HERMES in the same x range. These results suggest a strong dependence on Q^2 , which motivated repeating the COMPASS SIDIS analysis in several Q^2 ranges. This analysis is one of the topics of this thesis, and it will be discussed in detail.

Several global fits were performed to extract the Siverts distributions including SIDIS and $p-p$ data [71–73]. The comparison between the Siverts asymmetries for pions from COMPASS and these global fits is shown in Fig. 1.5. They reproduce well the COMPASS results. The extracted Siverts distributions from the global fit presented in [71] are shown in Fig. 1.6, for u and d quarks using the two evolution schemes, the so called DGLAP evolution and TMD evolution, the first assumes that the k_T dependent term of the Siverts function is not affected by the Q^2 evolution.

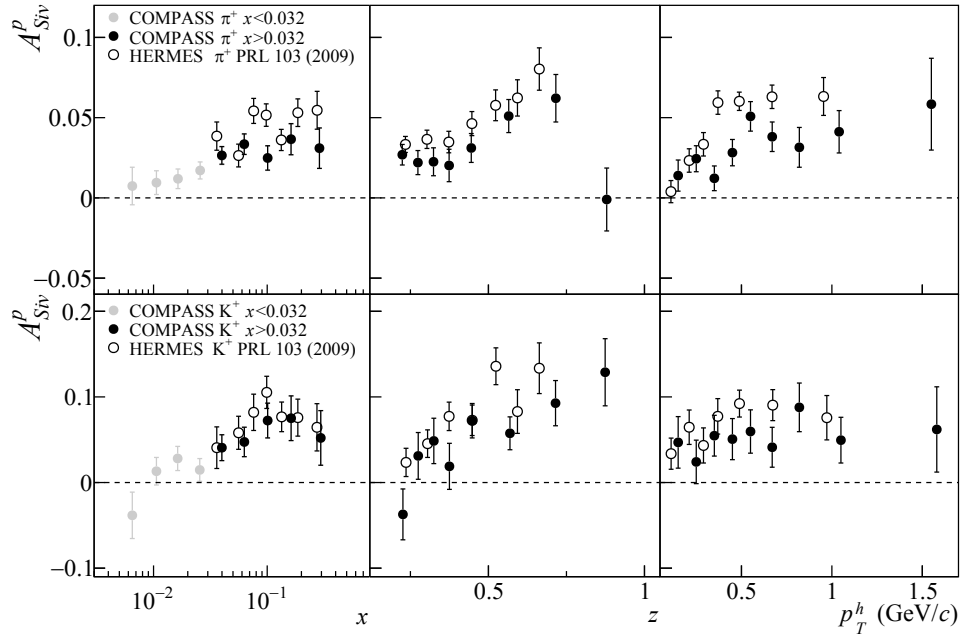


Figure 1.4: The Sivers asymmetries for positive pions (top) and kaons (bottom) on proton as a function of x , z and p_T^h , requiring $x > 0.032$. The COMPASS results [47] are compared to HERMES results [52].

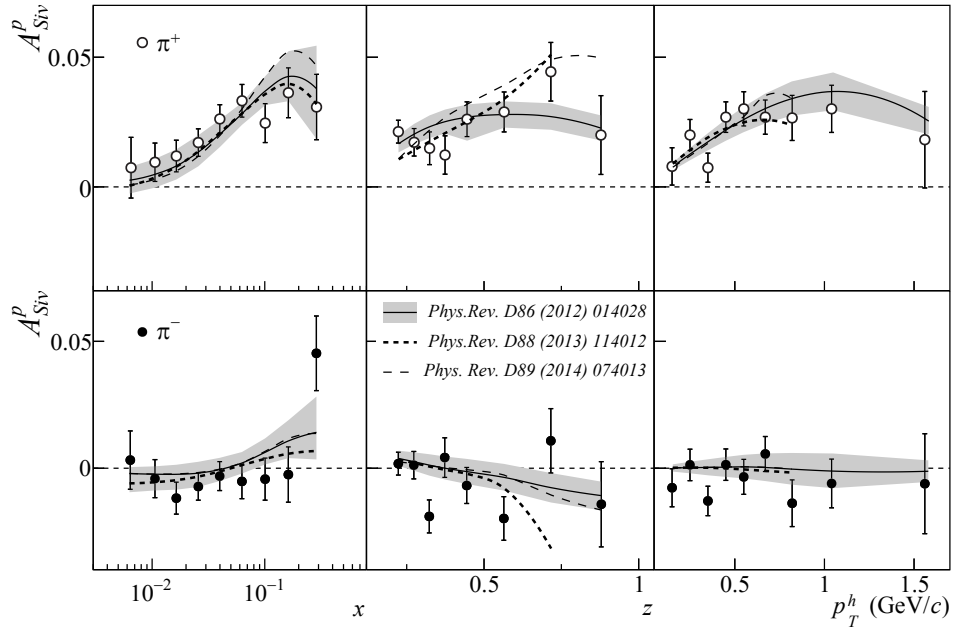


Figure 1.5: Comparison between the Sivers asymmetries for pions and three different global fits [72–74].

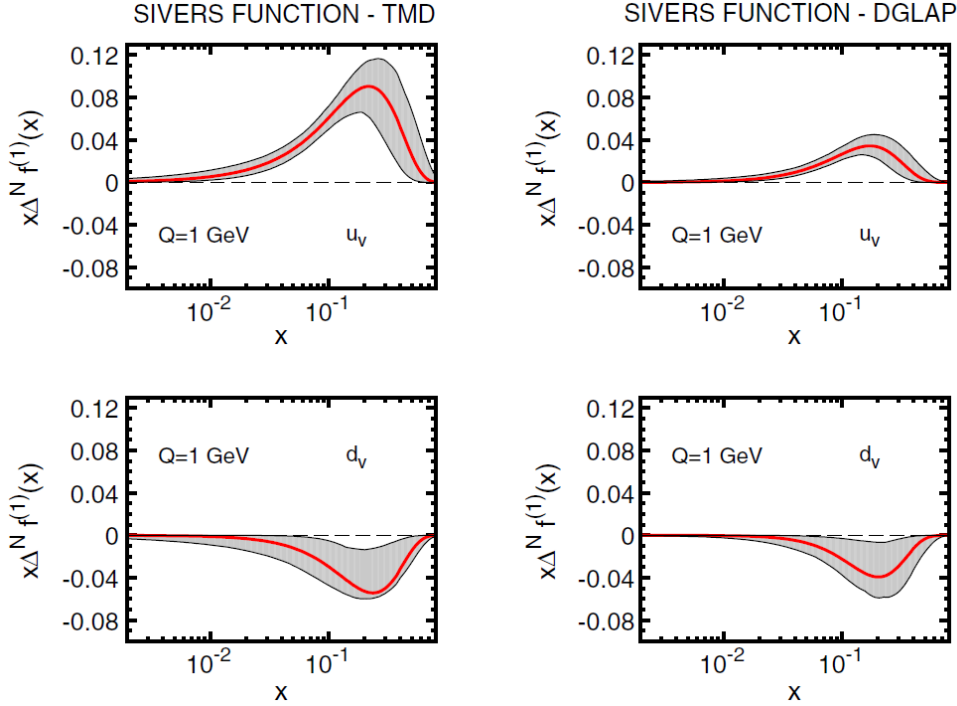


Figure 1.6: Sivers functions of the u -quark and the d -quark [74].

1.3.2 The Boer-Mulders Distribution

The Boer-Mulders distribution, proposed in 1998 by Boer and Mulders [75], describes the correlation between transversely polarised quarks in an unpolarised nucleon and its intrinsic transverse momentum. As referred previously this distribution is chiral-odd, and it appears coupled with another chiral-odd distribution. In SIDIS it is convoluted with the Collins FF. In DY it is convoluted with the Boer-Mulders function from the other initial-state hadron taking part in the reaction.

The Boer-Mulders distribution is also T-odd, as the Sivers distribution, thus it is expected to change sign when accessed by SIDIS or DY processes.

The NA10 experiment pioneered in the measurement of the azimuthal distributions sensitive to the Boer-Mulders effect through the DY process [76, 77]. They measured the three azimuthal modulations present in the unpolarised DY cross-section. Their result using a negative pion beam at 194 GeV/c is shown in Fig. 1.7, where ν is the modulation on $\cos 2\phi$, related with the Boer-Mulders effect, being the ϕ angle defined in the Collins-Soper frame, described in section 1.6. This result violated the Lam-Tung sum rule at high p_T , which predicted that $1 - \lambda = 2\nu$ [78].

Other DY experiments also contributed for these measurements, namely the E615 Collaboration [79] and the E866/NuSea Collaboration [80, 81]. The Boer-Mulders distributions have been extracted using DY data [82, 83], as shown in Fig. 1.8 for u , d , \bar{u} and \bar{d} quarks. For this extraction the Boer-Mulders functions are assumed to have the same behaviour as the unpolarised functions $f_1^q(x)$, and in the figure the dashed lines represent an upper limit for the Boer-Mulders functions.

Through the SIDIS process several experiments contributed for the measurement of the Boer-Mulders distribution, such as COMPASS [53], HERMES [54] and CLAS at JLab [55]. The COMPASS result is in Fig. 1.9. The difference between positive and negative hadrons is evident, the asymmetry is slightly larger for negative hadrons. HERMES measured larger

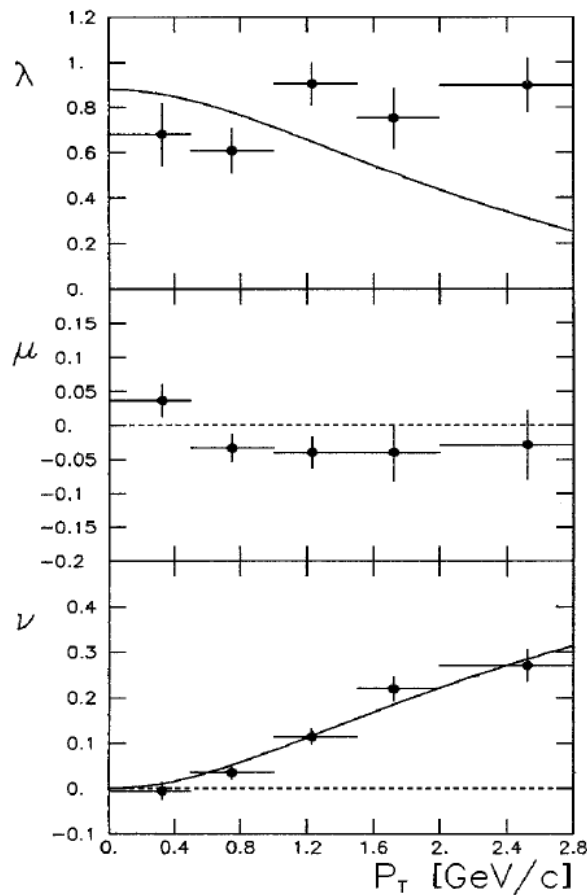


Figure 1.7: Azimuthal modulations from DY cross-section measured by the NA10 collaboration, using a negative pion beam at 194 GeV/c and a tungsten target.

amplitudes for kaons than for pions, which suggests a significant contribution from sea quarks, in particular from strange quarks. The amplitude for π^- has the opposite sign with respect to the amplitude for K^- . They have measured similar effects for proton and deuteron. The interpretation of the Boer-Mulders amplitudes from SIDIS is complicated, since it is mixed with the Cahn effect, which is nevertheless expected to be small at COMPASS kinematics [4, 84]; this effect accounts for the quarks intrinsic transverse momentum in the target nucleon and the fact that the produced hadrons might acquire transverse momentum during the fragmentation process. The first attempt to describe the observed effect in terms of the Cahn effect and the Boer-Mulders effect could not describe data well [85].

1.3.3 The Transversity Distribution and the Collins Fragmentation Function

The transversity distribution describes the transverse polarisation of quarks within a transversely polarised nucleon. As previously mentioned, this function survives the integration over the quarks intrinsic transverse momentum. Transversity can be accessed through the Collins effect in SIDIS, and also in DY.

The Collins Fragmentation Function describes a spin-momentum correlation in the hadronization process, $s_q \cdot (k_T \times p_T)$ [86, 87]. The produced hadron has a transverse momentum p_T with

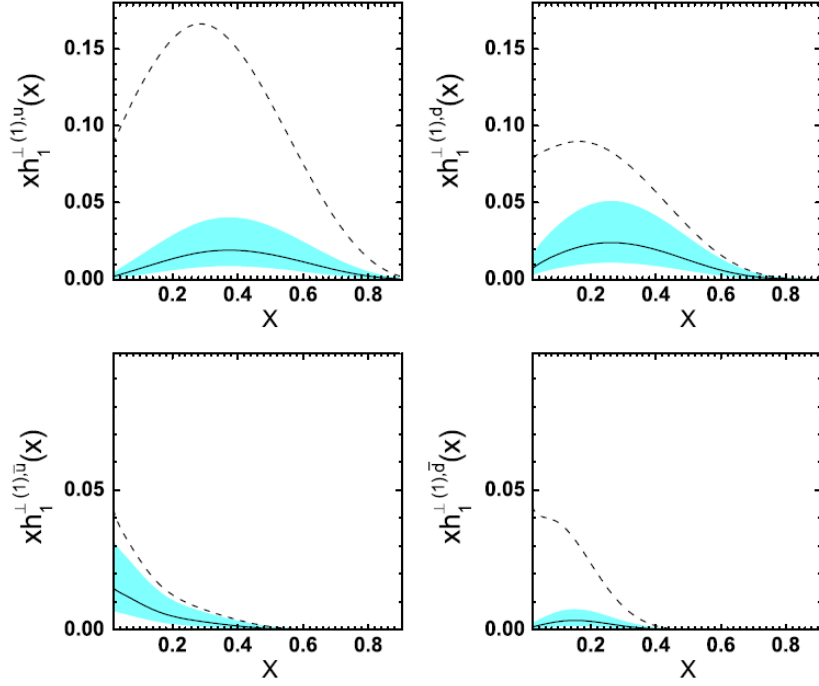


Figure 1.8: Boer-Mulders functions for u , d , \bar{u} and \bar{d} quarks for $Q^2 = 1$ $(\text{GeV}/c^2)^2$ (solid line). The dashed lines show $\frac{\langle p_T \rangle}{2M} x f_1^q(x)$.

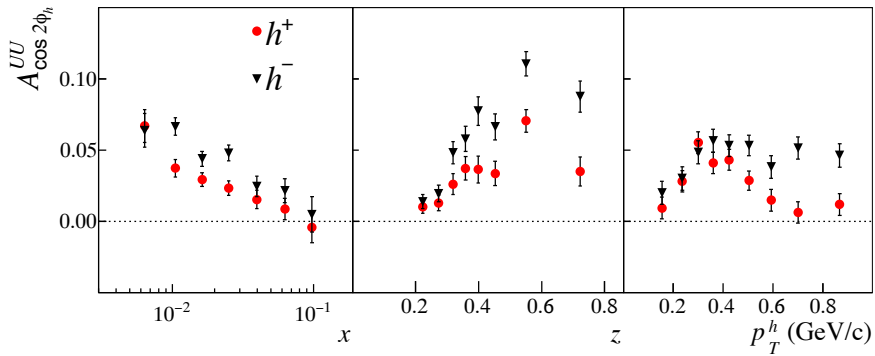


Figure 1.9: COMPASS deuteron results for $A_{\cos(2\phi_h)}^{UU}$ asymmetry for positive (red points) and negative (black triangles) hadrons as function of x , z and p_T^h . The error bars show statistical uncertainties only.

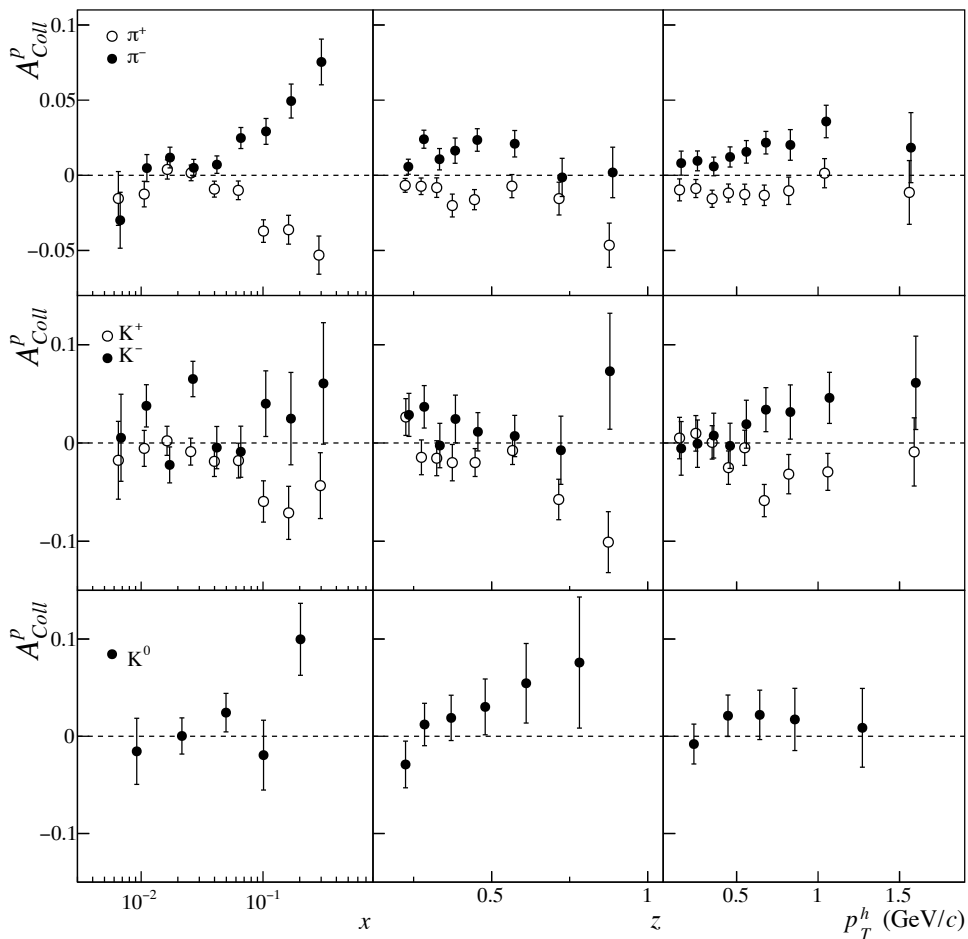


Figure 1.10: The Collins asymmetries for charged pions (top), charged kaons (middle) and neutral kaons (bottom) as a function of x , z and p_T^h from COMPASS [47].

respect to the intrinsic transverse momentum k_T of the transversely polarised struck quark with spin s_q in the parent nucleon.

The Collins FF has been investigated in SIDIS and in e^+e^- annihilation. This is a chiral-odd function and thus it appears together with another chiral-odd function. In SIDIS it appears convoluted with the transversity distribution or with the Boer-Mulders distribution. In e^+e^- annihilation it appears convoluted with a second Collins FF from the opposite jet.

In SIDIS three experiments contributed to the measurement of the transversity and the Collins FF: HERMES [48, 49], COMPASS [43–47] and JLab HALL A [50]. Their results are in good agreement. The COMPASS result for charged pions and kaons, and for neutral kaons is shown in Fig. 1.10. The Collins amplitude for negative pions is similar in size to the amplitude for positive pions but with the opposite sign. This may point for a similar size and opposite sign of the unfavoured Collins FF to the favoured Collins FF. BELLE [88, 89] and BABAR [90] have contributed to the Collins FF measurement in e^+e^- annihilation. They measured non-zero Collins functions for charged pions.

In Fig. 1.11 are shown the transversity distributions for u and d quarks and the favoured and unfavoured Collins FFs extracted using COMPASS, HERMES and BELLE data [91].

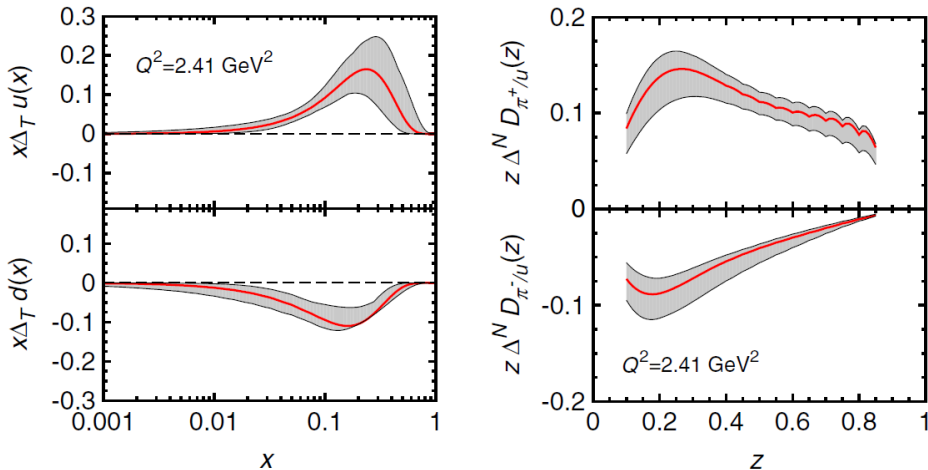


Figure 1.11: On the left side are the transversity distributions for u and d quarks, with their uncertainty bands (shaded areas), obtained from a fit to the SIDIS and e^+e^- data. On the right side are the favored and unfavored Collins functions. All results are given at $Q^2 = 2.41 \text{ (GeV}/c^2)^2$.

1.3.4 Breakthroughs on TMDs

In the last decade the study and understanding of the intrinsic transverse momentum and spin momentum correlations in QCD has been growing mainly motivated by the theoretical contributions supporting the non-vanishing T-odd TMD distributions [68, 70].

Collins has given definitions of the TMD distributions as well defined objects. This allowed the QCD evolution taking into account the TMDs to be applied rigorously for the first time with separately identifiable TMD PDFs and FFs. Based on that, the previous models and fits were redone taking into account this consistent TMD approach, for unpolarised TMD PDFs and FFs [92], and for the Sivers distribution [93]. This TMD evolution is now being applied to the phenomenological studies, starting with Sivers [74, 94], and will be crucial to interpret and compare results from the different experiments at different phase spaces. The main goal is the definition of the TMDs in terms of (x, k_T, Q^2) for all the quark flavours. The new definitions of TMDs made possible a determination of the hard parts for SIDIS and DY at next-to-leading order [95], which will contribute also for the improvement of the phenomenology. The unpolarised DY data currently available covers a wide mass range from around $4 \text{ GeV}/c^2$ to the Z boson mass, which is very promising for the study of the Q^2 evolution of TMDs. There are efforts on the lattice calculations of the Sivers and Boer-Mulders [96]. The implementation of the TMDs in MC event generators is under discussion [97, 98].

1.4 Recent and future projects

Since May 2012 CEBAF at JLab is undergoing a major upgrade to run with e^- at $12 \text{ GeV}/c$. HALL A and C suffered an upgrade and HALL B was completely renewed. There is also a new experimental hall, HALL D. The CEBAF commissioning has already started; in December 2015 a $12 \text{ GeV}/c$ electron beam was delivered to the newest experimental hall with success. The commissioning is expected to be complete in 2016. The new JLab data will contribute to improve the knowledge about the TMDs.

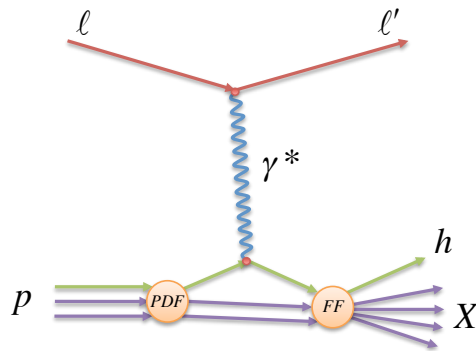


Figure 1.12: Diagram of the SIDIS process.

At CERN, COMPASS is now taking data which will contribute for both the TMD and GPD fields. The polarised DY experiment was performed in 2015, with a high intensity negative pion beam and a transversely polarised ammonia target. The years of 2016 and 2017 will be dedicated to the DVCS run and the extraction of the GPDs using positive and negative muon beams and an unpolarised liquid hydrogen target. In parallel, also SIDIS data will be taken on the pure unpolarised hydrogen target.

There are plans for a polarised fixed target DY program at Fermilab following the SeaQuest experiment, which completed the data taking in 2014.

There are a variety of possibilities for the medium-term future of RHIC, one of them being the use of a polarised ^3He source, giving the opportunity to study the neutron spin structure for the first time in colliders. Concerning the long-term future a possible Electron-Ion collider (EIC) is under consideration, which is being discussed in connection with the future of RHIC and of JLab.

There are other facilities interested in performing polarisation measurements, as the FAIR facility in Germany, the J-PARC in Japan, and the NICA in Russia.

1.5 The SIDIS Cross Section

In the SIDIS process a lepton scatters off a nucleon with the production of a hadron in the final state. Fig. 1.12 illustrates the process, which is defined by

$$\ell(l) + N(p) \rightarrow \ell'(l') + h(p_h) + X \quad (1.6)$$

where ℓ is the lepton beam, ℓ' is the scattered beam and l and l' are the initial and the final state lepton four-momenta, N is the nucleon target and p is the corresponding four-momentum, h represents the produced hadron with a four-momentum p_h and X denotes the accompanying produced particles.

The cross section was derived [99, 100] considering the one-photon exchange approximation and neglecting the lepton mass. The relevant kinematic variables are the nucleon target momentum fraction carried by the interacting quark, $x = Q^2/2p \cdot q$, the lepton beam momentum fraction carried by the virtual photon, $y = p \cdot q/p \cdot l$, and the photon energy fraction carried by the final state hadron, $z = p \cdot p_h/p \cdot q$.

In the above formulas $q = l - l'$ denotes the exchanged virtual photon four-momentum and $Q^2 = -q^2$ the photon virtuality. The cross section is defined in the target rest frame presented in Fig. 1.13, where the z -axis is defined along the virtual photon momentum, the x -axis is defined in the lepton scattering plane and the y -axis is perpendicular to the (z, x) plane to

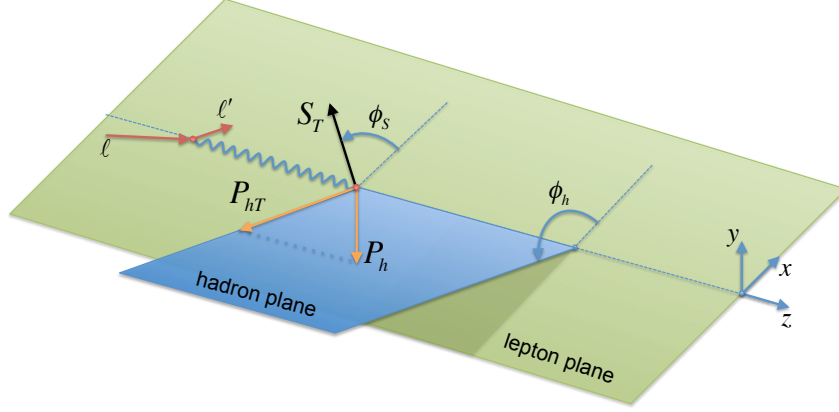


Figure 1.13: Definition of the azimuthal angles on the target rest frame.

form a right handed frame. p_{hT} and S_T are the transverse parts of p_h and S with respect to the virtual photon momentum, and ϕ_h and ϕ_s are the corresponding azimuthal angles. The cross section can be written as

$$\begin{aligned}
 \frac{d\sigma}{dx dy dz d\psi d\phi_h dp_{hT}^2} &= \frac{\alpha^2}{xyQ^2} \frac{y^2}{2(1-\varepsilon)} \left(1 + \frac{\gamma^2}{2x} \right) \left\{ F_{UU,T} + \varepsilon F_{UU,L} \sqrt{2\varepsilon(1+\varepsilon)} \cos\phi_h F_{UU}^{\cos\phi_h} + \right. \\
 &\quad + \varepsilon \cos(2\phi_h) F_{UU}^{\cos 2\phi_h} + P_l \sqrt{2\varepsilon(1-\varepsilon)} \sin\phi_h F_{LU}^{\sin\phi_h} \\
 &\quad + S_L \left[\sqrt{2\varepsilon(1+\varepsilon)} \sin\phi_h F_{UL}^{\sin\phi_h} + \varepsilon \sin(2\phi_h) F_{UL}^{\sin 2\phi_h} \right] \\
 &\quad + S_L P_l \left[\sqrt{1-\varepsilon^2} F_{LL} + \sqrt{2\varepsilon(1-\varepsilon)} \cos\phi_h F_{LL}^{\cos\phi_h} \right] \\
 &\quad + S_T \left[\sin(\phi_h - \phi_s) \left(F_{UT,T}^{\sin(\phi_h - \phi_s)} + \varepsilon F_{UT,L}^{\sin(\phi_h - \phi_s)} \right) \right. \\
 &\quad \quad + \varepsilon \sin(\phi_h + \phi_s) F_{UT}^{\sin(\phi_h + \phi_s)} + \varepsilon \sin(3\phi_h - \phi_s) F_{UT}^{\sin(3\phi_h - \phi_s)} \\
 &\quad \quad \left. + \sqrt{2\varepsilon(1+\varepsilon)} \sin\phi_s F_{UT}^{\sin\phi_s} + \sqrt{2\varepsilon(1+\varepsilon)} \sin(2\phi_h - \phi_s) F_{UT}^{\sin(2\phi_h - \phi_s)} \right] \\
 &\quad + S_T P_l \left[\sqrt{1-\varepsilon^2} \cos(\phi_h - \phi_s) F_{LT}^{\cos(\phi_h - \phi_s)} + \sqrt{2\varepsilon(1-\varepsilon)} \cos\phi_s F_{LT}^{\cos\phi_s} \right. \\
 &\quad \quad \left. + \sqrt{2\varepsilon(1-\varepsilon)} \cos(2\phi_h - \phi_s) F_{LT}^{\cos(2\phi_h - \phi_s)} \right] \left. \right\} \tag{1.7}
 \end{aligned}$$

where

$$\varepsilon = \frac{1 - y - \frac{1}{4}\gamma^2 y^2}{1 - y + \frac{1}{2}y^2 + \frac{1}{4}\gamma^2 y^2} \tag{1.8}$$

is the ratio of the longitudinal to the transverse photon flux and $\gamma = \frac{2Mx}{Q}$, with M being the nucleon mass. The parameter α is the fine structure constant, P_l is the lepton beam polarisation, ψ is the azimuthal angle of the scattered lepton around the lepton beam axis with respect to an arbitrary fixed direction, which in the case of a transversely polarised target is the spin direction. The relation between $d\psi$ and $d\phi_s$ can be found in [101], and for DIS kinematics $d\psi \approx d\phi_s$. The cross section includes 18 structure functions, the F 's in the expression, with the superscript corresponding to the azimuthal asymmetry described by the structure function and the first subscript to the polarisation of the beam, the second to the polarisation of the target and the third to the polarisation of the virtual photon; ‘‘U’’ stands for unpolarised, ‘‘L’’ longitudinal polarised and ‘‘T’’ transversely polarised. Considering only the transverse polarisation dependent azimuthal modulations, there are five single target spin dependent modulations and

three double beam-target spin dependent ones. The corresponding structure functions can be interpreted as convolutions of parton distribution functions and fragmentation functions as:

$$F_{UT,L}^{\sin(\phi_h - \phi_S)} = 0 \quad (1.9)$$

$$F_{UT,T}^{\sin(\phi_h - \phi_S)} \propto f_{1T}^{\perp q} \otimes D_{1q}^h \quad (1.10)$$

$$F_{UT}^{\sin(\phi_h + \phi_S)} \propto h_1^q \otimes H_{1q}^{\perp h} \quad (1.11)$$

$$F_{UT}^{\sin(3\phi_h - \phi_S)} \propto h_{1T}^{\perp q} \otimes H_{1q}^{\perp h} \quad (1.12)$$

$$F_{LT}^{\cos(\phi_h - \phi_S)} \propto g_{1T}^q \otimes D_{1q}^h \quad (1.13)$$

$$F_{UT}^{\sin(\phi_S)} \propto \frac{M}{Q} \left(h_1^q \otimes H_{1q}^{\perp h} + f_{1T}^{\perp q} \otimes D_{1q}^h \right) \quad (1.14)$$

$$F_{UT}^{\sin(2\phi_h - \phi_S)} \propto \frac{M}{Q} \left(h_{1T}^{\perp q} \otimes H_{1q}^{\perp h} + f_{1T}^{\perp q} \otimes D_{1q}^h \right) \quad (1.15)$$

$$F_{LT}^{\cos(\phi_S)} \propto \frac{M}{Q} \left(g_{1T}^q \otimes D_{1q}^h \right) \quad (1.16)$$

$$F_{LT}^{\cos(2\phi_h - \phi_S)} \propto \frac{M}{Q} \left(g_{1T}^q \otimes D_{1q}^h \right) \quad (1.17)$$

From the second to the fifth, the structure functions are described at twist-2 level. The remaining four asymmetries represent "higher-twist" effects, containing terms at sub-leading order in $1/Q$ which involve a mixture of twist-2 and induced by quark-gluon correlations twist-3 parton distribution and fragmentation functions. However, applying a widely adopted simplification approach and neglecting quark-gluon-quark correlators, so that all interaction-dependent terms vanish (Wandzura-Wilczek approximation), this higher twist objects can be simplified to the twist-2 level.

And the spin independent structure functions are

$$F_{UU,T} \propto f_1^q \otimes D_{1q}^h \quad , \quad (1.18)$$

$$F_{UU,L} = 0 \quad . \quad (1.19)$$

For more details on the evaluation of the cross section and the structure functions description see reference [100].

1.5.1 Cross Section in Terms of the Asymmetries

The SIDIS cross section can be represented in terms of asymmetries, which are the ratios of each spin dependent structure function to the unpolarised one:

$$A_{BeamTarget}^{w_i(\phi_h, \phi_S)} = \frac{F_{BeamTarget}^{w_i(\phi_h, \phi_S)}}{F_{UU,T} + \varepsilon F_{UU,L}} \quad (1.20)$$

where $w_i(\phi_h, \phi_S)$ represents the azimuthal modulation, the subscripts *Beam* and *Target* are the polarisations of the beam and the target ("U" for unpolarised, "L" for longitudinally polarised

and “ T ” for transversely polarised). Thus the cross section in Eq. 1.7 transforms into:

$$\begin{aligned}
 \frac{d\sigma}{dx dy dz d\psi d\phi_h dP_{hT}^2} &= \frac{\alpha^2}{xyQ^2} \frac{y^2}{2(1-\varepsilon)} \left(1 + \frac{\gamma^2}{2x} \right) (F_{UU,T} + \varepsilon F_{UU,L}) \times \\
 &\quad \left\{ 1 + \sqrt{2\varepsilon(1+\varepsilon)} \cos(\phi_h) A_{UU}^{\cos(\phi_h)} + \varepsilon \cos(2\phi_h) A_{UU}^{\cos(2\phi_h)} + P_l \sqrt{2\varepsilon(1-\varepsilon)} \sin(\phi_h) A_{LU}^{\sin(\phi_h)} \right. \\
 &\quad + S_L \left[\sqrt{2\varepsilon(1+\varepsilon)} \sin(\phi_h) A_{UL}^{\sin(\phi_h)} + \varepsilon \sin(2\phi_h) A_{UL}^{\sin(2\phi_h)} \right] \\
 &\quad + S_L P_l \left[\sqrt{1-\varepsilon^2} A_{LL} + \sqrt{2\varepsilon(1-\varepsilon)} \cos(\phi_h) A_{LL}^{\cos(\phi_h)} \right] \\
 &\quad + S_T \left[\sin(\phi_h - \phi_S) A_{UT}^{\sin(\phi_h - \phi_S)} \right. \\
 &\quad \quad + \varepsilon \sin(\phi_h + \phi_S - \pi) A_{UT}^{\sin(\phi_h + \phi_S - \pi)} + \varepsilon \sin(3\phi_h - \phi_S) A_{UT}^{\sin(3\phi_h - \phi_S)} \\
 &\quad \quad + \sqrt{2\varepsilon(1+\varepsilon)} \sin(\phi_S) A_{UT}^{\sin(\phi_S)} + \sqrt{2\varepsilon(1+\varepsilon)} \sin(2\phi_h - \phi_S) A_{UT}^{\sin(2\phi_h - \phi_S)} \left. \right] \\
 &\quad + S_T P_l \left[\sqrt{1-\varepsilon^2} \cos(\phi_h - \phi_S) A_{LT}^{\cos(\phi_h - \phi_S)} + \sqrt{2\varepsilon(1-\varepsilon)} \cos(\phi_S) A_{LT}^{\cos(\phi_S)} \right. \\
 &\quad \quad \left. + \sqrt{2\varepsilon(1-\varepsilon)} \cos(2\phi_h - \phi_S) A_{LT}^{\cos(2\phi_h - \phi_S)} \right] \left. \right\} \tag{1.21}
 \end{aligned}$$

The cross section is described by eight modulations considering just the transverse spin dependent part:

$$w_1(\phi_h, \phi_S) = \sin(\phi_h + \phi_S - \pi) \tag{1.22}$$

$$w_2(\phi_h, \phi_S) = \sin(3\phi_h - \phi_S) \tag{1.23}$$

$$w_3(\phi_h, \phi_S) = \sin(\phi_h - \phi_S) \tag{1.24}$$

$$w_4(\phi_h, \phi_S) = \sin(2\phi_h - \phi_S) \tag{1.25}$$

$$w_5(\phi_h, \phi_S) = \sin(\phi_S) \tag{1.26}$$

$$w_6(\phi_h, \phi_S) = \cos(\phi_h - \phi_S) \tag{1.27}$$

$$w_7(\phi_h, \phi_S) = \cos(\phi_S) \tag{1.28}$$

$$w_8(\phi_h, \phi_S) = \cos(2\phi_h - \phi_S) \tag{1.29}$$

The extracted asymmetries are the amplitudes of the above modulations. They contain the depolarization factors $D^{w_i(\phi_h, \phi_S)}(y)$, the target polarisation dilution factor f , and the target polarisation $|S_T|$ and/or the beam polarisation P_l . They are called the raw asymmetries:

$$A_{UT,raw}^{w_i(\phi_h, \phi_S)} = D^{w_i(\phi_h, \phi_S)}(y) f |S_T| A_{UT}^{w_i(\phi_h, \phi_S)}, (i = 1, 2, 3, 4, 5) \tag{1.30}$$

$$A_{LT,raw}^{w_i(\phi_h, \phi_S)} = D^{w_i(\phi_h, \phi_S)}(y) f |S_T| P_l A_{LT}^{w_i(\phi_h, \phi_S)}, (i = 6, 7, 8) \quad . \tag{1.31}$$

The depolarization factors are defined as:

$$D^{\sin(\phi_h - \phi_S)}(y) = 1 \tag{1.32}$$

$$D^{\sin(\phi_h + \phi_S - \pi)}(y) = D^{\sin(3\phi_h - \phi_S)}(y) = \varepsilon \tag{1.33}$$

$$D^{\sin(\phi_S)}(y) = D^{\sin(2\phi_h - \phi_S)}(y) = \sqrt{2\varepsilon(1+\varepsilon)} \tag{1.34}$$

$$D^{\cos(\phi_h - \phi_S)}(y) = \sqrt{1-\varepsilon^2} \tag{1.35}$$

$$D^{\cos(\phi_S)}(y) = D^{\cos(2\phi_h - \phi_S)}(y) = \sqrt{2\varepsilon(1-\varepsilon)} \quad . \tag{1.36}$$

From the modulations in Eqs. 1.22 to 1.29 5 combinations of the angles ϕ_h and ϕ_S can be seen:

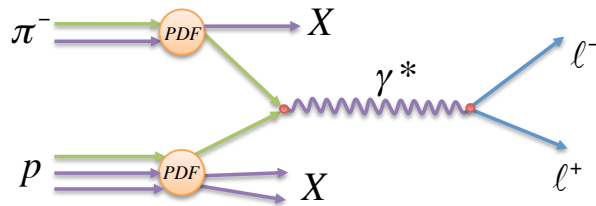


Figure 1.14: Diagram of the DY process.

$$\Phi_1 = \phi_h + \phi_S - \pi \quad (1.37)$$

$$\Phi_2 = 3\phi_h - \phi_S \quad (1.38)$$

$$\Phi_3 = \phi_h - \phi_S \quad (1.39)$$

$$\Phi_4 = \phi_S \quad (1.40)$$

$$\Phi_5 = 2\phi_h - \phi_S \quad (1.41)$$

Three of these angles have cosine and sine modulations, while two of them only have sine modulation:

$$W_1(\Phi_1) = A_{raw}^{w_1(\phi_h, \phi_S)} \sin(\Phi_1) \quad (1.42)$$

$$W_2(\Phi_2) = A_{raw}^{w_2(\phi_h, \phi_S)} \sin(\Phi_2) \quad (1.43)$$

$$W_3(\Phi_3) = A_{raw}^{w_3(\phi_h, \phi_S)} \sin(\Phi_3) + A_{raw}^{w_6(\phi_h, \phi_S)} \cos(\Phi_3) \quad (1.44)$$

$$W_4(\Phi_4) = A_{raw}^{w_5(\phi_h, \phi_S)} \sin(\Phi_4) + A_{raw}^{w_7(\phi_h, \phi_S)} \cos(\Phi_4) \quad (1.45)$$

$$W_5(\Phi_5) = A_{raw}^{w_4(\phi_h, \phi_S)} \sin(\Phi_5) + A_{raw}^{w_8(\phi_h, \phi_S)} \cos(\Phi_5) \quad (1.46)$$

The experimental angular distributions are fitted with these functions to extract the corresponding amplitudes. This procedure will be explained in detail in Chapter 4.

1.6 The DY Cross Section

In the DY process a quark and an anti-quark annihilate with the production of a lepton pair. Fig. 1.14 illustrates the process, which is defined by

$$H_a(p_a) + H_b(p_b) \rightarrow \gamma^*(q) + X \rightarrow \ell^-(l) + \ell^+(l') + X \quad (1.47)$$

where H_a and H_b are the beam hadron and target hadron, and p_a and p_b their momenta; $q = l + l'$ is the momentum of the virtual photon γ^* ; and l and l' are the momenta of the lepton ℓ^- and the anti-lepton ℓ^+ ; and X denotes the accompanying produced particles.

The general formula for the DY cross section was derived by Arnold, Metz and Schlegel [102]. It is defined in the Collins-Soper (CS) frame presented in Fig. 1.15, which is a virtual photon rest frame, where the z -axis is the bisector between the beam momentum and the target momentum, the x -axis is defined in the plane of beam and target momenta and the y -axis is perpendicular to the (z, x) plane to form a right handed frame. The CS frame can be obtained from the target rest frame (TF) presented in Fig. 1.16, where the z -axis is defined along the beam momentum, the x -axis is defined along virtual photon transverse to the beam direction component and the y -axis is perpendicular to the (z, x) plane. The angle ϕ_S is the azimuthal angle of the target transverse polarisation in the TF. The angles ϕ and θ are the azimuthal and polar angles of the lepton momentum in the CS frame.

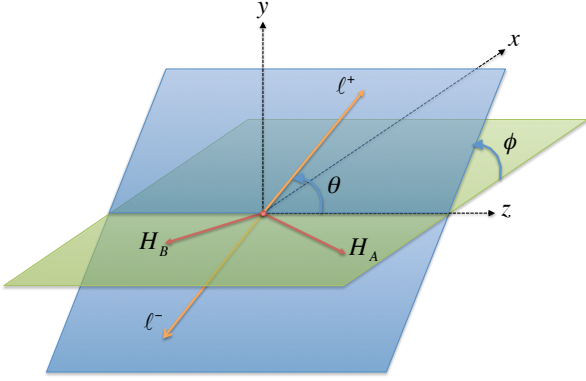


Figure 1.15: Definition of the azimuthal angles on the Collins Soper frame.

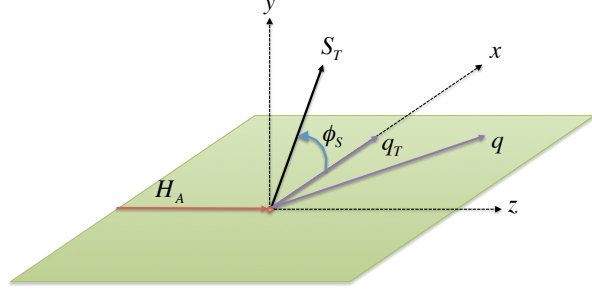


Figure 1.16: Definition of the azimuthal angles on the target rest frame.

In the DY COMPASS measurement only the target hadron is polarised. Taking this into account the general formula for the cross-section is simplified [103]. It can be written as:

$$\begin{aligned}
 \frac{d\sigma}{d^4q d\Omega} = & \frac{\alpha^2}{Fq^2} \left\{ ((1 + \cos^2(\theta))F_{UU}^1 + (1 - \cos^2(\theta))F_{UU}^2) \right. \\
 & + \sin(2\theta)F_{UU}^{\cos(\phi)} \cos(\phi) + \sin^2(\theta)F_{UU}^{\cos(2\phi)} \cos(2\phi) \\
 & + S_L \left(\sin(2\theta)F_{UL}^{\sin(\phi)} \sin(\phi) + \sin^2(\theta)F_{UL}^{\sin(2\phi)} \sin(2\phi) \right) \\
 & + |\vec{S}_T| \left[\left(F_{UT}^{\sin(\phi_S)} + \cos^2(\theta)\tilde{F}_{UT}^{\sin(\phi_S)} \right) \sin(\phi_S) \right. \\
 & + \sin(2\theta) \left(F_{UT}^{\sin(\phi+\phi_S)} \sin(\phi + \phi_S) + F_{UT}^{\sin(\phi-\phi_S)} \sin(\phi - \phi_S) \right) \\
 & \left. \left. + \sin^2(\theta) \left(F_{UT}^{\sin(2\phi+\phi_S)} \sin(2\phi + \phi_S) + F_{UT}^{\sin(2\phi-\phi_S)} \sin(2\phi - \phi_S) \right) \right] \right\}
 \end{aligned} \tag{1.48}$$

where $F = 4\sqrt{(p_a \cdot p_b)^2 - M_a^2 M_b^2}$ represents the flux of incoming hadrons and α is the fine structure constant. The cross-section includes 12 structure functions, the F 's in the expression, with the superscript corresponding to the azimuthal modulation described by the structure function and the subscript to the polarisation of the beam and of the target; where ‘‘U’’ stands for unpolarised, ‘‘L’’ longitudinal polarised and ‘‘T’’ transversely polarised, similarly to the notation in the SIDIS cross section expression.

1.6.1 Cross Section in Terms of the Asymmetries

The DY cross-section can be represented in terms of the asymmetries, which are the ratios between the spin dependent structure function to the unpolarised ones,

$$A_{Beam\ Target}^{w_i(\phi, \phi_S)} = \frac{F_{Beam\ Target}^{w_i(\phi, \phi_S)}}{F_{UU}^1 + F_{UU}^2} \tag{1.49}$$

where $w_i(\phi, \phi_S)$ represent the azimuthal modulations, and the subscripts *Beam* and *Target* are the polarisations of the beam and of the target.

The part of the cross-section which survives an integration over the azimuthal angles is

$$\hat{\sigma}_U = (F_{UU}^1 + F_{UU}^2) (1 + A_{UU}^1 \cos^2(\theta)) \quad . \tag{1.50}$$

Defining the depolarisation factors as

$$D_{[f(\theta)]} = \frac{f(\theta)}{1 + A_U^1 \cos^2(\theta)} \quad , \quad (1.51)$$

the cross section in terms of the asymmetries can be written as

$$\begin{aligned} \frac{d\sigma}{d^4q d\Omega} = \frac{\alpha^2}{Fq^2} \hat{\sigma}_U \left\{ \right. & \left(1 + D_{[\sin(2\theta)]} A_{UU}^{\cos(\phi)} \cos(\phi) + D_{[\sin^2(\theta)]} A_{UU}^{\cos(2\phi)} \cos(2\phi) \right) \\ & + S_L \left(D_{[\sin(2\theta)]} A_{UL}^{\sin(\phi)} \sin(\phi) + D_{[\sin^2(\theta)]} A_{UL}^{\sin(2\phi)} \sin(2\phi) \right) \\ & + |\vec{S}_T| \left[\left(D_{[1]} A_{UT}^{\sin(\phi_S)} + D_{[\cos^2(\theta)]} \tilde{A}_{UT}^{\sin(\phi_S)} \right) \sin(\phi_S) \right. \\ & + D_{[\sin(2\theta)]} \left(A_{UT}^{\sin(\phi+\phi_S)} \sin(\phi + \phi_S) + A_{UT}^{\sin(\phi-\phi_S)} \sin(\phi - \phi_S) \right) \\ & \left. \left. + D_{[\sin^2(\theta)]} \left(A_{UT}^{\sin(2\phi+\phi_S)} \sin(2\phi + \phi_S) + A_{UT}^{\sin(2\phi-\phi_S)} \sin(2\phi - \phi_S) \right) \right] \right\} \quad (1.52) \end{aligned}$$

At Leading Order the cross section simplifies, as demonstrated in [103], and for simplicity the the beam polarisation subscript is omitted

$$\begin{aligned} \frac{d\sigma}{d^4q d\Omega} = \frac{\alpha^2}{Fq^2} \hat{\sigma}_U \left\{ \right. & \left(1 + D_{[\sin^2(\theta)]} A_U^{\cos(2\phi)} \cos(2\phi) \right) + |\vec{S}_T| \left[A_T^{\sin(\phi_S)} \sin(\phi_S) \right. \\ & \left. \left. + D_{[\sin^2(\theta)]} \left(A_T^{\sin(2\phi+\phi_S)} \sin(2\phi + \phi_S) + A_T^{\sin(2\phi-\phi_S)} \sin(2\phi - \phi_S) \right) \right] \right\} \quad (1.53) \end{aligned}$$

where

$$\hat{\sigma}_U = F_U^1 (1 + \cos^2(\theta)) \quad (1.54)$$

and

$$D_{[f(\theta)]} = \frac{f(\theta)}{1 + \cos^2(\theta)} \quad . \quad (1.55)$$

The asymmetries can be related to convolutions of PDFs, one corresponding to the interacting beam quark and the second one corresponding to the interacting target quark:

$$A_U^{\cos(2\phi)} \propto h_{1, Beam}^\perp \otimes h_{1, Target}^\perp \quad , \quad (1.56)$$

$$A_T^{\sin(\phi_S)} \propto f_{1, Beam} \otimes f_{1T, Target}^\perp \quad , \quad (1.57)$$

$$A_T^{\sin(2\phi+\phi_S)} \propto h_{1, Beam}^\perp \otimes h_{1T, Target}^\perp \quad , \quad (1.58)$$

$$A_T^{\sin(2\phi-\phi_S)} \propto h_{1, Beam}^\perp \otimes h_{1, Target} \quad . \quad (1.59)$$

$$(1.60)$$

The procedure to extract these asymmetries from DY data will be similar to the procedure used for SIDIS data, which will be explained in detail in Chapter 4.

The COMPASS Experiment

In 1995, two distinct groups created two different physics projects, one to study the spin structure of the nucleons using a muon beam and the other to study hadron spectroscopy using hadron beams. Both presented their proposals to CERN to create an experiment. In response, CERN proposed to unify the two projects and create a single experiment. This was possible due to the existence of a beam line with the possibility to have both muon and hadron beams. This strong community for QCD studies originated the COmmon Muon and Proton Apparatus for Structure and Spectroscopy (COMPASS) collaboration. Many efforts were done to merge the experimental requirements of the two projects. These resulted in a highly flexible and versatile setup, giving the possibility of different experimental measurements.

The spectrometer started to be built in October 1998, just after the CERN approval. The physics data taking started in 2002. Up to 2007 mainly muon beams were used, apart from a short hadron test run in 2004. From 2002 to 2004 a 160 GeV/ c muon beam was scattered off a ${}^6\text{LiD}$ target, which was either longitudinally or transversely polarised. During 2005 profiting from a long (more than one year) CERN shutdown the target system was upgraded, the dipole magnet was exchanged, and the target cells were modified from two to three cells, for better cancelling systematic errors. In 2007 the beam was kept but a longitudinally and transversely polarised ammonia target was used. The data taking with hadron beams started in 2008 and extended to 2009. In 2009 a short DY beam test took place, the analysis of these data will be presented in Chapter 5. In 2010 and 2011 the DIS data taking resumed, with muon beams and ammonia target. The year of 2010 was dedicated to the target transverse polarisation. The analysis of these data is part of this thesis and will be presented in Chapter 4. The year of 2011 was dedicated to the longitudinal polarisation. The physics program approved in the beginning of COMPASS was finished in 2011. A proposal [104] with the physics program for a second phase of COMPASS, named COMPASS-II, was submitted to the CERN scientific committee in 2010. This proposal contemplates three physics programs: The Primakoff measurement, the polarised DY measurement, and the DVCS measurement. This proposal was approved and the data taking started in 2012, dedicated to the Primakoff measurement. In 2013 and most of 2014 there were no data taking since CERN had a shutdown to perform upgrades in the Super-Proton-Synchrotron (SPS) and in the Large Hadron Collider (LHC). The beam availability for some weeks at the end of 2014 made possible a dedicated DY data taking pilot run, which was followed by the polarised DY data taking run in 2015. The analysis of the 2014 data will be presented in Chapter 6 and the analysis of the 2015 data in Chapter 7. The years of 2016 and 2017 are going to be dedicated to the DVCS measurement. In 2018 it is expected a run dedicated to DY again.

COMPASS is a fixed target experiment located at the end of the M2 SPS beam line at

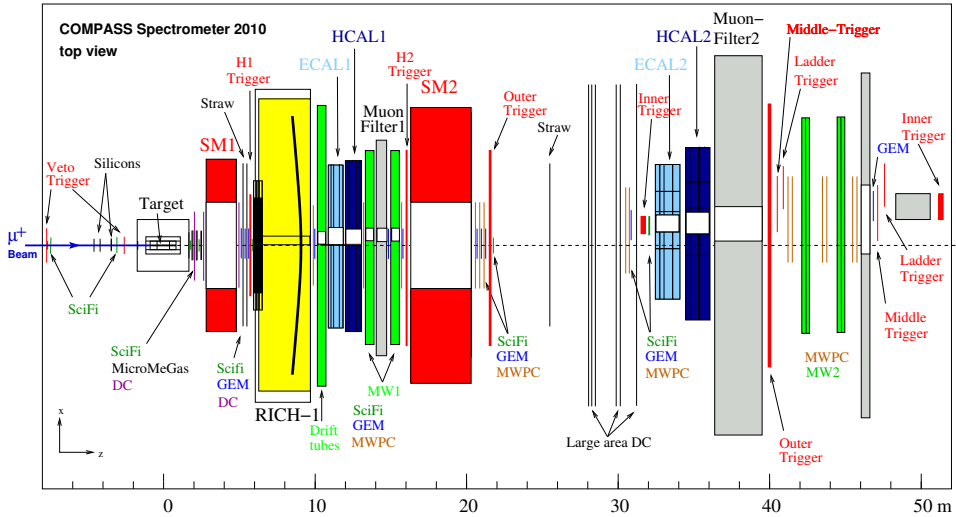


Figure 2.1: 2010 COMPASS setup for the SIDIS measurement.

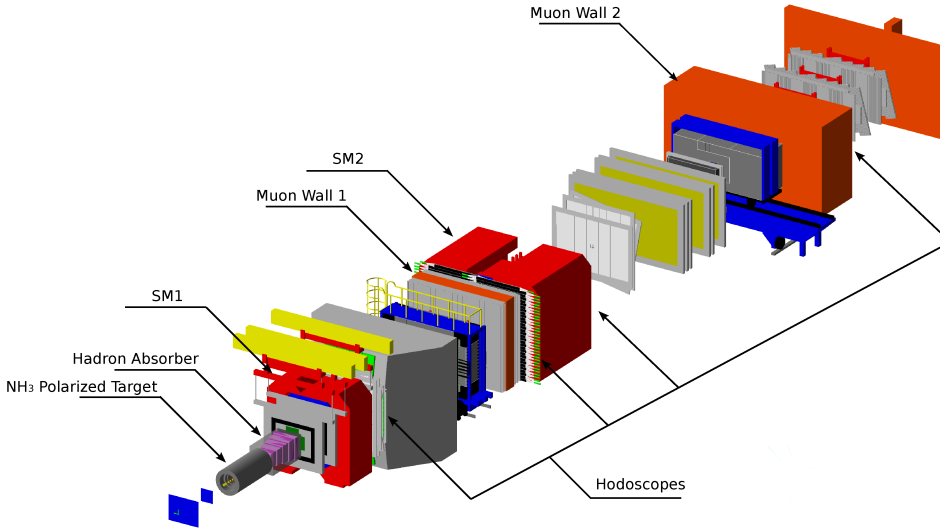


Figure 2.2: 2014 COMPASS setup for the DY measurement.

CERN. It is a two staged spectrometer comprising two dipole magnets. The first stage contains the SM1 magnet with a field integral of 1.0 Tm and it is called the Large Angle Spectrometer (LAS). The second contains the SM2 magnet with a field integral of 4.4 Tm and it is called the Small Angle Spectrometer (SAS). The LAS is dedicated to the detection of small momentum particles emitted at large angles, as its name suggests. It contains a Ring Imaging Cerenkov (RICH) detector for particles identification. The SAS is dedicated to the detection of high momentum particles emitted at small angles. Both spectrometers contain an electromagnetic calorimeter and a hadronic calorimeter. They also contain a Muon Wall, which provides muon identification. Each contains a variety of tracking detectors, which will be introduced along this chapter.

This chapter is giving a brief description of the apparatus in general and to the 2010 setup and the Drell-Yan setups in particular. A sketch of the 2010 setup is shown in Fig. 2.1, and a sketch of the DY setup is shown in Fig. 2.2. The main difference between the two setups is the inclusion of a hadron absorber just downstream of the target in the case of the DY setup. This is mandatory because DY has a low cross section and is needed a high intensity beam, without the

absorber the detectors occupancy would increase significantly and they would not support such rates, also the combinatorial background increases, quadratically with the beam intensity and with the absorber this is kept under control. Table 2.1 lists the detectors used in the 2010 run and in DY runs, ordered by z position along the beam line. For more details on the COMPASS experiment consult [105] and [106].

2.1 The Beam

Both muon and hadron beams are available in COMPASS. In 2010 for the SIDIS measurement a μ^+ beam with 160 GeV/ c was used. In DY runs a negative hadron beam with 190 GeV/ c was used. This negative hadron beam is mainly composed by π^- , with a contamination of $\sim 2.5\%$ of K^- and $\sim 0.5\%$ of \bar{p} . In 2015 DY run two differential Cherenkov counters (Cedars) were used, which give the possibility to identify the beam particles.

The beam arrives to the COMPASS hall through the M2 beam line from SPS. The SPS super-cycle and spill length vary according to the several CERN experiments requirements. The beam delivery conditions during the data taking periods studied in this thesis are summarized in Table 2.2. During the spill the primary proton beam accelerated at the SPS impinges the T6 target with a momentum of 400 GeV/ c . The T6 production beryllium target thickness is adjustable such that different secondary beam intensities can be achieved. The maximum and typical length is 500 mm long. The interaction of the proton beam in this target produces a hadron secondary beam, made of π^\pm , K^\pm , p and \bar{p} . This secondary beam is then selected by an array of quadrupoles and dipoles set to a chosen momentum range. A pion beam with momentum of 172 GeV/ c is chosen in order to obtain a tertiary muon beam of 160 GeV/ c in the COMPASS target. Part of the hadrons, mainly pions in the case of the negative beam are going to decay along a 600 m tunnel with a series of focusing and defocusing quadrupoles. At the end of this decay line the hadron component can be removed by a series of hadron absorbers, or in the case of interest in the hadron beam these absorbers are not used, and both hadron and muon components follow together, the muon component being removed mainly due to its lower momentum. The beam is deflected upwards to the surface level and its momentum selected by an array of quadrupoles. It reaches the surface ~ 100 m upstream of the COMPASS target and it is bent to the horizontal orientation by three consecutive dipole magnets, the B6. This together with 6 detector planes (BM01 – 06) form the Beam Momentum Station (BMS) and it is used to measure the beam momentum with good precision, $\leq 1\%$. The BMS is the most upstream part of the COMPASS apparatus. A schematic drawing of the BMS is shown in Fig. 2.3. Finally the beam is focused and steered on the COMPASS target. During the transverse polarisation data taking a chicane with additional magnets is used to fine-steer the beam and compensate the horizontal deflection induced by the transverse dipole field of the polarised target. The mean beam intensities in the relevant periods for this thesis are summarized in Table 2.2.

The tertiary muon beam results from the decay of $\pi^+ \rightarrow \mu^+ \nu_\mu$ and $K^+ \rightarrow \mu^+ \nu_\mu$. The resulting muons are naturally polarised due to the presence of a left-handed neutrino in the final state. In the rest frame of the π^+ they are 100% polarised. In the laboratory frame the muon polarisation depends on its energy and on the energy of the parent pion. For $E_\pi \simeq 172$ GeV and $E_\mu \simeq 160$ GeV, the muon polarisation is around 80%. The polarisation of the beam muons is estimated for each event. A set of values provided by CERN is interpolated and this is used for the analysis. The 2010 beam polarisation is shown in Fig. 2.4 as a function of the momentum.

The muon beam that enters the COMPASS hall has a near halo component and a far halo that can extend for many meters. Halo induced events can be partially removed by the use of the Veto detectors taking part in the trigger selection, explained later in this chapter.

2. THE COMPASS EXPERIMENT

Detector	# Planes	Projections	z position (cm)			size (cm ²)	σ_s (μ m)
			2010	2009	2014/2015		
FI01	2	X,Y		-759		3.94×3.94	130
FI15	3	U(45°),X,Y	-547	×	-547	4.51×4.51	150
SI01	4	U,V,Y,X	-440	-378	×	7×5	10
SI02	4	U,V,Y,X	-390	-330	×	7×5	10
SI03	4	U,V,Y,X	-340	-279	×	7×5	10
FI02/FI03	3	U(45°),X,Y	-290	×	-350	5.25×5.25	130
Target			0	-183	-230		
FI35	3	U(45°),X,V(-45°)		×	-90	16×16, 23×23, 16×16	
Absorber			×	-113 to 87	-135 to 125		
FI03	3	X,Y,U (45°)	132	×		5.25×5.25	130
MM01/MP01	4	V(-45°),U(45°),X,Y		145		40×40	110
DC00	8	2Y,2X,2U(-20°),2V(20°)		165		180×130	250
MM02/MP02	4	V(-45°),U(45°),X,Y		195		40×40	110
FI04	3	X,Y,U(45°)	215	×	215	5.25×5.25	120
MM03/MP03	4	V(-45°),U(45°),X,Y		245		40×40	110
DC01	8	2Y,2X,2U(-20°),2V(20°)		265		180×130	250
SM1				364			
DC04	8	2U(-10°),2V(10°),2X,2Y		465		240×200	250
GM01	4	U(45°),V(-45°),Y,X		477		32×32	110
ST02	6	X,Y,U(10°),V(-10°),Y,X		505	×	320×270	400
DC05	6	2U(-10°),2V(10°),2Y		×	505	240×200	250
GM02	4	U(45°),V(-45°),Y,X		520		32×32	110
ST03	6	X,Y,U(10°),V(-10°),Y,X		540		320×270	400
GM03	4	U(45°),V(-45°),Y,X		560		32×32	110
HG01	1	Y	583	×	583	230×192	
FI05	2	X,Y		602	×	230×192	
RICH				765			
PS01	4	Y,U(10°),X,V(-10°)		750		180×120	600
GM04	4	U(45°),V(-45°),Y,X		960		32×32	110
DR	8	2X,2Y,2X,2Y	1010	1278	1010	520×380	600
EC01			1110	1400	1010		
HC01			1260	1574	1260		
GP02	4	U(45°),V(-45°),Y,X	1375	×	1375	10×10	110
PA01	3	U(10°),X,V(-10°)	1390	1665	1390	180×120	600
GM05	4	U(45°),V(-45°),Y,X	1395	1673	1395	32×32	110
FI55	2	U(45°),V(-45°)	1418	×		32×32	110
MA01	8	2X,2Y,2X,2Y	1455	1718	1455	480×410	3000
MF1			1494	1772	1494		
FI06	2	X,V(-45°),Y	1530	×		10×10	210
MA02	8	2Y,2X,2Y,2X	1555	1828	1555	480×410	3000
PA02	3	U(10°),X,V(-10°)	1580	1870	1580	180×120	600
GM06	4	U(10°),V(-10°),Y,X	1590	1879	1590	32×32	110
HG02	1	Y	1600	×	1600	500×420	
SM2			1825	2097	1825		
PA03	3	U(10°),X,V(-10°)	2040	2315	2040	180×120	600
GM07	4	U(45°),V(-45°),Y,X	2050	2324	2050	32×32	110
PA04	3	U(10°),X,V(-10°)	2070	2345	2070	180×120	600
GM08	4	U(45°),V(-45°),Y,X	2080	2354	2080	32×32	110
PA05	3	U(10°),X,V(-10°)	2100	2375	2100	180×120	600
GM09	4	U(45°),V(-45°),Y,X	2110	2384	2110	32×32	110
GP03	4	U(45°),V(-45°),Y,X	2115	×	2110	10×10	110
HO03	1	Y	2150	2396	2150	250×120	
FI07	2	X,	2170	×		10×10	210
ST05	3	Y,X,U(10°)	2500	2558	2500	320×270	400
DW01	4	2X,2Y		2800		520×260	
DW02	4	2X,2Y		2834		520×260	
DW03	4	2V(30°),2Y		2860		520×260	1500
DW04	4	2Y,2U(-30°)		3010		520×260	1500
DW05	4	2X,2V(30°)		3040		520×260	1500
PA11	3	U(10°),X,V(-10°)		3070		180×120	600
PA06	3	U(10°),X,V(-10°)		3100		180×120	600
GM10	4	U(45°),V(-45°),Y,X		3110		32×32	110
DW06	4	2U(-30°),2X		3125		520×260	1500
FI08	2	X,Y		3170	×	12×12	210
HI04	1	X	3212	×		17×40	
EC02				3325			
HC02				3570			
MF2				3820			
HO04	1	Y		3970		245×230	
HM04	1	Y		4025		120×35	
HL04	1	Y	4057	×		128×40	
PB01	2	X,U(10°)		4190		180×90	600
PB02	1	V(-10°)		4200		180×90	600
MB01	6	2X,2Y,2V(-15°)		4270		450×200	1400
PB03	2	X,U(10°)		4395		180×90	600
PB04	1	V(-10°)		4410		180×90	600
MB02	6	2X,2Y,2V(-15°)		4470		450×200	1400
PB05	2	X,U(10°)		4615		180×90	600
PB06	1	V(-10°)		4630		180×90	600
GM11	4	U(45°),V(-45°),Y,X	4713	×		300×42	
HM05	2	X,Y		4785		300×42	
26 HL05	1	Y	4810	×		170×48	
HI05	1	Y	5100	×		35×50	

Table 2.1: Detectors used in 2010 SIDIS run and in 2009, 2014 and 2015 DY runs.

Run	super-cycle (s)	spill (s)	Beam Intensity
SIDIS 2010	33 and 39	1×9.6	$3.7 \times 10^7 \mu^+/\text{s}$
DY 2009	36 and 51.6	1×9.6	$8.3 \times 10^6 \pi^-/\text{s}$
DY 2014	33.6 and 48.9	2×4.8	$6 \times 10^7 \pi^-/\text{s}$
DY 2015	36, 51.2 and 58	2×4.8	$8.1 \times 10^7 \pi^-/\text{s}$

Table 2.2: Beam parameters.

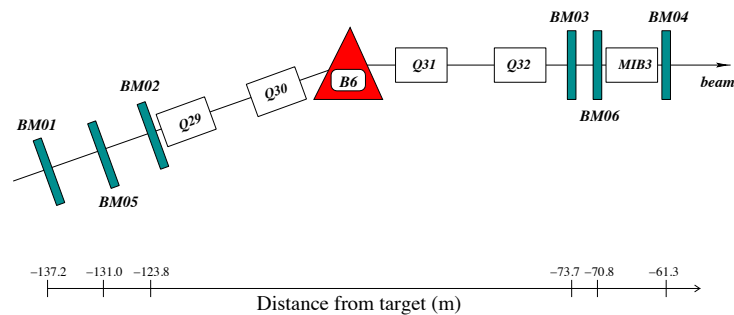
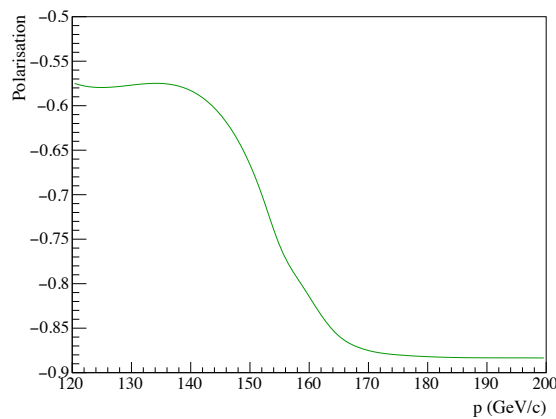


Figure 2.3: BMS schematic drawing [105].

Figure 2.4: μ^+ beam polarisation as a function of its momentum.

2.2 The Target

The polarised target is one of the most complex and important features of COMPASS, essential for the measurement of transverse and longitudinal spin asymmetries.

A polarised target sketch is shown in Fig. 2.5. The polarisable solid state material is kept inside two or three cylindrical cells. They are surrounded by a superconducting solenoid magnet, capable of creating a strong longitudinal magnetic field of 2.5 T. The required polarisation is kept “frozen” by a helium cooling bath at ~ 60 mK, using a helium dilution refrigerator. A dipole with a field strength of 0.63 T is used to run in transverse spin mode. Once the longitudinal polarisation is built up the dipole field is applied and the polarised proton spins become perpendicular to the beam direction.

For the measurement of the muon scattering off polarised protons the target material used is ammonia, NH_3 ; in this case only the hydrogen protons are polarisable. The polarisation is built

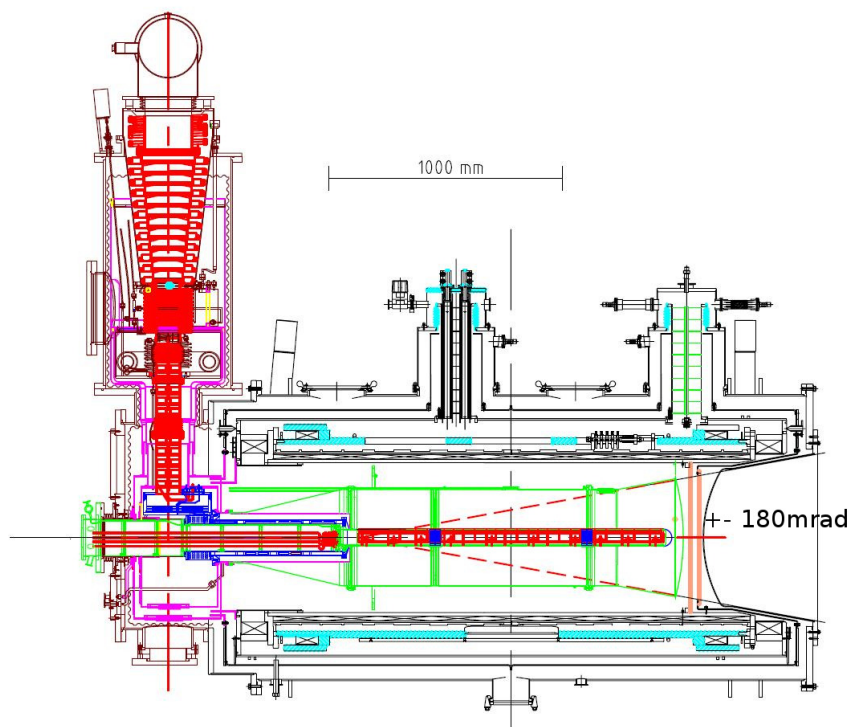


Figure 2.5: Target device.

using the technique of Dynamic Nucleon Polarisation (DNP) [107]. This consists in transferring the polarisation of the electrons to the polarisation of the nucleons. The electrons are much easier to polarise than the nucleons, due to their higher magnetic moment. This technique is quite efficient, taking around three days to reach a polarisation of around 90% for the protons of the ammonia target. The transfer of the polarisation from the electron to the proton is done using microwave radiation tuned to a specific frequency such that the proton's spin gets parallel or anti-parallel to the magnetic field. The polarisation is measured using 10 NMR coils placed directly in the target cells and its value is saved in a database run by run, to be used afterwards in the analysis.

In 2010 three target cells filled with ammonia were used. They had a diameter of 4 cm, the outer cells were 30 cm long and the inner cell was 60 cm long, with gaps between them of 5 cm. The mean value for the polarisation was 80%. The polarisation of the outer cells is opposite to the polarisation of the inner cell to allow the simultaneous measurement with the two spin configurations. This polarisation configuration is reversed periodically to minimize possible systematic errors originated by the different acceptances of the three cells. In longitudinal runs this is done by reversing the solenoid field. For transverse runs the reversal cannot be done by reversing the dipole field, because then the particles crossing their field would be bend in the opposite direction, and this would introduce systematic uncertainties due to the different geometrical acceptance. The beam telescope already takes into account the target dipole field: the beam enters the target field action zone with an angle such that it crosses the target cells center centred with the zero beam line. The dead zones of the detectors are also set to accompany the beam through the spectrometer. For these reasons, when running in transverse mode the polarisation is destroyed and rebuilt again every 2 weeks in opposite spin configurations; the dipole field has always the same orientation. As the polarisation decreases along the time it is rebuilt every week.

In 2015 for the DY run, there were two NH_3 cells, each 55 cm long, with a diameter of 4

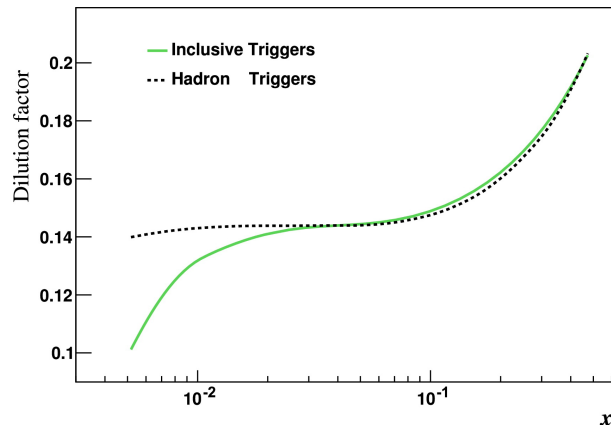


Figure 2.6: Dilution factor of the NH_3 polarised target as a function of x for inclusive and for semi-inclusive hadron triggers [25].

cm and a gap of 20 cm between them. In the DY case the three cells were not considered since the vertex resolution would not be enough to separate the events between the cells. The vertex resolution suffer from the hadrons absorber presence just downstream of the target. A vertex detector, a scintillating fibres detector, was placed between the target and the absorber in order to improve the vertex reconstruction and have a better resolution. However this detector suffer from a high occupancy and its inclusion in the reconstruction is still under development.

For the extraction of the asymmetries an important factor to take into account is the dilution factor, which accounts for the fact that only a fraction of the target material is polarised. In the case of the ammonia, as the only polarisable nucleons are the protons from hydrogen, one expects a dilution factor of $3/17$. However it has to account also to the dilution due to radiative effects on unpolarised protons and the fact that we are not only in the presence of pure ammonia. The dilution factor is

$$f = \frac{\sigma_p^{1\gamma}}{\sigma_p^{tot}} \frac{n_p \sigma_p^{tot}}{\sum_A n_A \sigma_A^{tot}} = \frac{n_p \sigma_p^{1\gamma}}{\sum_A n_A \sigma_A^{tot}} \quad (2.1)$$

where n_p is the number of polarisable protons, σ_p^{tot} is the spin independent cross section per proton, n_A is the number of nucleons in a nuclei with mass A , σ_A^{tot} is the spin independent cross section per nucleon and $\sigma_p^{1\gamma}$ is the one photon exchange Born cross section, which is related with the total cross section,

$$\sigma_p^{tot} = \lambda \sigma_p^{1\gamma} + \sigma_{tail}^{inel} + \sigma_{tail}^{qel} + \sigma_{tail}^{el} \quad (2.2)$$

where λ takes into account the higher order contributions such as the “vertex correction” and the “vacuum polarisation”. The inelastic tail accounts for the real photon radiation before or after the virtual photon emission. The quasi elastic tail accounts for the interaction with the proton and not with its content. The elastic tail account for the interaction with the nucleus itself and not the nucleons. In the SIDIS case only the inelastic tail needs to be taken into account since it is required at least one hadron in the spectrometer. The dilution factor is calculated for each event and depends on the kinematic variables x and y . Its dependence on other kinematic variables was studied but no significant variation was observed at COMPASS energies. The dilution factor increases with x as shown in Fig. 2.6. Its mean value is around 0.15 for the ammonia target.

2.3 Tracking Detectors

The COMPASS spectrometer has a large variety of tracking detectors. They cover different angular acceptance regions and can be divided in three main groups. The very small angle trackers are intended to measure particles near to the beam axis, essentially the beam particles. The small area trackers, as the name suggests, are used to measure particles at low angle, however these detectors have central dead zones, or recently, pixelized high flux capable central regions, that coincide with the coverage area of the very small angle trackers. The last set are the large area trackers, covering the larger angles. All together give the opportunity to measure a wide particles angular range, up to 180 mrad. Each detector has at least two projections of wires or sensitive elements, but the majority has more; this is very important to avoid ambiguities in the track reconstruction. These detectors are of different types; a brief summary of them and their features follows.

2.3.1 Very Small Angle Trackers

These trackers are intended to measure the beam and other particles trajectories very close to the beam axis, namely the scattered muon in the DIS case. They need to be capable to stand high particle fluxes. In these category two types of detectors are used; the Scintillating Fiber (SciFi) detectors and the Silicon Microstrip detectors. They complement each other since the former has a very good time resolution and the latter has a very good spatial resolution.

There are ten SciFi stations in COMPASS. Their sizes vary from $3.9 \times 3.9 \text{ cm}^2$ to $12.3 \times 12.3 \text{ cm}^2$. The fibres diameter is 0.5, 0.75 or 1 nm depending on the station, corresponding to a spatial resolution of 130, 170 and 210 μm . The time resolution is very good, 400 ps.

The silicon detectors, three stations in total, have an active area of $5 \times 7 \text{ cm}^2$. A time resolution of 2.5 ns and a spatial resolution of 10 μm .

In 2009 DY test run and in 2010 SIDIS run both the SciFi and Silicon detectors were used. The beam telescope, upstream of the target, had 3 SciFis and 3 Silicons. The other SciFis were placed along the spectrometer.

In 2014 and 2015 DY runs the Silicons were not used, because they could not stand the beam high intensity. The beam telescope was only formed by three SciFis, and there was only one SciFi in the spectrometer in the region upstream the SM1, since the particles at very small angles downstream of the absorber are not relevant for the DY measurement.

2.3.2 Small Angle Trackers

The Small Angle Trackers are essential to measure particles at small angle. In this category COMPASS has two kinds of gaseous detectors, the MicroMegas (Micromesh Gaseous Structure) and the GEMs (Gas Electron Multipliers).

In COMPASS there are 3 MicroMega Stations, each with 4 different projection planes. They are located in between the target and the first magnet, SM1. The MicroMegas are gaseous detectors with a conversion region and an amplification region, separated by a metallic micromesh. The produced ions go to the mesh and the electrons go to the read-out strips. Due to the thickness (100 μm) of the amplification region the produced avalanches do not spread much transversely which allows a high precision in position. The MicroMegas spatial resolution is around 100 μm . These detectors cover an active area of $40 \times 40 \text{ cm}^2$, with a central dead zone of 5 cm in diameter. The time resolution is 9 ns. A sketch of the principle of operation of the MicroMegas is shown in Fig. 2.7. In 2015 all the MicroMegas were upgraded to have a pixelised

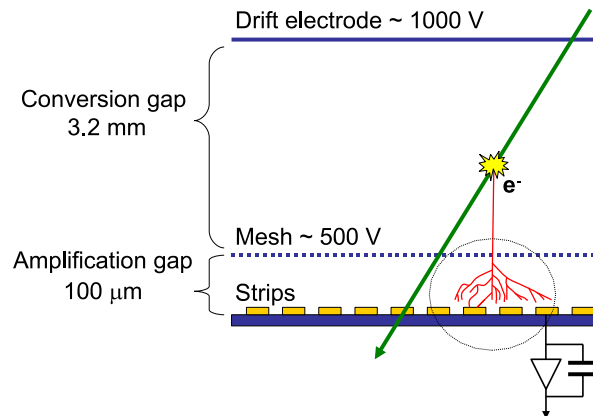


Figure 2.7: MicroMegas principle of operation [105].

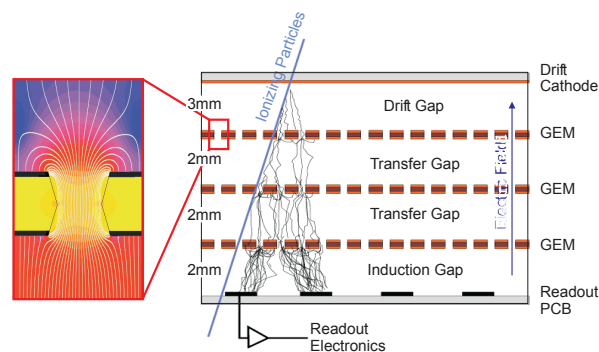


Figure 2.8: GEMs principle of operation [105].

region on its center, however these is not very relevant for the DY measurement due to its very low angle coverage.

There are 11 GEMs in the COMPASS spectrometer, distributed from the downstream side of the SM1 magnet to the end of the spectrometer. They are gaseous detectors with three thin foils of polyamide ($50 \mu\text{m}$), each with a large number of drifting holes ($\sim 10^4$ holes/ cm^2) with a strong electric field of several 100 V. The electrons drifting through the holes generate avalanches which go to the next foil up to the readout, which are sets of strips. The GEMs have an active area of $31 \times 31 \text{ cm}^2$ and a central region of 5 cm diameter that is deactivated during the normal high intensity runs. These central regions are activated in the alignment runs to increase the statistics. Its time resolution is 10 ns. A sketch of the principle of operation of the GEMs is in Fig. 2.8. There are also two pixelised GEMs in the spectrometer, which are not relevant for the DY measurement since they cover very small angle particles.

2.3.3 Large Angle Trackers

The large area trackers are intended to measure particles at larger angles and are subject to lower particle fluxes. Their dead regions mostly coincide with the active areas of the small angle trackers described previously. They are also gaseous detectors, with worse time and space resolutions, but with much larger active areas. In this category are the Drift Chambers (DCs), the Straw tube detectors (Straws), the Multi Wire Proportional Chambers (MWPCs), the SAS large area drift chambers (W45) and the RichWall, a large size tracking station just downstream of the RICH detector.

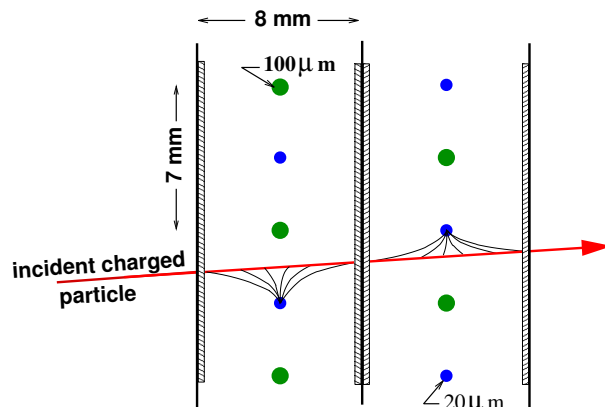


Figure 2.9: DCs principle of operation [105].

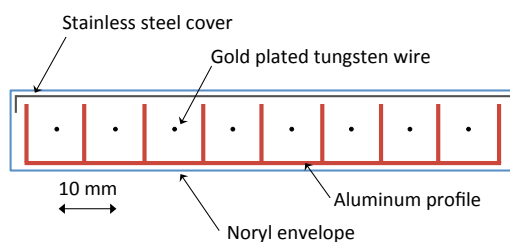


Figure 2.10: MDT module [106].

There are four DCs in COMPASS; two of them are upstream of the SM1, DC00 and DC01, and the other two are downstream of SM1, DC04 and DC05, the latter was only included in the 2015 run. The first two are smaller, $180 \times 127 \text{ cm}^2$, and the DC04 and DC05 are $240 \times 204 \text{ cm}^2$. The rate is higher upstream of SM1 due to the low energy background, however these particles are then bent away by the magnet. This makes the reconstruction upstream of the SM1 more difficult. It is therefore very important to have high resolution and high efficiency detectors there. These detectors are deactivated in the central region, which is 30 cm in diameter, in the normal intensity runs, and their central parts are only used during the alignment runs. Each DC is made of 4 pairs of layers, 2 layers for each projection. Each layer has a set of sensitive wires of $20 \mu\text{m}$ diameter and of potential wires of $10 \mu\text{m}$ diameter. They are enclosed by two cathode foils with a gas gap of 8 mm. Thus each drift cell is $8 \times 7 \text{ mm}^2$. A sketch of the principle of operation of the DCs is shown in Fig. 2.9. The DCs have a spatial resolution of around $250 \mu\text{m}$.

There are also large area drift chambers in SAS, the so called W45. They are 6 stations, each made of two pairs of layers, one pair per projection. They cover an active area of $520 \times 260 \text{ cm}^2$, with a central dead zone of 50 cm or 100 cm, depending on the station. Each drift cell is $40 \times 10 \text{ mm}^2$, 4 cm between sensitive wires and 1 cm between the two cathode foils. The spatial resolution is around $1500 \mu\text{m}$.

The RichWall detector is a large size tracking station just downstream of RICH. It is done by 8 layers of Mini Drift Tubes (MDT) modules. Each MDT module, see Fig. 2.10, is done by a comb of aluminum with 8 spaces covered with an inox layer; in each space a gold plated tungsten wire with a diameter of $50 \mu\text{m}$ acts as an anode. The module is insulated by plastic material. A better accuracy for the track position is obtained reading the MDT in drift mode.

The Straws are made of tubes; each tube has in its center a gold plated tungsten anode wire which attracts the electrons from ionization. In COMPASS there are 3 Straw detectors, two

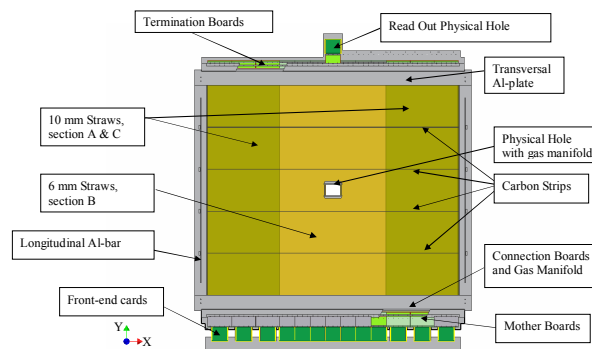


Figure 2.11: Schematic view of a COMPASS straw detector [105].

of them in LAS and the third one in SAS. Each Straw detector has two planes per projection. The planes with vertical straws and 10 degree inclined straws have an active area of $323 \times 272 \text{ cm}^2$. The planes with horizontal straws have an active area of $350 \times 243 \text{ cm}^2$. Each plane is divided in three pieces, the two outer parts with larger diameter straws, 9.6 mm, and the inner piece with straws of 6.1 mm in diameter. In the inner piece there is a dead zone in the center of $20 \times 20 \text{ cm}^2$. These detectors have a spatial resolution of around $400 \mu\text{m}$. The schematic view of a Straw plane is in Fig. 2.11.

The last kind of detectors are the MWPCs. These differ from the previous detectors because they have multiple layers of wires embedded into a single gas volume. There are 14 stations of MWPCs placed along the COMPASS spectrometer, both in LAS and in SAS. These 14 stations can be divided in three different types. The so called type A, with three projections, u (10 degree rotated wires), x (vertical wires) and v (-10 degree rotated wires). There are 7 stations of type A. The second type is the A*, which is similar to A type with an additional y projection plane. There is only one station of this type, the so called PS. These stations have an active area of $178 \times 120 \text{ cm}^2$. The last is the B type, which has x , u or v projections. These are smaller covering an active area of $178 \times 90 \text{ cm}^2$. The MWPCs have dead zones of 16, 20 and 22 cm in diameter. Their spatial resolution is around $1600 \mu\text{m}$.

2.4 Particle Identification

For the particles identification COMPASS has four kinds of detectors. The Ring Imaging Cherenkov (RICH) detector is used to identify pions, kaons and protons. Two electromagnetic calorimeters (ECAL1 and ECAL2) are used to measure the energy of photons and electrons. Two hadronic calorimeters (HCAL1 and HCAL2) are used to measure the energy of the hadrons. Finally, two muon walls (MW1 and MW2) are used to identify muons. RICH, ECAL1, HCAL1 and MW1 are in LAS and are placed by this order along z ; ECAL2, HCAL2 and MW2 are part of SAS.

The RICH detector is used to determine the velocity of particles and to separate them into pions, kaons and protons, starting from a different momentum threshold for each particle type ($2.5 \text{ GeV}/c$ for pions, $9 \text{ GeV}/c$ for kaons and $17 \text{ GeV}/c$ for protons) up to $50 \text{ GeV}/c$. The principle of operation of the RICH is based on the Cherenkov effect: a particle travelling in a medium with a velocity larger than the velocity of the light in that medium emits photons in a cone with axis coinciding with the track axis. The emitted light is reflected and focused by two mirrors to the photon detection areas outside of the LAS geometrical acceptance. The RICH principle of operation and a sketch with its dimensions are in Fig. 2.12.

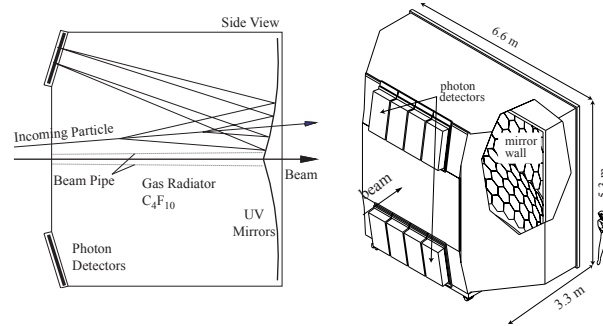


Figure 2.12: Principle of operation of the RICH detector and its schematic view [105].

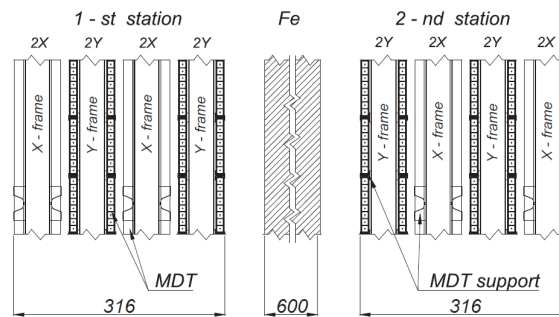


Figure 2.13: Schematic view of MW1 [105].

The calorimeters are used to measure the energy of the particles. The ECALs are made of blocks of lead glass which are readout on one side by photomultipliers. They are used to detect photons and electrons. These particles produce electromagnetic showers which generate a light signal, and the detected light intensity is proportional to the deposited energy. The HCALs are made of alternating layers of iron and scintillating material. In the iron layers a hadron generates a shower of secondary particles, which produces a light signal in the scintillators, proportional to the deposited energy. They fully absorb hadrons with energies from 10 to 100 GeV.

The Muon Walls are used to identify the muons. Because of the muon's low interaction probability these detectors are placed at the end of each spectrometer stage, just after the calorimeters. The MW1 is in the LAS. It has eight tracking planes upstream and eight planes downstream of a 60 cm thick hadron absorber made of iron that filters out the remaining hadronic particles at this point, the Muon Filter 1 (MF1). The chambers have an active area of around $480 \times 410 \text{ cm}^2$ with a central hole of $140 \times 80 \text{ cm}^2$. The MW1 detector is similar to the RichWall, described before, done with MDT modules. Each plane has a spatial resolution of 3 mm in proportional chamber mode. A schematic view of the detector is in Fig. 2.13. The MW2 is part of the SAS; it is downstream of the two calorimeters and a hadron absorber made of concrete, 2.4 m long. The MW2 consists of 12 planes with an active area of 450 cm^2 with a central hole of $90 \times 70 \text{ cm}^2$. Each plane is done by drift tubes with 29 mm diameter; 2 layers with the same inclination are attached making a double layer. The spatial resolution of each layer is around 1.4 mm.

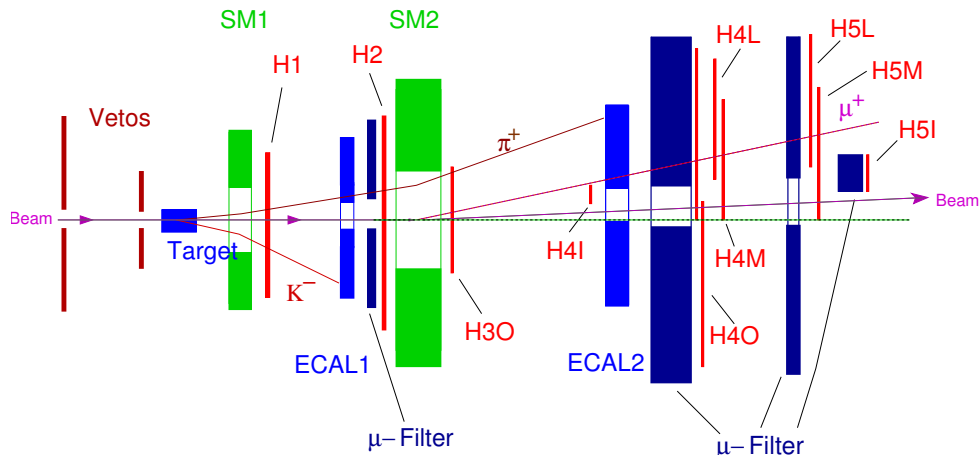


Figure 2.14: Schematic view of the hodoscopes positions.

2.5 Trigger

The trigger system is a very important part of the data taking, which allows to select the good event candidates to be recorded on tape, depending on the physics processes under study. It has the capability to select such events in a high rate environment. Due to the limited buffering time of detectors the trigger should be able to rapidly decide if the data in detectors should be saved or not. This is possible with the use of hodoscopes, made by scintillating slabs connected to photomultipliers, which have a very good time resolution of around 1 ns.

There are five stations of hodoscopes. Each station is done by 2 hodoscopes and the trigger is based on the coincidence signal between them. The Inner Trigger (IT) is formed by HI04X and HI05X hodoscopes, which have vertical slabs and are sensitive to the x coordinate, sensitive to the bending of particles in the dipole magnetic fields. The Middle Trigger (MT) is done by four hodoscope planes, HM04X, HM05X, HM04Y and HM05Y. The x ones with vertical slabs, and the y with horizontal slabs, which are not sensitive to the magnets bending. The Ladder Trigger (LT) relies on HL04X and HL05X. And the Outer Trigger on HO03Y and HO04Y. All these hodoscopes are placed in the SAS. A schematic view of the positions of the hodoscopes in the spectrometer is in Fig. 2.14. During the 2010 run (starting in W31) a new trigger system was introduced in LAS, the Large Angle Spectrometer Trigger (LAST). It is composed by two hodoscopes, the HG01Y just upstream the RICH and the HG02Y just upstream the SM2. It covers the events with large angle muon tracks and is mandatory for the DY events selection. The calorimeters can also be used as trigger by itself or in combination with the hodoscopes, selecting events with energy deposits above a certain threshold. Before the usage of LAST, the pure calorimeter trigger (CT) was used to select the high Q^2 events outside of the Outer trigger acceptance.

For the selection of SIDIS events all the above trigger systems were used. The trigger hodoscopes with only horizontal slabs, the OT, MT and LAST, were used without any calorimeter requirement, just selecting events with a particle in coincidence in the hodoscopes pair and obeying to the matrix coincidences, which allows only events from the target region. In addition, the veto signal was added to these triggers to avoid events from beam halo. In Fig. 2.15 an event is illustrated, with two muon tracks which produce a veto signal. The disadvantage of the usage of vetos is that they introduce a veto dead time during which a good event candidate cannot be accepted. For the low Q^2 events, with the scattered muon emitted at a small angle, the target pointing technique is not used. In this case the hodoscopes with vertical slabs are used, the

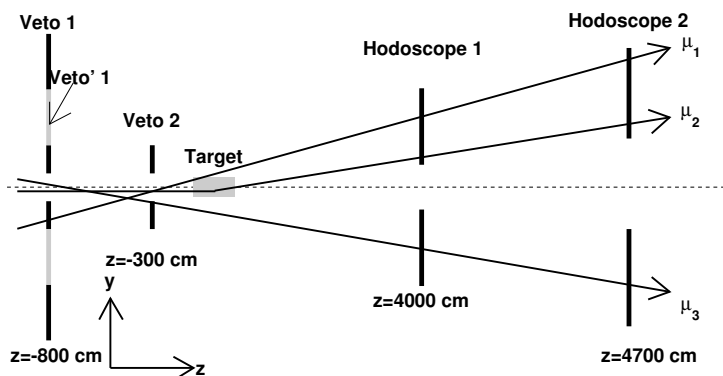


Figure 2.15: Principle of veto signals. The tracks μ_1 and μ_3 produce a veto signal, while the track μ_2 does not.

IT, the MT and the LT. Taking into account the scattered muon bending in the spectrometer magnets, correlated to its energy, it is possible to select the events stemming from the target. In addition, in SIDIS case is also required an energy deposit above a certain threshold in the calorimeters to select events with emitted hadrons. The SIDIS trigger concept is illustrated in Fig. 2.16.

For the selection of DY events the topology of the event is to have in the final state two muons in coincidence. In order to select dimuon events the double triggers are mandatory. Single muon signals in the LAST system were used in coincidence with those in the Outer system or in the Middle system. A double signal in the LAST, selecting events with at least two signals in LAST, also selects DY events. The coincidence matrices were optimized using high mass MC DY events. These triggers had the veto signals taken into account. In the 2009 DY beam test run, to select the events with one muon or more than one muon in LAS, the hadronic calorimeter HCAL1 was used, with two thresholds selecting multiplicity.

2.6 Data Acquisition

The COMPASS data acquisition system has to deal with a large amount of data from more than 250000 detector channels, with a typical event size of around 45 kB and a trigger rate of around 30 kHz during the spill time. The data is handled and saved in steps. This structure was developed to avoid data losses and minimize the DAQ dead time. The schematic of the data flow is in Fig. 2.17.

The analogic detectors output signals are digitized and buffered on the detectors front-end boards. The readout modules CATCH (COMPASS Accumulate, Transfer and Control Hardware) and GeSiCA (GEM and Silicon Control and Acquisition) receive the trigger signals from the TCS (Trigger Control System) and collect the data buffered within a specific time window on the front-end boards and build local sub-events; one CATCH module can combine the data from up to 16 front-end boards. The data are transferred to read-out buffers (ROBs) via fast links and then stored on Spill buffers during the spill time duration. The remaining SPS super-cycle, the off-spill period, is used to send the data to the Event Builders (EBs) via Gigabit Ethernet switches. The sub-events are combined together to build the full events. The events are then transferred to the CERN data center and stored on tape at the CERN Advanced Storage System (CASTOR). In case of problems with the tape recording, the EBs system has

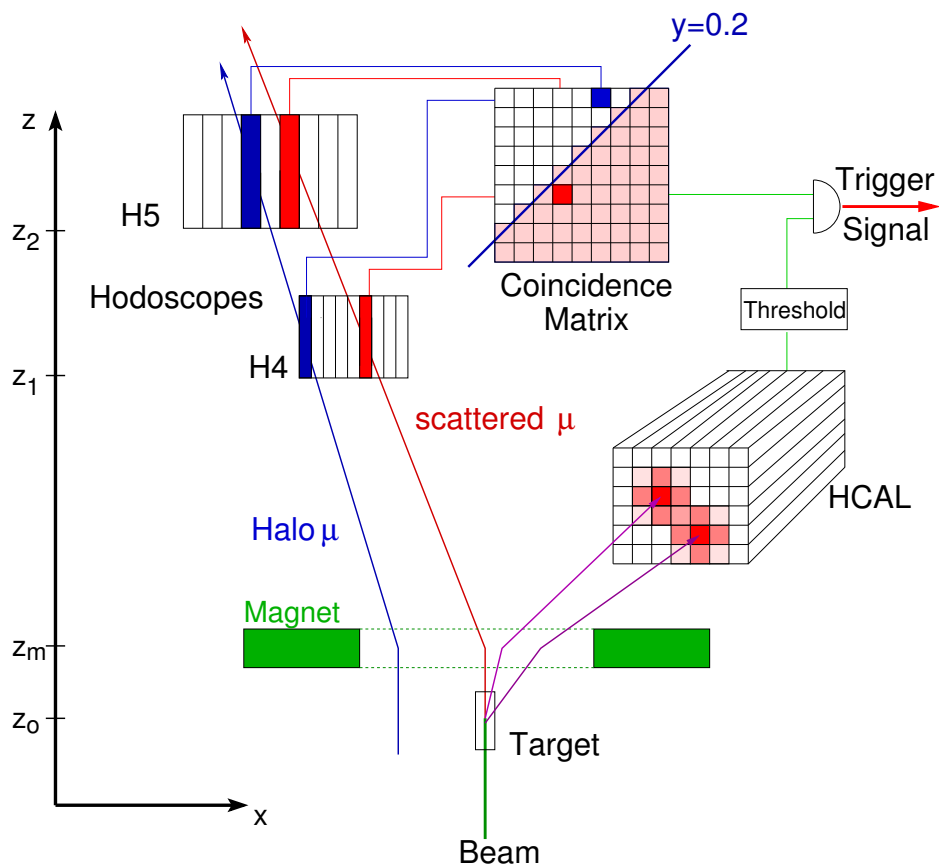


Figure 2.16: Trigger concept to select low Q^2 SIDIS events.

around 8 TB of available disk space. For COMPASS-II a new readout module was developed, it was used for the first time in the 2014 and 2015 DY runs.

In addition to the saved raw data there are other important information saved during the data-taking, these can be found in the COMPASS data base and in the Detector Control System (DCS). DCS is very useful during the data taking, providing the user interface to control several detector parameters, which are kept and can be used later during the analysis to judge on the data quality.

2.7 Data Production

The raw data saved on tape need to be produced, which means the events need to be reconstructed. The reconstruction program is the CORAL (COmpass ReConstruction and AnaLysis), which receives the raw data files and produce mDST files (mini Data Summary Tapes) with the reconstructed events. In the raw data files the saved information is the fired detectors channels that are going to be decoded and these information will be put together taking into account the detectors geometry, this stage is called the clustering. The next step is the tracks reconstruction, initially the spectrometer is divided in different zones, one zone before the target, one zone between the target and the SM1, one zone between SM1 and SM2, one zone between SM2 and MF2 and the last zone downstream MF2. The first part of the tracks reconstruction is the patterns recognition, reconstruct track segments in each of these zones. Then these segments are

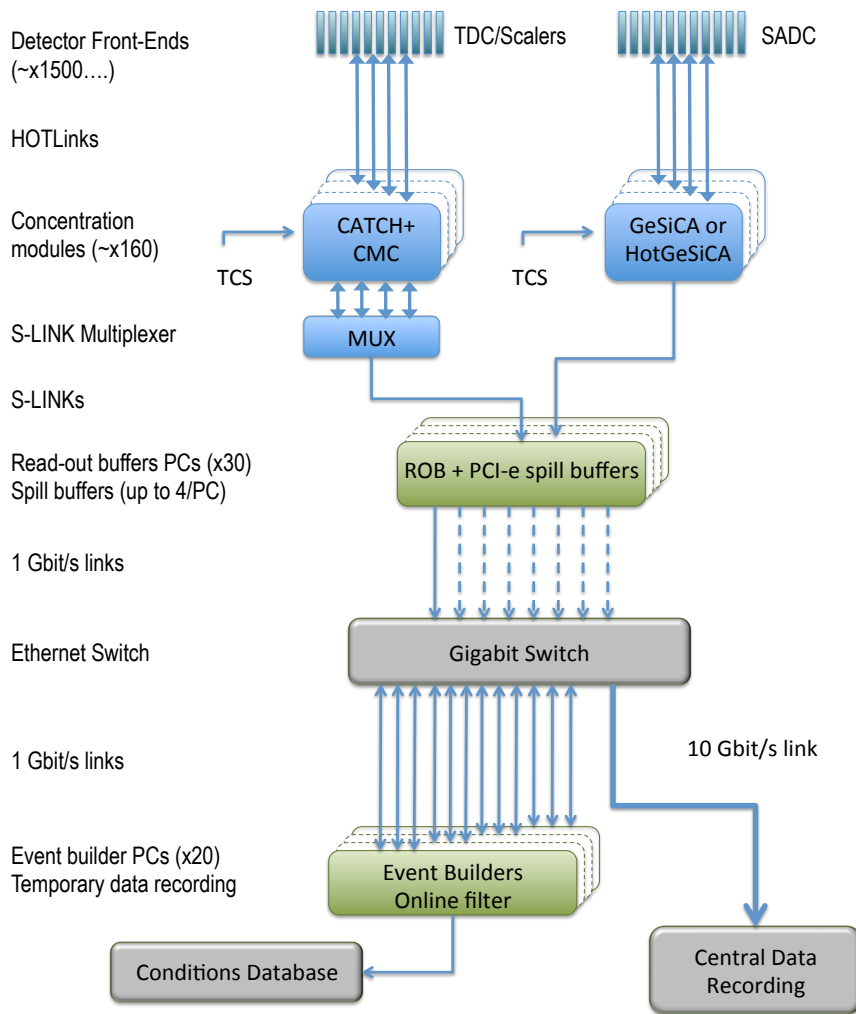


Figure 2.17: Schematic of the DAQ system in COMPASS.

connected taking into account the magnetic field and the materials present in the connection of the zones, this is called the bridging. The last part of the tracking is the fit of the track taking into account the whole information. The last step of the reconstruction is the vertexing, which uses all the previous reconstructed tracks to reconstruct the vertices. The reconstructed events can then be analyzed with PHAST (PHysics Analysis Software and Tools) which allows to access the information saved in the mDSTs for each event, such as the tracks, the vertices and all the parameters related to them.

Spectrometer Alignment

The spectrometer alignment is a very important task taking place during any data taking. The author was responsible for the alignment during the 2014 data taking. The goal of this task is to align the trackers and produce a file called *detectors.dat* with a detailed description of all the detectors, namely their positions in the spectrometer to be further used in the data reconstruction. Dedicated alignment runs are taken, typically every week.

The alignment is a difficult task since there are around 200 planes and for each plane it is necessary to tune several parameters: the translation along the coordinate measured by the detector plane; the rotation in the detector plane, the translation along the beam direction, and the effective pitch of the detector, which is somehow correlated with the z position along the beam line.

The alignment procedure consists in the minimization of the distances of the hits to the tracks in the detectors. This results in a huge number of parameters, the track parameters and the detector parameters of each track for each detector plane. This is possible due to some matrix manipulations, developed at DESY by W. Blobel [108].

In this chapter the alignment procedure is presented. For a more complete description see the COMPASS note [109].

3.1 Alignment Procedure

As a starting point a *detectors.dat* with some nominal values for the detectors positions, which were provided by a trigonometric survey with a precision of around 1 mm, is used. However there are detectors with much better resolutions and, furthermore, their supports can be affected by their weight, the temperature and the magnetic field. This is the reason why sets of two dedicated runs are taken, one with the magnetic fields of the spectrometer magnets off and another one with the magnetic fields on. These two dedicated runs are taken using a low intensity muon beam in order to have in average only one track per event. A dedicated trigger configuration is used, selecting only beam, veto inner and halo triggers to illuminate all the detector planes. The alignment is done using all the tracks reconstructed from the field off run and, in a subsequent interaction, using all the tracks reconstructed from the field on run. These correspond to around 10^5 tracks per iteration.

3.1.1 Alignment Parameters

In order to introduce the alignment parameters, it is necessary to define a local reference system for each detector plane.

The COMPASS main reference system ($Oxyz$) is defined by a z axis along the beam line; a vertical y axis and orientated upwards; and a horizontal x axis perpendicular to the z and y axes and orientated such that the system is right-handed. The origin O is located at the target center for the original setup of COMPASS and remains fixed even if the target center has been changed over the years depending on the physics program.

The local reference system ($O'uvz$) is defined by a z axis as in main reference system; u is perpendicular to the detector strips or wires, coinciding with the detector measurements; and v is parallel to them. The origin O' is the intersection of the z axis with the detector plane.

The alignment parameters are the following:

- δu , a transverse offset perpendicular to the wires;
- $\delta\theta$, a rotational offset in the plane perpendicular to the beam axis;
- δz , a longitudinal offset along the z axis;
- δp , the effective pitch of the detector; the quantity $1+\delta p$ can be seen as a scaling factor for the detector.

3.1.2 Alignment Program

3.1.2.1 The χ^2 Minimization and Matrix Inversion

The principle of the alignment is to fit all the hits measured in the detectors with a certain track model, which depends on the track parameters α_t and the alignment parameters α_a for all the detectors contributing to the track. Considering straight tracks, 4 track parameters are needed: (x_0, y_0) , the track position in a reference frame located at z_0 , and $(t_{x,0}, t_{y,0})$, the tangent of the track angles with respect to the beam axis.

There is a set of track parameters for each track, while the alignment parameters are the same for all tracks.

The alignment consists in the minimization of the following χ^2 :

$$\chi^2 = \sum_{i=1}^{n_{tracks}} \sum_{j=1}^{n_{detectors}} \frac{[F_j(u_{ij}, \alpha_{t,i}, \alpha_a)]^2}{\sigma_j} \quad (3.1)$$

where σ_j is the resolution of the detector j , F_j is the distance between the hit position measured by the detector, u_{ij} , and the track position in the detector according to the track model. F_j depends on the track and alignment parameters, and will be defined later in the text.

The χ^2 minimization is done requiring that all the partial derivatives of χ^2 over all the alignment and track parameters are zero, which can be written as the following matrix:

$$\begin{pmatrix} \overline{\sum C_i} & \cdots & \overline{G_i} & \cdots \\ \vdots & \ddots & 0 & 0 \\ \overline{G_i^T} & 0 & \overline{\Gamma_i} & 0 \\ \vdots & 0 & 0 & \ddots \end{pmatrix} \begin{pmatrix} \overline{\alpha_a} \\ \vdots \\ \overline{\alpha_{t,i}} \\ \vdots \end{pmatrix} = \begin{pmatrix} \overline{\sum b_i} \\ \vdots \\ \overline{\beta_i} \\ \vdots \end{pmatrix} \quad (3.2)$$

where $\sum C_i$ and $\sum b_i$ include only derivatives of F_j with respect to the alignment parameters $\partial F_j/\partial\alpha_a$; Γ_i and β_i include only derivatives of F_j with respect to the track parameters $\partial F_j/\partial\alpha_t$; and G_i includes mixed terms of type $\partial F_j/\partial\alpha_a \partial F_j/\partial\alpha_t$. The first matrix in the equation should be inverted to obtain the solution for this system. However it is unrealistic to invert this matrix directly; it would lead to a huge CPU time consumption. For example, for 1000 straight tracks (with 4 track parameters each) and 200 detectors (with 4 alignment parameters each) the size of the matrix is 4800 ($1000 \times 4 + 200 \times 4$). Fortunately, due to the special structure of the matrix with many zeros it is possible to split it in several smaller matrices and do the inversion in simpler steps.

It was shown [108] that the alignment parameters are obtained using

$$\alpha_a = C'^{-1}b' \quad (3.3)$$

where

$$C' = \sum_i C_i - \sum_i G_i \Gamma_i^{-1} G_i^T \quad (3.4)$$

and

$$b' = \sum_i b_i - \sum_i G_i \Gamma_i^{-1} \beta_i \quad (3.5)$$

thus only Γ_i matrices need to be inverted one by one to end up with an inversion of C' , which has the dimension of the number of alignment parameters.

3.1.2.2 The Function F_j

Consider that tracks are straight lines, which is the case whenever the magnetic fields are off. In a first stage only the track parameters x_0 , y_0 , $t_{x,0}$ and $t_{y,0}$ are used and not the alignment ones. The track coordinates at z_j , the z coordinate of the detector j are:

$$x_j = x_0 + t_{x,0}(z_j - z_0) \quad (3.6)$$

$$y_j = y_0 + t_{y,0}(z_j - z_0) \quad , \quad (3.7)$$

and the distance F_j between the hit measured by the detector j , u_j , and the track position in the same detector is

$$F_j = \{\cos\theta[x_0 + t_{x,0}(z_j - z_0)] + \sin\theta[y_0 + t_{y,0}(z_j - z_0)]\} - u_j \quad (3.8)$$

where θ is the angle between u and x .

Adding the alignment parameters, F_j transforms into

$$F_j = (1 + \delta p)\{\cos(\theta + \delta\theta)[x_0 + t_{x,0}(z_j + \delta z - z_0)] + \sin(\theta + \delta\theta)[y_0 + t_{y,0}(z_j + \delta z - z_0)]\} - (u_j + \delta u) \quad (3.9)$$

where δu is a correction to the measured u_j ; $\delta\theta$ is a correction to the θ angle between x and u ; δz is a correction to z_j , the z position of the detector; and δp is the pitch parameter. δp should affect the measurement u_j , however it was decided to apply this to the first term instead, in order to keep the derivatives of F_j independent of u_j . This is equivalent to scaling F_j by the pitch of the corresponding detector.

All the derivatives of F_j were linearized so that the alignment parameters do not appear. The partial derivatives of F_j with respect to the tracking parameters are:

$$\frac{\partial F_j}{\partial x_0} = \cos(\theta + \delta\theta) \quad (3.10)$$

$$\frac{\partial F_j}{\partial y_0} = \sin(\theta + \delta\theta) \quad (3.11)$$

$$\frac{\partial F_j}{\partial t_{x,0}} = \cos(\theta + \delta\theta)(z_j + \delta z - z_0) \quad (3.12)$$

$$\frac{\partial F_j}{\partial t_{y,0}} = \sin(\theta + \delta\theta)(z_j + \delta z - z_0) \quad (3.13)$$

and with respect to the alignment parameters:

$$\frac{\partial F_j}{\partial \delta u} = -1 \quad (3.14)$$

$$\frac{\partial F_j}{\partial \delta z} = t_{x,0} \cos(\theta + \delta\theta) + t_{y,0} \sin(\theta + \delta\theta) \quad (3.15)$$

$$\frac{\partial F_j}{\partial \delta \theta} = -x_j \sin(\theta + \delta\theta) + y_j \cos(\theta + \delta\theta) \quad (3.16)$$

$$\frac{\partial F_j}{\partial \delta p} = x_j \cos(\theta + \delta\theta) + y_j \sin(\theta + \delta\theta) \quad (3.17)$$

Consider now the case of charged tracks in the presence of a magnetic field. The track model should be modified. In this case the tracks as determined by the reconstruction program CORAL are used, together with a linear deviation to them. Considering a track with parameters x_j^0 , y_j^0 , $t_{x,j}$ and $t_{y,j}$ in the detector plane located at z_j , the aligned track coordinates at this detector are defined by a linear deviation with respect to the parameters obtained during the reconstruction:

$$x_j = x_j^0 + \delta x_0 + t_{x,j} \delta z + \delta t_{x,0} \delta z \quad (3.18)$$

$$y_j = y_j^0 + \delta y_0 + t_{y,j} \delta z + \delta t_{y,0} \delta z \quad (3.19)$$

where δx_0 , δy_0 , $\delta t_{x,0}$ and $\delta t_{y,0}$ are small deviations relative to the CORAL parameters. So F_j becomes:

$$F_j = (1 + \delta p) \{ \cos(\theta + \delta\theta) [x_j^0 + t_{x,j} \delta z + \delta x_0 + \delta t_{x,0} \delta z] + \sin(\theta + \delta\theta) [y_j^0 + t_{y,j} \delta z + \delta y_0 + \delta t_{y,0} \delta z] \} - (u_j + \delta u) \quad (3.20)$$

In this case the derivatives are:

$$\frac{\partial F_j}{\partial \delta x_0} = \cos(\theta + \delta\theta) \quad (3.21)$$

$$\frac{\partial F_j}{\partial \delta y_0} = \sin(\theta + \delta\theta) \quad (3.22)$$

$$\frac{\partial F_j}{\partial \delta t_{x,0}} = \cos(\theta + \delta\theta) \delta z \quad (3.23)$$

$$\frac{\partial F_j}{\partial \delta t_{y,0}} = \sin(\theta + \delta\theta) \delta z \quad (3.24)$$

and:

$$\frac{\partial F_j}{\partial \delta u} = -1 \quad (3.25)$$

$$\frac{\partial F_j}{\partial \delta z} = (t_{x,j} + \delta t_{x,0}) \cos(\theta + \delta\theta) + (t_{y,j} + \delta t_{y,0}) \sin(\theta + \delta\theta) \quad (3.26)$$

$$\frac{\partial F_j}{\partial \delta \theta} = -x_j \sin(\theta + \delta\theta) + y_j \cos(\theta + \delta\theta) \quad (3.27)$$

$$\frac{\partial F_j}{\partial \delta p} = x_j \cos(\theta + \delta\theta) + y_j \sin(\theta + \delta\theta) \quad (3.28)$$

3.1.3 Quality Criteria

After the alignment is performed, its quality needs to be assessed. For that both absolute and relative criteria are used.

The absolute criteria rely on the analysis of the following distributions:

- The residuals distribution $\Delta u = u_{hit} - u_{track}$, where u_{hit} is the hit position in the detector, measured in the direction perpendicular to its strips or wires, and u_{track} is the track position along the same axis. The residual average $\langle u \rangle$ is sensitive to the transverse offset δu , and should be equal to zero. The RMS of the distribution should be compatible with the detector resolution.
- The distribution Δu versus v , the track position in the direction parallel to the detector strips or wires. The slope of the distribution $\partial\langle u \rangle/\partial v$ is sensitive to the rotational offset $\delta\theta$, and should be equal to zero.
- The distribution Δu versus u , the track position in the direction perpendicular to the detector strips or wires. The slope of the distribution $\partial\langle u \rangle/\partial u$ is sensitive to the pitch factor δp , and should be equal to zero.

The relative criteria consist in a general overview of the reconstruction performance and in the analysis of some physics quantities, such as:

- The number of reconstructed tracks per event.
- The number of reconstructed vertices per event.
- The number of tracks per vertex.
- The χ^2/ndf of the tracks.
- The mass width of the resonances, e.g. the J/ψ mass resolution.

3.1.4 Results

As a starting point a *detectors.dat* from the previous year was used. The vertex detector description was added since this detector was included in the setup for the first time. The MicroMega 1 started to be changed in 2012. During that period 2 of the planes included already a pixelised part in its center, and the 2 others were added in 2014. Thus its description was added to the *detectors.dat* as well. In the beginning of the alignment procedure the misalignment was huge for some detectors. In some cases the tracks were not using the information of the detectors since they were very deviated, by some centimetres from their current position in the *detectors.dat*. In these cases a Coral feature was used allowing the reconstruction of tracks excluding a specific detector or plane and checking which is the distance from the reconstructed track to the closest hit in the excluded detector plane. The alignment procedure is an iterative process and it evolved together with the data taking. After a certain stability was achieved, meaning that all the detector planes had enough statistics, it was decided that the best alignment strategy should follow the next 4 steps or iterations:

1. Alignment using the run with the magnetic field off, using all the detectors in the spectrometer except the three SciFi's in the beam telescope, the vertex detector and the Muon Wall 1. The MW1, although very important for the DY program, is a delicate detector

because it has a 60 cm iron block in between their two sets of planes and, therefore, the reconstruction is more difficult in this region.

2. Alignment using the run with field on, with all the detectors included except the vertex detector and the three SciFi's in the beam telescope.
3. Alignment using the run with field on, using the same detectors except vertex detector to align the beam telescope detectors; the alignment parameters for all the detectors except the beam telescope ones are fixed.
4. Alignment using the run with field on, using all the detectors to align the vertex detector; the alignment parameters for all the detectors except the vertex detector are fixed.

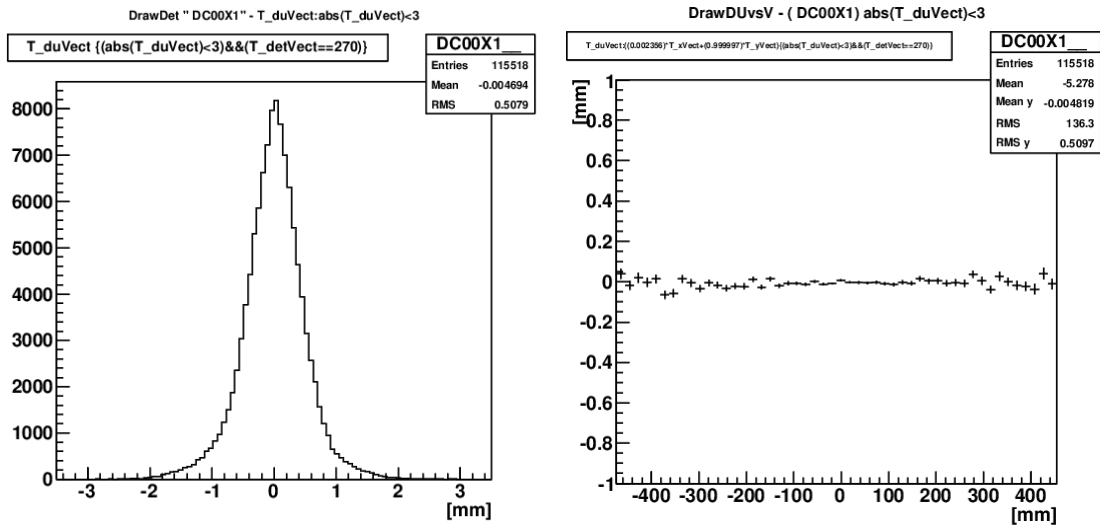
In Fig. 3.1 one example is shown of the distributions used to control the alignment for one single plane of DC00. Fig. 3.1a shows the residuals for plane X1 of the DC00. The distribution is centered at zero, with a mean value of $-4.7 \mu m$ and a RMS of $508 \mu m$, which is ~ 2 times the expected spatial resolution of this detector, $250 \mu m$. The real resolution of this detector is evaluated in a dedicated analysis to the double residuals and it was found to be worse, around $350 \mu m$. In Fig. 3.1b the residuals along the v direction, parallel to the wires, are shown. As the distribution is flat, the angle of the wires with the x axis is well defined. In Fig. 3.1c the residuals along u direction, perpendicular to the wires, show a flat distribution meaning that there is no systematic effect depending on the detector wire. If a slope appears it means that either the pitch or the z position of the detector were not correct.

As a summary all the detectors used in 2014 alignment are listed in Table 3.1. The spatial resolution of the detectors is quoted, as well as the minimum and maximum RMS of the residuals distributions. The RMS of the residuals for each detector plane is aimed to be of the same order as the spatial resolution of the detector. The results achieved are around one or two spatial resolutions. Only for the vertex detector the RMS is around 6 times its expected spatial resolution. This is understood since the detector is placed in the middle of the absorber and the tracks crossing the absorber will suffer enormous multiple scattering and may associate hits further from their linear extrapolation.

Detector	resolution (μm)	Residuals RMS	# σ
FI01	130	160-165	1.3
FI15	150	217-237	1.6
FI03	130	158-170	1.3
FI35	150	862-873	5.8
MP01	110	130-175	1.6
DC00	250	418-566	2.3
MM02	110	96-106	1.0
FI04	120	236-269	2.2
MM03	110	92-177	1.6
DC01	250	426-491	2.0
DC04	250	449-577	2.3
GM01	110	97-111	1.0
GM02	110	93-108	1.0
ST03	400	442-629	1.6
GM03	110	95-105	1.0
PS01	600	602-634	1.1
GM04	110	94-100	0.9
DR	600	639-954	1.6
GP02	110	92-168	1.5
PA01	600	634-641	1.1
GM05	110	91-105	1.0
MA01	3000	2725-2997	1.0
MA02	3000	2603-3674	1.2
PA02	600	567-580	1.0
GM06	110	96-120	1.1
PA03	600	548-556	0.9
GM07	110	72-86	0.8
PA04	600	556-562	0.9
GM08	110	80-96	0.9
PA05	600	551-555	0.9
GM09	110	71-85	0.8
GP03	110	70-162	1.5
ST05	400	545-880	2.2
DW01	1500	976-1018	0.7
DW02	1500	932-979	0.7
DW03	1500	866-994	0.7
DW04	1500	898-926	0.6
DW05	1500	850-872	0.6
PA11	600	533-543	0.9
PA06	600	525-544	0.9
GM10	110	69-76	0.7
DW06	1500	890-908	0.6
PB01	600	577-605	1.0
PB02	600	598	1.0
MB01	1400	1189-1718	1.2
PB03	600	550-552	0.9
PB04	600	551	0.9
MB02	1400	1204-1489	1.1
PB05	600	561-585	1.0
PB06	600	586	1.0

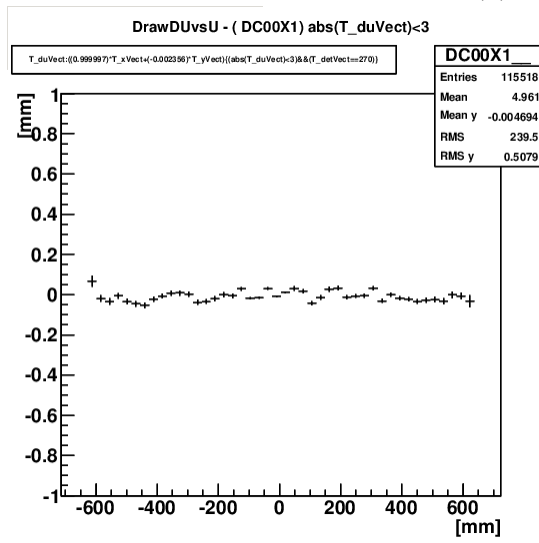
Table 3.1: Detectors used in 2014 alignment.

3. SPECTROMETER ALIGNMENT



(a) Δu

(b) Δu versus v



(c) Δu versus u

Figure 3.1: Alignment control distributions for DC00X1 plane.

Extraction of Transverse Spin Asymmetries from SIDIS

The 2010 COMPASS data taking was exclusively dedicated to the measurement of the target spin dependent azimuthal asymmetries in semi-inclusive deep inelastic scattering of muons off transversely polarised protons. A positive muon beam with 160 GeV/ c and three ammonia target cells transversely polarised with respect to the direction of the beam were used, the two outer cells being oppositely polarised with respect to the inner one. This measurement was successfully performed for the first time in 2007. A second year was dedicated to this measurement with the goal of improving the statistics and consequently reduce the errors associated with the asymmetries, and thus giving the opportunity to perform the analysis as a function of the relevant kinematic variables and in several bins. The analysis presented in this thesis was done using the 2010 data. The transverse spin dependent asymmetries were extracted in a multi-dimensional grid dividing the statistics by different phase space regions. In this chapter the data selection will be presented, followed by the extraction of the asymmetries.

4.1 The 2010 Data Taking

The data collected during the 2010 run is divided in 12 periods. Each period comprises 2 sub-periods with opposite spin configurations. One period has exceptionally 3 sub-periods such that the statistics are balanced in the sub-periods with opposite polarisations. The division of the periods and their statistics is shown in Table 4.1; the 12 periods are named by the calendar week and from 1 to 12. The spin configuration by sub-period is in the Table as well as the range of runs. The last two columns present the data volume collected and the number of events per period. In total 1815 TBytes were collected and saved in tape, corresponding to 37×10^9 events.

The polarisation reversal requires more than a day, because it implies a new polarisation built-up, and in order to use effectively the beam time the sub-periods have to last for some days. Each sub-period corresponds to 3 to 6 days. Very strict stability conditions of the data taking during a period are required to minimize possible acceptance variations in the data of two sub-periods since they can potentially introduce systematic effects at the level of physics asymmetries. The data quality tests performed to ensure that such stability exists will be presented.

Period	Sub-period	Runs range	Collected data	
			TBytes	# events
w23_p1	↓↑↓	85026-85070	54.3	1099896305
	↑↓↑	85093-85164		
w24_p2	↑↓↑	85197-85301	73.8	1479139255
	↓↑↓	85362-85445		
w26_p3	↓↑↓	85468-85512	57.5	1158982236
	↑↓↑	85569-85638		
w27_p4	↑↓↑	85669-85713	66.9	1331925927
	↓↑↓	85771-85850		
w29_p5	↑↓↑	86202-86323	101.0	2090396862
	↓↑↓	86355-86446		
w31_p6	↓↑↓	86462-86600	166.6	3321755884
	↑↓↑	86641-86703		
w33_p7	↑↓↑	86784-86945	184.4	3689568241
	↓↑↓	87024-87135		
w35_p8	↓↑↓	87354-87468	200.4	4028866060
	↑↓↑	87518-87619		
w37_p9	↑↓↑	87633-87711	206.7	4148031518
	↓↑↓	87780-87871		
w39_p10	↓↑↓	87902-88013	294.3	5910841333
	↑↓↑	88055-88204		
	↓↑↓	88245-88255		
w42_p11	↓↑↓	88512-88590	204.8	4173112436
	↑↓↑	88651-88767		
w44_p12	↑↓↑	88850-88933	204.5	4216917860
	↓↑↓	89046-89209		
Total			1815.3	36649433917

Table 4.1: 2010 data taking organization.

4.2 Data Quality Tests

The first stage of the data quality assessment comes before the events reconstruction. On a run by run basis all the detector performances are monitored and in case of problems in a specific detector plane it may be decided to exclude it from the reconstruction for the full period. A main effort is done during the data taking, tagging all the possible problems run by run. For the 2010 data also an off-line detector-profile analysis was developed, described in [110]. For each run the profiles in each detector plane, the mean value, the RMS and the total number of hits normalized to the beam intensity were checked. From this analysis some problems were identified. A list with all the problematic detectors per period was produced. To ensure the stability of the data during each period and the balance of statistics between the 2 sub-periods all the decisions have to affect the 2 sub-periods equally. Only runs with more than 20 spills were produced, since short runs usually mean the data taking was interrupted due to some problem identified. After this first selection the number of collected events to be produced was reduced by a bit less than 3%, as can be seen in Table 4.2.

A total of 35.7×10^9 events are reconstructed and only the ones with at least one primary

vertex are saved in mDSTs, which leads to a rejection of 15% of the processed events, as Table 4.2 shows. The second stage of the data quality evaluation is done after the production and consists in the analysis of some reconstructed quantities on a spill by spill basis, like the number of tracks per event, the number of beam particles per event, the number of primary vertices per event and the trigger rates. If the quantity under study deviates considerably in one spill comparing with the neighbouring spills, then the spill is tagged as bad. The outcome of this analysis is a list of bad spills to be removed from the final data sample. If one run has more than 80% of bad spills it is removed from the data set. In the end around 4% of the events are rejected.

The third stage of the data quality evaluation is the check of the K^0 mass stability. This test is done in a run by run basis and already without the bad spills. It consists in the analysis of the decay $K^0 \rightarrow \pi^+\pi^-$. The invariant mass distribution is fitted and the mass pole, the mass resolution and the number of K^0 's are checked. If any of these variables deviates by more than 3σ from the mean value in one of the runs, the run is rejected. Regarding this test 3% of the runs were rejected, corresponding to less than 1% of events.

The fourth stage of evaluation is the kinematic stability. This is checked after the rejection of the bad spills and runs and also after applying the events selection which will be explained in section 4.3. In this test several kinematic distributions are checked: x , y , Q^2 , E_h , $E_{\mu'}$, p_{Th} , $\theta_{\mu'}$, $\phi_{\mu'}$, θ_h , ϕ_h . The ratios between the distributions in each sub-period for all triggers and also trigger by trigger are checked. The ratios between the distributions of each run of a sub-period with the distribution of the whole other sub-period are evaluated. The ratios are fitted with constant functions and based on the quality of the fits problematic runs or triggers are identified. After a first cleaning the same process is repeated. From this test it was found out an instability of the calorimeter trigger in the period w29_p5. Events where at least one of the triggers which does not rely on the calorimeter (Ladder Trigger, Outer Trigger and Middle Trigger inclusive) are kept.

After all the quality tests a list of bad spills and runs was produced and is used in all the analyses of the 2010 data. From all the events saved in the mDSTs the ones that survived after removing the bad spills and runs are present in Table 4.2. The rejection fraction from period to period oscillates, being the higher rejection 30.4% for w24_p2 and the lower 3.6% for w35_p8. In average a fraction of 8.4 % of the mDST events are rejected.

For more details on the quality checks see for example [110–112].

4.3 Events Selection

For the events selection it was decided first to save all the events with a best primary vertex and a scattered muon (μ') candidate in a ROOT-tree, and then perform all the selection over those events.

1. From the 27.9×10^9 events surviving bad spills/runs rejection, 24.8×10^9 have a best primary vertex with a scattered muon candidate, according to the criteria:
 - a) Each event can have more than one primary vertex, a vertex of interaction with a beam track associated. The best primary is the one with more outgoing particles. If there is more than one with the same number of outgoing particles, the one with the best χ^2 is selected.
 - b) This vertex must have a μ' candidate. This is ensured with the Phast function `PaVertex::iMuPrim(bool checkYokeSM2=false, bool reject2MuEvents=true, bool checkCanBeMuon=true, bool checkHodos=false, double XX0=30)`.

Period	# collected events	# processed events	# events written on mDSTs	# events surviving bad spill/run lists
w23_p1	1099896305	1084347851	1084329288	941346551
w24_p2	1479139255	1441053660	1441053289	1002579645
w26_p3	1158982236	1092470850	1085994178	1017431291
w27_p4	1331925927	1300928879	1300928535	1140832466
w29_p5	2090396862	1920225638	1919284113	1756881580
w31_p6	3321755884	3259631794	3236654884	3107158038
w33_p7	3689568241	3538950178	2834498735	2557409273
w35_p8	4028866060	3980228336	3196433756	3082362882
w37_p9	4148031518	4134543986	3297953878	2994785876
w39_p10	5910841333	5791379164	4615996872	4400587680
w42_p11	4173112436	3992870533	3175199093	2975143736
w44_p12	4216917860	4154062680	3287441273	2935798808
Total	36649433917	35690693549	30475767894	27912317826

Table 4.2: Statistics reduction due to quality tests.

- i. The first argument was used in the past to reject μ' candidates passing through the SM2 yoke, because the field was not well known there; however this is not necessary anymore since the CORAL revision used in 2010 production was modified to evaluate the momentum of these tracks using only SM1.
 - ii. The second argument requires the rejection of cases with more than one μ' candidate, being a μ' candidate a track with momentum, the same charge as the beam, the last measured point after muon filter 1 and more than 30 radiation lengths crossed (as defined by the fifth argument).
 - iii. The third argument rejects cases with tracks pointing to the absorber holes, because these tracks can be muons which do not pass enough radiation lengths to be assigned as a μ' candidate.
 - iv. The fourth argument requires the μ' candidate to cross the active area of the trigger hodoscope pair corresponding to one of the fired triggers. This criterion has a negligible impact and it was decided not to use it.
 - v. The fifth argument requires that the μ' candidate has to cross more than 30 radiation lengths.
2. The best primary vertex must have at least 2 outgoing particles. For the selection of the beam particle associated to it, one requires the incoming particle to have:
 - a) $\chi^2/ndf < 10$, to reject cases with a poorly reconstructed beam track.
 - b) $140 < p < 180$ GeV/c, as measured by the BMS.
 - c) $\delta p < 4$ GeV/c, corresponds to the rejection of beam particles without BMS reconstruction.
 3. Requirement that the beam track passes all the cells of the target, in order to ensure an identical muon beam flux in both cells; for this there is a dedicated Phast function, PaAlgo::CrossCells(). It is required that the beam particle when extrapolated to the most upstream and the most downstream parts of the target cells is in their acceptance in transverse plane. The target cells limits are described in the function PaAlgo::InTarget(), described below.

4. Requirement that the primary vertex is inside the target material, using a dedicated Phast function, `PaAlgo::InTarget()`. This takes into account the center of the cells in the transverse plane, and its position along the beam. In 2010 the cells were centered at $(x, y) = (-0.2, 0.02)$ cm. The vertices within a radius of 1.9 cm from the center are kept. Along the beam direction, a selection is also made, $-62.5 < Z_{vtx} < -32.5$ cm for the upstream cell, $-27.5 < Z_{vtx} < 32.5$ cm for the central cell and $37.5 < Z_{vtx} < 67.5$ cm for the downstream cell. The impact of this cut after all the other cuts are applied is visible in Fig. 4.1. The separation between the target cells is well pronounced showing a good vertex resolution. This selection rejects 9.6% of hadrons as visible in Fig. 4.1.
5. The μ' selection. The track selected with the function `PaVertex::iMuPrim()` previously described must pass the following criteria:
 - a) $\chi^2/ndf < 10$, to reject cases with a poorly reconstructed muon track.
 - b) the first measured point before SM1, $Z_{first} < 350$ cm.
6. $Q^2 > 1$ (GeV/c)², to select events from deep-inelastic scattering region, the Q^2 coverage is visible in the Fig. 4.2.
7. $W > \sqrt{10}$ GeV/c², a cut on the invariant mass of the hadronic final state, allowing the rejection of events from the region of the nucleon resonances, where the struck quark fragments into resonances instead of into hadrons. The impact of this cut in the final hadrons sample is visible in Fig. 4.3. Its rejection is less than 1/1000000 of the hadrons. There is a strong correlation between W and y , and therefore cutting at low y has an impact at low W .
8. $0.1 < y < 0.9$, where y is the fractional energy of the virtual photon. The cut on $y < 0.1$ rejects events from the elastic scattering regime and possibly also events where halo muons are falsely identified as scattered muons. The cut on $y > 0.9$ removes events where radiative corrections are crucial. The impact of this cut is shown in Fig. 4.4. This cut rejects 17.7% of hadrons.
9. DIS events should be within the range $0.003 < x < 0.7$ taking into account the beam energy and the geometrical acceptance of COMPASS. The impact of this cut is shown in Fig. 4.5. This cut rejects 1/5000 of the hadrons. The x coverage is visible in the Fig. 4.2, which shows the phase space, Q^2 versus x .

The event selection impact on the statistics is shown in Table 4.3. From all the events saved on the tree, with one primary vertex and one scattered muon candidate only 0.5% of them survive all the cuts.

The next step is the hadron selection. The following criteria are applied to all the outgoing tracks from best primary vertex, apart from the μ' :

1. $\chi^2/ndf < 10$, to reject cases with a poorly reconstructed hadron track.
2. $x/X_0 < 10$, the number of radiation lengths crossed by the track smaller than 10 to avoid muons.
3. $Z_{first} < 350$ cm and $350 < Z_{last} < 3300$ cm, to ensure that the hadrons start before SM1 and end between SM1 and Muon Filter 2.
4. $p_{Th} > 0.1$ GeV/c, to ensure a good resolution in the measured azimuthal angle. The impact of this cut is visible in Fig. 4.6. It rejects 5% of the hadrons.

Cut	# events	% of events after the cut
1. Number of events in tree	24809139074	100 %
2. $N_{outgoing\ particles} \geq 2$ and beam selection	6971097200	28.1 %
3. Cross cells	6672878582	26.9 %
4. In target	5481323084	22.1 %
5. μ' selection	1315137021	5.3 %
6. $Q^2 > 1$	159354287	0.6 %
7. $W > \sqrt{10}$	152323753	0.6 %
8. $0.1 < y < 0.9$	121397224	0.5 %
9. $0.003 < x < 0.7$	121378566	0.5 %

Table 4.3: Impact of the selection cuts on the number of events.

	Cut	# hadrons		# positive hadrons		# negative hadrons	
	After events selection	388751525	100 %	207585397	100 %	181166128	100 %
1.	$\chi^2/ndf < 10$	383108787	98.5 %	204513348	98.5 %	178595439	98.6 %
2.	$x/X_0 < 10$	381654097	98.2 %	204129681	98.3 %	177524416	98.0 %
3.	$350 < Z_{last} < 3300$ cm and $Z_{first} < 350$ cm	359447735	92.5 %	192502202	92.7 %	166945533	92.1 %
4.	$p_{Th} > 0.1$ GeV/c	312168594	80.3 %	168438270	81.1 %	143730324	79.3 %
5.	$z > 0.1$	156616961	40.3 %	85533933	41.2 %	71083028	39.2 %

Table 4.4: Impact of the selection cuts on the number of hadrons.

5. $z > 0.1$, the fraction of the photon energy transferred to the hadron larger than 0.1. To avoid hadrons coming from the target fragmentation region, a hadron not resulting from the quark which interacted with the virtual photon but from the fragmentation of other quarks. The impact of this cut is visible in Fig. 4.7. It cuts 50% of the hadrons at low z . The analysis was performed in two other z ranges. The small z region, $0.1 < z < 0.2$, and the large one, $z > 0.2$, this being the standard sample used so far in the COMPASS analysis, which has half of the statistics, but it is considered to be cleanest. The results on these two ranges are presented on the end of the chapter.

The hadrons are divided by charge to give the opportunity to draw conclusions regarding the flavour dependence of the corresponding PDFs and FFs to be extracted.

The hadrons selection impact on the statistics is shown in Table 4.4. The impact of the cuts is shown sequentially. From all the particles accompanying the scattered muon which were hadron candidates, only 40% of them fulfil all the criteria.

The azimuthal angles ϕ_S and ϕ_h distributions, defined in Chapter 1, are in Fig. 4.8 and Fig. 4.9. The distribution of the azimuthal angle of the hadron has a symmetric shape, while the azimuthal angle of the target spin shows a huge decrease of hadrons for $-\pi/2$ rad, which is explained since there is a hole in the COMPASS acceptance along the beam trajectory in spectrometer.

The analysis is done in 4 Q^2 kinematic ranges:

- $1 < Q^2 < 4$ (GeV/c)²
- $4 < Q^2 < 6.25$ (GeV/c)²
- $6.25 < Q^2 < 16$ (GeV/c)²

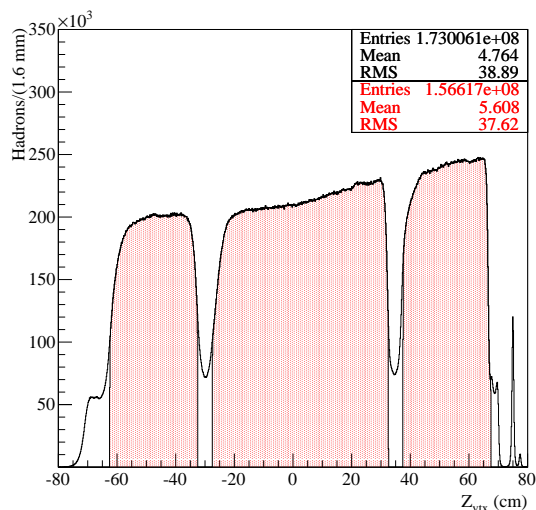


Figure 4.1: Distribution of the vertex position along the beam direction. The black distribution is obtained after all the selection cuts apart from the cut requiring that the vertex is inside the target material (using the function `InTarget()`). The red distribution is obtained after this cut.

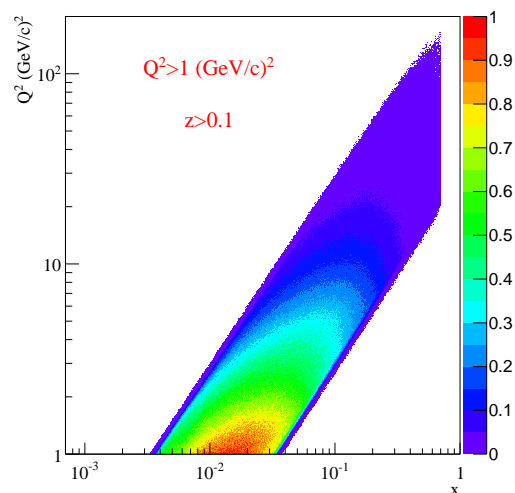


Figure 4.2: Q^2 versus x distribution.

Range (GeV/c^2)	# hadrons		# positive hadrons		# negative hadrons	
$1 < Q^2 < 4$	116627804	74.5 %	63044747	73.7 %	53583057	75.4 %
$4 < Q^2 < 6.25$	18065931	11.5 %	10035280	11.7 %	8030651	11.3 %
$6.25 < Q^2 < 16$	17738788	11.3 %	10041468	11.7 %	7697320	10.8 %
$16 < Q^2 < 81$	4161395	2.7 %	2398857	2.8 %	1762538	2.5 %
All Q^2	156593918	100 %	85520352	100 %	71073566	100 %

Table 4.5: Distribution of the hadrons by the 4 Q^2 kinematic ranges.

- $16 < Q^2 < 81$ (GeV/c^2)

The division of the number of hadrons per each Q^2 bin is shown in Table 4.5. The number of hadrons in the “All Q^2 ” range is a bit less than the final number of hadrons shown in Table 4.4 because “All Q^2 ” means $1 < Q^2 < 81$ (GeV/c^2), rejecting some cases above 81. The division of statistics is 75% of hadrons in the lowest Q^2 range, 11% in each intermediate range, and 3% in the highest range.

Fig. 4.10 shows the W distribution for each Q^2 range. The Q^2 range has not a big impact in the W , however it is visible that for the highest Q^2 , the low W is more relevant. This was one of the motivations to select events with $W > \sqrt{10}$ GeV/c^2 instead of $W > 5$ GeV/c^2 as in previous analyses. Fig. 4.11 shows the y distribution for each Q^2 range. The mean value increases slightly with Q^2 as expected. Fig. 4.12 shows the x distribution for each Q^2 range. x increases with Q^2 as already seen in the phase space distribution in Fig. 4.2. Fig. 4.13 shows the p_{Th} distributions for each Q^2 range. Also the p_{Th} has a slight increase with Q^2 . Finally, Fig. 4.14 shows the distributions of z for each Q^2 range where no z dependence on Q^2 is seen.

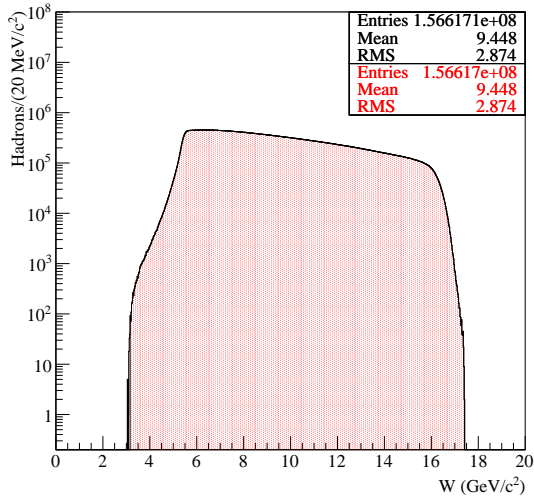


Figure 4.3: Mass distribution of the final hadronic state. The black distribution is obtained after all the selection cuts apart from the W cut are applied. The red distribution is obtained after the cut on $W < \sqrt{10} \text{ GeV}/c^2$.

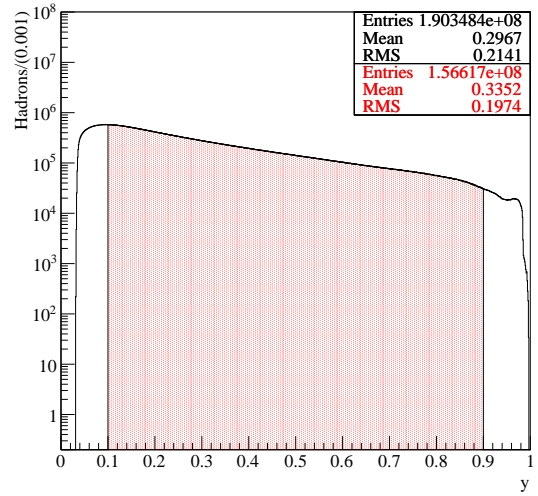


Figure 4.4: Distribution of the fractional energy of the virtual photon. The black distribution is obtained after all the selection cuts apart from the y cut are applied. The red distribution is obtained after the cut on $0.1 < y < 0.9$.

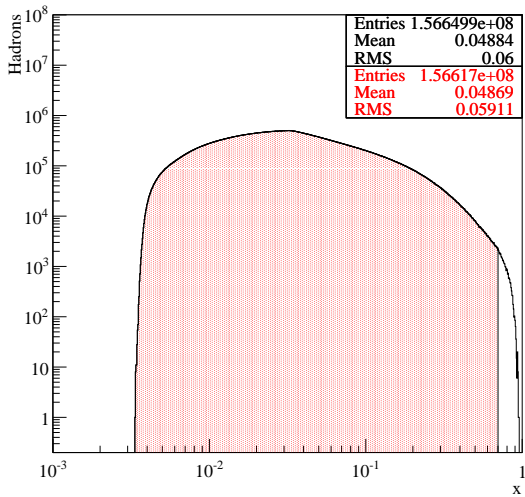


Figure 4.5: Distribution of the momentum fraction carried by the struck quark from proton. The black distribution is obtained after all the selection cuts apart from the x cut are applied. The red distribution is obtained after the cut on x .

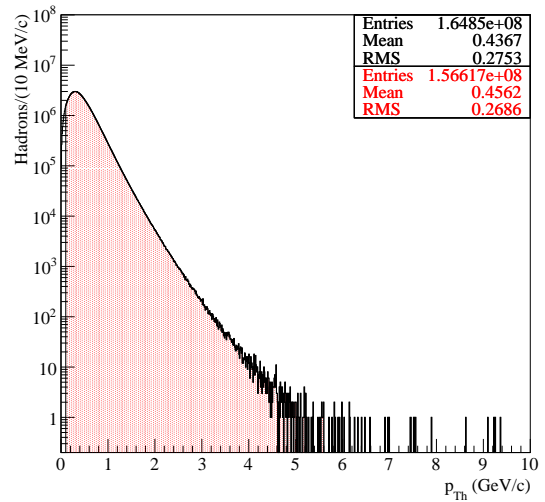


Figure 4.6: Distribution of the transverse momentum of the hadrons. The black distribution is obtained after all the selection cuts apart from the p_{Th} cut are applied. The red distribution is obtained after the cut on $p_{Th} < 0.1 \text{ GeV}/c$.

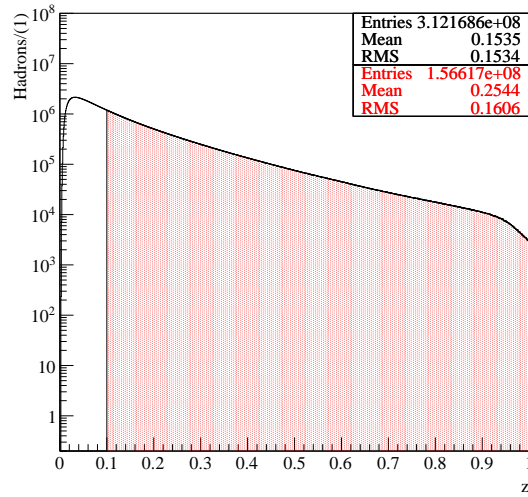


Figure 4.7: Distribution of the fraction of the photon energy transferred to the hadron. The black distribution is obtained after all the selection cuts apart from the z cut. The red distribution is obtained after the cut on $z < 0.1$.

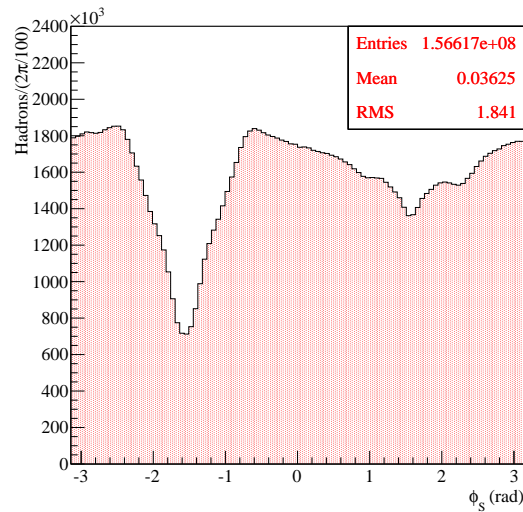
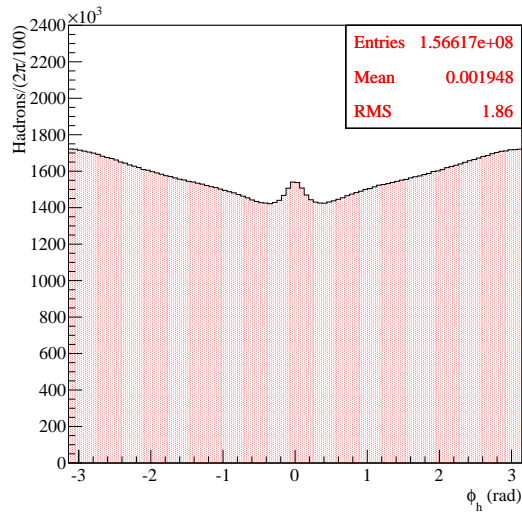
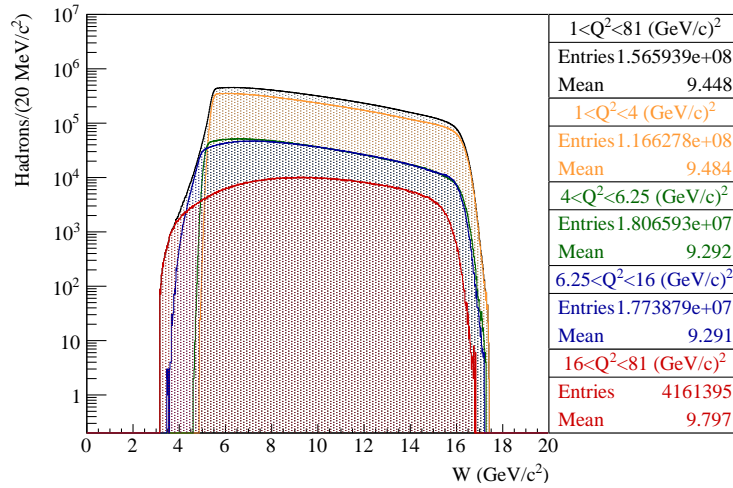
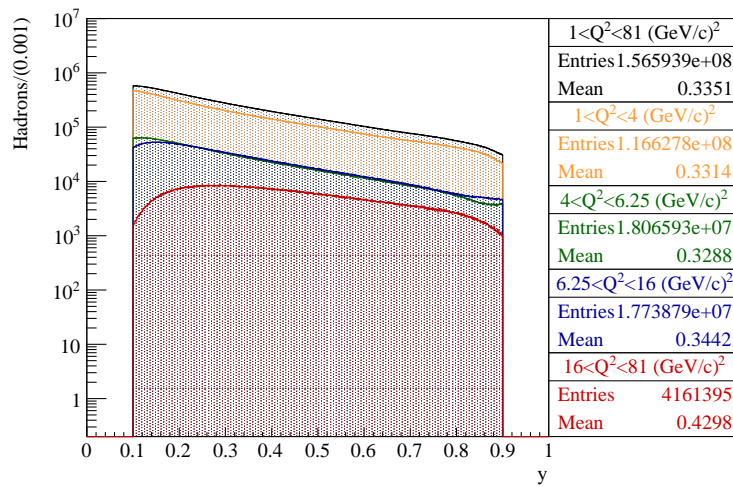
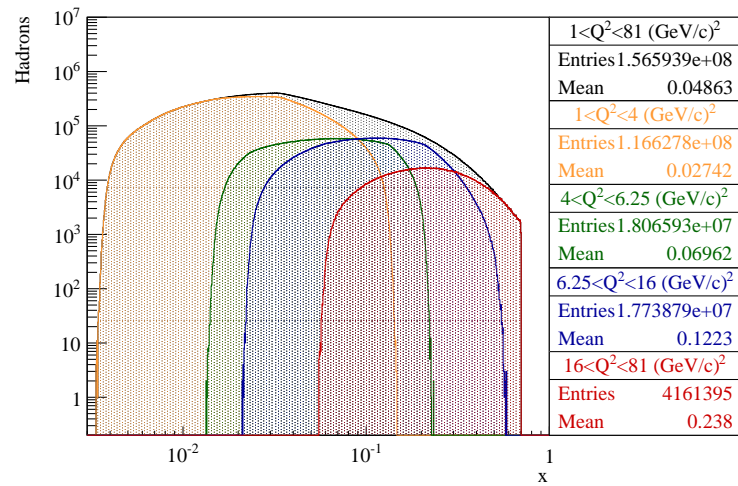
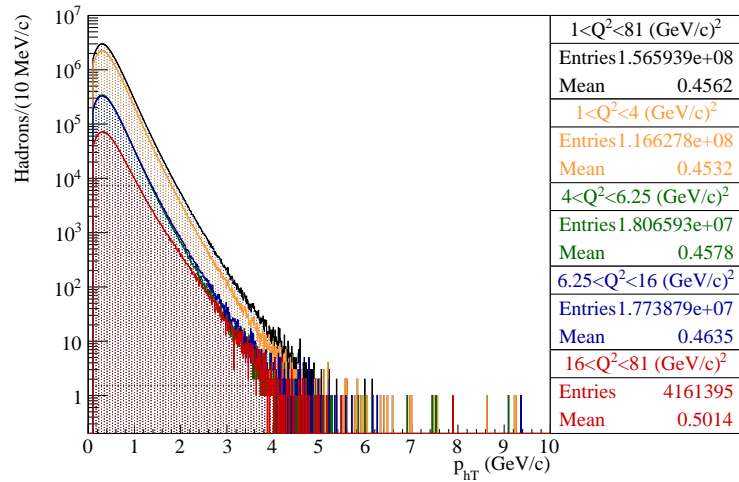
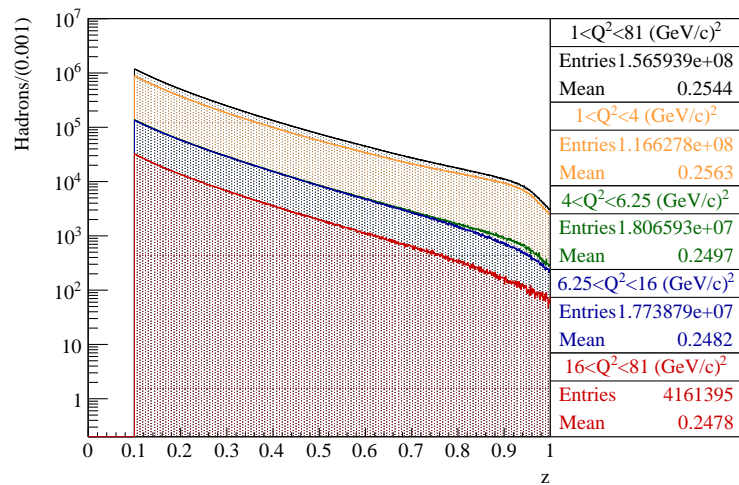


Figure 4.8: Distribution of ϕ_S azimuthal angle.


 Figure 4.9: Distribution of ϕ_h azimuthal angle.

 Figure 4.10: Mass distribution of the final hadronic state for each Q^2 bin.

 Figure 4.11: Distribution of the fractional energy of the virtual photon for each Q^2 bin.

Figure 4.12: Distribution of x for each Q^2 bin.Figure 4.13: Hadrons transverse momentum distribution for each Q^2 bin.Figure 4.14: Fraction of the photon energy transferred to the hadron for each Q^2 bin.

4.4 Binning

The asymmetries were evaluated for each one of the 4 Q^2 kinematic ranges as function of x , p_{Th} , z , y and W kinematic variables. This is a 2 dimensional analysis since for each Q^2 bin, a bin in another kinematic variable is chosen, integrating over the other variables. The x binning depends on the Q^2 range. The number of bins and their limits are shown in Table 4.6. For the other kinematic variables, p_{Th} , z , y and W the bins are the same in all the 4 Q^2 ranges. They are defined in Table 4.7. Thus the analysis is done in 86 bins.

For each kinematic bin, in each Q^2 range the mean values of the variables Q^2 , x , p_{Th} , z , y and W are showed in Fig. 4.15.

Q^2 range	# bins	x bin limits							
$1 < Q^2 < 4$	7	0.003	0.008	0.013	0.02	0.032	0.055	0.1	0.21
$4 < Q^2 < 6.25$	5	0.013	0.02	0.032	0.055	0.1	0.21	-	-
$6.25 < Q^2 < 16$	6	0.02	0.032	0.055	0.1	0.21	0.4	0.7	-
$16 < Q^2 < 81$	4	0.055	0.1	0.21	0.4	0.7	-	-	-

Table 4.6: x bins to be used in the analysis, for each Q^2 bin.

# bins	p_{Th} bin limits (GeV/c)				
4	0.1	0.3	0.5	0.75	10.0
# bins	z bin limits				
4	0.1	0.2	0.3	0.4	1.0
# bins	y bin limits				
4	0.1	0.2	0.3	0.5	0.9
# bins	W bin limits (GeV/c ²)				
4	5	7	8.5	10.5	18.0

Table 4.7: p_{Th} , z , y and W bins to be used in the analysis. The bins are the same for all the Q^2 ranges.

4.5 Asymmetry Extraction Methods

4.5.1 1D Binned Method - Double Ratio

The expected number of produced hadrons, $N_{cell}^{\uparrow\downarrow}(\Phi_j)$, depends on the target composition and dimension, $Trg_{cell}^{\uparrow\downarrow}$, on the beam flux, $Flux_{cell}^{\uparrow\downarrow}$, on the spectrometer geometrical acceptance and efficiency, $Acc_{cell}^{\uparrow\downarrow}(\Phi_j)$, and on the SIDIS cross section, $\sigma(\Phi_j)$.

$$\begin{aligned}
 N_{cell}^{\uparrow\downarrow}(\Phi_j) &= Trg_{cell}^{\uparrow\downarrow} \times Flux_{cell}^{\uparrow\downarrow} \times Acc_{cell}^{\uparrow\downarrow}(\Phi_j) \times \sigma(\Phi_j) \\
 &= Trg_{cell}^{\uparrow\downarrow} \times Flux_{cell}^{\uparrow\downarrow} \times Acc_{cell}^{\uparrow\downarrow}(\Phi_j) \times \left(\sigma_0 + \sigma^{\uparrow\downarrow}(\Phi_j) \right) \\
 &= Trg_{cell}^{\uparrow\downarrow} \times Flux_{cell}^{\uparrow\downarrow} \times Acc_{cell}^{\uparrow\downarrow}(\Phi_j) \times \sigma_0 (1 \pm W_j(\Phi_j))
 \end{aligned} \tag{4.1}$$

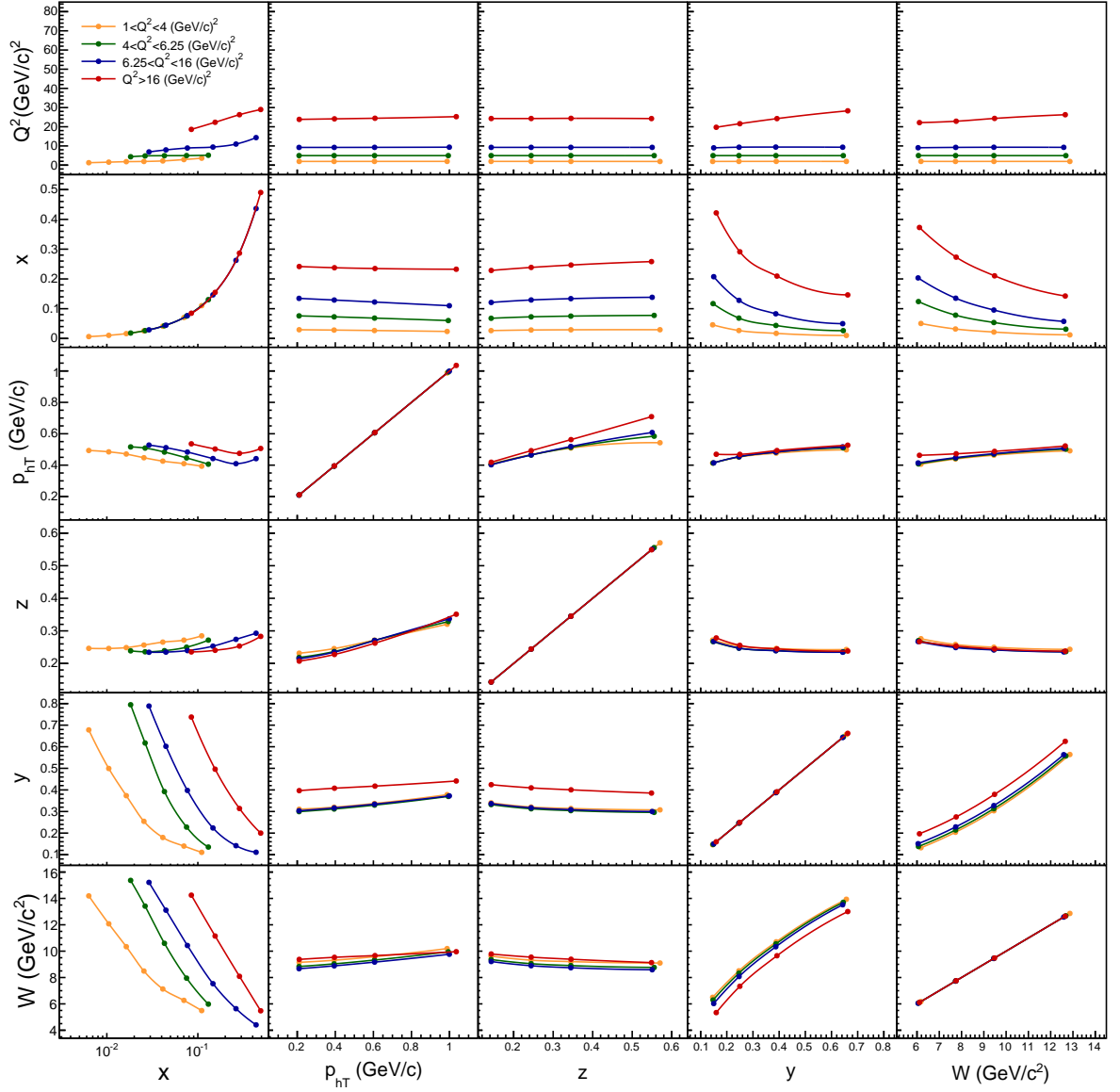


Figure 4.15: Mean values of the variables Q^2 , x , p_{Th} , z , y and W for each kinematic bin in x , p_{Th} , z , y and W . The colors distinguish different Q^2 ranges.

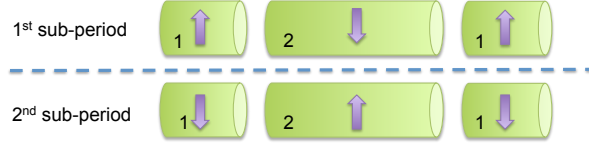


Figure 4.16: Cells numeration in double ratio method.

The cross section can be written in terms of the unpolarised and polarised parts, and the ratios between them are proportional to the asymmetries to extract, $W_j(\Phi_j)$, defined in section 1.5.1. In Eq. 4.1 the superscript represent the target cell polarisation; the subscript represent the cell.

For the evaluation of the asymmetries the double ratio method is used. For one period (two sub-periods with opposite sign target polarisations) the following ratio is built, considering the division of events as in Fig 4.16,

$$R(\Phi_j) = \frac{N_1^\uparrow(\Phi_j)N_2^\uparrow(\Phi_j)}{N_1^\downarrow(\Phi_j)N_2^\downarrow(\Phi_j)} \quad (4.2)$$

with the corresponding error:

$$\delta_{R(\Phi_j)} = R(\Phi_j) \sqrt{\frac{1}{N_1^\uparrow(\Phi_j)} + \frac{1}{N_2^\uparrow(\Phi_j)} + \frac{1}{N_1^\downarrow(\Phi_j)} + \frac{1}{N_2^\downarrow(\Phi_j)}} \quad (4.3)$$

Replacing eq. 4.1 in the ratio $R(\Phi_j)$ gives:

$$R(\Phi_j) = \frac{Trg_1^\uparrow Flux_1^\uparrow Acc_1^\uparrow(\Phi_j) \sigma_0 (1 + W_j(\Phi_j)) Trg_2^\uparrow Flux_2^\uparrow Acc_2^\uparrow(\Phi_j) \sigma_0 (1 + W_j(\Phi_j))}{Trg_1^\downarrow Flux_1^\downarrow Acc_1^\downarrow(\Phi_j) \sigma_0 (1 - W_j(\Phi_j)) Trg_2^\downarrow Flux_2^\downarrow Acc_2^\downarrow(\Phi_j) \sigma_0 (1 - W_j(\Phi_j))} \quad (4.4)$$

For each target cell, its composition is the same in the 2 sub-periods, thus $Trg_{cell}^{\uparrow\downarrow}$ factors can be removed from the formula. The flux is constant in both cells, as required in the selection criteria and can also be removed. The ratio becomes:

$$R(\Phi_j) = \frac{Acc_1^\uparrow(\Phi_j) Acc_2^\uparrow(\Phi_j) (1 + W_j(\Phi_j))^2}{Acc_1^\downarrow(\Phi_j) Acc_2^\downarrow(\Phi_j) (1 - W_j(\Phi_j))^2} \quad (4.5)$$

As a simplification the binomial expansion at first order is used:

$$R(\Phi_j) = \frac{Acc_1^\uparrow(\Phi_j) Acc_2^\uparrow(\Phi_j)}{Acc_1^\downarrow(\Phi_j) Acc_2^\downarrow(\Phi_j)} (1 + 4W_j(\Phi_j)) \quad (4.6)$$

The extraction of the asymmetry is unbiased if:

$$\frac{Acc_1^\uparrow(\Phi_j) Acc_2^\uparrow(\Phi_j)}{Acc_1^\downarrow(\Phi_j) Acc_2^\downarrow(\Phi_j)} = constant \quad (4.7)$$

This is true if the ratio of the acceptances for cells with opposite polarisations stays the same before and after the polarisation reversal. In this case the ratio has no more a dependence on the acceptance. This assumption is named “reasonable assumption” and will be considered and tested in 4.6.1. The double ratio is then simplified to:

$$R(\Phi_j) = C(1 + 4W_j(\Phi_j)) \quad (4.8)$$

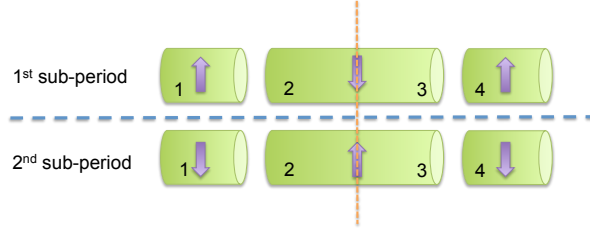


Figure 4.17: Cells numeration in quadruple ratio method.

As discussed in section 1.5.1, in transversely polarised target SIDIS there are 5 relevant modulations to consider, 5 double ratios are evaluated using the previously selected data. They are built in 16 equidistant bins of Φ_j from $-\pi$ to π and then fitted with:

$$C_0(1 + 4C_1 \sin(\Phi_j)), (j = 2, 3) \quad (4.9)$$

or,

$$C_0(1 + 4[C_1 \sin(\Phi_j) + C_2 \cos(\Phi_j)]), (j = 1, 4, 5) \quad (4.10)$$

where C_1 and C_2 are the raw asymmetries as in equations from 1.42 to 1.46.

4.5.2 1D Binned Method - Quadruple Ratio

The quadruple ratio is similar to the double ratio but the cells are considered in a different way. The central cell is split in two cells, in each sub-period are considered 4 cells. The cells numeration is shown in Fig. 4.17. The rate in each cell is defined as in equation 4.1, and the ratio $R(\Phi_j)$ comes now:

$$R(\Phi_j) = \frac{N_1^\uparrow(\Phi_j)N_2^\uparrow(\Phi_j)N_3^\uparrow(\Phi_j)N_4^\uparrow(\Phi_j)}{N_1^\downarrow(\Phi_j)N_2^\downarrow(\Phi_j)N_3^\downarrow(\Phi_j)N_4^\downarrow(\Phi_j)} \quad (4.11)$$

with the corresponding error:

$$\delta_{R(\Phi_j)} = R(\Phi_j) \sqrt{\frac{1}{N_1^\uparrow(\Phi_j)} + \frac{1}{N_2^\downarrow(\Phi_j)} + \frac{1}{N_3^\downarrow(\Phi_j)} + \frac{1}{N_4^\uparrow(\Phi_j)} + \frac{1}{N_1^\downarrow(\Phi_j)} + \frac{1}{N_2^\uparrow(\Phi_j)} + \frac{1}{N_3^\uparrow(\Phi_j)} + \frac{1}{N_4^\downarrow(\Phi_j)}} \quad (4.12)$$

As for the double ratio $R(\Phi_j)$, it can be written as

$$R(\Phi_j) = \frac{Acc_1^\uparrow(\Phi_j)Acc_2^\uparrow(\Phi_j)Acc_3^\uparrow(\Phi_j)Acc_4^\uparrow(\Phi_j)}{Acc_1^\downarrow(\Phi_j)Acc_2^\downarrow(\Phi_j)Acc_3^\downarrow(\Phi_j)Acc_4^\downarrow(\Phi_j)} (1 + 8W_j(\Phi_j)) \quad (4.13)$$

If the acceptance in one cell has the same modulation in the two sub-periods, and this applies for all cells, the double ratio $R(\Phi_j)$ can be simplified as:

$$R(\Phi_j) = C(1 + 8W_j(\Phi_j)) \quad (4.14)$$

The 5 combinations of angles Φ_j are now fitted with:

$$C_0(1 + 8C_1 \sin(\Phi_j)), (j = 2, 3) \quad (4.15)$$

or,

$$C_0(1 + 8[C_1 \sin(\Phi_j) + C_2 \cos(\Phi_j)]), (j = 1, 4, 5) \quad (4.16)$$

The quadruple ratio is advantageous with respect to the double ratio, since it has a better acceptance cancellation.

4.5.3 Unbinned Maximum Likelihood Method

The extraction of the asymmetries from binned methods suffers from statistical fluctuations and this is the reason to consider the unbinned maximum likelihood method. In this case each hadron i is associated with a probability density function $p_{cell,i}^{\uparrow\downarrow}(\phi_h, \phi_S)$, which is given by the product of the number of nucleons per unit of area, $n_{cell}^{\uparrow\downarrow}$, the acceptance, $Acc_{cell}^{\uparrow\downarrow}(\phi_h, \phi_S)$, and the cross-section, written in terms of the asymmetries already shown in section 1.5.1:

$$\begin{aligned}
 p_{cell,i}^{\uparrow\downarrow}(\phi_h, \phi_S) = & n_{cell}^{\uparrow\downarrow} Acc_{cell}^{\uparrow\downarrow}(\phi_h, \phi_S) \{1 + U_1 \cos(\phi_h) + U_2 \cos(2\phi_h) \pm \\
 & \left[A_{UT,raw}^{\sin(\phi_h + \phi_S - \pi)} \sin(\phi_h + \phi_S - \pi) + A_{UT,raw}^{\sin(\phi_h - \phi_S)} \sin(\phi_h - \phi_S) + \right. \\
 & A_{UT,raw}^{\sin(3\phi_h - \phi_S)} \sin(3\phi_h - \phi_S) + A_{LT,raw}^{\cos(\phi_h - \phi_S)} \cos(\phi_h - \phi_S) + \\
 & A_{UT,raw}^{\sin(\phi_S)} \sin(\phi_S) + A_{UT,raw}^{\sin(2\phi_h - \phi_S)} \sin(2\phi_h - \phi_S) + A_{LT,raw}^{\cos(\phi_S)} \cos(\phi_S) + \\
 & \left. A_{LT,raw}^{\cos(2\phi_h - \phi_S)} \cos(2\phi_h - \phi_S) \right] \}
 \end{aligned} \tag{4.17}$$

where U_1 and U_2 are the amplitudes of the unpolarised asymmetries and the A 's are the amplitudes of the 8 transverse spin dependent asymmetries.

Considering the extended unbinned maximum likelihood method [113], the procedure gives access to all the asymmetries simultaneously through the minimization of the function $-\ln(\mathcal{L})$, the likelihood being given by the product:

$$\begin{aligned}
 \mathcal{L} = & \left(e^{-\mathcal{I}_1^{\uparrow}} \prod_{i=0}^{N_1^{\uparrow}} p_{1,i}^{\uparrow}(\phi_h, \phi_S) \right)^{\frac{1}{N_1^{\uparrow}}} \left(e^{-\mathcal{I}_2^{\downarrow}} \prod_{i=0}^{N_2^{\downarrow}} p_{2,i}^{\downarrow}(\phi_h, \phi_S) \right)^{\frac{1}{N_2^{\downarrow}}} \\
 & \left(e^{-\mathcal{I}_1^{\downarrow}} \prod_{i=0}^{N_1^{\downarrow}} p_{1,i}^{\downarrow}(\phi_h, \phi_S) \right)^{\frac{1}{N_1^{\downarrow}}} \left(e^{-\mathcal{I}_2^{\uparrow}} \prod_{i=0}^{N_2^{\uparrow}} p_{2,i}^{\uparrow}(\phi_h, \phi_S) \right)^{\frac{1}{N_2^{\uparrow}}} .
 \end{aligned} \tag{4.18}$$

The normalization by $\frac{1}{N_{cell}^{\uparrow\downarrow}}$ is done to avoid a possible bias due to different statistics in cell i in the 2 sub-periods cells, where $N_{cell}^{\uparrow\downarrow}$ is the total number of hadrons in the corresponding cell. $\mathcal{I}_{cell}^{\uparrow\downarrow}$ represents the total number of expected hadrons in the transverse geometric section:

$$\mathcal{I}_{cell}^{\uparrow\downarrow} = \int_{-\pi}^{\pi} \int_{-\pi}^{\pi} p_{cell,i}^{\uparrow\downarrow}(\phi_h, \phi_S) d\phi_h d\phi_S = 4\pi^2 n_{cell}^{\uparrow\downarrow} \tag{4.19}$$

where $n_{cell}^{\uparrow\downarrow}$ is the number of nucleons per unit of area.

Thus the function to be minimised is

$$\begin{aligned}
-\ln(\mathcal{L}) &= -\frac{1}{N_1^\uparrow} \left(-\mathcal{I}_1^\uparrow + \sum_{i=0}^{N_1^\uparrow} \ln \left(p_{1,i}^\uparrow(\phi_h, \phi_S) \right) \right) - \frac{1}{N_2^\downarrow} \left(-\mathcal{I}_2^\downarrow + \sum_{i=0}^{N_2^\downarrow} \ln \left(p_{2,i}^\downarrow(\phi_h, \phi_S) \right) \right) \\
&\quad - \frac{1}{N_1^\downarrow} \left(-\mathcal{I}_1^\downarrow + \sum_{i=0}^{N_1^\downarrow} \ln \left(p_{1,i}^\downarrow(\phi_h, \phi_S) \right) \right) - \frac{1}{N_2^\uparrow} \left(-\mathcal{I}_2^\uparrow + \sum_{i=0}^{N_2^\uparrow} \ln \left(p_{2,i}^\uparrow(\phi_h, \phi_S) \right) \right) = \\
&= \frac{4\pi^2 n_1^\uparrow}{N_1^\uparrow} - \frac{\sum_{i=0}^{N_1^\uparrow} \ln \left(p_{1,i}^\uparrow(\phi_h, \phi_S) \right)}{N_1^\uparrow} + \frac{4\pi^2 n_2^\downarrow}{N_2^\downarrow} - \frac{\sum_{i=0}^{N_2^\downarrow} \ln \left(p_{2,i}^\downarrow(\phi_h, \phi_S) \right)}{N_2^\downarrow} \\
&\quad + \frac{4\pi^2 n_1^\downarrow}{N_1^\downarrow} - \frac{\sum_{i=0}^{N_1^\downarrow} \ln \left(p_{1,i}^\downarrow(\phi_h, \phi_S) \right)}{N_1^\downarrow} + \frac{4\pi^2 n_2^\uparrow}{N_2^\uparrow} - \frac{\sum_{i=0}^{N_2^\uparrow} \ln \left(p_{2,i}^\uparrow(\phi_h, \phi_S) \right)}{N_2^\uparrow}
\end{aligned} \tag{4.20}$$

which has 14 free parameters, n_1^\uparrow , n_2^\downarrow , n_1^\downarrow , n_2^\uparrow , the 2 unpolarised asymmetries and the 8 spin dependent ones. The minimisation was performed using the MINUIT ROOT package.

The method was tested taking into account the parametrisation of the acceptance as a two dimensional Fourier decomposition. As a result, it was shown that the extracted asymmetries did not depend on the description of the acceptance within the statistical uncertainty[114].

The 8 spin dependent extracted asymmetries are the raw ones and they need to be corrected by the depolarisation factor, D , the dilution factor, f , and the polarisation of the target, S_T , and/or the beam polarisations, P_i , as shown in equations 1.30 and 1.31. Other approach is to perform the minimization taking these corrections already into account, the so called unbinned maximum likelihood weighting method. In this method the probability density function comes

$$\begin{aligned}
p_{cell,i}^{\uparrow\downarrow}(\phi_h, \phi_S) &= n_{cell}^{\uparrow\downarrow} Acc_{cell}^{\uparrow\downarrow}(\phi_h, \phi_S) \left\{ 1 + U_1 \cos(\phi_h) + U_2 \cos(2\phi_h) \pm \right. \\
&\quad \left[D^{\sin(\phi_h + \phi_S - \pi)}(y) f |S_T| A_{UT}^{\sin(\phi_h + \phi_S - \pi)} \sin(\phi_h + \phi_S - \pi) + \right. \\
&\quad D^{\sin(\phi_h - \phi_S)}(y) f A_{UT}^{\sin(\phi_h - \phi_S)} \sin(\phi_h - \phi_S) + \\
&\quad D^{\sin(3\phi_h - \phi_S)}(y) f A_{UT}^{\sin(3\phi_h - \phi_S)} \sin(3\phi_h - \phi_S) + \\
&\quad D^{\sin(\phi_h - \phi_S)}(y) f P L A_{LT}^{\cos(\phi_h - \phi_S)} \cos(\phi_h - \phi_S) + \\
&\quad D^{\sin(\phi_S)}(y) f A_{UT}^{\sin(\phi_S)} \sin(\phi_S) + \\
&\quad D^{\sin(2\phi_h - \phi_S)}(y) f A_{UT}^{\sin(2\phi_h - \phi_S)} \sin(2\phi_h - \phi_S) + \\
&\quad D^{\cos(\phi_S)}(y) f P L A_{LT}^{\cos(\phi_S)} \cos(\phi_S) + \\
&\quad \left. \left. D^{\cos(2\phi_h - \phi_S)}(y) f P L A_{LT}^{\cos(2\phi_h - \phi_S)} \cos(2\phi_h - \phi_S) \right] \right\} .
\end{aligned} \tag{4.21}$$

The dilution factors D 's are defined in equations from 1.32 to 1.36.

4.6 Systematic Effects

In this section the systematic studies are presented, in the end a value for the systematic uncertainty to be assigned to each asymmetry is obtained.

4.6.1 Azimuthal Stability

The azimuthal stability is checked using 4 different tests. These tests are the R-test, the T-test, the RA-test and the last is a combination of the T-test and the RA-test.

R-test

The R-test searches for eventual changes in the azimuthal spectrometer acceptance between the two sub-periods. Taking into account the event rate in each cell, as described in Eq. 4.1, the following double ratio is built:

$$R(\Phi_j) = \frac{N_1^\uparrow(\Phi_j)N_2^\downarrow(\Phi_j)}{N_1^\downarrow(\Phi_j)N_2^\uparrow(\Phi_j)} \simeq \frac{Acc_1^\uparrow(\Phi_j)Acc_2^\downarrow(\Phi_j)}{Acc_1^\downarrow(\Phi_j)Acc_2^\uparrow(\Phi_j)} \quad (4.22)$$

See Fig. 4.16 for the definitions of the superscripts and the subscripts. This ratio cancels the physics modulation and only the acceptance modulation is considered. The ratio of acceptances is expected to be flat if there is no change in the azimuthal acceptance from sub-period to sub-period. As for the extraction of the asymmetries, the ratio is evaluated in 16 equidistant bins of Φ_j , from $-\pi$ to π , and then fitted with a constant. The quality of the fits is checked taking into account the χ^2 values from each case. Their distribution taking into account all the kinematic bins should follow a theoretical χ^2 distribution with the corresponding number of degrees of freedom.

The result of this test is shown in Fig. 4.18, the χ^2 distributions are divided per modulation and per hadron charge; the first two lines are for positive hadrons and the last two for negative ones. For a better comparison the theoretical χ^2 distribution for 15 ndf (16 data points and 1 free parameter of the zero-degree polynomial fit) is also plotted, normalised to the total number of entries. The number of entries correspond to 86 kinematic bins \times 12 weeks = 1032 entries.

There are 2 modulations, $\sin(\phi_S)$ and $\cos(\phi_S)$, where the azimuthal stability is not as good as the others. This is attributed to the fact that these modulations are only on the ϕ_S angle, which is highly affected by a statistical decrease at $-\pi/2$ rad, as shown in Fig. 4.8. For all the others the mean value of the distributions deviates from 15 by around 3σ , while for these ϕ_S modulations it deviates by $\sim 24\sigma$ for positive hadrons and by $\sim 16\sigma$ for negative hadrons. These distributions were done also depending on the period and the conclusions were always the same.

T-test

The T-test is similar to the R-test but in this case what is checked is the possible existence of an acceptance modulation compatible with the physics modulation under study. For this test, considering the event rate described in 4.1, the quadruple ratio is built:

$$T(\Phi_j) = \frac{N_1^\uparrow(\Phi_j)N_2^\downarrow(\Phi_j)N_3^\downarrow(\Phi_j)N_4^\uparrow(\Phi_j)}{N_1^\downarrow(\Phi_j)N_2^\uparrow(\Phi_j)N_3^\uparrow(\Phi_j)N_4^\downarrow(\Phi_j)} \simeq \frac{Acc_1^\uparrow(\Phi_j)Acc_2^\downarrow(\Phi_j)Acc_3^\downarrow(\Phi_j)Acc_4^\uparrow(\Phi_j)}{Acc_1^\downarrow(\Phi_j)Acc_2^\uparrow(\Phi_j)Acc_3^\uparrow(\Phi_j)Acc_4^\downarrow(\Phi_j)} \quad (4.23)$$

The acceptance terms can be written as:

$$Acc_{1,2}^{\uparrow\downarrow}(\Phi_j) = c_{1,2}^{\uparrow\downarrow}(1 + a_{1,2}^{\uparrow\downarrow}Y(\Phi_j)) \quad (4.24)$$

being $Y(\Phi_j)$ the modulation under study. Thus:

$$\frac{Acc_1^\uparrow(\Phi_j)}{Acc_1^\downarrow(\Phi_j)} = \frac{c_1^\uparrow(1 + a_1^\uparrow Y(\Phi_j))}{c_1^\downarrow(1 + a_1^\downarrow Y(\Phi_j))} = C_0(1 + a_1^\uparrow Y(\Phi_j))(1 - a_1^\downarrow Y(\Phi_j)) = C_0(1 + (a_1^\uparrow - a_1^\downarrow)Y(\Phi_j) - a_1^\uparrow a_1^\downarrow Y(\Phi_j)^2) \quad (4.25)$$

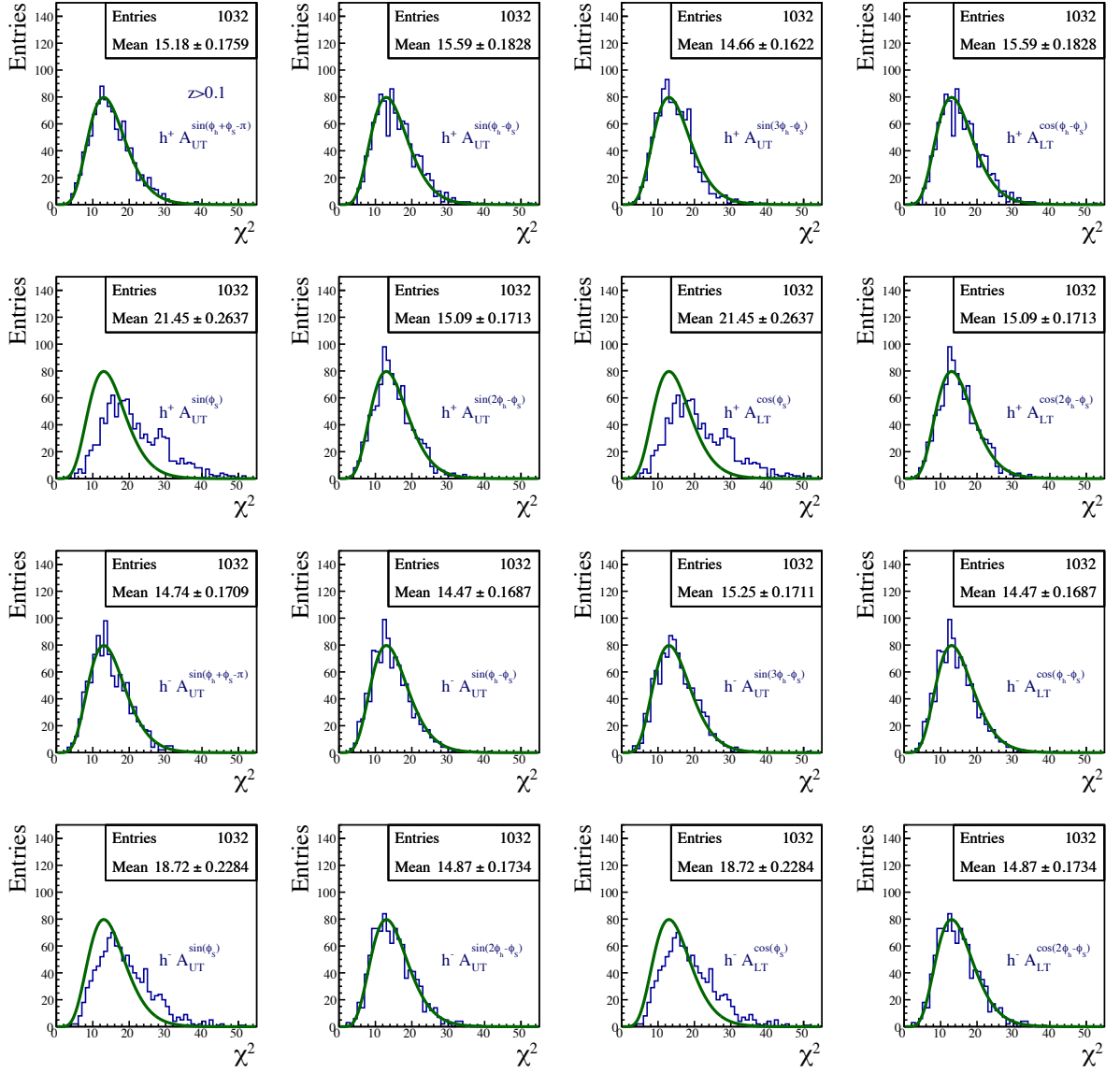


Figure 4.18: R-test results for the z range $z > 0.1$. The results are divided by hadron charge and by modulation. The first two lines are for positive hadrons and the last two for negative hadrons. The 8 modulations are specified in the plots.

Considering only first order terms:

$$T(\Phi_j) = C_0(1 + [(a_1^\uparrow - a_1^\downarrow) + (a_2^\downarrow - a_2^\uparrow) + (a_3^\downarrow - a_3^\uparrow) + (a_4^\uparrow - a_4^\downarrow)]Y(\Phi_j)) \quad (4.26)$$

The T ratio is evaluated in 16 equidistant bins of Φ_j , from $-\pi$ to π , and then fitted with the function

$$f(\Phi_j) = C_0(1 + C_1Y(\Phi_j)) \quad (4.27)$$

If the acceptance does not change between the 2 sub-periods C_1 is expected to be zero. In order to confirm its compatibility with zero the following χ^2 is built:

$$\chi^2 = \left(\frac{C_1}{\sigma_{C_1}}\right)^2 \quad (4.28)$$

The result from this test is shown in Fig. 4.19, the χ^2 distributions are divided per modulation and per charge, the first two lines are for positive hadrons and the last two for negative ones. For a better comparison the theoretical χ^2 distribution for 1 degree of freedom is also plotted, normalised to the total number of entries. The number of entries corresponds to 86 kinematic bins \times 12 weeks = 1032 entries.

The mean value should be 1, the only two modulations that deviate more than 3σ from 1 are again the modulations in ϕ_S .

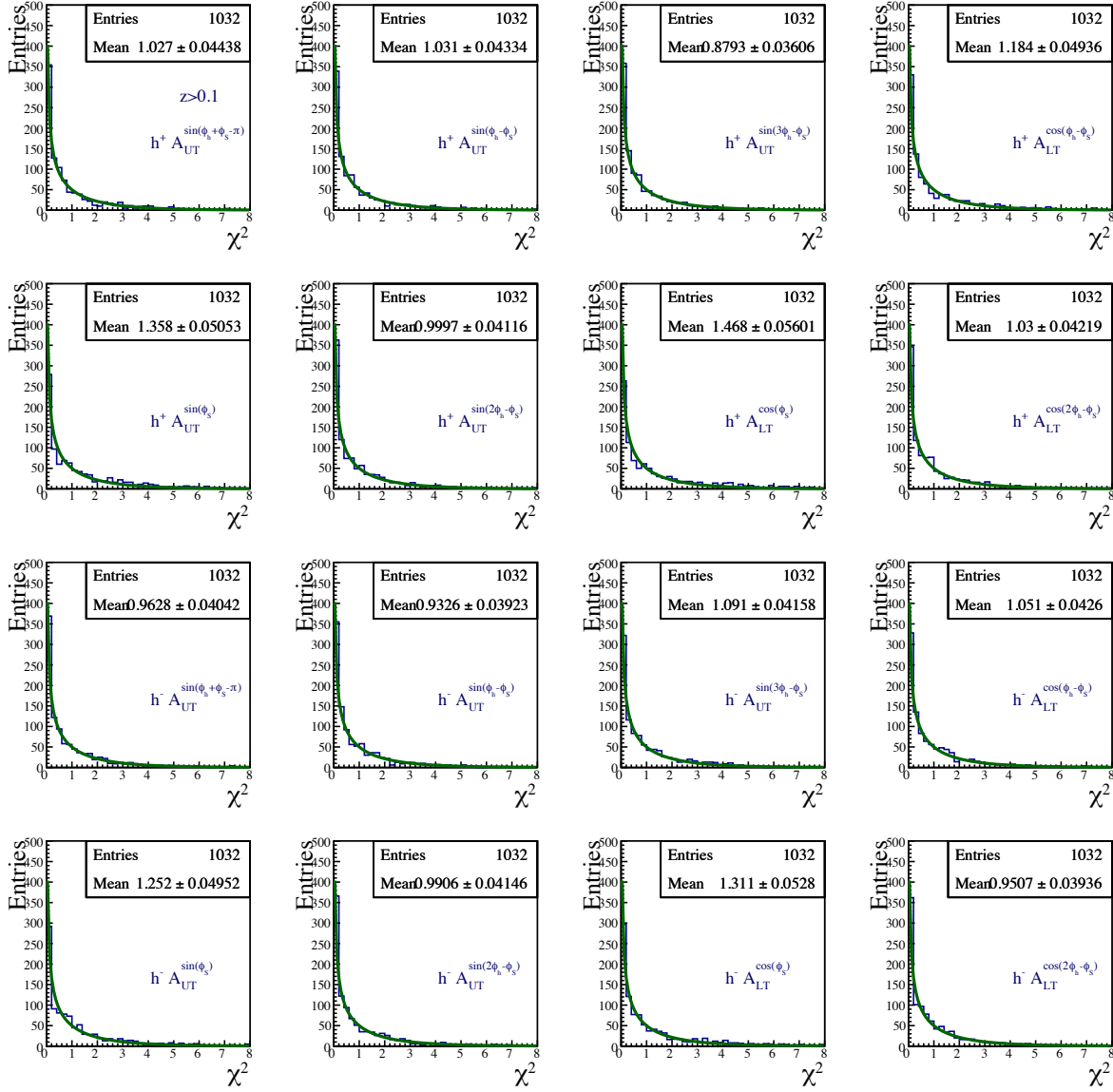


Figure 4.19: T-test results for the z range $z > 0.1$. The results are divided by hadron charge and by modulation. The first two lines are for positive hadrons and the last two for negative hadrons. The 8 modulations are specified in the plots.

RA-test

For the so-called reasonable assumption test (RA-test) the ratio between the azimuthal distributions for each cell is built separately. Contrary to the two previous tests, in this case

the physics asymmetries do not cancel. The ratios for each cell can be written as

$$\frac{N_1^\uparrow(\Phi_j)}{N_1^\downarrow(\Phi_j)} = C_1(1 + ((a_1^\uparrow - a_1^\downarrow) + 2A_1)Y(\Phi_j)) \xrightarrow{\text{from fit}} \epsilon_1 \pm \sigma_1 \quad (4.29)$$

$$\frac{N_2^\downarrow(\Phi_j)}{N_2^\uparrow(\Phi_j)} = C_2(1 + ((a_2^\downarrow - a_2^\uparrow) + 2A_2)Y(\Phi_j)) \xrightarrow{\text{from fit}} \epsilon_2 \pm \sigma_2 \quad (4.30)$$

$$\frac{N_3^\downarrow(\Phi_j)}{N_3^\uparrow(\Phi_j)} = C_3(1 + ((a_3^\downarrow - a_3^\uparrow) + 2A_3)Y(\Phi_j)) \xrightarrow{\text{from fit}} \epsilon_3 \pm \sigma_3 \quad (4.31)$$

$$\frac{N_4^\uparrow(\Phi_j)}{N_4^\downarrow(\Phi_j)} = C_4(1 + ((a_4^\uparrow - a_4^\downarrow) + 2A_4)Y(\Phi_j)) \xrightarrow{\text{from fit}} \epsilon_4 \pm \sigma_4 \quad . \quad (4.32)$$

The ratios are evaluated in 16 equidistant bins of Φ_j , from $-\pi$ to π , and then fitted with the function

$$f(\Phi_j) = C_i(1 + \epsilon_i Y(\Phi_j)) \quad (4.33)$$

In order to evaluate the result from this test the following χ^2 is built:

$$\chi_{RA}^2 = \sum_{i=1}^4 \left(\frac{\epsilon_i - \alpha_i}{\sigma_i} \right)^2 \quad (4.34)$$

where the amplitudes ϵ_i and the uncertainties σ_i result from the fit. The α_i are the expected values of the measured amplitudes:

$$\alpha_1 = 2\epsilon + t \quad (4.35)$$

$$\alpha_2 = -2\epsilon + t \quad (4.36)$$

$$\alpha_3 = -2\epsilon + t \quad (4.37)$$

$$\alpha_4 = 2\epsilon + t \quad (4.38)$$

where ϵ is the expected value for the physics modulation and t is the variation due to the change in the azimuthal acceptance between the 2 sub-periods; here it is considered that the physics asymmetries are the same for each cell, $A_1 = A_2 = A_3 = A_4 = \epsilon$, and that the acceptance variation from sub-period to sub-period is the same in each cell $(a_1^\uparrow - a_1^\downarrow) = (a_2^\downarrow - a_2^\uparrow) = (a_3^\downarrow - a_3^\uparrow) = (a_4^\uparrow - a_4^\downarrow) = t$:

$$\epsilon = \frac{\epsilon_1 - \epsilon_2 - \epsilon_3 + \epsilon_4}{8} \quad (4.39)$$

$$t = \frac{\epsilon_1 + \epsilon_2 + \epsilon_3 + \epsilon_4}{4} \quad (4.40)$$

The result from the RA-test is shown in Fig. 4.20, the χ^2 distributions are divided per modulation and per charge; the first two lines are for positive hadrons and the last two for negative ones. For a better comparison the theoretical χ^2 distribution for 2 degrees of freedom is also plotted, normalised by the total number of entries. The azimuthal stability is considered to be good for all the modulations. Nevertheless, as before the mean value deviates more than 3σ from 2 for the modulations in ϕ_S for the both hadron charges.

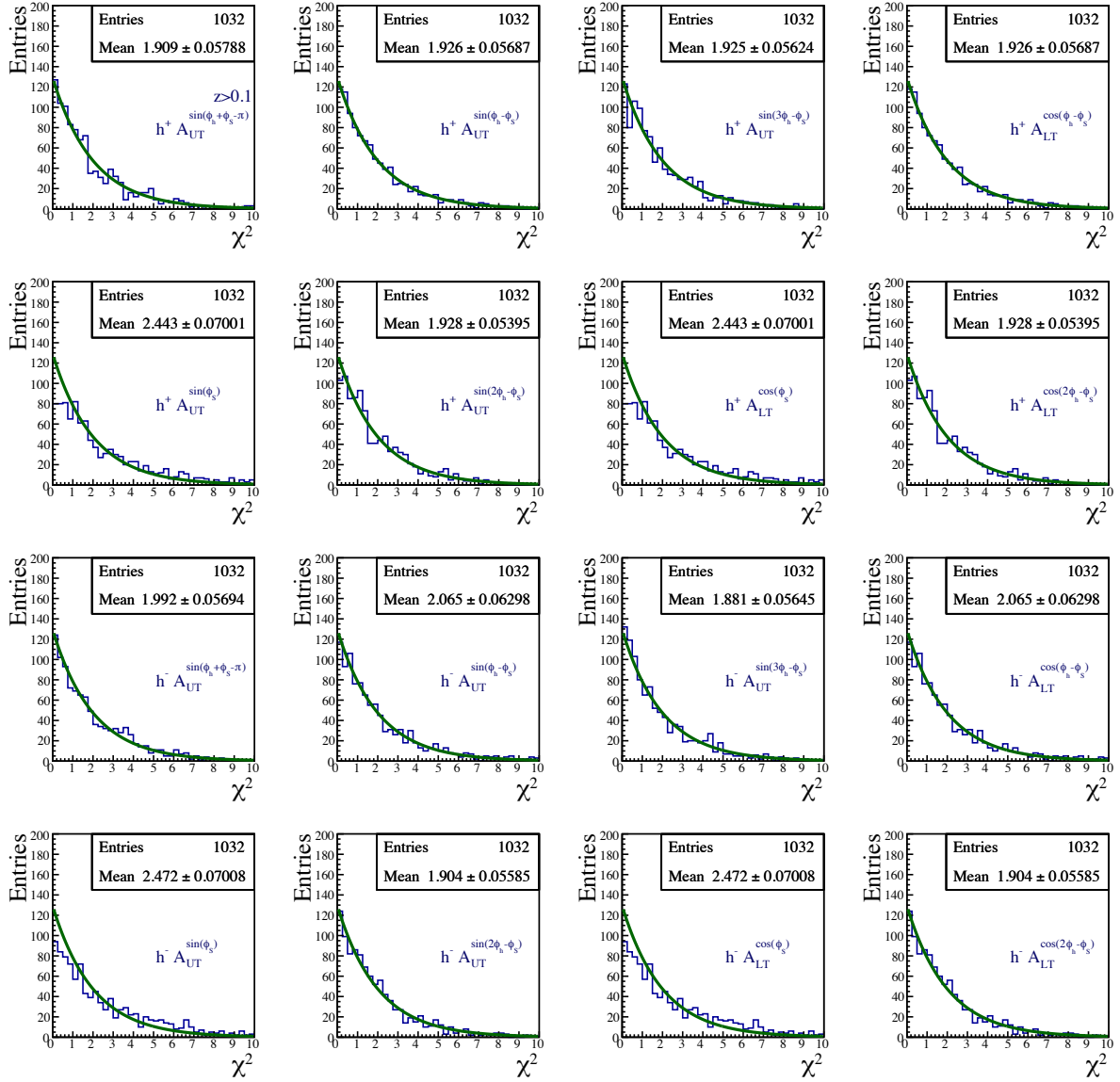


Figure 4.20: RA-test results for the z range $z > 0.1$. The results are divided by hadron charge and by modulation. The first two lines are for positive hadrons and the last two for negative hadrons. The 8 modulations are specified in the plots.

RA-test and T-test

In addition to the previous three tests and their χ^2 , a χ^2 is built which combines the results from the T-test and the RA-test:

$$\chi_{RA+T}^2 = \chi_{RA}^2 + \chi_T^2 \quad . \quad (4.41)$$

In the case of the combination between the RA and T tests the results are shown in Fig. 4.21. For a better comparison the theoretical χ^2 distribution for 3 degrees of freedom is also plotted, normalised by the total number of entries.

In what concerns the RA-T test the mean value of the 2 modulations in ϕ_S , both for positive and negative hadrons, deviates more than 3σ from 3.

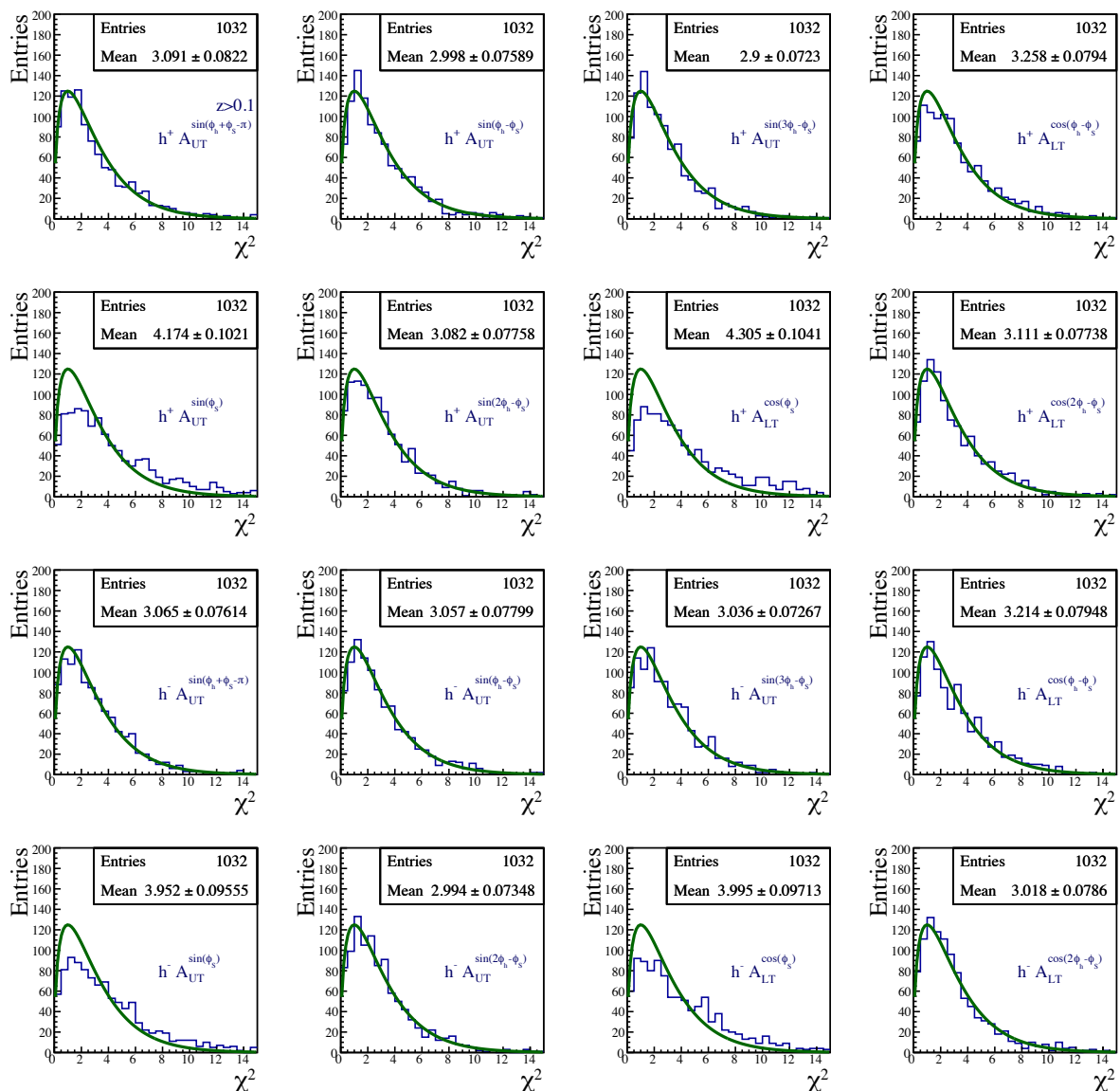


Figure 4.21: RA-T-test results for the z range $z > 0.1$. The results are divided by hadron charge and by modulation. The first two lines are for positive hadrons and the last two for negative hadrons. The 8 modulations are specified in the plots.

All the four tests show deviations from the expected distributions for the modulations in ϕ_S , both for positive and for negative hadrons. This can be related with the non-uniform shape of the ϕ_S distribution, see Fig. 4.8. Anyway, this issue is reflected also in the study of the false-asymmetries. There the effect is more evident and is going to be taken into account at the level of systematic uncertainties.

4.6.2 Compatibility of Results between Different Data Taking Periods

The check of compatibility between the data taking periods is important to ensure that the spectrometer was stable during the whole data taking. This check is done comparing the measured value of the asymmetry in one single period with the mean value considering all

periods. The pulls are

$$Pull_{period} = \frac{A_{period} - \langle A \rangle}{\sqrt{\sigma_{A_{period}}^2 - \sigma_{\langle A \rangle}^2}} \quad (4.42)$$

where A_{period} is the asymmetry in one single period, $\langle A \rangle$ is the weighted mean of the A_{period} values from all the periods and $\sigma_{A_{period}}^2$ and $\sigma_{\langle A \rangle}^2$ are the corresponding variances. The pulls are expected to follow the standard normal distribution, the differences among results from different periods being only statistical.

The pulls distributions are shown in Fig. 4.22, divided per modulation and per charge, the first two lines are for positive hadrons and the last two for negative ones. The distributions are fitted with a gaussian and all of them are centred at zero with a sigma around 1, as expected. This study reveals that all periods are well compatible with each other.

4.6.3 Compatibility between Different Extraction Methods

The asymmetries were extracted with different methods, as explained in previous sections. A possible source of systematics is the extraction method itself. In this sense the comparison of the results coming from the different methods is done. Two pulls are built:

$$Pull_{asym} = \frac{A_{QR} - A_{UL}}{\frac{\sigma_{QR} + \sigma_{UL}}{2}} \quad (4.43)$$

and

$$Pull_{error} = \frac{\sigma_{QR} - \sigma_{UL}}{\frac{\sigma_{QR} + \sigma_{UL}}{2}} \quad (4.44)$$

The pulls between the asymmetries extracted using the quadruple ratio binned method and the unbinned maximum likelihood method are shown in Fig. 4.23. The pulls between the asymmetry errors are shown in Fig. 4.24. The distributions are divided per asymmetry and per charge, the first two lines are for positive hadrons and the last two for negative ones. All the distributions are centred at zero and with a RMS of 0.2-0.3 times the statistical error of the asymmetry, in the case of the pulls between asymmetry values, and less than 0.1 times the statistical error of the asymmetry in the case of the errors.

4.6.4 False Asymmetries

The systematic errors can be assessed by the evaluation of the so-called false asymmetries. The false asymmetries are measured combining the data in such a way that spin effects cancel out. Two combinations are built, the two outer cells are combined

$$FA_{ext} = \frac{N_1^\uparrow N_4^\downarrow}{N_1^\downarrow N_4^\uparrow} = 1 + A_{ext} W_j(\Phi) \quad (4.45)$$

and in a similar way for the two halves of the central cell

$$FA_{int} = \frac{N_2^\uparrow N_3^\downarrow}{N_2^\downarrow N_3^\uparrow} = 1 + A_{int} W_j(\Phi) \quad (4.46)$$

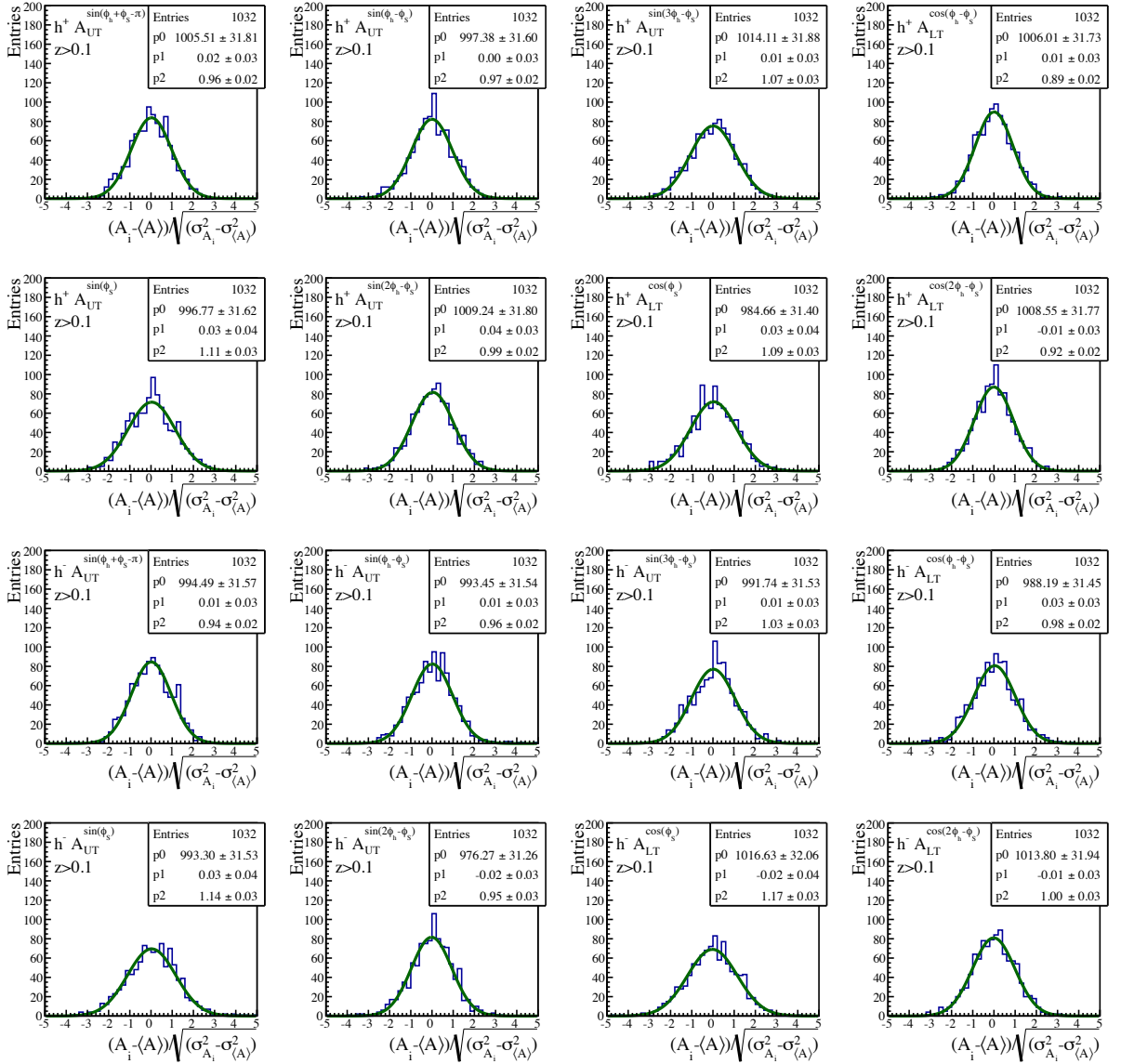


Figure 4.22: Compatibility between the results from different data taking periods for the z range $z > 0.1$. The results are divided by hadron charge and by modulation. The first two lines are for positive hadrons and the last two for negative hadrons. The 8 modulations are specified in the plots.

The estimator of the systematic error is the mean value of the two estimators:

$$FA_+ = \frac{|A_{ext} + A_{int}|}{\sqrt{\sigma_{A_{ext}}^2 + \sigma_{A_{int}}^2}} \quad (4.47)$$

and

$$FA_- = \frac{|A_{ext} - A_{int}|}{\sqrt{\sigma_{A_{ext}}^2 + \sigma_{A_{int}}^2}} \quad (4.48)$$

The two asymmetries, A_{ext} and A_{int} , are expected to be zero, assuming that they are normal distributions $N(0, 4\sqrt{2}e_A)$ centred at zero and with $\sigma = 4\sqrt{2}e_A$, e_A being the error of the physics asymmetry. The difference $d = A_{ext} - A_{int}$ is then $N(0, 8e_A)$. The distribution of $|d|$ is a half

4. EXTRACTION OF TRANSVERSE SPIN ASYMETRIES FROM SIDIS

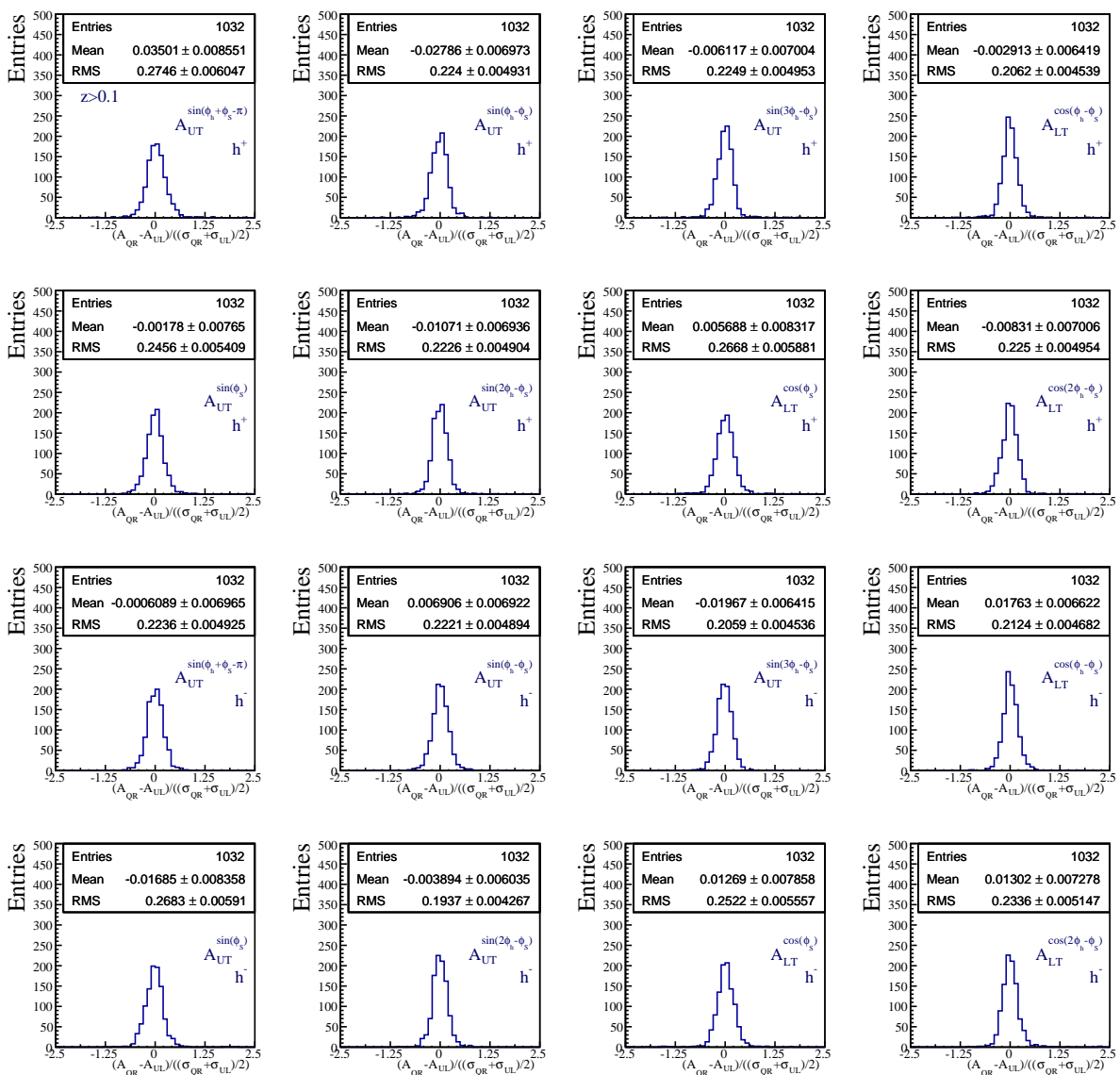


Figure 4.23: Compatibility between the two different extraction methods, the 1D quadruple ratio and the Unbinned Maximum Likelihood, for the z range $z > 0.1$. The pulls between the asymmetries are divided by hadron charge and by asymmetry. The two first lines are for positive hadrons and the two last for negative hadrons. The 8 possible asymmetries are specified in the plots.

Gaussian like shape that goes from 0 to infinity, its median is $0.68 \times 8e_A$. Thus if d is centred at zero its absolute value is not, and this is taken into account to evaluate the distance from zero.

This will be calculated for all the kinematic bins, 86 in total and for each period, i :

$$\frac{\sigma_{sys}}{\sigma_{stat}} = \alpha_i = \frac{\sqrt{FA_+^2 - 0.68^2} + \sqrt{FA_-^2 - 0.68^2}}{2} . \quad (4.49)$$

If $FA_{\pm} \leq 0.68$, the corresponding square root is set to zero. The α_i are checked to be stable from period to period and, as a final result, the mean value of the systematic error due to false

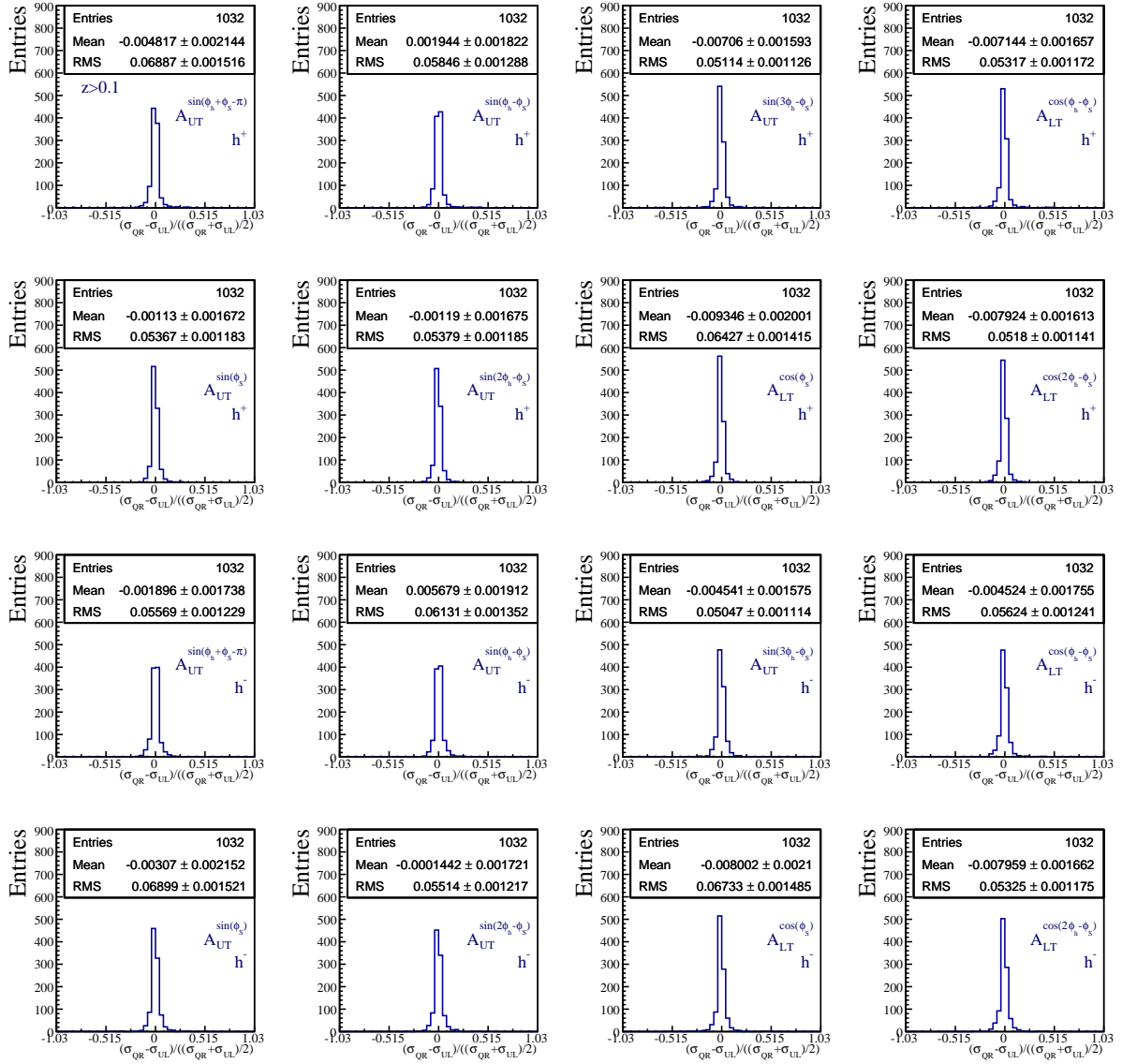


Figure 4.24: Compatibility between the two different extraction methods, the 1D quadruple ratio and the Unbinned Maximum Likelihood, for the z range $z > 0.1$. The pulls between the asymmetries errors are divided by hadron charge and by asymmetry. The first two lines are for positive hadrons and the last two for negative hadrons. The 8 asymmetries are specified in the plots.

asymmetries is calculated for all periods:

$$\frac{\sigma_{sys}}{\sigma_{stat}} = \alpha = \frac{\sum_i \alpha_i}{12} . \quad (4.50)$$

In the study of false asymmetries, several tests were performed in order to estimate a safe limit below which systematic effects cannot be separated from statistical uncertainties [115, 116]. This limit was chosen at $0.5\sigma_{stat}$. Thus if systematic uncertainties are around $0.5\sigma_{stat}$, there is no evidence of systematic effects and this value can be safely taken into account as an upper limit for the systematic error. If the mean values are larger than $0.5\sigma_{stat}$ then they should be considered.

The systematic uncertainty related to false asymmetries in units of the statistical error is shown in Fig. 4.25, the mean values of alpha are between 0.5 and 0.8 and they will be considered in the evaluation of the systematic error.

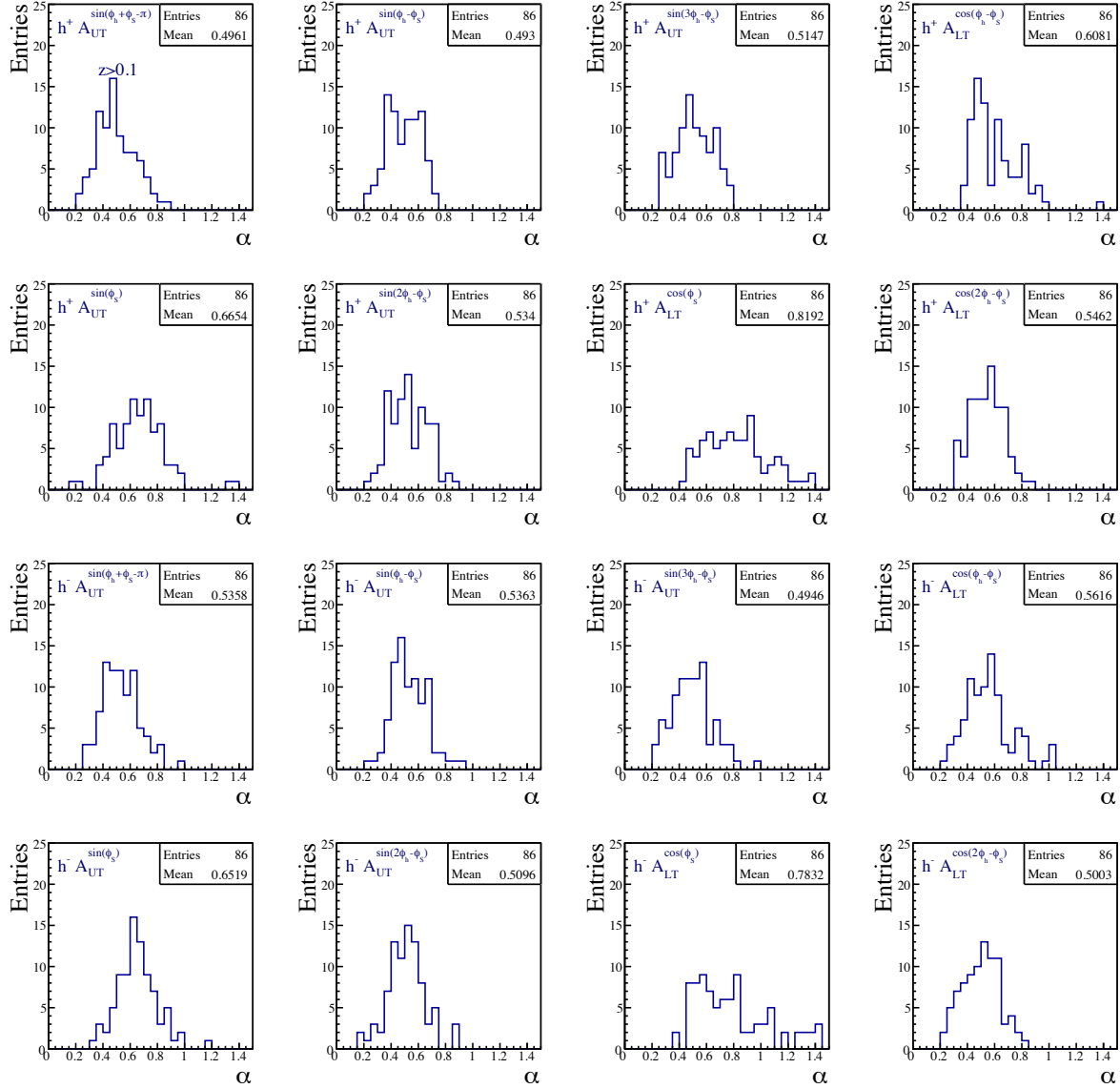


Figure 4.25: Evaluation of the systematic error in terms of the statistical one taking into account the false asymmetries, for the z range $z > 0.1$. The results are divided by hadron charge and by asymmetry. The first two lines are for positive hadrons and the last two for negative hadrons. The 8 asymmetries are specified in the plots.

4.6.5 Summary of Systematic Studies

All the previously described tests that have been performed to evaluate the systematic effects did not show significant deviations from the expected values. The false asymmetries are considered to be the main indicator of possible systematic deviations, and they are considered as a safe limit for the systematic errors.

The final results are presented in Table 4.8 divided by asymmetry and by charge.

For the final error of the asymmetry an additional scale uncertainty of 3% for the target polarisation and of 1% for the dilution factor should be taken into account. Concerning the “LT”-asymmetries, an error of 5% for the beam polarisation should be also considered. Thus the asymmetry error is

$$\sigma_A = \sqrt{\sigma_{stat}^2 + (0.03A)^2 + (0.01A)^2 + (0.05A)^2 + \sigma_{sys}^2} . \quad (4.51)$$

$\sigma_{sys}/\sigma_{stat}$	h^+	h^-
$A_{UT}^{\sin(\phi_h+\phi_S-\pi)}$	0.50	0.54
$A_{UT}^{\sin(\phi_h-\phi_S)}$	0.50	0.54
$A_{UT}^{\sin(3\phi_h-\phi_S)}$	0.51	0.50
$A_{LT}^{\cos(\phi_h-\phi_S)}$	0.61	0.56
$A_{UT}^{\sin(\phi_S)}$	0.67	0.65
$A_{UT}^{\sin(2\phi_h-\phi_S)}$	0.53	0.51
$A_{LT}^{\cos(\phi_S)}$	0.82	0.78
$A_{LT}^{\cos(2\phi_h-\phi_S)}$	0.55	0.50

Table 4.8: Systematic uncertainty in units of statistical one for each asymmetry.

4.7 Transverse Spin Asymmetries

The results for the asymmetries were obtained using the Unbinned Maximum Likelihood method, explained in section 4.5.3. The asymmetries were extracted in the kinematic bins defined in section 4.4. In Figures 4.26 to 4.33 the results for the 8 transverse spin asymmetries are presented.

In Fig. 4.26 the Sivers asymmetry is shown. This asymmetry gives access to the Sivers TMD PDF, $f_{1T}^{\perp q}$, convoluted with a fragmentation function, D_{1q}^h . The Sivers PDF is expected to have opposite sign when accessed through SIDIS process or through Drell-Yan process. Thus it is of particular interest to compare the results from SIDIS and Drell-Yan analyses from COMPASS. COMPASS has already published results on the Sivers asymmetry integrated in Q^2 [51] and [47]. The Sivers asymmetry is positive for positive hadrons and compatible with zero for negative hadrons in almost all kinematic bins. It increases with x for positive hadrons. For negative hadrons it shows a positive sign at high x and high Q^2 . The Q^2 region larger than 16 (GeV/c)² overlaps with the DY high mass range ($4 < M_{\mu\mu} < 9$ GeV/c², i.e. in DY $16 < Q^2 < 81$ GeV/c²) and it is of particular interest. The statistics is lower in this range; nevertheless for positive hadrons the asymmetry increases with x and it is still positive.

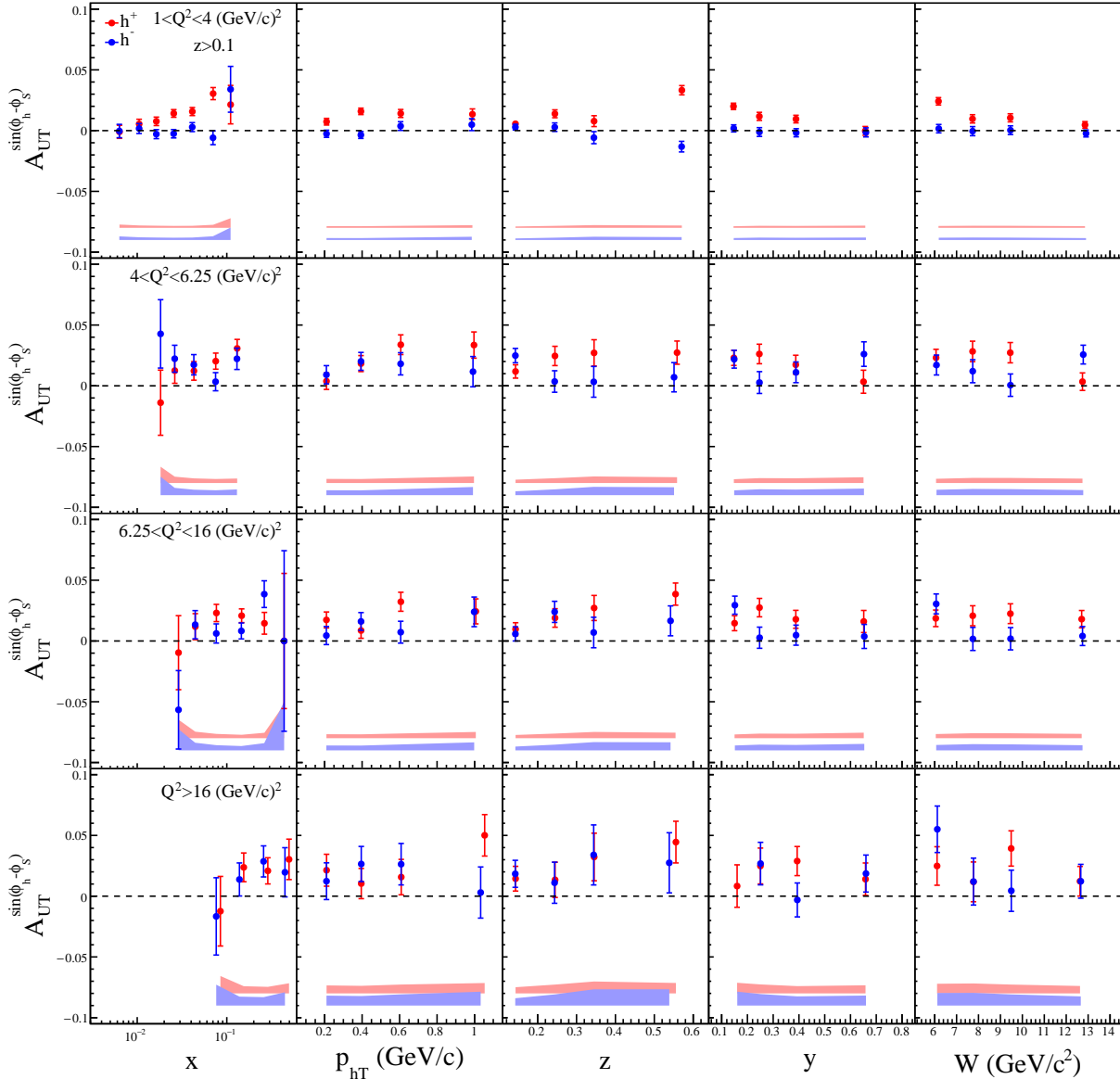


Figure 4.26: $A_{UT}^{\sin(\phi_h - \phi_S)}$ asymmetry, the so called Sivers asymmetry, in bins of x , p_{Th} , z , y , W and Q^2 . The results are divided by hadron charge; in red are results for positive hadrons and in blue for negative ones. The systematic error is presented as a band in the bottom of each plot.

Fig. 4.27 shows the Collins asymmetry, the convolution between transversity PDF, h_1^q , and the Collins fragmentation function, $H_{1q}^{\perp h}$. It has been extensively studied and several COMPASS results have been already published [46] and [47]. This asymmetry is positive for negative hadrons and negative for positive hadrons in almost all kinematic bins.

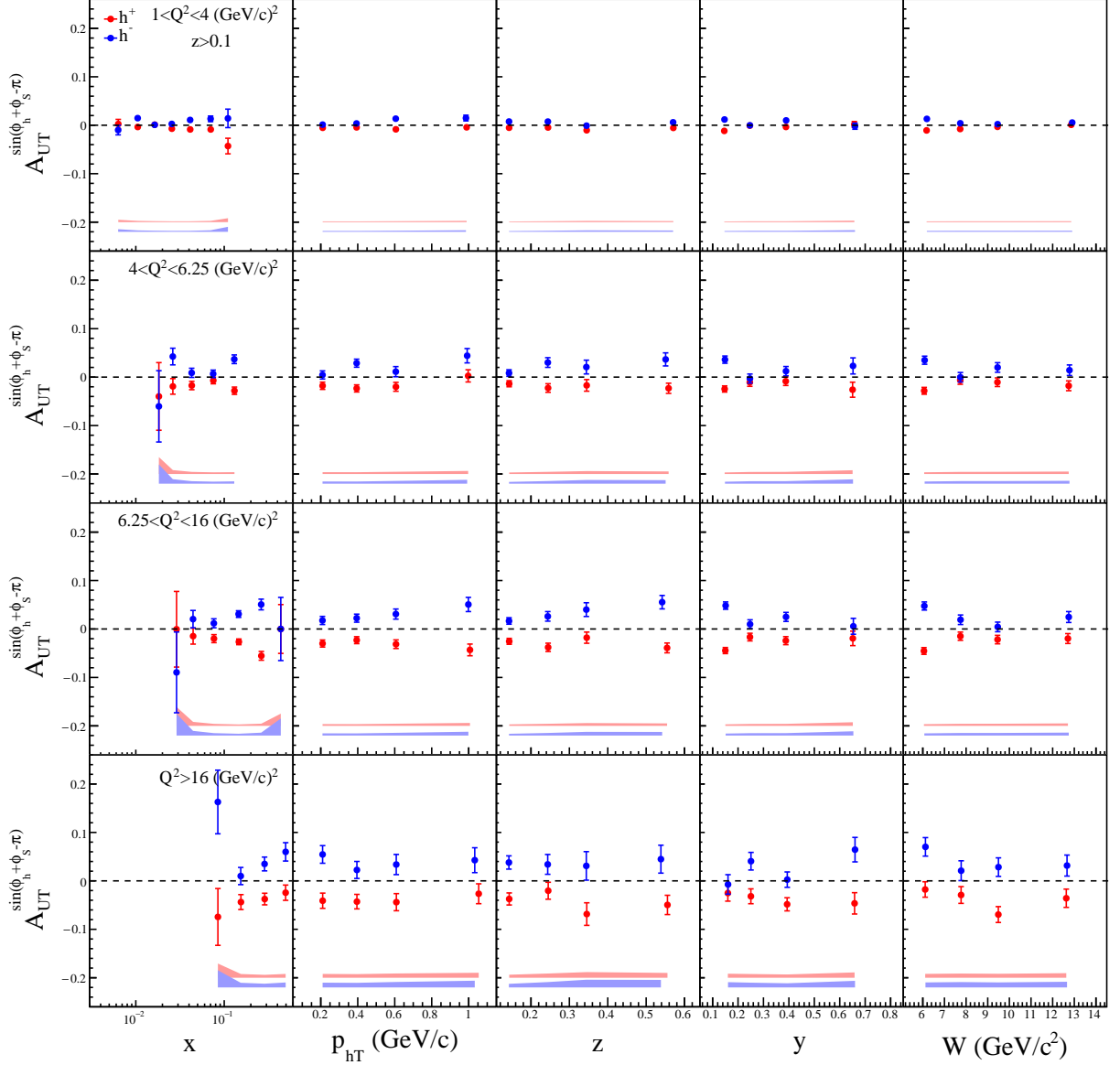


Figure 4.27: $A_{UT}^{\sin(\phi_h + \phi_S - \pi)}$ asymmetry, the so called Collins asymmetry, in bins of x , p_{Th} , z , y , W and Q^2 . The results are divided by hadron charge; in red are results for positive hadrons and in blue for negative ones. The systematic error is presented as a band in the bottom of each plot.

4. EXTRACTION OF TRANSVERSE SPIN ASYMMETRIES FROM SIDIS

In Fig. 4.28 the $A_{UT}^{\sin(3\phi_h - \phi_S)}$ asymmetry is shown. It gives access to the Pretzelosity TMD PDF, $h_{1T}^{\perp q}$, convoluted with the fragmentation function, $H_{1q}^{\perp h}$. This asymmetry is compatible with zero in the majority of the kinematic bins. There is a prediction for this asymmetry pointing for a very small effect, even compatible with zero [119].

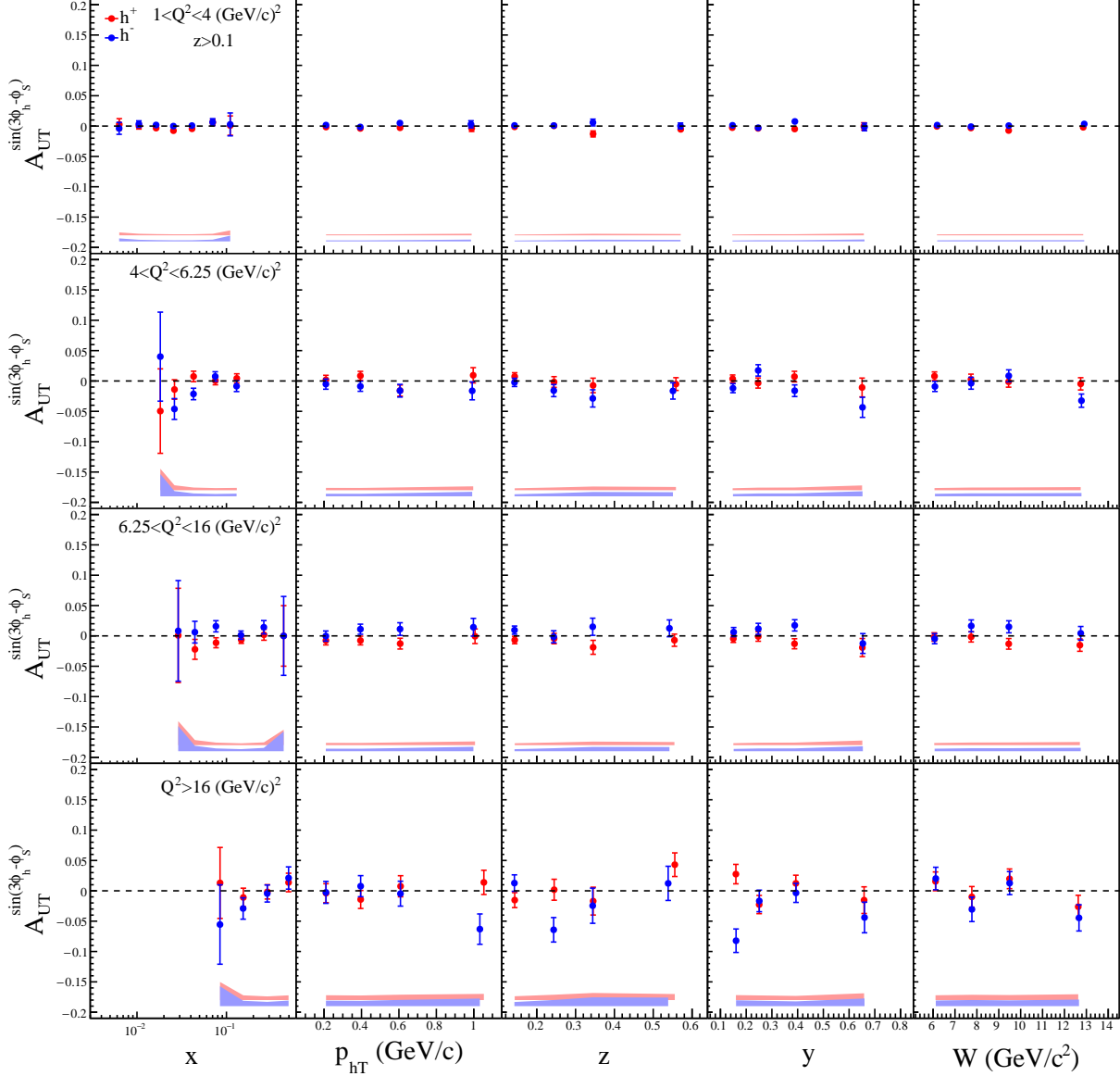


Figure 4.28: $A_{UT}^{\sin(3\phi_h - \phi_S)}$ asymmetry in bins of x , $p_{T,h}$, z , y , W and Q^2 . The results are divided by hadron charge; in red are results for positive hadrons and in blue for negative ones. The systematic error is presented as a band in the bottom of each plot.

In Fig. 4.29 the asymmetry $A_{LT}^{\cos(\phi_h - \phi_S)}$ is shown. It is a convolution of the worm-gear-T PDF, g_{1T}^q , with the fragmentation function, D_{1q}^h . This asymmetry is compatible with zero within the statistical accuracy of the data in the majority of bins. However this effect is not zero at large x and Q^2 . There are theoretical predictions for this asymmetry pointing for a non zero effect [117–119].

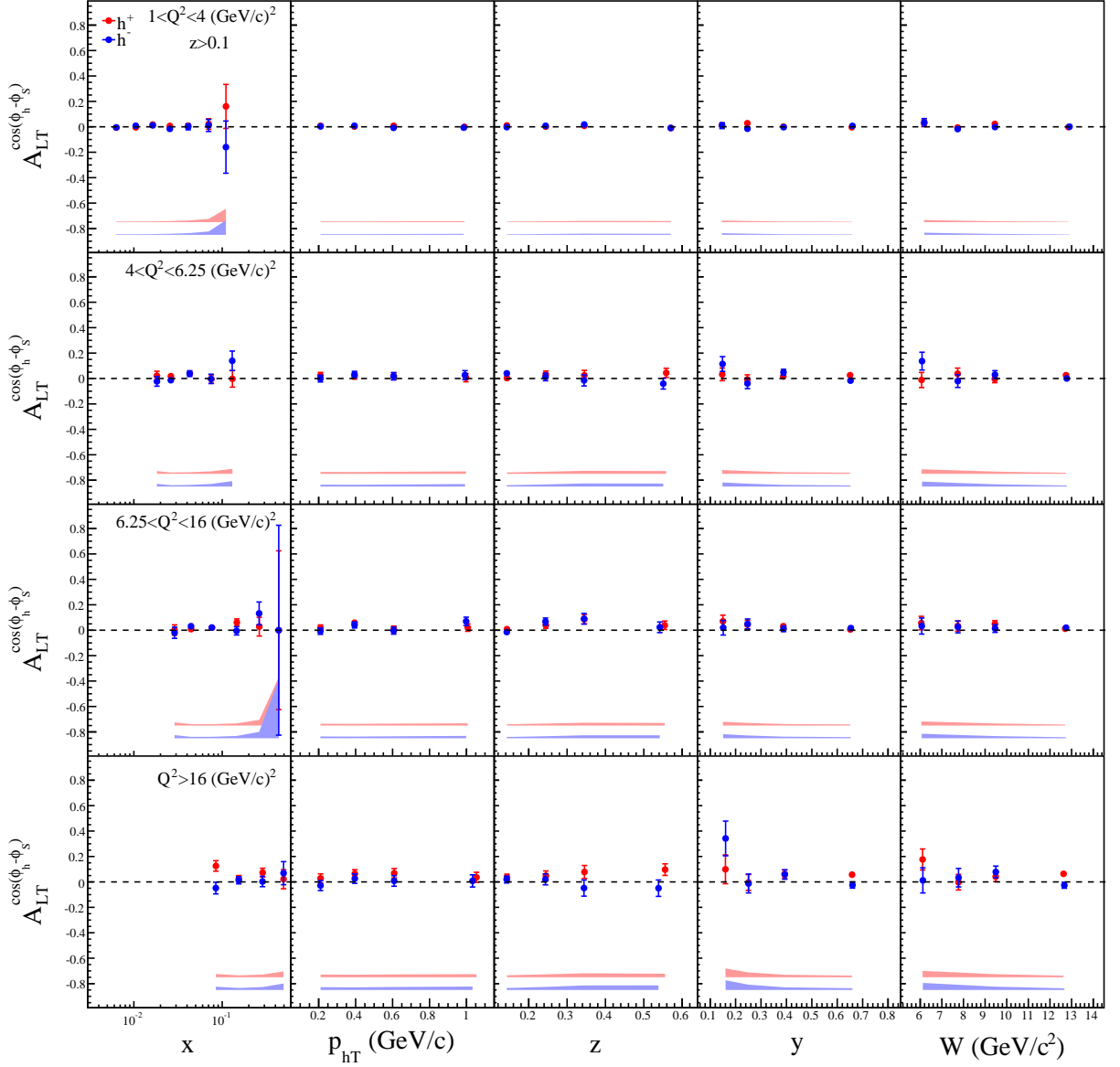


Figure 4.29: $A_{LT}^{\cos(\phi_h - \phi_S)}$ asymmetry in bins of x , p_{hT} , z , y , W and Q^2 . The results are divided by hadron charge; in red are results for positive hadrons and in blue for negative ones. The systematic error is presented as a band in the bottom of each plot.

4. EXTRACTION OF TRANSVERSE SPIN ASYMMETRIES FROM SIDIS

In Fig. 4.30 the asymmetry $A_{UT}^{\sin(\phi_S)}$ is shown. This asymmetry is a higher twist asymmetry and gives access to a convolution of more than one PDF and one FF. It is related to Collins and Sivers effects. It is compatible with zero in the majority of the bins, within the accuracy. Nevertheless it shows a possible non-zero values for negative hadrons at large x .

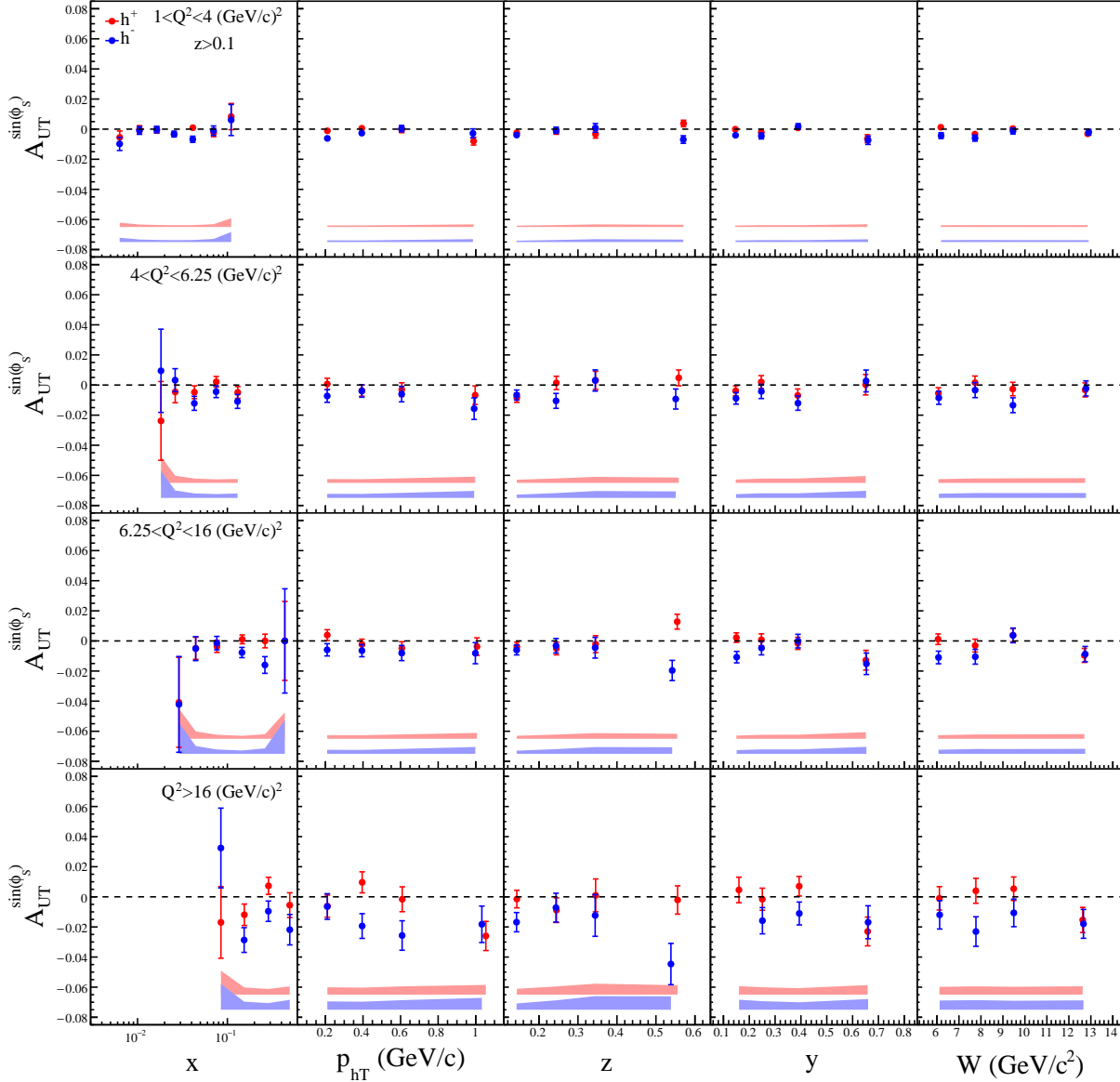


Figure 4.30: $A_{UT}^{\sin(\phi_S)}$ asymmetry in bins of x , $p_{T,h}$, z , y , W and Q^2 . The results are divided by hadron charge; in red are results for positive hadrons and in blue for negative ones. The systematic error is presented as a band in the bottom of each plot.

In Fig. 4.31 the asymmetry $A_{UT}^{\sin(2\phi_h - \phi_S)}$ is shown. It is a higher twist asymmetry and gives access to a convolution of several effects. This asymmetry is compatible with zero.

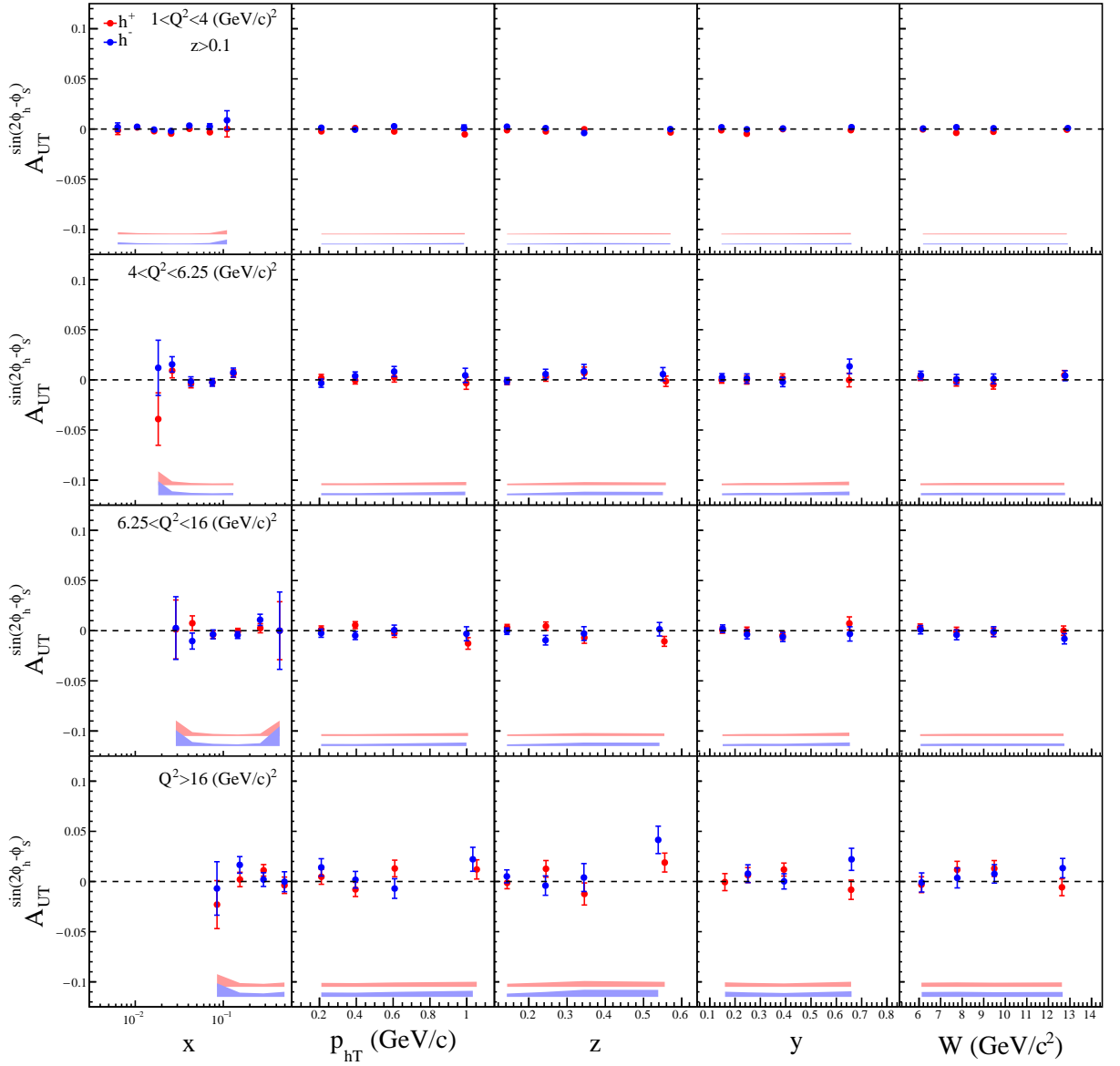


Figure 4.31: $A_{UT}^{\sin(2\phi_h - \phi_S)}$ asymmetry in bins of x , p_{Th} , z , y , W and Q^2 . The results are divided by hadron charge; in red are results for positive hadrons and in blue for negative ones. The systematic error is presented as a band in the bottom of each plot.

4. EXTRACTION OF TRANSVERSE SPIN ASYMMETRIES FROM SIDIS

In Fig. 4.32 the asymmetry $A_{LT}^{\cos(\phi_S)}$ is shown. This asymmetry is a higher twist asymmetry. It is compatible with zero.

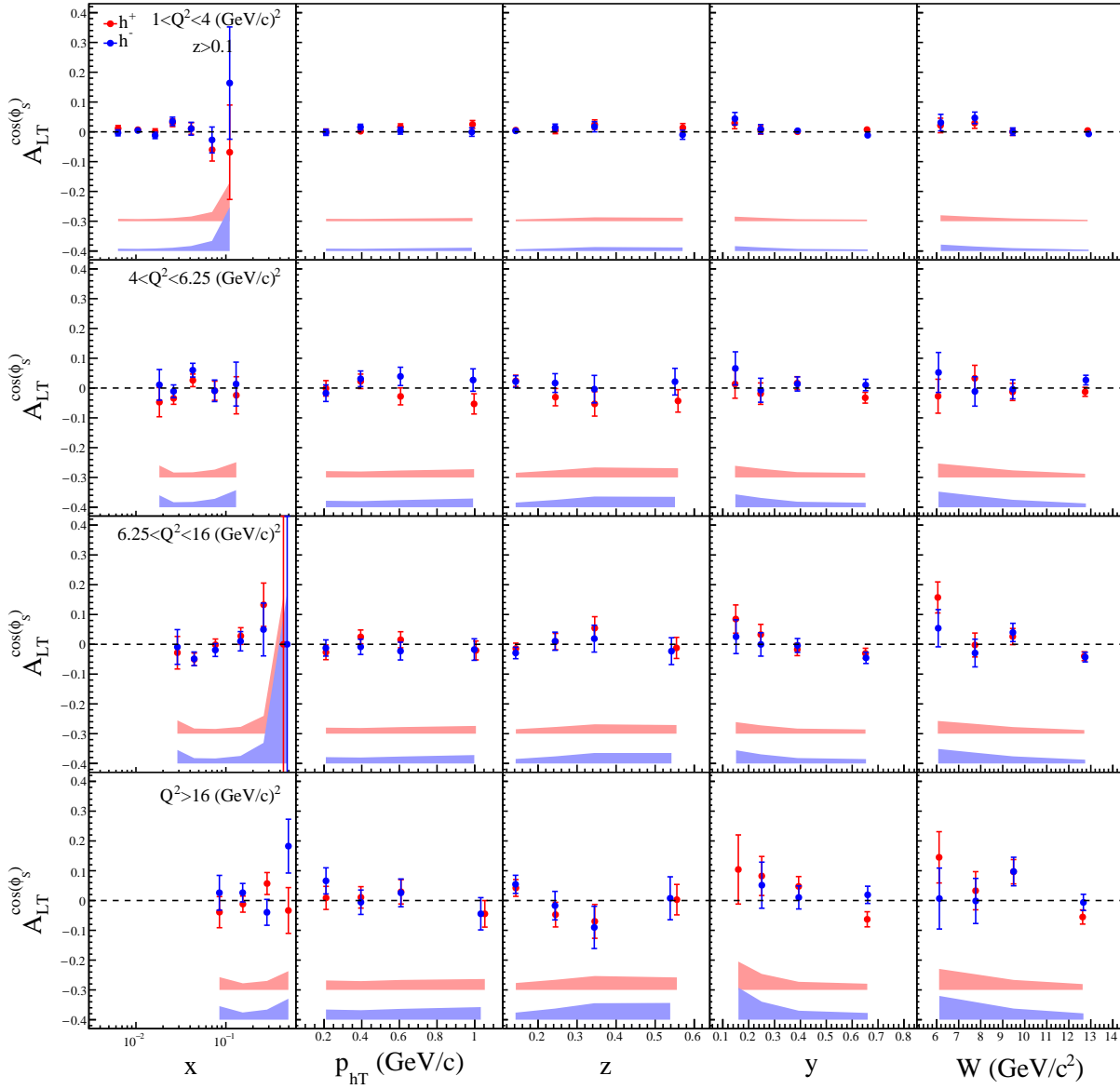


Figure 4.32: $A_{LT}^{\cos(\phi_S)}$ asymmetry in bins of x , p_{Th} , z , y , W and Q^2 . The results are divided by hadron charge; in red are results for positive hadrons and in blue for negative ones. The systematic error is presented as a band in the bottom of each plot.

In Fig. 4.33 the asymmetry $A_{LT}^{\cos(2\phi_h - \phi_S)}$ is shown. This is a higher twist asymmetry and is compatible with zero.

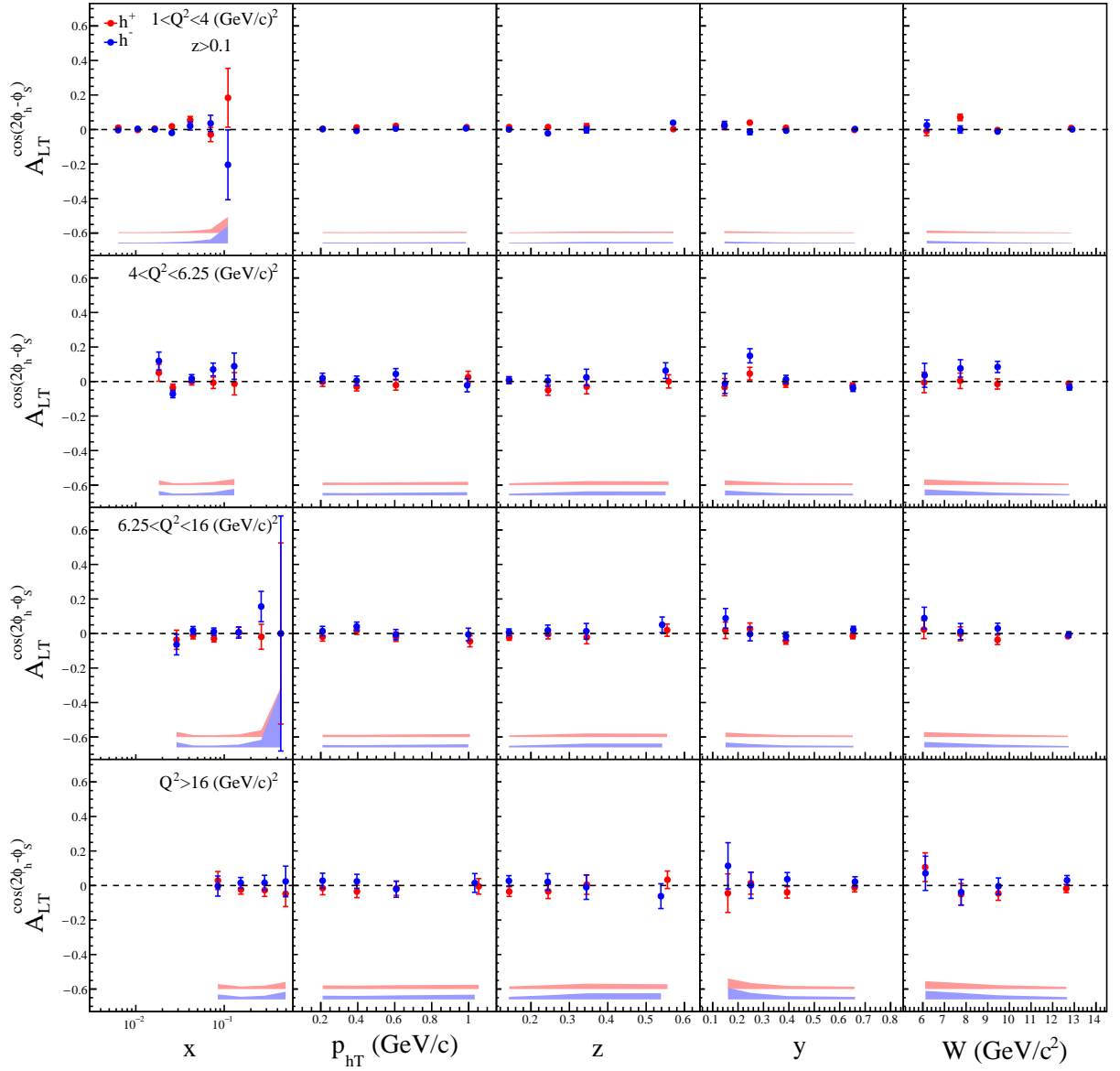


Figure 4.33: $A_{LT}^{\cos(2\phi_h - \phi_S)}$ asymmetry in bins of x , p_{hT} , z , y , W and Q^2 . The results are divided by hadron charge; in red are results for positive hadrons and in blue for negative ones. The systematic error is presented as a band in the bottom of each plot.

4.8 Selection of a Different z Range

The analysis was performed dividing the z domain covered by $z > 0.1$ in two ranges. The small z range, $0.1 < z < 0.2$, which may suffer from contamination from the target fragmentation region, and the large z range, $z > 0.2$. The final statistics for the three z ranges is in Table 4.9. The number of hadrons divided by the Q^2 bins is in Table 4.10. The division of statistics by Q^2

Range	# hadrons	# positive hadrons	# negative hadrons
$z < 0.1$	156616961	85533933	71083028
$0.1 < z < 0.2$	78464810	41771815	36692995
$z > 0.2$	78152151	43762118	34390033

 Table 4.9: Final number of hadrons depending on the z range selected.

0.1 < z < 0.2						
Range (GeV/ c^2)	# hadrons		# positive hadrons		# negative hadrons	
$1 < Q^2 < 4$	58257915	74.3 %	30891717	74.0 %	27366198	74.6 %
$4 < Q^2 < 6.25$	9120538	11.6 %	4884913	11.7 %	4235625	11.5 %
$6.25 < Q^2 < 16$	8963231	11.4 %	4843998	11.6 %	4119233	11.2 %
$16 < Q^2 < 81$	2111249	2.7 %	1144749	2.7 %	966500	2.6 %
All Q^2	78452933	100 %	41765377	100 %	36687556	100 %
$z > 0.2$						
Range (GeV/ c^2)	# hadrons		# positive hadrons		# negative hadrons	
$1 < Q^2 < 4$	58369889	74.7 %	32153030	73.5 %	26216859	76.2 %
$4 < Q^2 < 6.25$	8945393	11.4 %	5150367	11.8 %	3795026	11.0 %
$6.25 < Q^2 < 16$	8775557	11.2 %	5197470	11.9 %	3578087	10.4 %
$16 < Q^2 < 81$	2050146	2.6 %	1254108	2.9 %	796038	2.3 %
All Q^2	78140985	100 %	43754975	100 %	34386010	100 %

 Table 4.10: Distribution of the hadrons by the 4 Q^2 ranges and for $0.1 < z < 0.2$ and $z > 0.2$.

bin is the same as for the region $z > 0.1$, 75% of the hadrons in the lowest Q^2 region, 11% in each intermediate Q^2 region and 3% in the highest Q^2 region.

The kinematic bins selected for the extraction of the asymmetries are the same as described in Section 4.4 apart for the bins in z , which cannot be the same. The bin limits in z are in Table 4.11.

z range	# bins	z bins limits				
$0.1 < z < 0.2$	4	0.1	0.125	0.15	0.175	0.2
$z > 0.2$	4	0.2	0.25	0.3	0.4	1.0

 Table 4.11: z bins to be used in analysis for for $0.1 < z < 0.2$ and $z > 0.2$. The bins are the same for all the Q^2 ranges.

4.8.1 Systematic Effects

The preformed systematic studies are the same as the ones presented in section 4.6 for the region $z > 0.1$.

The azimuthal stability is checked with four tests. For the R-test the results are presented in the Fig. 4.34 for the two z ranges. As for $z > 0.1$, the azimuthal stability for the modulations on $\sin(\phi_S)$ and on $\cos(\phi_S)$ is not good.

The results for the T-test are in Figure 4.35 for the two z ranges. This test reveals a good stability for all the modulations apart for the modulations on ϕ_S , as also seen for $z > 0.1$.

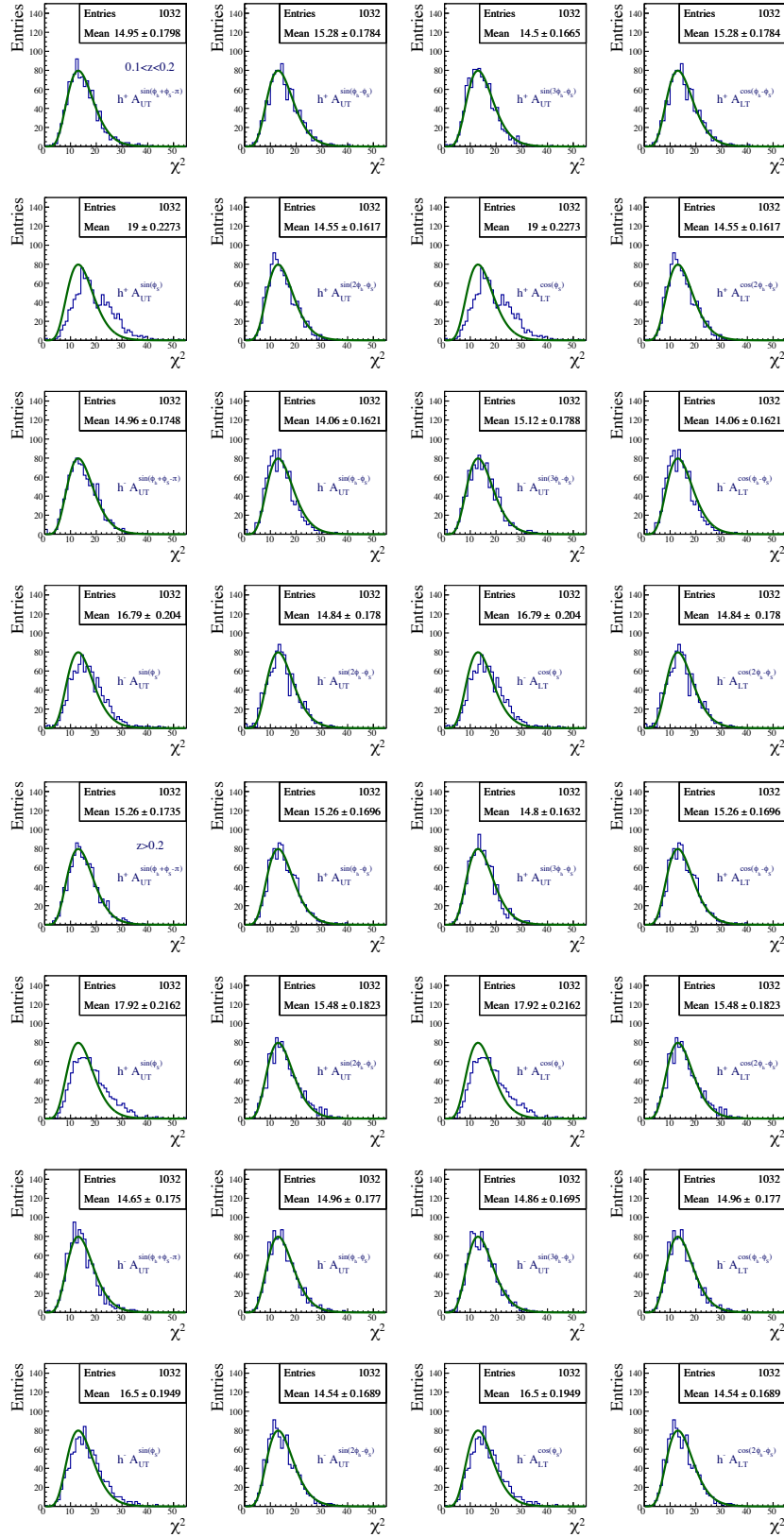


Figure 4.34: R-test results. The first four lines are for the z range $0.1 < z < 0.2$ and the last four ones for the z range $z > 0.2$. The results are divided by hadron charge and by asymmetry. The first two lines are for positive hadrons and the last two for negative hadrons. The 8 asymmetries are specified in the plots.

4. EXTRACTION OF TRANSVERSE SPIN ASYMETRIES FROM SIDIS

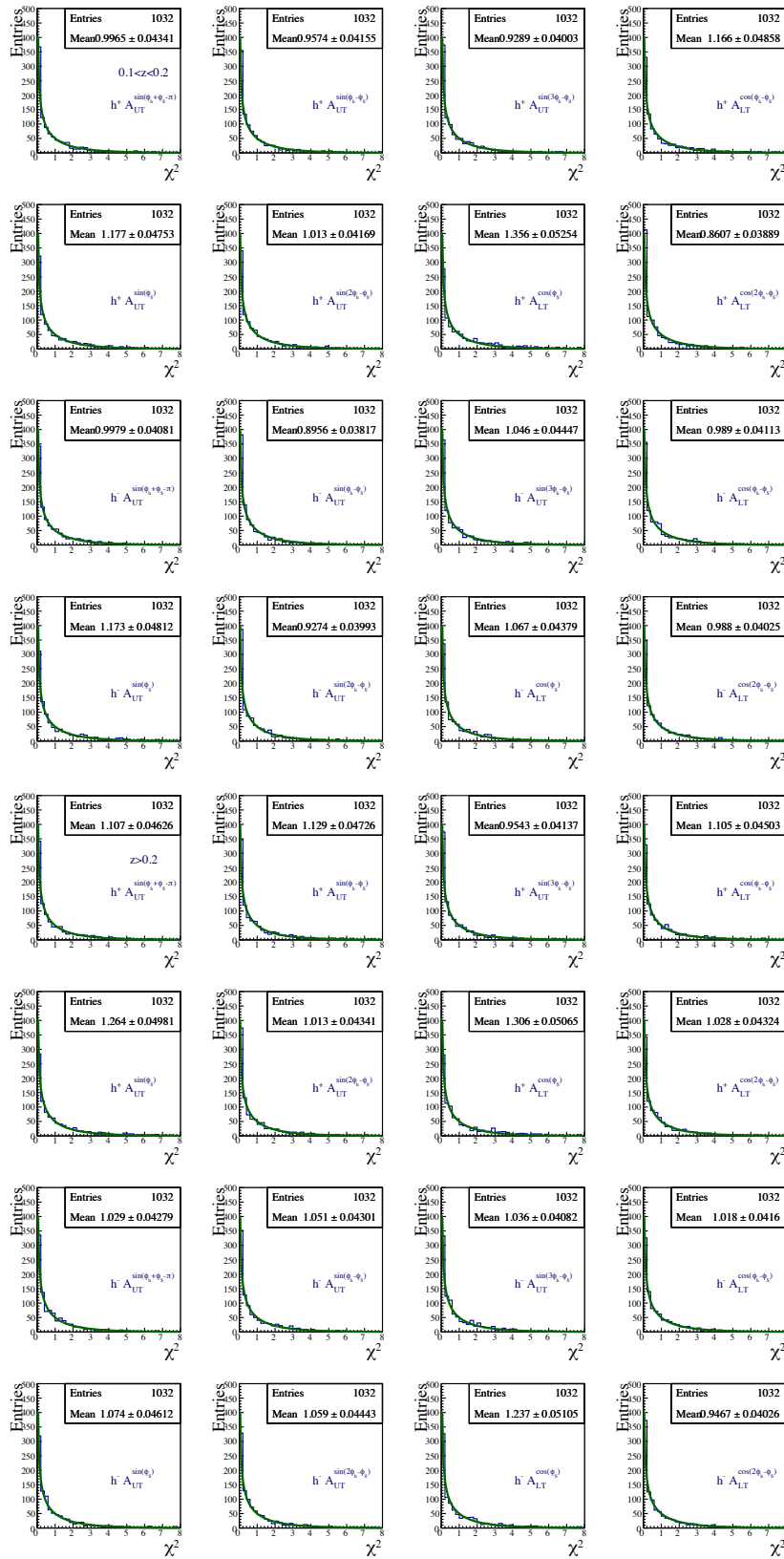


Figure 4.35: T-test results. The first four lines are for the z range $0.1 < z < 0.2$ and the last four ones for the z range $z > 0.2$. The results are divided by hadron charge and by asymmetry. The first two lines are for positive hadrons and the last two for negative hadrons. The 8 asymmetries are specified in the plots.

The results for the RA-test are in Figure 4.36. The same two modulations in ϕ_S show problems for all the z regions.

The results for the RA-T test are in Figure 4.37. The same two modulations present problems. As for the range $z > 0.1$, these issues are also related with the false asymmetries and are considered there.

As for the $z > 0.1$ range the compatibility between the periods is checked. The results are in Fig. 4.38 for the two z ranges. The asymmetries from all the periods are compatible with each other.

The compatibility between the different extraction methods was also verified. The pulls between the asymmetries are in Fig. 4.39 and the pulls between the asymmetry errors are in Fig. 4.40, for the two z ranges.

The estimates of possible systematics are smaller than the systematics evaluated based on the false asymmetries and it is enough to consider the systematics from false asymmetries.

Finally, the results from the false asymmetries study are in Figures 4.41. The mean values from these distributions are going to be taken as the systematic uncertainty in terms of the statistical error. The systematic errors to be considered for each asymmetry, by hadron charge, are in Table 4.12.

	$0.1 < z < 0.2$		$z > 0.2$	
$\sigma_{sys}/\sigma_{stat}$	h^+	h^-	h^+	h^-
$A_{UT}^{\sin(\phi_h + \phi_S - \pi)}$	0.52	0.51	0.50	0.52
$A_{UT}^{\sin(\phi_h - \phi_S)}$	0.51	0.50	0.51	0.53
$A_{UT}^{\sin(3\phi_h - \phi_S)}$	0.53	0.50	0.53	0.53
$A_{LT}^{\cos(\phi_h - \phi_S)}$	0.53	0.50	0.60	0.56
$A_{UT}^{\sin(\phi_S)}$	0.59	0.62	0.59	0.56
$A_{UT}^{\sin(2\phi_h - \phi_S)}$	0.55	0.51	0.52	0.52
$A_{LT}^{\cos(\phi_S)}$	0.76	0.67	0.67	0.71
$A_{LT}^{\cos(2\phi_h - \phi_S)}$	0.55	0.54	0.52	0.50

Table 4.12: Systematic uncertainty for each asymmetry and for $0.1 < z < 0.2$ and $z > 0.2$.

4. EXTRACTION OF TRANSVERSE SPIN ASYMETRIES FROM SIDIS

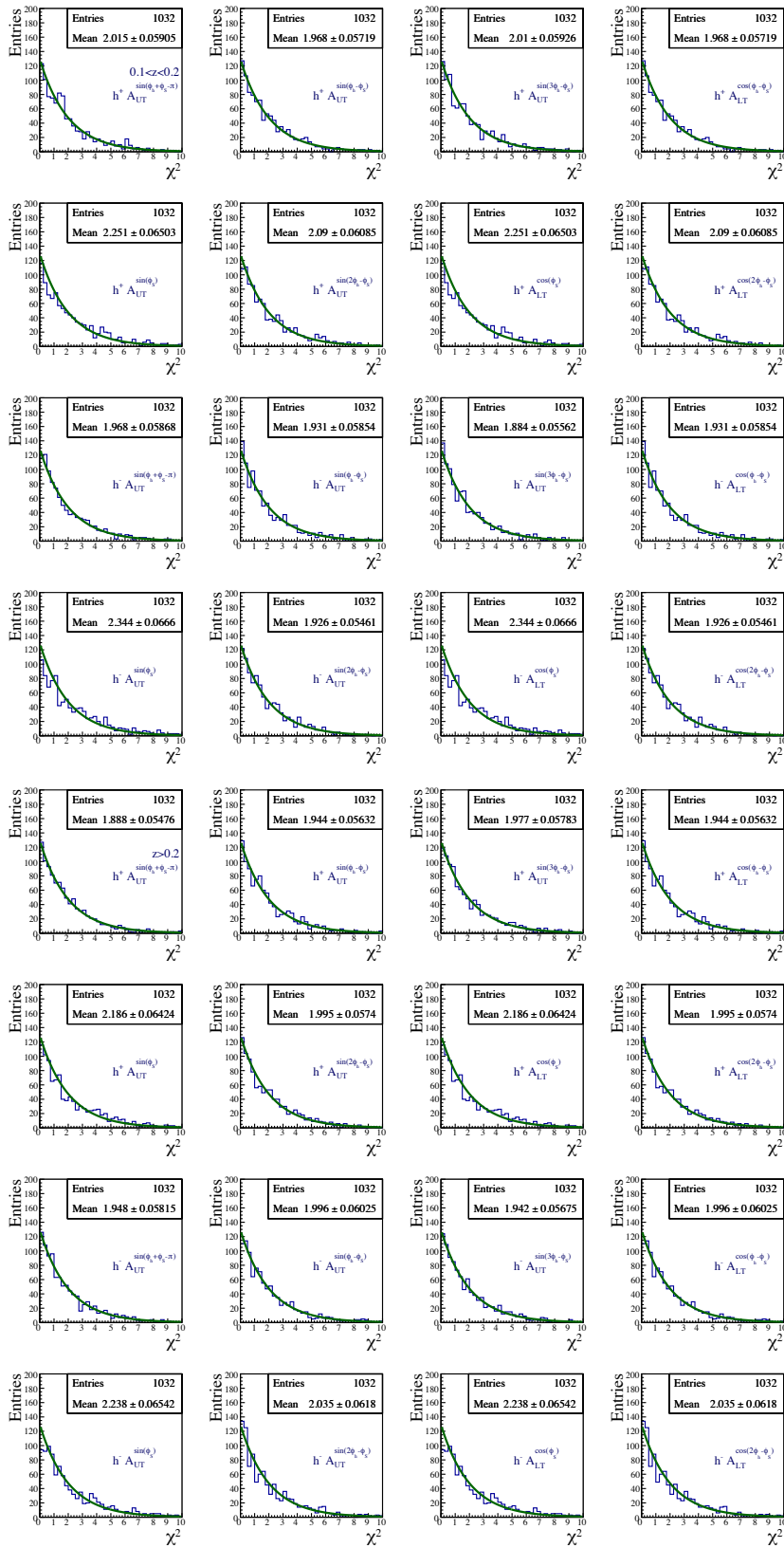


Figure 4.36: RA-test results. The first four lines are for the z range $0.1 < z < 0.2$ and the last four ones for the z range $z > 0.2$. The results are divided by hadron charge and by asymmetry. The first two lines are for positive hadrons and the last two for negative hadrons. The 8 asymmetries are specified in the plots.

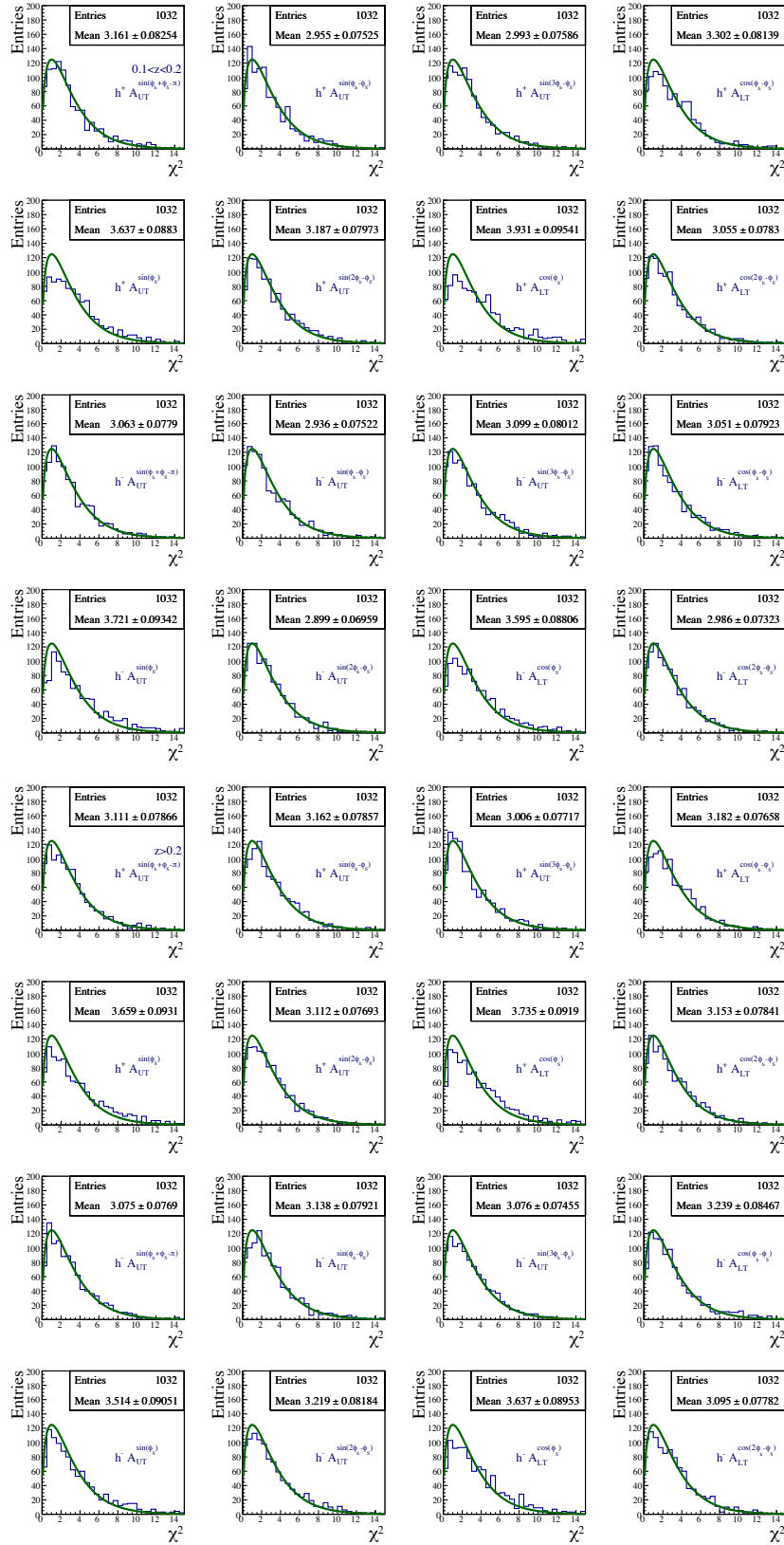


Figure 4.37: RA-T-test results. The first four lines are for the z range $0.1 < z < 0.2$ and the last four ones for the z range $z > 0.2$. The results are divided by hadron charge and by asymmetry. The first two lines are for positive hadrons and the last two for negative hadrons. The 8 asymmetries are specified in the plots.

4. EXTRACTION OF TRANSVERSE SPIN ASYMETRIES FROM SIDIS

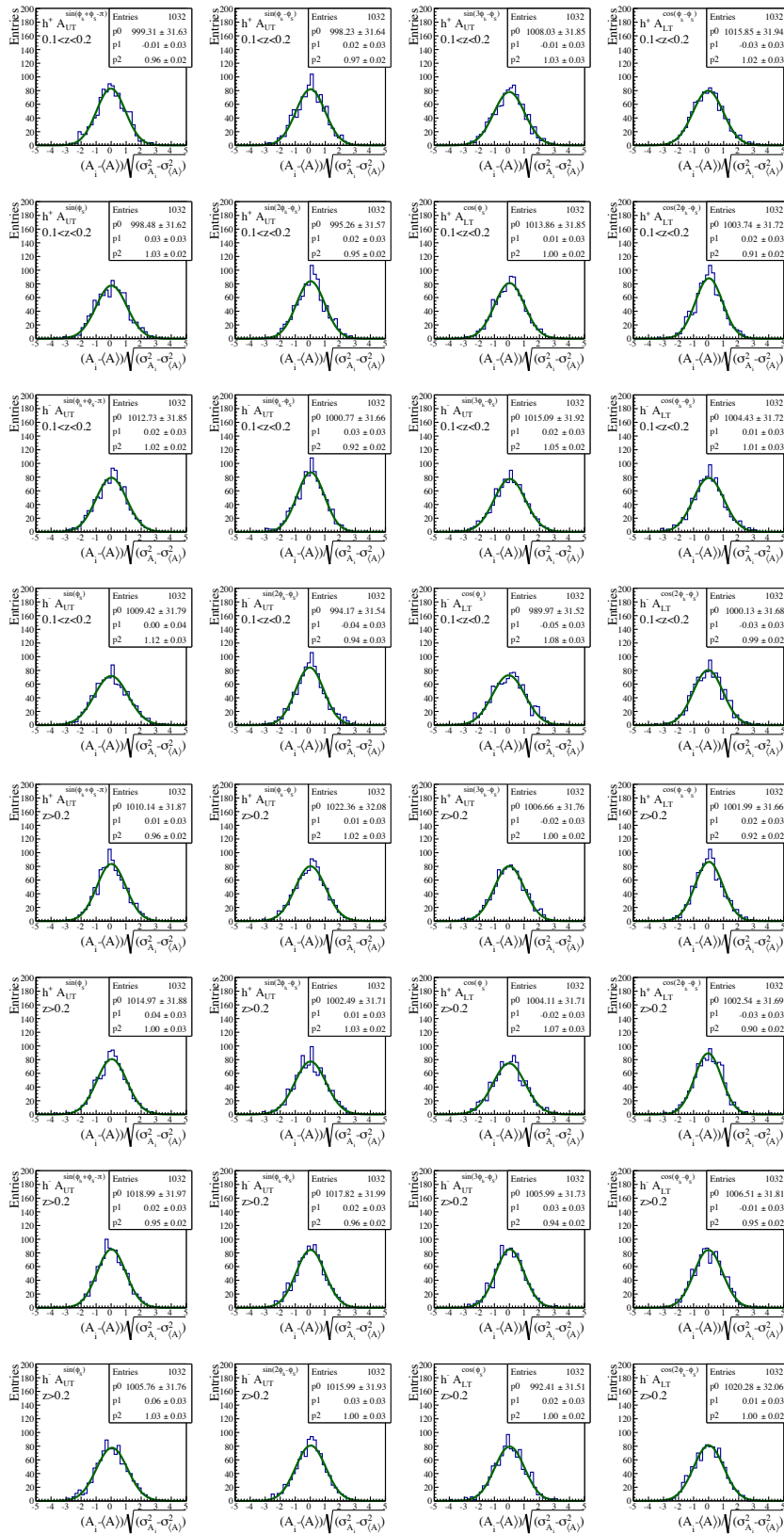


Figure 4.38: Compatibility between the results from different data taking periods. The first four lines are for the z range $0.1 < z < 0.2$ and the last four ones for the z range $z > 0.2$. The results are divided by hadron charge and by asymmetry. The first two lines are for positive hadrons and the last two for negative hadrons. The 8 asymmetries are specified in the plots.

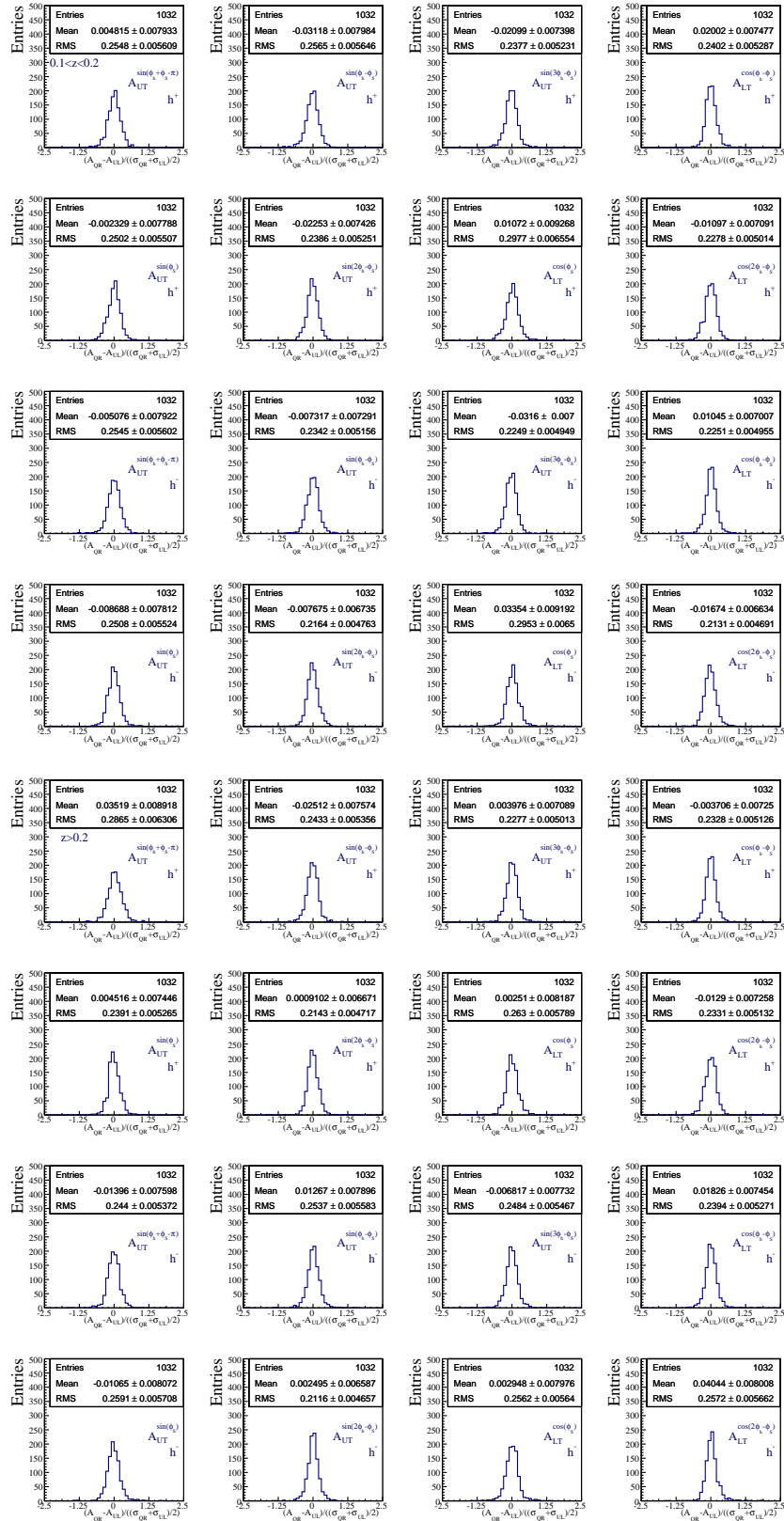


Figure 4.39: Compatibility between the two different extraction methods, the 1D quadrupole ratio and the Unbinned Maximum Likelihood. The first four lines are for the z range $0.1 < z < 0.2$ and the last four ones for the z range $z > 0.2$. The pulls between the asymmetries are divided by hadron charge and by asymmetry. The first two lines are for positive hadrons and the last two for negative hadrons. The 8 asymmetries are specified in the plots.

4. EXTRACTION OF TRANSVERSE SPIN ASYMETRIES FROM SIDIS

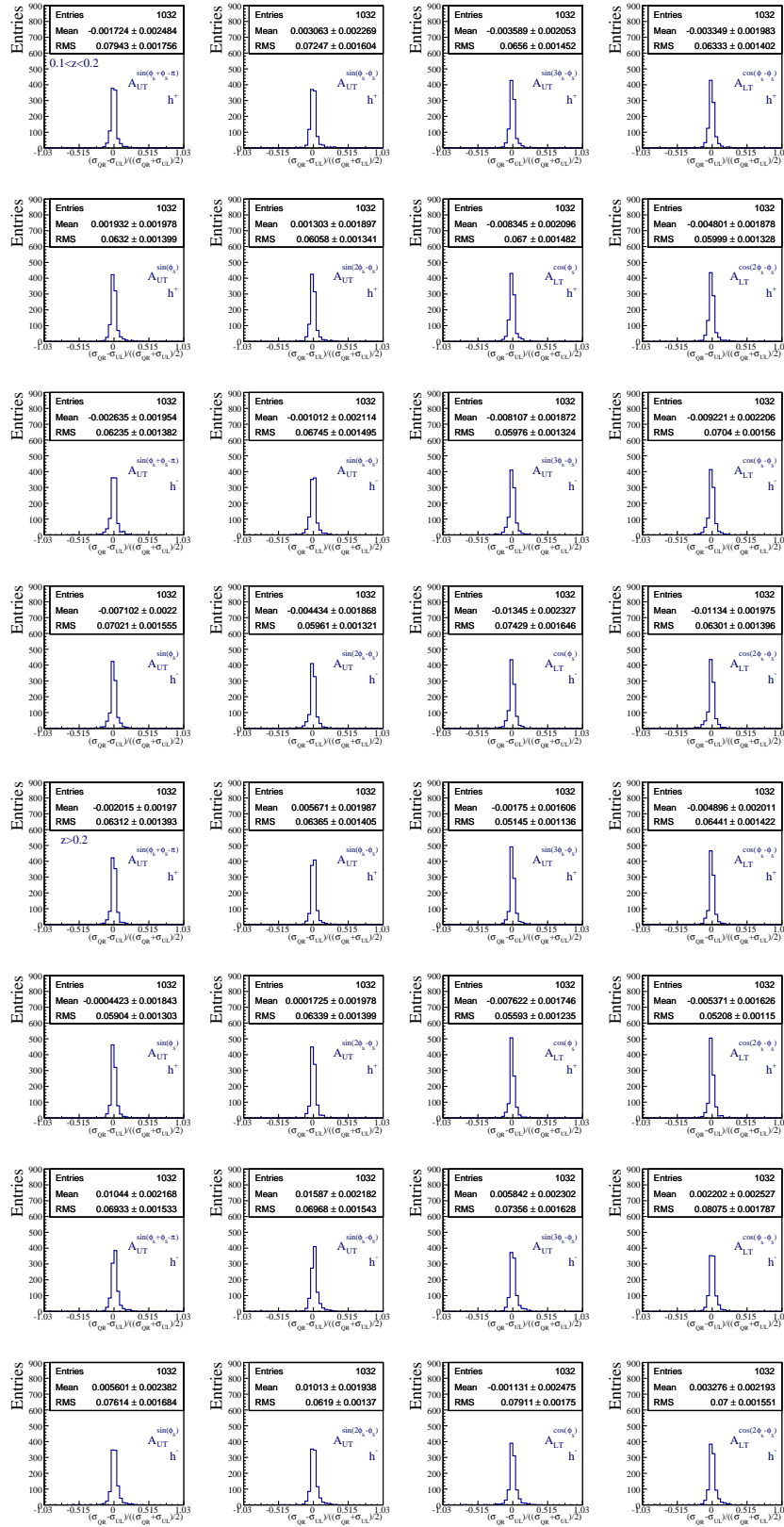


Figure 4.40: Compatibility between the two different extraction methods, the 1D quadrupole ratio and the Unbinned Maximum Likelihood. The first four lines are for the z range $0.1 < z < 0.2$ and the last four ones for the z range $z > 0.2$. The pulls between the asymmetry errors are divided by hadron charge and by asymmetry. The first two lines are for positive hadrons and the last two for negative hadrons. The 8 asymmetries are specified in the plots.

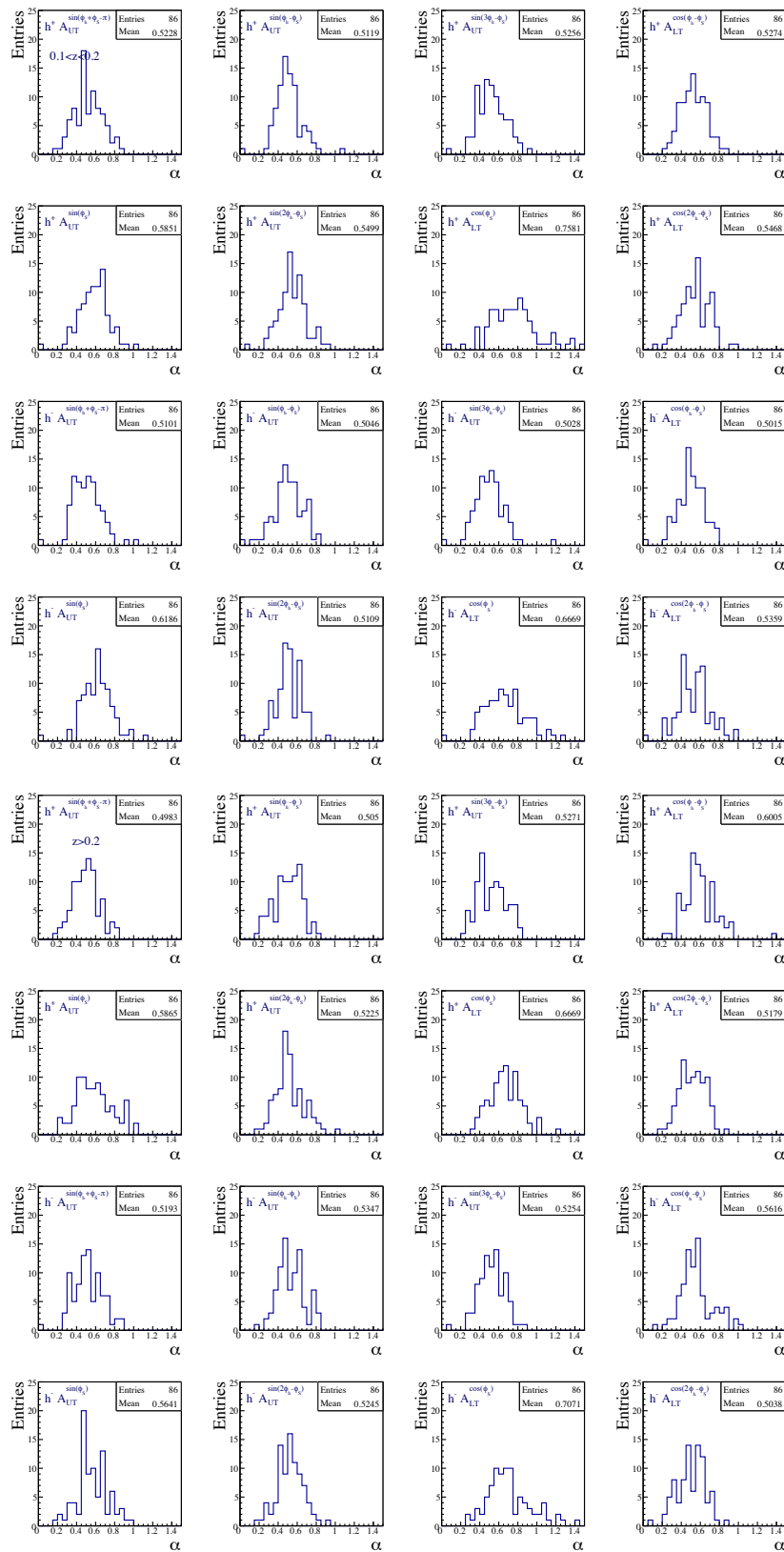


Figure 4.41: Evaluation of the systematic error in terms of the statistical one taking into account the false asymmetries. The first four lines are for the z range $0.1 < z < 0.2$ and the last four ones for the z range $z > 0.2$. The results are divided by hadron charge and by asymmetry. The first two lines are for positive hadrons and the last two for negative hadrons. The 8 asymmetries are specified in the plots.

4.8.2 Transverse Spin Asymmetries for $0.1 < z < 0.2$ and $z > 0.2$

The transverse spin asymmetries in the ranges $0.1 < z < 0.2$ and $z > 0.2$ are in Figures from 4.42 to 4.49.

This multi-dimensional analysis, 3 dimensions, (Q^2, z, x) , (Q^2, z, p_{hT}) , (Q^2, z, y) , (Q^2, z, W) , is a first step towards a more detailed analysis of the SIDIS data. These data are very important as input for theoretical studies. They can help to test the models taking into account the different evolution scenarios.

The statistical errors in the range $0.1 < z < 0.2$ are practically the same as in the range $z > 0.2$, and they are around 40% larger than in the range $z > 0.1$. In general the asymmetries are compatible within the errors in the three z ranges, nevertheless showing different values. The asymmetries tend to be smaller for the small z range. In what concerns the Sivers asymmetry, in the larger Q^2 range and in x bins, for positive hadrons it is smaller for $0.1 < z < 0.2$ than for $z > 0.2$.

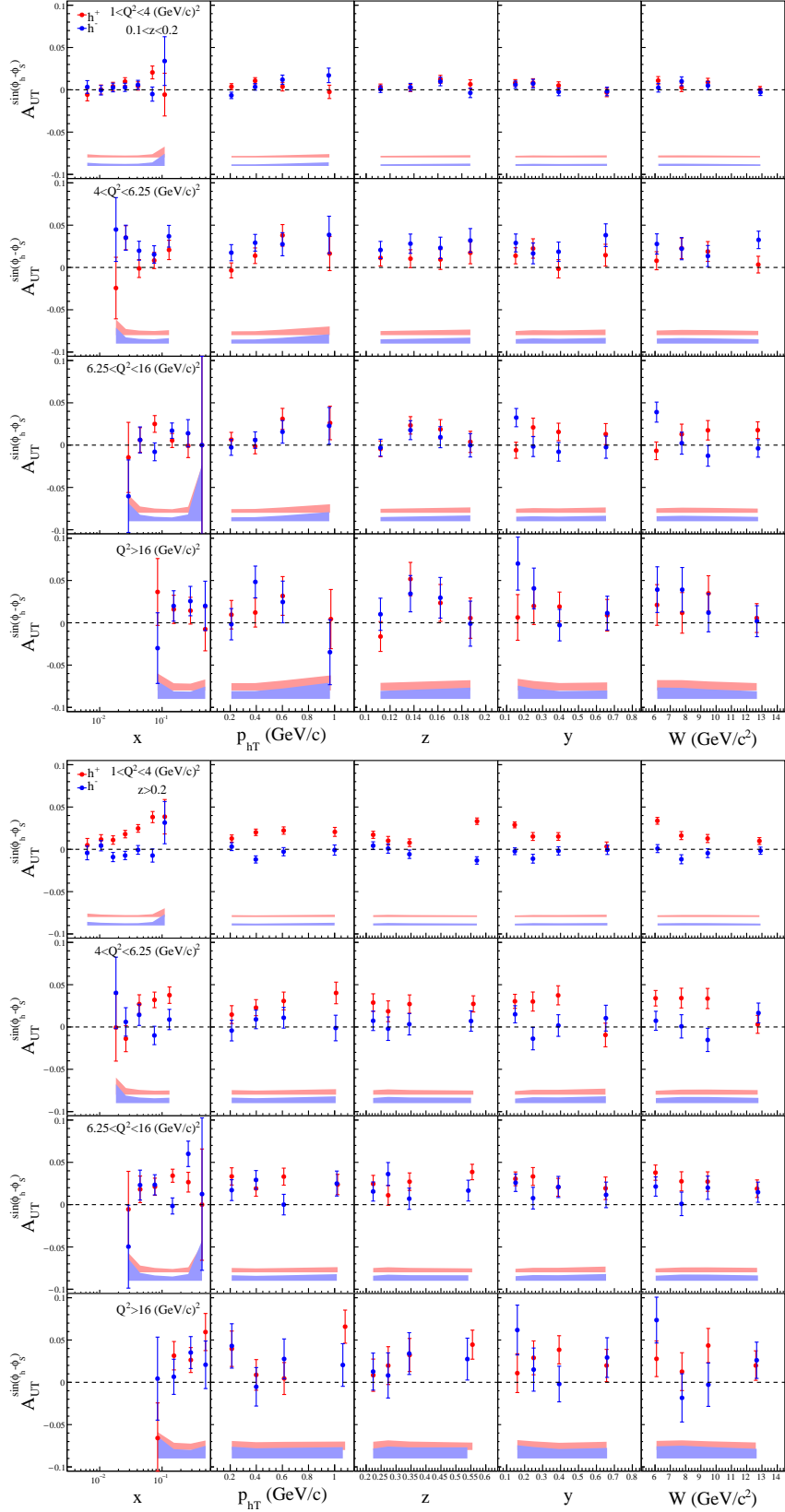


Figure 4.42: $A_{UT}^{\sin(\phi_h - \phi_s)}$ asymmetry, the so called Sivers asymmetry, in bins of x , p_{T^h} , z , y , W and Q^2 , for the z ranges $0.1 < z < 0.2$ and $z > 0.2$. The results are divided by hadron charge; in red are results for positive hadrons and in blue for negative ones. The systematic error is presented as a band in the bottom of each plot.

4. EXTRACTION OF TRANSVERSE SPIN ASYMMETRIES FROM SIDIS

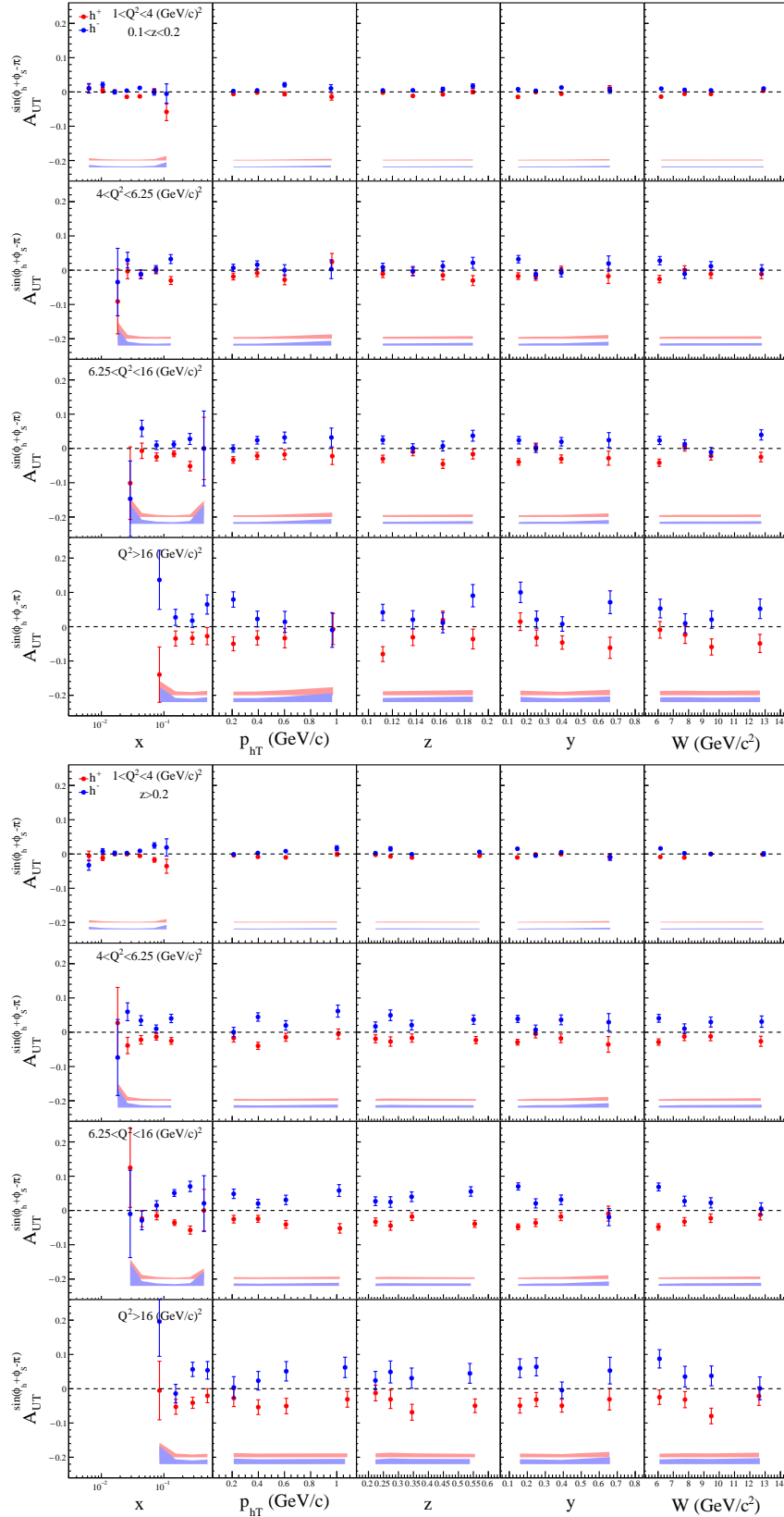


Figure 4.43: $A_{UT}^{\sin(\phi_h + \phi_s - \pi)}$ asymmetry, the so called Collins asymmetry, in bins of x , p_{T^h} , z , y , W and Q^2 , for the z ranges $0.1 < z < 0.2$ and $z > 0.2$. The results are divided by hadron charge; in red are results for positive hadrons and in blue for negative ones. The systematic error is presented as a band in the bottom of each plot.

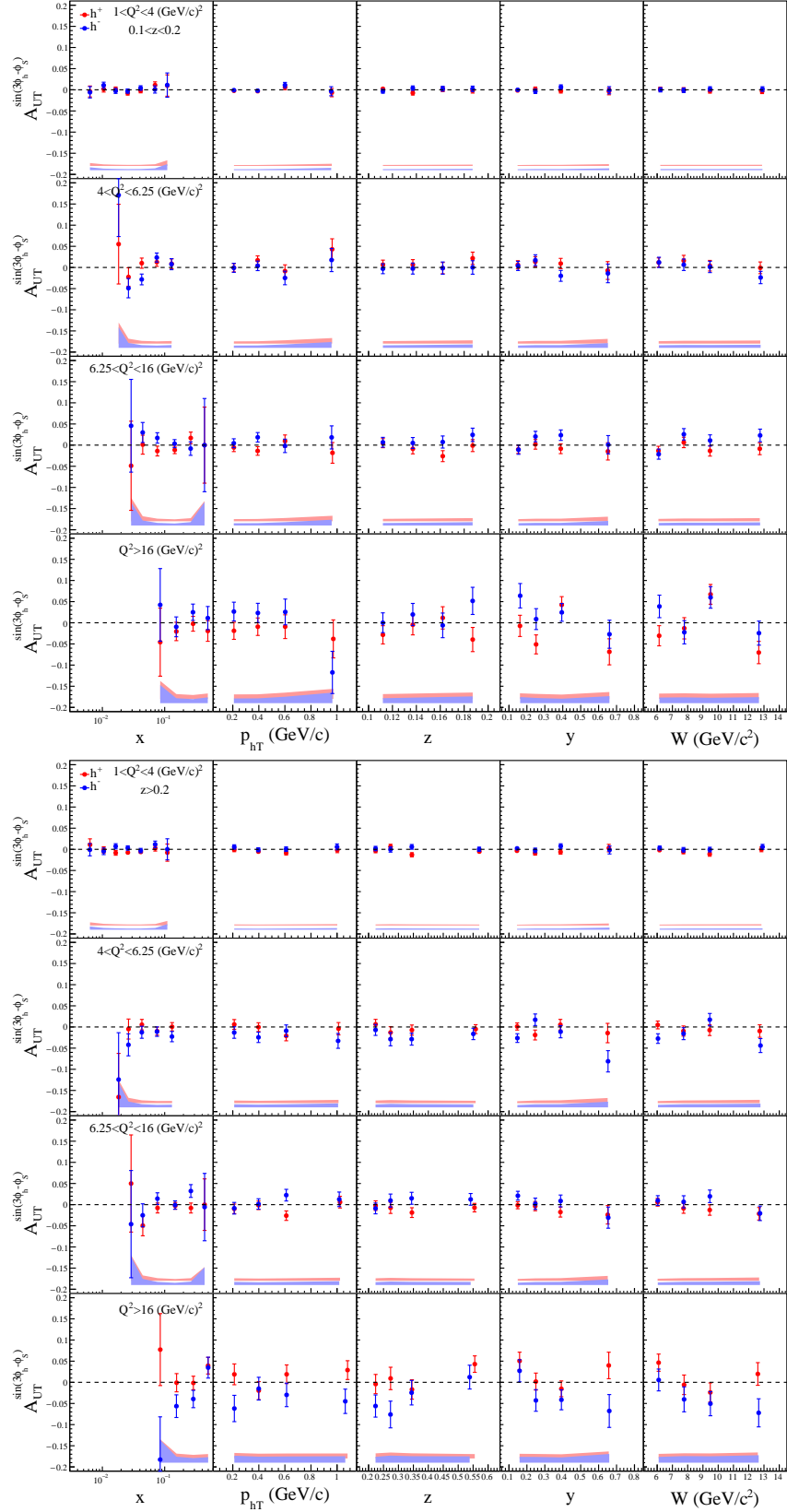


Figure 4.44: $A_{UT}^{\sin(3\phi_h - \phi_S)}$ asymmetry in bins of x , p_{T_h} , z , y , W and Q^2 , for the z ranges $0.1 < z < 0.2$ and $z > 0.2$. The results are divided by hadron charge; in red are results for positive hadrons and in blue for negative ones. The systematic error is presented as a band in the bottom of each plot.

4. EXTRACTION OF TRANSVERSE SPIN ASYMMETRIES FROM SIDIS

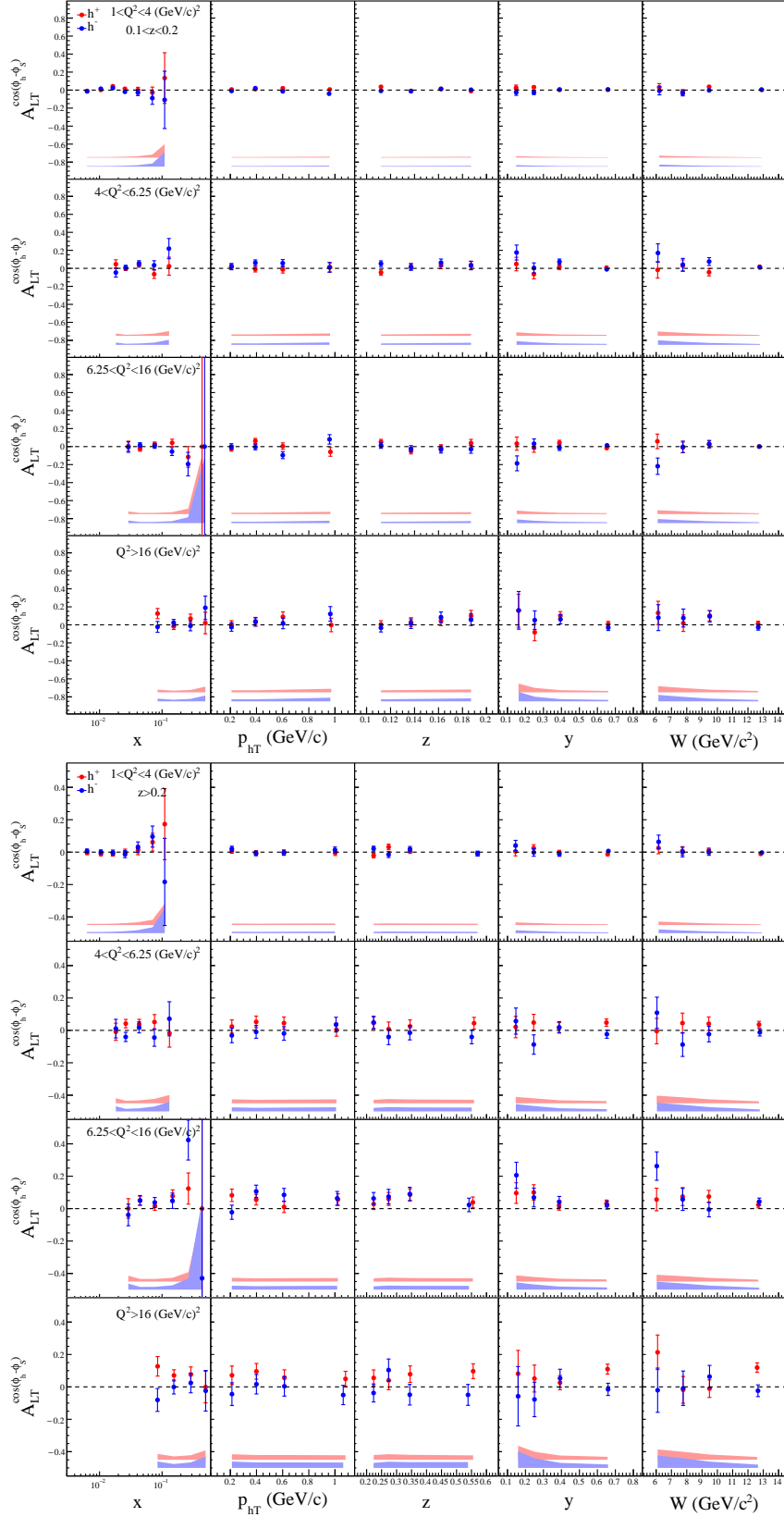


Figure 4.45: $A_{LT}^{\cos(\phi_h - \phi_S)}$ asymmetry in bins of x , $p_{T,h}$, z , y , W and Q^2 , for the z ranges $0.1 < z < 0.2$ and $z > 0.2$. The results are divided by hadron charge; in red are results for positive hadrons and in blue for negative ones. The systematic error is presented as a band in the bottom of each plot.

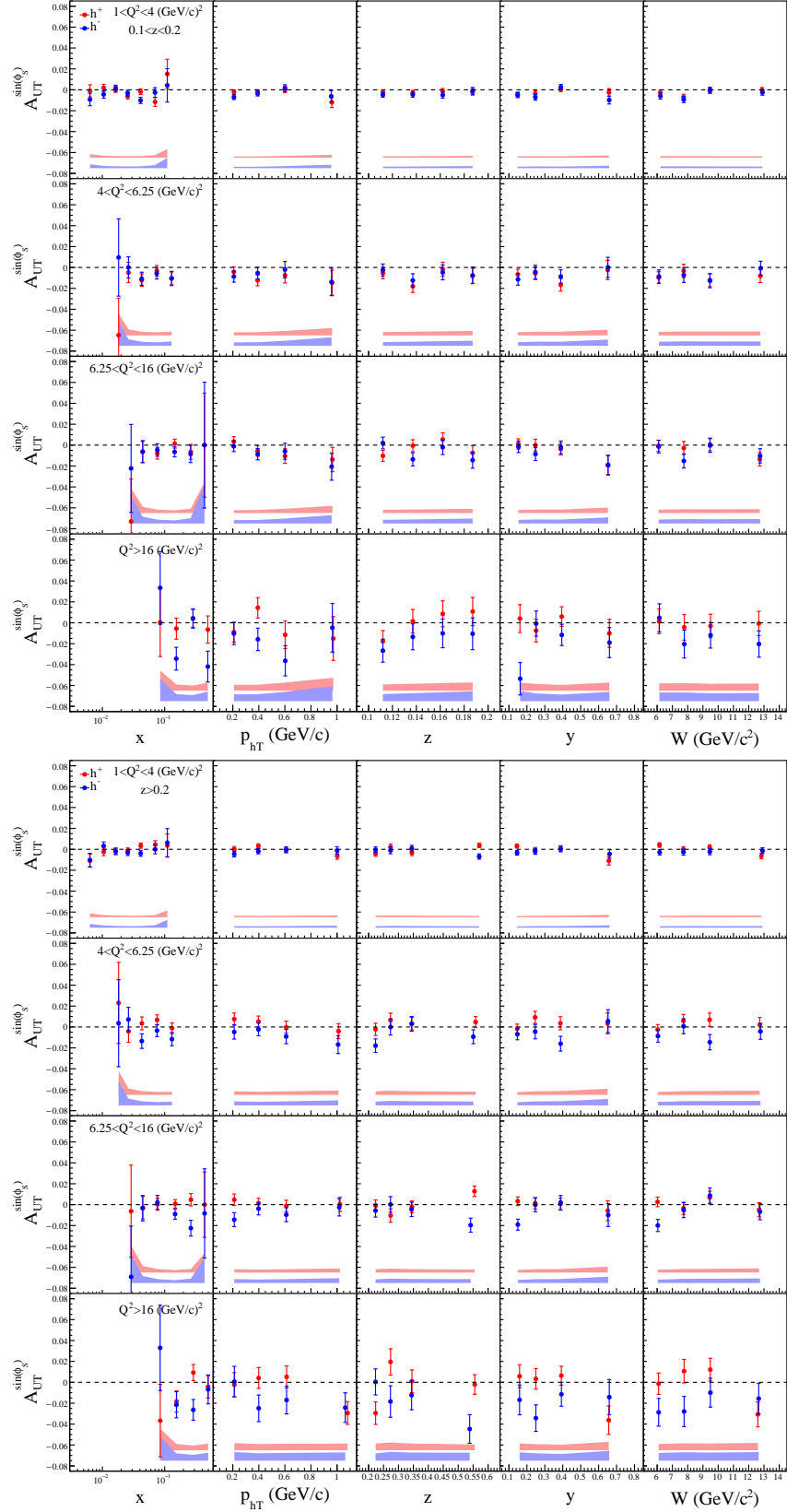


Figure 4.46: $A_{UT}^{\sin(\phi_S)}$ asymmetry in bins of x , $p_{T,h}$, z , y , W and Q^2 , for the z ranges $0.1 < z < 0.2$ and $z > 0.2$. The results are divided by hadron charge; in red are results for positive hadrons and in blue for negative ones. The systematic error is presented as a band in the bottom of each plot.

4. EXTRACTION OF TRANSVERSE SPIN ASYMMETRIES FROM SIDIS

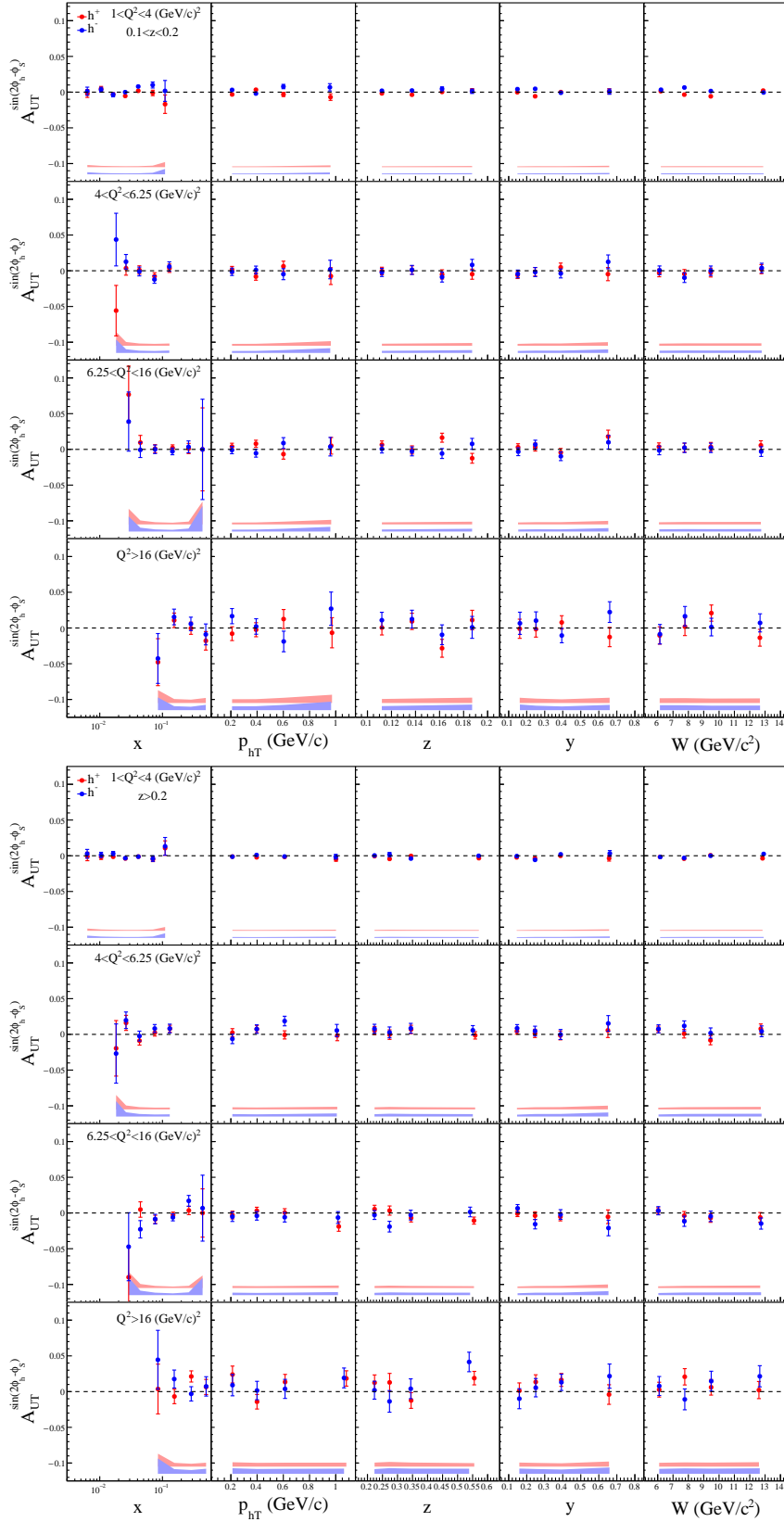


Figure 4.47: $A_{UT}^{\sin(2\phi_h - \phi_S)}$ asymmetry in bins of x , p_{T_h} , z , y , W and Q^2 , for the z ranges $0.1 < z < 0.2$ and $z > 0.2$. The results are divided by hadron charge; in red are results for positive hadrons and in blue for negative ones. The systematic error is presented as a band in the bottom of each plot.

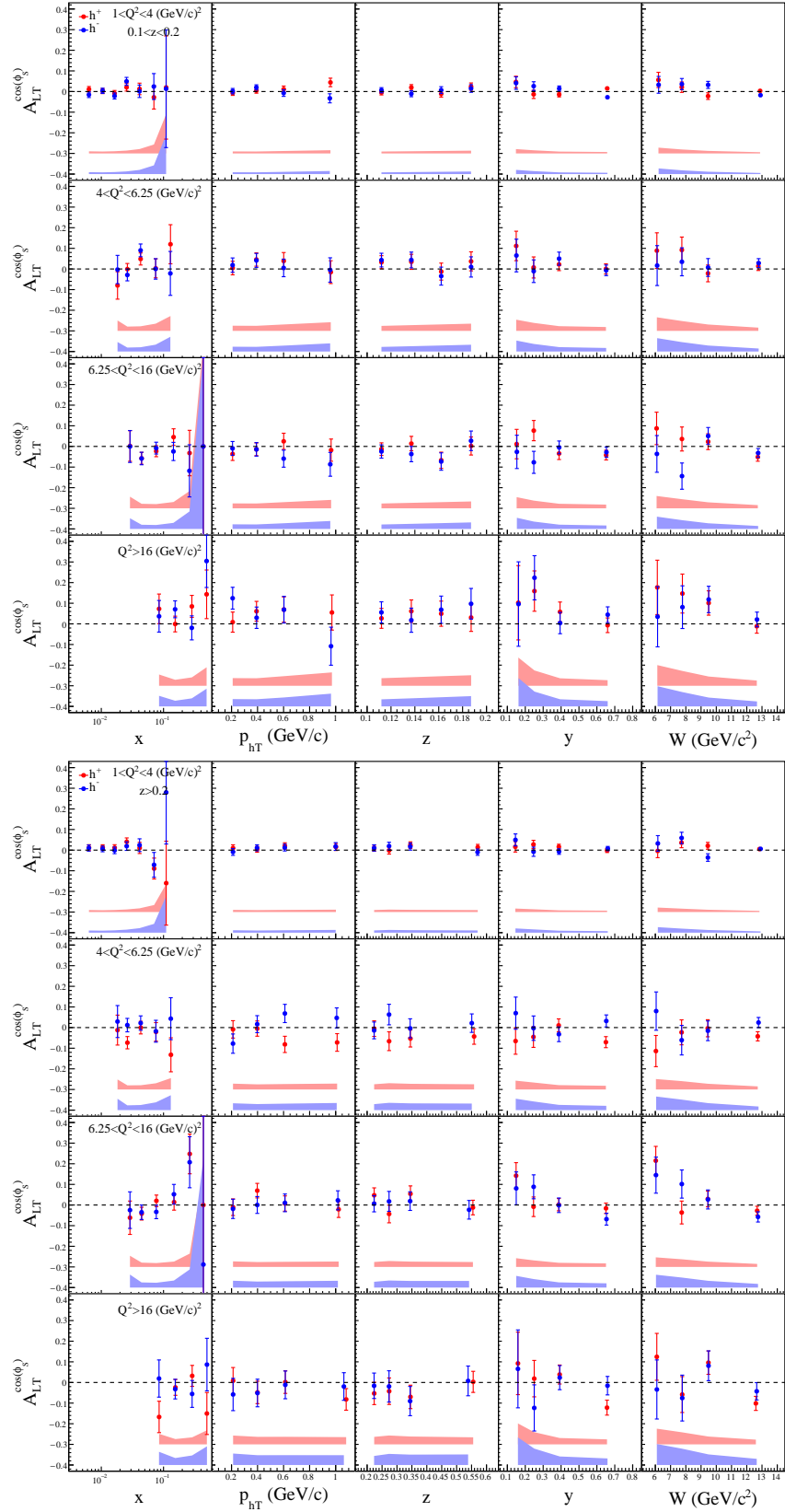


Figure 4.48: $A_{LT}^{\cos(\phi_S)}$ asymmetry in bins of x , $p_{T,h}$, z , y , W and Q^2 , for the z ranges $0.1 < z < 0.2$ and $z > 0.2$. The results are divided by hadron charge; in red are results for positive hadrons and in blue for negative ones. The systematic error is presented as a band in the bottom of each plot.

4. EXTRACTION OF TRANSVERSE SPIN ASYMMETRIES FROM SIDIS

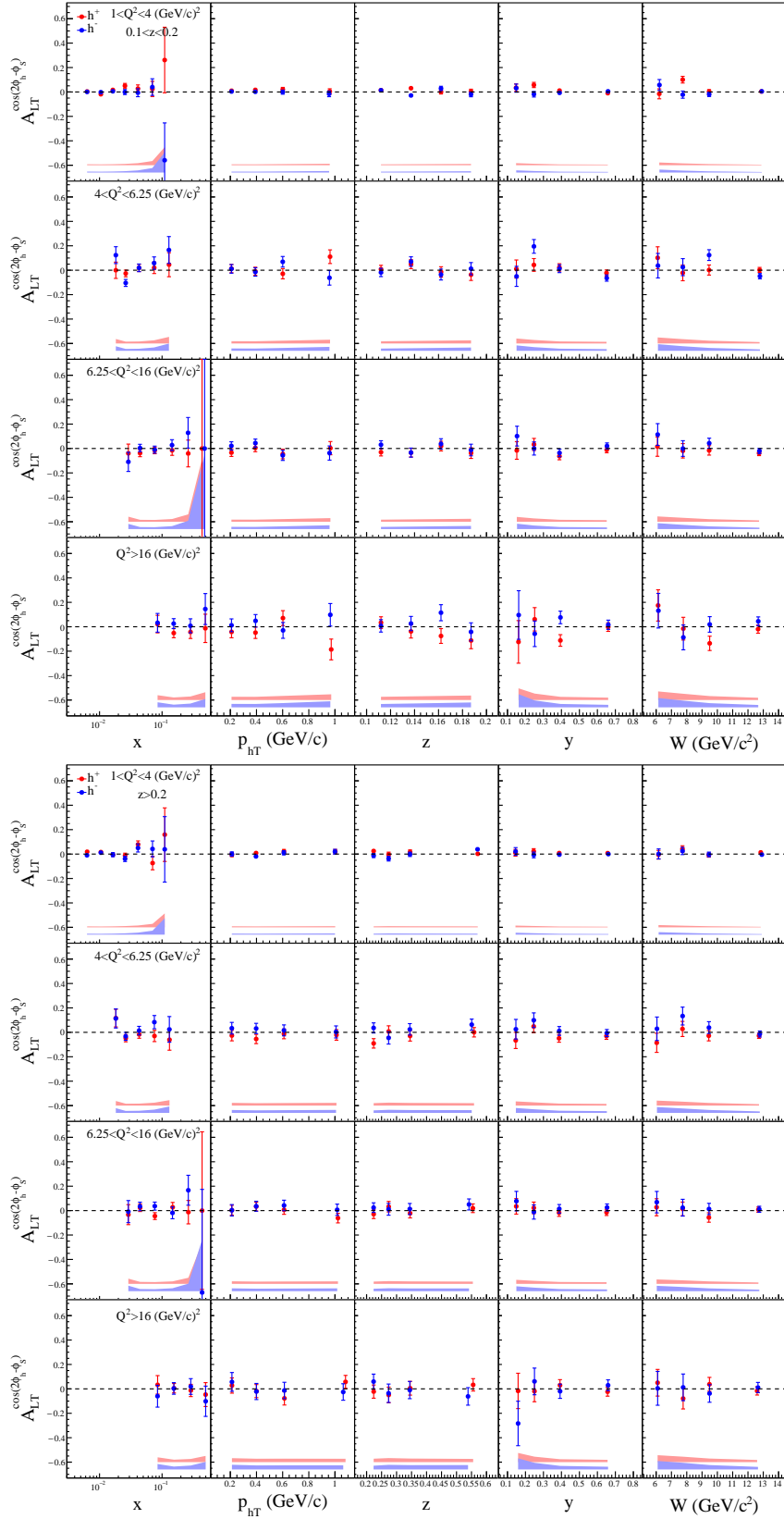


Figure 4.49: $A_{LT}^{\cos(2\phi_h - \phi_S)}$ asymmetry in bins of x , p_{T_h} , z , y , W and Q^2 , for the z ranges $0.1 < z < 0.2$ and $z > 0.2$. The results are divided by hadron charge; in red are results for positive hadrons and in blue for negative ones. The systematic error is presented as a band in the bottom of each plot.

The 2009 Drell-Yan Beam Test

The polarised DY measurement at COMPASS was considered a challenge since the spectrometer was developed for a very different physics process, the DIS process, and it was not optimized for DY. However the possibility to have a hadron beam, namely a pion beam, and a polarised proton target encouraged the measurement. The main change to be included in the spectrometer was a hadron absorber just downstream of the target, to suppress the flux of secondary particles produced in the interaction of the beam with the target. This is mandatory since the DY process has a very small cross-section. The inclusion of the absorber permits a high intensity beam without being overloaded with combinatorial background from uncorrelated pion and kaon decays into muons. This is also indispensable to protect detectors from high occupancies and possible radiation damage. In the center of the absorber, along the beam line, is a beam plug to stop the non-interacting beam in the target cells. For the DIS process the SAS spectrometer has a main role in the detection of the scattered muon, while for DY the large angle spectrometer is more important. In fact the DY geometrical acceptance is divided: around half of cases with the two muons in LAS acceptance and half of cases with one muon in LAS acceptance and the other in SAS acceptance. This implies the need for a very good performance of the detectors covering large angles. The vertex reconstruction is also a very delicate and important part in the whole reconstruction process. Since it was optimized for the DIS process, the algorithm needs now to be optimized for the DY case taking into account the amount of material in between the target and the tracking detectors. It is mandatory to have a good vertex resolution to be able to distinguish events coming from one or the other target cell, since the two cells have different polarisations, which cannot be wrongly addressed in the asymmetries extraction process.

5.1 Data Taking Conditions

The 2009 DY beam test was a three days long data taking period between 19 and 23 of November. The goal of this test was the feasibility study of the DY measurement with the COMPASS spectrometer including a hadron absorber prototype, to validate the J/ψ and DY event rates expected, to estimate the combinatorial background and to evaluate the vertex and dimuon mass resolutions.

A negative pion beam with 190 GeV/ c momentum was used, as proposed for the polarised DY data taking. This beam has the advantage that the DY process is dominated by the interaction of two valence quarks, the \bar{u} quark from the negative pion and the u quark from the proton, which is important since the TMD approach is valid in the valence phase space. The beam spot

at target region was around 0.3 cm, which is narrower than the beam used in the polarised case, with $\sigma_{x,y} \simeq 1$ cm. The larger beam spot was required by the target group to keep the target polarisation under control, otherwise the target could overheat locally, degrading the properties of the material and the polarisation.

The average beam intensity measured by the Ion Chamber 2 (not a COMPASS detector) was $8.33 \times 10^6 \pi^-/\text{s}$, except for two runs (82337 and 82338) that it was around twice higher, $1.56 \times 10^7 \pi^-/\text{s}$.

The target consisted in two cells of polyethylene ($(\text{C}_2\text{H}_4)_n$), two cylinders, 40 cm long each and with a diameter of 5 cm. The cells were separated by 20 cm. The target was centred at -183 cm, thus each cell being centred at -213 cm and -153 cm respectively. The total cells length corresponded to 0.65 pion interaction lengths and 1.59 radiation lengths.

The SM2 was moved 3 m downstream with respect to its DIS position, with a new z position of 2100 cm (as used in the 2009 hadron run). The detectors in between the RICH and the SM2 were also moved accordingly, except for the PS01 and GM04.

The hadron absorber was placed just downstream the target, between -113 cm and 87 cm. The 200 cm long absorber contains two blocks of material, 100 cm long each and with transverse dimensions $80 \times 80 \text{ cm}^2$. The upstream block was concrete and the downstream part non-magnetic stainless steel. The total length of the absorber was 6.7 pion interaction lengths and 66.2 radiation lengths.

The beam plug in the center of the absorber was made of 8 cylinders, 6 of tungsten and 2 of stainless steel, 20 cm long each and with increasing diameters, 2 cm, 2.5 cm, 3.4 cm, 4 cm, 5 cm, 5 cm, 6 cm and 7 cm. The first 40 cm of the central part of absorber was empty, the beam plug started at -73 cm. This beam plug has a length of 12.6 pion interaction lengths and 365.6 radiation lengths. It also works as a target, and the produced events there can also be used in the analysis of unpolarised DY data.

The trigger system was adapted to have two dedicated double triggers. The so called double 1 trigger was based on the coincidence of one single signal from the HCAL1 (any cluster with more than 0.7 MIP and none with more than 2.5 MIP) and one single signal from one of the SAS hodoscope systems (Middle, Outer and Ladder). The second double trigger, the so called double 2 was based on a double signal in HCAL1 (at least two clusters with more than 0.7 MIP each and none with more than 2.5 MIP). In addition there were also triggers based on just single signals.

5.2 Data Production

There were three productions of the 2009 data.

The first production revealed that the standard CORAL vertex reconstruction had very low efficiency, working only in around 50% of the cases. This was due to the presence of the absorber placed between the target and the tracking detectors that was not being correctly taken into account. This problem motivated a new production of the data.

The second production was done after tuning a set of reconstruction parameters in a small data sample. The major modification introduced in the reconstruction was the inclusion of the so called ROOT Geometry, which is used to describe the energy loss and the multiple scattering of the particles in matter, namely in the absorbers. This new method passes to CORAL as input the detailed description of the materials in the spectrometer as described in MC. CORAL uses a formula for the energy loss by ionization and also the radiative corrections taking into account the materials crossed by the particles during the reconstruction process. This allowed the removal of all the empirical factors used by CORAL to correct the particles energies. The

former method was based on the use of maps with the mean energy loss as function of the mean particles momentum. The disadvantage of this approach was that these maps were defined for limited regions and they had a limited granularity.

In general the CORAL standard options for vertexing were relaxed to accommodate for the presence of the hadron absorber. Some tracking parameters were adapted to optimize the reconstruction, namely in LAS, which is more important for the DY case.

From the second production a problem of hit-to-track association in the LAS reconstruction became evident, namely to correctly take into account MW1, an essential detector for the muons identification in LAS. This motivated new efforts to improve the reconstruction program, which originated the third production.

The analysis and results of the third production, as well as a reference to the improvements, are going to be presented in the following sections.

5.3 Event Selection

In total 51 runs were produced with run numbers between 82223 and 82350 inclusive, for a total of 4935 spills. The processed events were saved in mDSTs, 1.07×10^9 events in total. For the analysis only the events with at least one primary vertex and 2 outgoing charged particles were used. These events were selected and saved in microDSTs, 1.01×10^8 events in total, they correspond to around 9% of the processed events.

From this pre-selected sample the following selection criteria was applied:

1. Two opposite sign muons reconstructed in the spectrometer. The muons were selected by requiring more than 30 radiation lengths crossed between the first and the last measured points.
2. The trigger bit corresponding to one of the double triggers equal to 1.
3. The last measured point of each muon being downstream of the MuonFilter 1, $Z_{last} > 1750$ cm.
4. The first measured point of each muon being upstream of the SM1 magnet, $Z_{first} < 300$ cm.
5. Select a common vertex between the two particles within the polyethylene target region, and if more than one vertex select the one with the best χ^2 . The target region was selected requiring $-253 < Z_{vtx} < -113$ cm, 20 cm away from the cell limits, and $r_{vtx} < 1$ cm, position of the vertex in the transverse plane within a circumference with radius 1 cm and centered in (0,0). The distribution of the vertices within the cells region is shown in Fig. 5.1. The distribution of the vertices in the transverse plane is shown in Fig. 5.2, the beam was very narrow, with a spread of around 0.3 cm in x and even smaller in y , reason why the 1 cm cut was considered safe.
6. $p_{\mu^-} < 100$ GeV/ c , to reject muons from pion beam decays since the minimum possible energy for a muon decaying from a pion with 190 GeV/ c is around 106 GeV/ c . In Fig. 5.3 the distributions of the muons momentum before applying the selection of the $p_{\mu^-} < 100$ GeV/ c are shown, where it is visible a superposition of distribution for negative muons. Fig. 5.4 shows the distributions after applying the selection. It is evident that the momentum distributions of the negative and positive muons are asymmetric, this asymmetry is due to the fact that the SAS is charge asymmetric, and accepts mainly negative muons.

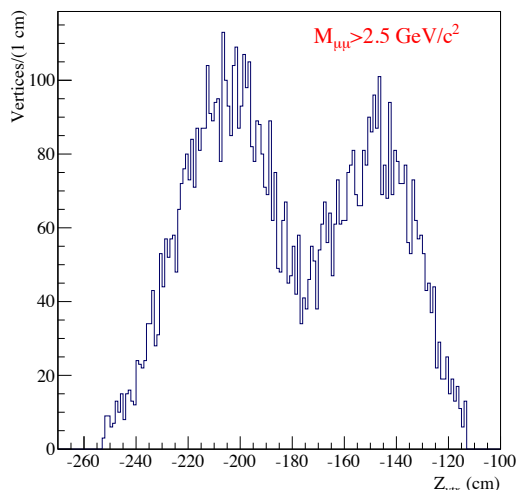
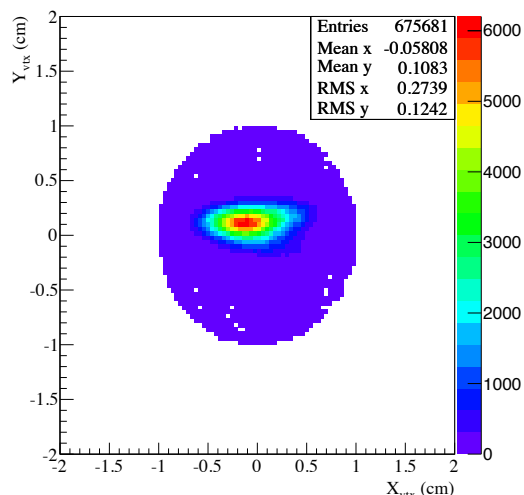
Figure 5.1: Z_{vtx} distribution.

Figure 5.2: Transverse position of the vertex.

The asymmetry of SAS is clear in Fig. 5.5, where only double 1 trigger events are included (LAS-SAS dimuons). On the other hand the symmetry of LAS is clear in Fig. 5.6 where dimuon 2 trigger events (LAS-LAS dimuons) are included.

7. Trigger validation, to ensure that the selected muons were the ones that fired the trigger.

- a) In case of double 1, which corresponds to one muon in HCAL1 and one muon in one of the SAS hodoscopes, one of the muons must have one associated cluster in the HCAL1 or at least 4 hits in the second part of the MW1 (i.e. at least half of the planes of MW1 after muon filter have hits associated to the track) and the other muon has to point to the SAS hodoscope pair having fired (i.e. its extrapolation to the z position of each hodoscope plane must be in its active area). In the case of the outer system the muon must have associated hits there. During this analysis it was discovered that the outer system had a very low efficiency. The cause was the downstream movement of their HO03 plane by 3 m and this was not properly considered in the trigger timing.
- b) In case of double 2, which corresponds to two muons in HCAL1, each muon must have an associated cluster in the calorimeter or at least 4 hits in the second part of MW1 associated to the track.

The impact of the cuts in terms of the number of pairs is visible in Table 5.1. From the pre-selected 101M events only around 6M have one opposite sign muon pair. The dimuon mass spectrum is shown in Fig. 5.7, where the cleaning effect of the cuts is evident.

5.4 Dimuon Mass Distribution

The dimuon mass distribution is produced using the selection criteria described before. As expected, due to the fact that the beam test had only the duration of three days, the number of high mass dimuons ($M_{\mu\mu} > 4 \text{ GeV}/c^2$) is negligible. Thus, the J/ψ resonance is used to take conclusions about the test performance.

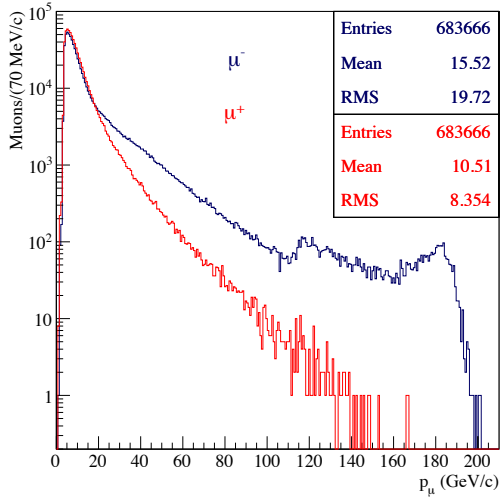


Figure 5.3: Momenta of muons before the selection of $p_{\mu^-} < 100$ GeV/c.

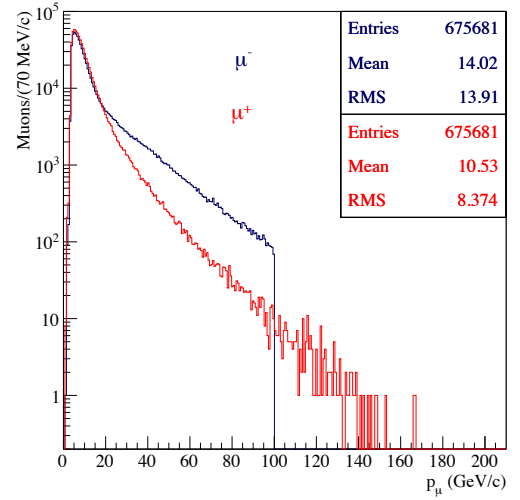


Figure 5.4: Momenta of muons after the selection of $p_{\mu^-} < 100$ GeV/c.

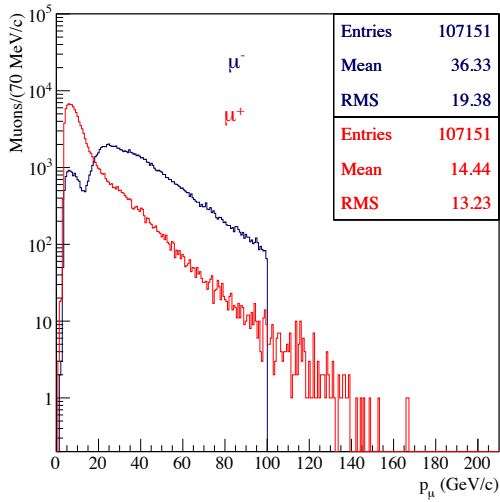


Figure 5.5: Momenta of muons before the selection of $p_{\mu^-} < 100$ GeV/c and selecting only events with double 1 trigger.

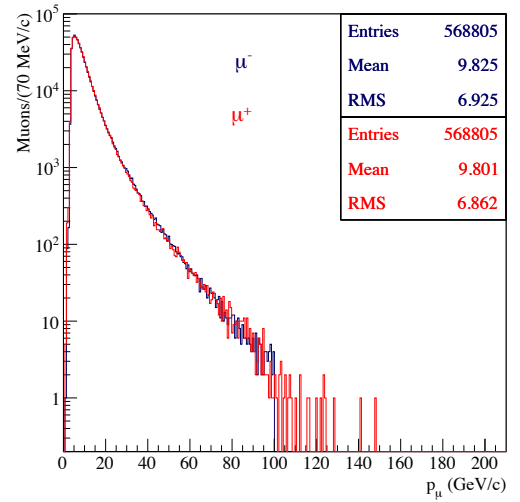


Figure 5.6: Momenta of muons before the selection of $p_{\mu^-} < 100$ GeV/c and selecting only events with double 2 trigger.

Cut		#pairs	statistics (%)
1.	$\mu^+\mu^-$ pair	6,488,143	100
2.	double trigger	3,268,797	50.4
3.	$Z_{last} > 1750$ cm	3,233,888	49.8
4.	$Z_{first} < 300$ cm	2,679,093	41.3
5.	$-253 < Z_{vtx} < -113$ cm & $r_{vtx} < 1$ cm	718,499	11.1
6.	$p_{\mu^-} < 100$ GeV/c	706,713	10.9
7.	trigger validation	675,681	10.4

Table 5.1: The impact of each selection criterion in the statistics.

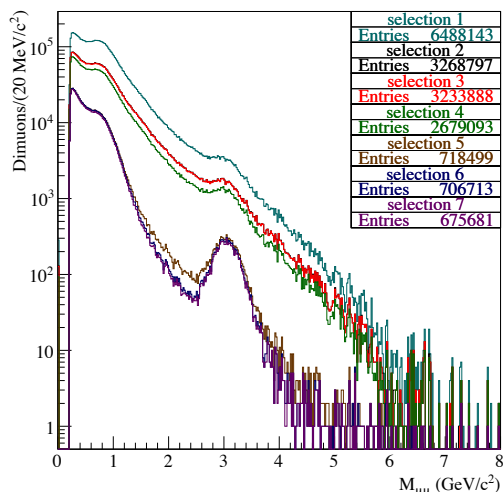


Figure 5.7: The impact of the selection criteria in the dimuon mass distribution.

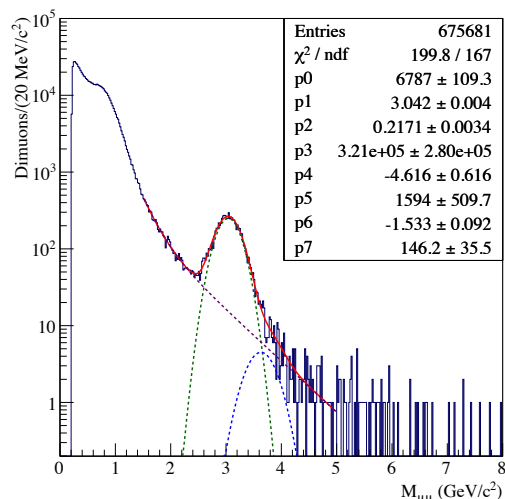


Figure 5.8: Dimuon mass distribution.

The dimuon mass distribution is shown in Fig. 5.8. The fit function used in the region from 1.5 to 5.0 GeV/c^2 is a sum of two Gaussians, one for the J/ψ resonance and the other for the ψ' resonance, and two exponentials to fit the continuum under the resonances,

$$f = \frac{\#J/\psi \times \text{bin width}}{\sqrt{2\pi}\sigma_{J/\psi}} \exp\left(-0.5 \left(\frac{x - M_{J/\psi}}{\sigma_{J/\psi}}\right)^2\right) + p_3 \exp(M_{\mu\mu}^{p_4}) + p_5 \exp(M_{\mu\mu}^{p_6}) + \frac{\#\psi' \times \text{bin width}}{\sqrt{2\pi}\sigma_{\psi'}} \exp\left(-0.5 \left(\frac{x - M_{\psi'}}{\sigma_{\psi'}}\right)^2\right) \quad (5.1)$$

the mass of ψ' and its width are constrained in the fit. The mass is forced by $M_{\psi'} = M_{J/\psi} + 0.589 \text{ GeV}/c$ (this factor corresponds to the difference between the mass of the two resonances in PDG) and the width by $\sigma_{\psi'} = \frac{\sigma_{J/\psi}}{M_{J/\psi}} M_{\psi'}$.

The number of J/ψ given by the fit is 6787 ± 109 , which compares with 3170 ± 70 J/ψ from the analysis of the first produced data, and with 6134 ± 91 J/ψ from the analysis of the second produced data. The increase in the number of J/ψ from the first to the second production is explained by the improvements implemented in the reconstruction program and also the enlargement of a cut on the mean time difference between the two muons. This cut was not useful because there is a large amount of tracks without a defined time. Applying it leads to a removal of 15% of dimuons and 40% of J/ψ . The tracks without time defined are the ones reconstructed in LAS, where in 2009 there is not any hodoscope involved in the tracking, and tracks associating hits only in drift based detectors have no mean time defined from the reconstruction. This problem is not present in the 2014/2015 data. The tracks with defined mean time have nevertheless a large uncertainty, of around 5 ns, and there is not enough precision for the time difference cut to be effective. The increase in the number of J/ψ from the second to the third production is mainly due to some improvements on the reconstruction of tracks in the region between SM1 and SM2, which can still be further improved. If there is no PID requirement the number of fitted J/ψ is 8488 ± 114 as it is shown in Fig. 5.9, which represents a PID efficiency of 80%, while from the second production the PID efficiency was 70%.

The J/ψ mass extracted from the fit is $3.042 \pm 0.004 \text{ GeV}/c^2$, which is $55 \text{ MeV}/c^2$ lower than the PDG mass value, $3.097 \text{ GeV}/c^2$. A similar mass shift is also present in MC. As it will be seen

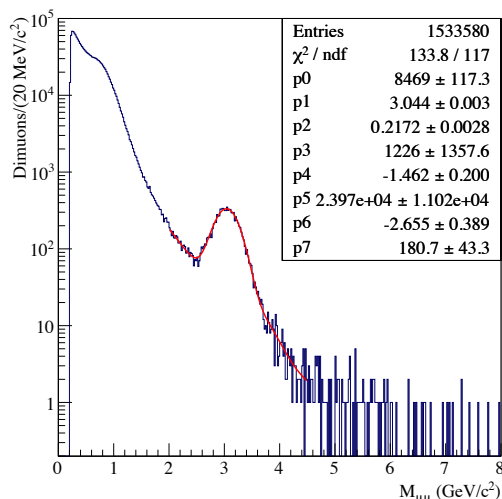


Figure 5.9: Dimuon mass distribution after the selection criteria but without PID requirement.

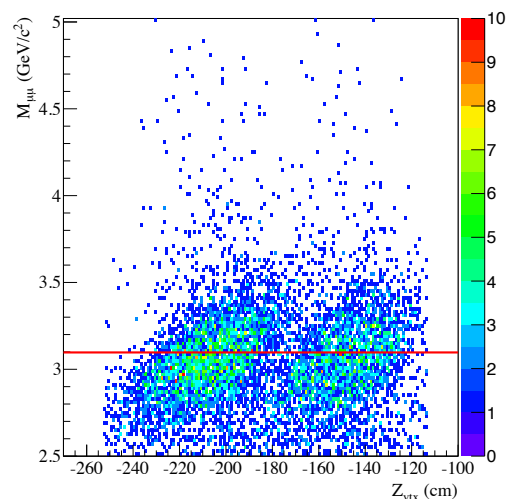


Figure 5.10: Dimuon mass distribution as a function of the Z_{vtx} position.

in Section 5.11, the reconstructed mass is systematically smaller than the true value. The J/ψ mass shift has a correlation with the Z_{vtx} position. In Fig. 5.10 the dimuon mass distribution is presented as a function of the Z_{vtx} position. The correlation between the mass and the Z_{vtx} position is similar for the upstream and the downstream cells separately. In red the value of the J/ψ mass from PDG is shown. The J/ψ mass increases along the Z_{vtx} within each individual cell.

The J/ψ mass resolution is $217 \pm 3 \text{ MeV}/c^2$, which is compatible with the expectations from MC.

The number of ψ' is 146 ± 36 with the constraint on its mass value and mass resolution.

The continuum under the J/ψ peak includes three contributions: the contribution from the Drell-Yan process, the combinatorial background and the open charm background. The ratio of the J/ψ signal over the continuum is 9.8 ± 0.4 in the range from 2.7 to 3.5 GeV/c^2 .

5.5 Distribution of Events by Trigger

In Figures 5.11 to 5.13 the dimuon mass distributions for each individual trigger of the double 1 trigger are presented. These distributions were fitted with a Gaussian function plus two exponential functions, the ψ' was not considered for the fit due to the low statistics. Fig. 5.14 shows the dimuon mass distribution selecting double 1 trigger. The fit function used in this case is the same as in Eq. 5.1. In Fig. 5.15 is shown the dimuon mass distribution selecting double 2 trigger and the same fit function as in Eq. 5.1. These mass distributions were produced selecting the inclusive triggers, that means requesting that the corresponding trigger fired irrespective of the other possible triggers.

The total number of pairs per trigger and the J/ψ parameters from the fits are summarized in Table 5.2. The distribution of J/ψ per trigger is $\sim 13\%$ with one muon in LAS and one muon in SAS and $\sim 88\%$ with two muon in LAS. These percentages were not expected, pointing to some problem in the trigger. The double 1 and double 2 triggers have a small overlap of 0.9%. The distribution of J/ψ per trigger in case of the double 1 is $\sim 39\%$ in middle, $\sim 29\%$ in ladder and $\sim 36\%$ in outer. These three triggers being part of the double 1 have a small overlap of 4%.

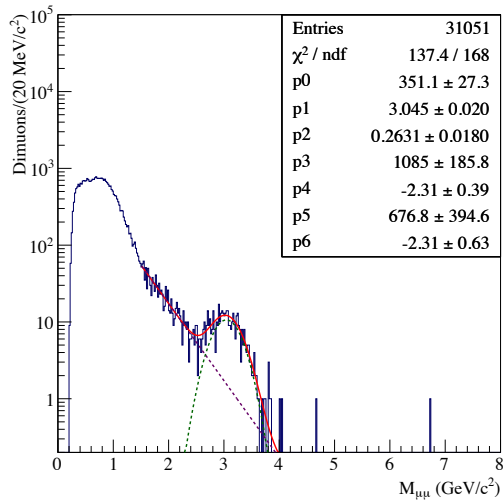


Figure 5.11: Trigger double 1, one muon in HCAL1 and one muon in Middle.

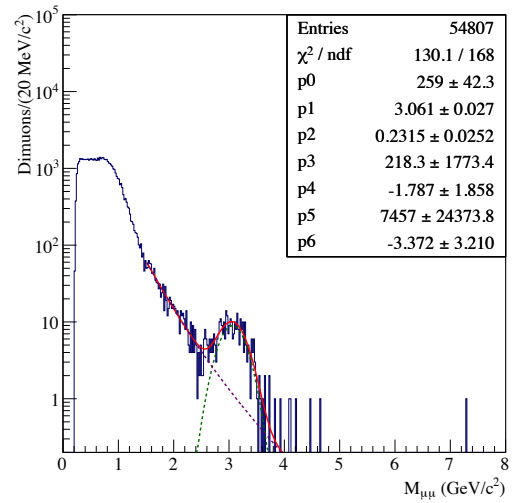


Figure 5.12: Trigger double 1, one muon in HCAL1 and one muon in Ladder.

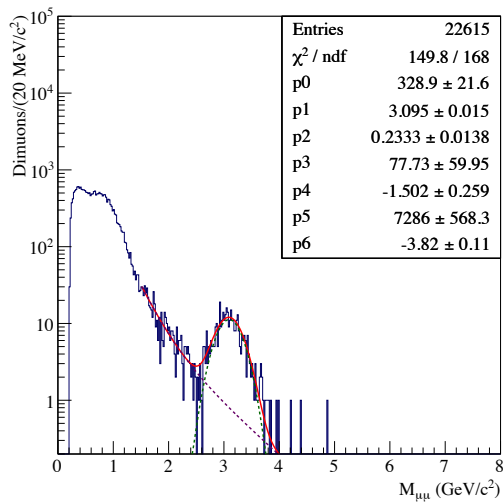


Figure 5.13: Trigger double 1, one muon in HCAL1 and one muon in Outer.

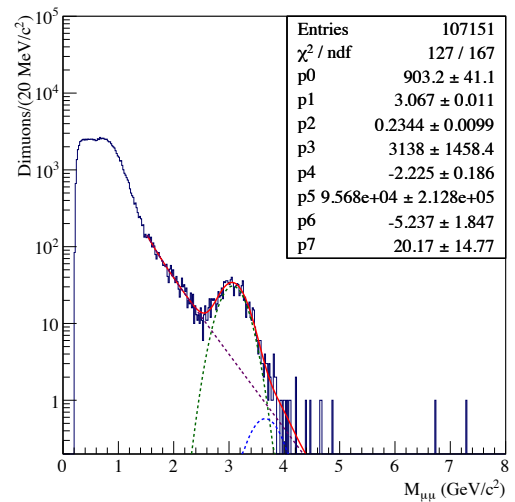


Figure 5.14: Trigger double 1, one muon in HCAL1 and one muon in one SAS hodoscope system.

Trigger	#events	# J/ψ	$M_{J/\psi}$ (GeV/ c^2)	$\sigma_{J/\psi}$ (MeV/ c^2)
1 μ HCAL1 + 1 μ middle	31051	351 \pm 27	3.045 \pm 0.020	263.1 \pm 18.0
1 μ HCAL1 + 1 μ ladder	54807	259 \pm 42	3.061 \pm 0.027	231.5 \pm 25.2
1 μ HCAL1 + 1 μ outer	22615	329 \pm 22	3.095 \pm 0.015	233.3 \pm 13.8
Double_1: 1 μ HCAL1 + 1 μ hodoscope	107151	903 \pm 41	3.067 \pm 0.011	234.4 \pm 9.9
Double_2: 2 μ HCAL1	568805	5945 \pm 97	3.038 \pm 0.004	216.0 \pm 3.0
Double_1 Double_2	675681	6787 \pm 109	3.042 \pm 0.004	217.1 \pm 3.4

Table 5.2: Statistics divided by trigger.

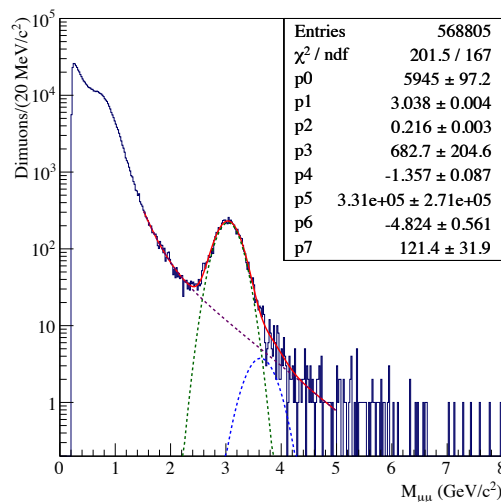


Figure 5.15: Trigger double 2, two muons in HCAL1.

5.6 Trigger Purity

To estimate the trigger purity a simple test was done. For one single run the number of events with double 1 trigger was counted as well as the number of events with double 2 trigger: 12720 and 604647 events, respectively. From these the ones having a dimuon with both muons identified, assigning the validity criteria $Z_{first} < 300$ cm, $Z_{last} > 1750$ cm and satisfying the trigger validation are 1159 for double 1 and 11561 for double 2. This corresponds to a trigger purity of $\sim 9.1\%$ for double 1 and $\sim 1.9\%$ for double 2. Both triggers have a very low purity, nevertheless the trigger based only in the calorimeter is less selective than the trigger based on calorimeter and hodoscopes.

5.7 Double Triggers Efficiency

The trigger efficiency is extracted taking into account a reference sample. In this data taking there was not an independent dedicated trigger for this purpose, so the best to be considered is the beam trigger as a sort of “minimum bias” trigger. The goal is to verify from the pairs which were in the good condition to give trigger and the ones that actually fired it. So, the events with the beam trigger obeying the quality criteria in Table 5.1, except the trigger selection, were selected. Additionally it was required that the events are in the good conditions to give the corresponding trigger, the so called trigger validation. This constitutes the reference in the denominator. The numerator is the subsample of these events which actually fired the trigger. The results are shown in Table 5.3.

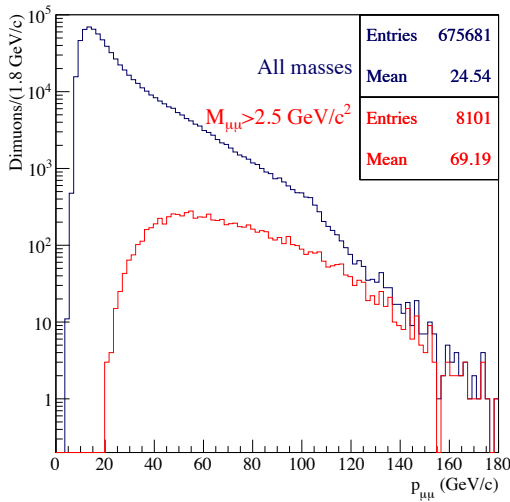
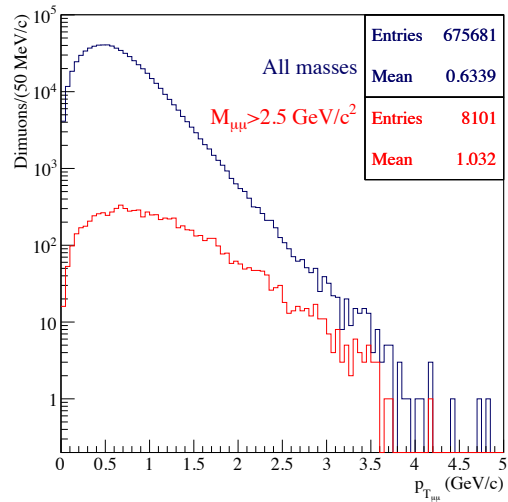
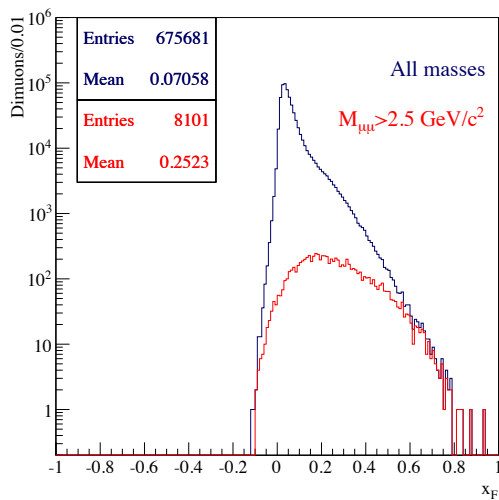
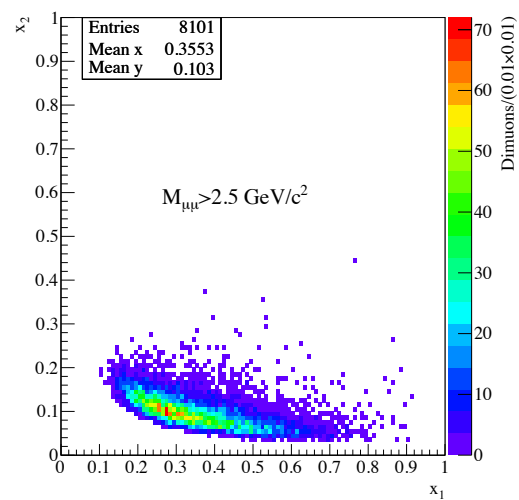
$$\text{Trigger eff.} = \frac{\text{beam trigger \& selection criteria \& trigger validation \& trigger bit on}}{\text{beam trigger \& selection criteria \& trigger validation}} \quad (5.2)$$

5.8 Kinematic Distributions

In figures 5.16 to 5.22 several kinematic distributions are shown. Fig. 5.16 shows the dimuon momentum distribution for all masses and also for masses larger than $2.5 \text{ GeV}/c^2$, the region

Trigger	Denominator Eq. 5.2	Numerator Eq. 5.2	Efficiency (%)
1μ HCAL1 + 1μ middle	287 ± 17	98 ± 10	34.2 ± 2.8
1μ HCAL1 + 1μ ladder	228 ± 15	115 ± 11	50.4 ± 3.3
1μ HCAL1 + 1μ outer	521 ± 23	43 ± 7	8.3 ± 1.2
Double_1: 1μ HCAL1 + 1μ hodoscope	973 ± 31	252 ± 16	25.9 ± 1.4
Double_2: 2μ HCAL1	2714 ± 52	1482 ± 39	54.6 ± 1.0
Double_1 Double_2	3685 ± 61	1734 ± 42	47.1 ± 0.8

Table 5.3: Triggers efficiency.


 Figure 5.16: Dimuon momentum distribution for all masses (in blue) and for $M_{\mu\mu} > 2.5 \text{ GeV}/c^2$ (in red).

 Figure 5.17: Dimuon transverse momentum distribution for all masses (in blue) and for $M_{\mu\mu} > 2.5 \text{ GeV}/c^2$ (in red).

 Figure 5.18: x_F distribution for all masses (in blue) and for $M_{\mu\mu} > 2.5 \text{ GeV}/c^2$ (in red).

 Figure 5.19: x_2 versus x_1 distribution for $M_{\mu\mu} > 2.5 \text{ GeV}/c^2$.

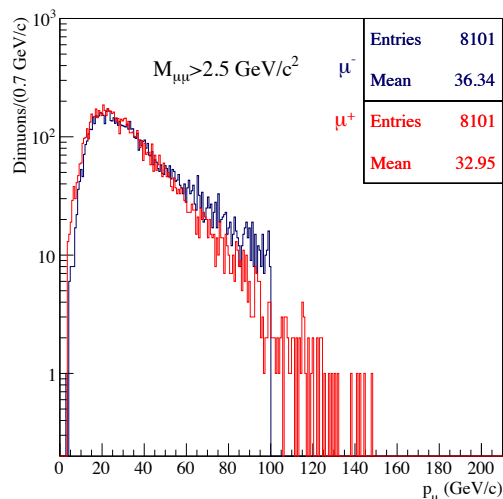


Figure 5.20: Momentum distribution of each muon for $M_{\mu\mu} > 2.5 \text{ GeV}/c^2$ and double trigger.

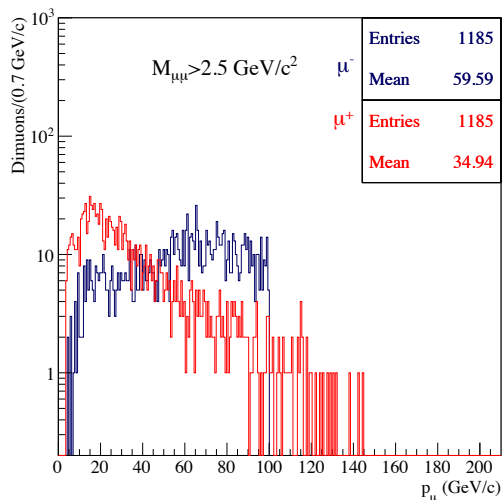


Figure 5.21: Momentum distribution of each muon for $M_{\mu\mu} > 2.5 \text{ GeV}/c^2$ and double 1 trigger.

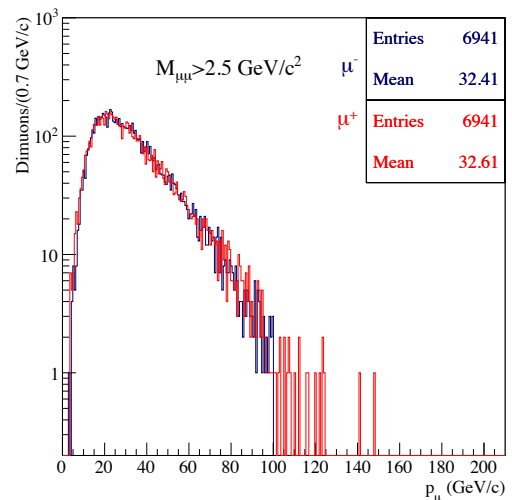


Figure 5.22: Momentum distribution of each muon for $M_{\mu\mu} > 2.5 \text{ GeV}/c^2$ and double 2 trigger.

mainly dominated by the J/ψ and DY dimuons. In Fig. 5.17 is the dimuon transverse momentum distribution, which is expected to be around $1 \text{ GeV}/c$ for DY high mass dimuons. Indeed, for $M_{\mu\mu} > 2.5 \text{ GeV}/c^2$ it is also $\langle p_T \rangle \sim 1 \text{ GeV}/c$. The Feynman x distribution is in Fig. 5.18, defined as the difference between x_1 , the momentum fraction from beam parton, and x_2 , the momentum fraction from target parton. COMPASS being a fixed target experiment x_F is mainly positive, and for high masses ($M_{\mu\mu} > 2.5 \text{ GeV}/c^2$) the mean value is around 0.25. In Fig. 5.19 is the phase space coverage, x_2 versus x_1 ; for masses larger than $2.5 \text{ GeV}/c^2$ the valence regions of pion beam and target nucleon ($x > 0.05$) dominate.

In Fig. 5.20 the momentum distributions of each muon for masses larger than $2.5 \text{ GeV}/c^2$ are shown. Comparing these distributions with the distributions from Fig. 5.4, one sees that also for high mass events the two muon distributions are asymmetric, the mean values being apart by $\sim 3.4 \text{ GeV}/c$, this asymmetry coming from events with one muon in LAS and one in SAS as in Fig. 5.21, which are around 15% of the cases. For the events with the two muons in

LAS the distributions are quite symmetric, see Fig. 5.22.

5.9 Contributions for the Measured J/ψ Yields

The expected number of J/ψ is

$$\#J/\psi = \mathcal{L} B_{\mu\mu} \sigma_{\pi p \rightarrow J/\psi} A_{eff}^\alpha d_{spill} n_{spill} \Omega \varepsilon_{rec} \varepsilon_{trigger} \varepsilon_{SPS} \varepsilon_{spectrometer} \quad (5.3)$$

as used in the Proposal [104], where the luminosity \mathcal{L} is

$$\mathcal{L} = L_{eff} \frac{\rho N_A}{A_{eff}} I_{beam} \quad . \quad (5.4)$$

Considering the flux

$$Flux = I_{beam} d_{spill} n_{spill} \varepsilon_{SPS} \varepsilon_{spectrometer} \quad (5.5)$$

the number of J/ψ can be written as

$$\#J/\psi = L_{eff} \frac{\rho N_A}{A_{eff}} A_{eff}^\alpha B_{\mu\mu} \sigma_{\pi p \rightarrow J/\psi} Flux \Omega \varepsilon_{rec} \varepsilon_{trigger} \quad . \quad (5.6)$$

The following values are considered:

- $B_{J/\psi \rightarrow \mu\mu} \sigma_{\pi p \rightarrow J/\psi} = 6.3 \pm 0.8$ nb/proton, as obtained from NA3 experiment using incident negative pions at 200 GeV/c on a H₂ target [120];
- $\alpha = 0.925 \pm 0.009$, to take into account the J/ψ absorption in nuclear matter, as measured by the NA50 experiment [121];
- Two polyethylene target cells : $L_{eff} = 58$ cm, $\rho = 0.95$ g/cm³, $A_{eff} = 10.4$ g/mol;
- $Flux = 3.69311135 \times 10^{11}$ (from PHAST dedicated function method #2) considering the runs with double 1 (all the runs) and $Flux = 2.83054820 \times 10^{11}$ for double 2 because it was not present in all the runs.

and the acceptances, as extracted from the J/ψ MC:

- For one μ in LAS and the other in SAS (double_1) $\rightarrow \Omega = 19.5 \pm 0.2$ %;
- For both muons accepted in LAS (double_2) $\rightarrow \Omega = 22.7 \pm 0.2$ %.

At the end, the only remaining factors are the efficiencies, namely the reconstruction efficiency and the trigger efficiency:

$$\text{Double trigger: } \#J/\psi = (23906 \pm 2159) \varepsilon_{rec} \varepsilon_{trigger} \quad (5.7)$$

The dimuons reconstruction efficiency was obtained from MC and it is 79.4 ± 0.4 % (using the same quality cuts as in the data analysis). The trigger efficiency was obtained using the data as it is explained in the section 5.7 and it is 47.1 ± 0.8 %.

Using these efficiencies the expected number of J/ψ is 8932 ± 1063 , which is higher than the obtained 6787 ± 109 , they differ by around two sigma. This difference can be attributed to some factors in this estimation, namely the flux estimation and the efficiencies. The flux should be calculated by a dedicated analysis using the scalers information, which was considered very sophisticated for this purpose. The reconstruction efficiency was estimated based on the MC with basically only pure J/ψ events, being the detectors occupancies lower than in reality, which simplifies the reconstruction when compared to real data. The trigger efficiency was estimated using the beam trigger and not a dedicated random trigger, which can also introduce a bias in the estimations.

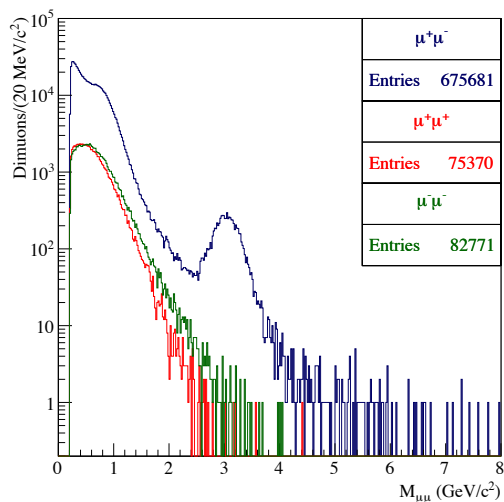


Figure 5.23: Mass distributions. The lines with blue, red, and green colours represent the opposite sign muon pairs, the positive like-sign and the negative like-sign pairs, respectively.

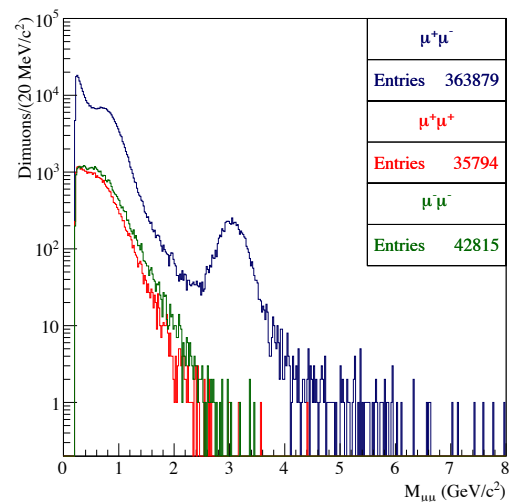


Figure 5.24: Mass distributions after applying the image cut. The lines with blue, red, and green colours represent the opposite sign muon pairs, the positive like-sign and the negative like-sign pairs, respectively.

5.10 Combinatorial Background Studies

The combinatorial background is originated from uncorrelated muon pairs from pion and kaon decays. Its evaluation can be done using the muon like-sign pairs. Thus, the uncorrelated opposite sign pairs can be statistically evaluated using the following relation

$$N_{\mu^+\mu^-}^{Bg} = 2\sqrt{N_{\mu^+\mu^+}N_{\mu^-\mu^-}} \quad . \quad (5.8)$$

For more details see Appendix A.

This relation is only correct if the sample is totally charge-symmetric, i.e. the μ^+ and μ^- acceptances have to be equal.

One of the methods to obtain a charge symmetric sample is called the “image cut method”. It consists in checking if each muon from the dimuon would also be geometrically accepted if it had an opposite charge. If at least one of the muons does not obey the condition, the pair is rejected.

The opposite-sign dimuon mass distribution as well as the like-sign pairs distributions are shown in Fig. 5.23. After the image cut procedure is applied to these samples they result in the distributions presented in Fig. 5.24. From these distributions the statistical impact of the image cut is evaluated, the remaining statistics of opposite sign pairs is $53.9 \pm 0.1\%$, being $47.5 \pm 0.3\%$ for positive like-sign pairs and $51.7 \pm 0.3\%$ for negative like-sign pairs. The statistics reduces by almost a factor 2.

The combinatorial background is evaluated after the application of the image cut, which is plotted in Fig. 5.25 together with the dimuon mass distribution. The combinatorial background error is

$$\delta N_{\mu^+\mu^-}^{Bg} = \sqrt{N_{\mu^+\mu^+} + N_{\mu^-\mu^-}} \quad . \quad (5.9)$$

The number of J/ψ decreases from 6787 ± 109 to 5728 ± 89 , which means that the image cut leads to a loss of $\sim 15\%$ of J/ψ . This loss is dominated by the fact that the SAS trigger system

was not symmetric at that time. In 2014 and 2015 runs a more symmetric trigger is used. The combinatorial background in the region of the J/ψ signal is negligible. In the region from 2.7 to 3.5 GeV/c^2 the contamination from the background is only 0.2%.

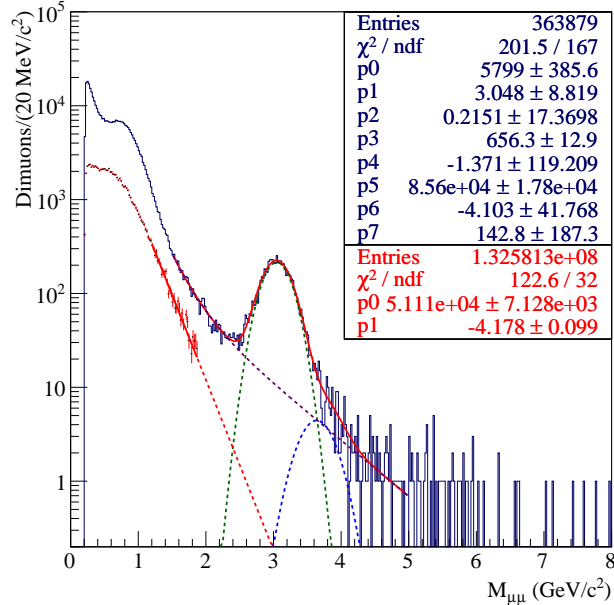


Figure 5.25: In blue is the dimuon mass distribution after the image cut. In red is the combinatorial background calculated after the image cut procedure and using the like-sign pairs.

5.11 J/ψ Monte-Carlo

A MC simulation was used to study the J/ψ production in the 2009 beam test conditions. The J/ψ production from $\pi^- p/n$ collisions was obtained from PYTHIA generator version 6.4 [122], considering the process $f + \bar{f} \rightarrow \gamma^*/Z^0$ (MSEL 11, which calls MSUB 1), and setting $\gamma^* \rightarrow c\bar{c}$ as the only conversion allowed. Feed-down of J/ψ from χ_c family was also set. J/ψ was allowed only to decay to a muon pair. Initial and final state radiation is allowed (to provide the necessary gluon for the $c\bar{c}g$ state, prior to J/ψ formation, required by the quantum numbers conservation). Charm mass was set to $1.275 \text{ GeV}/c^2$ (according to the PDG value). The events were then processed by COMGEANT, taking into account the 2009 geometry with a beam $\sigma_{x,y} = 3 \text{ mm}$ and momentum $190 \text{ GeV}/c$. The internal COMGEANT pileup was simulated obeying to a 3 mm sigma Gaussian distribution and with an intensity of $8.3 \times 10^6 \pi^-/\text{s}$ in a time window of 100 ns. The reconstruction of these events was done in CORAL using the same conditions as in the production of real data. The results are presented in the next subsections.

5.11.1 Geometrical Acceptance

The number of generated events was 100000, corresponding to 100053 $\mu^+\mu^-$ pairs at the end. From those, 38415 were accepted in LAS&LAS or in LAS&SAS, which means that both muons have a minimum number of hits in the second part of MW1 (at least 4 hits, corresponding to

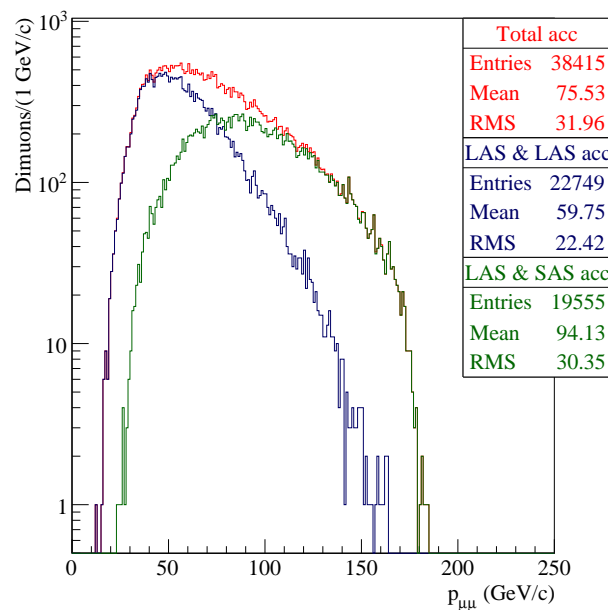


Figure 5.26: The accepted dimuon momentum distributions per zone (MC truth). In red are the accepted dimuons regardless of the zone, in blue are the dimuons accepted in LAS (2 μ in LAS) and in green the dimuons accepted in LAS & SAS (one μ in each spectrometer).

Zone	Geo. Acc. (%)
All	38.4 ± 0.2
LAS & LAS	22.7 ± 0.2
LAS & SAS	19.5 ± 0.2

Table 5.4: Geometrical acceptance.

at least half of the planes of the detector) or one of the muons is detected in one of the SAS hodoscopes pairs (Outer, Middle or Ladder systems). Fig. 5.26 shows the reconstructed dimuon momentum distributions per zone. The geometrical acceptance per zone is in Table 5.4.

5.11.2 Reconstruction Efficiency

The reconstruction efficiency was calculated using the generated events in the acceptance and the sub-sample of those that could be reconstructed (requiring the same minimum number of hits in detectors for the reconstructed tracks, as explained in section 5.11.1, and also requiring that the reconstructed vertex is inside the cells ± 20 cm). These sub-samples are shown in Fig. 5.27. The reconstruction efficiency per zone is in Table 5.5.

5.11.3 Z Vertex Resolution and Cells Contamination

The resolutions are calculated, in an event-by-event basis, from the difference between the reconstructed and the generated values. In the 2009 DY run, the Z vertex resolution is about 14 cm, cf. Fig. 5.28. As expected it is worse for the upstream cell (15 cm), cf. 5.30, than for

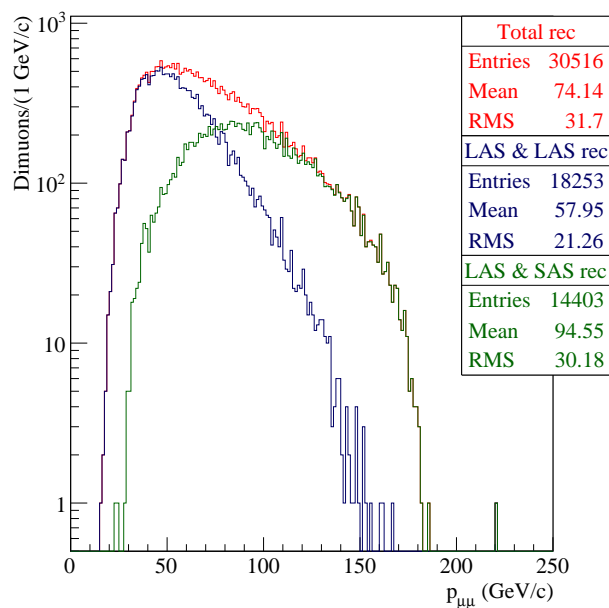


Figure 5.27: The reconstructed MC dimuon momentum distributions per zone. In red are the reconstructed dimuons associated to the accepted ones regardless of the zone, in blue are the reconstructed dimuons associated to the accepted ones in LAS (2 μ in LAS), in green the reconstructed dimuons accepted in LAS & SAS (one μ in each spectrometer).

Zone	Rec. Eff. (%)
All	79.4 ± 0.4
LAS & LAS	80.2 ± 0.5
LAS & SAS	73.7 ± 0.5

Table 5.5: Reconstruction efficiency.

the downstream one (12 cm), cf. Fig. 5.30. The separation between cells is 20 cm, which means that, due to this resolution, cells contamination is not negligible (events generated in one cell and badly reconstructed in the other one). This is shown in Fig. 5.29. The number of events reconstructed strictly inside the upstream cell corresponds to $54.4 \pm 0.7\%$ of the ones which actually belong there, and from these $1.9 \pm 0.1\%$ were generated in the downstream cell. The number of events reconstructed inside the downstream cell corresponds to $64.0 \pm 0.9\%$ of the ones which actually belong there, and from these $5.1 \pm 0.2\%$ were generated in upstream cell.

5.11.4 Mass and Momentum Resolutions

The mass resolution is shown in Fig. 5.32. The RMS of the distribution is $250 \text{ MeV}/c^2$, while the sigma obtained from the fit is $229 \pm 1 \text{ MeV}/c^2$, which is closer to the J/ψ mass resolution of $217 \pm 3 \text{ MeV}/c^2$ obtained from data (from Fig. 5.8). A shift of $42 \text{ MeV}/c^2$ in the reconstructed mass is present. In the data the J/ψ mass shift is also present, it is $55 \text{ MeV}/c^2$ in the same direction.

Fig. 5.33 shows the dimuon transverse momentum resolution, which is $139 \text{ MeV}/c$. The momentum resolution of the negative muons is shown in Fig. 5.34, for positive muons is in

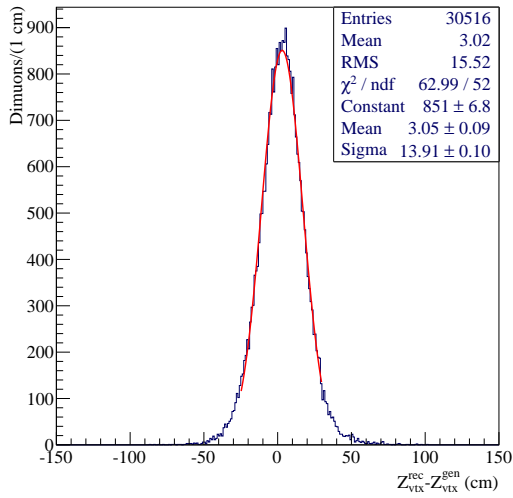


Figure 5.28: Z vertex resolution.

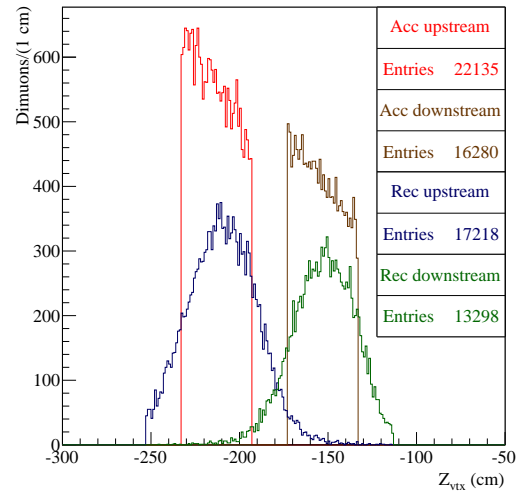


Figure 5.29: Z vertex distributions of the accepted events in red; the reconstructed events generated in the upstream cell are in blue and the reconstructed ones generated in the downstream cell in green.

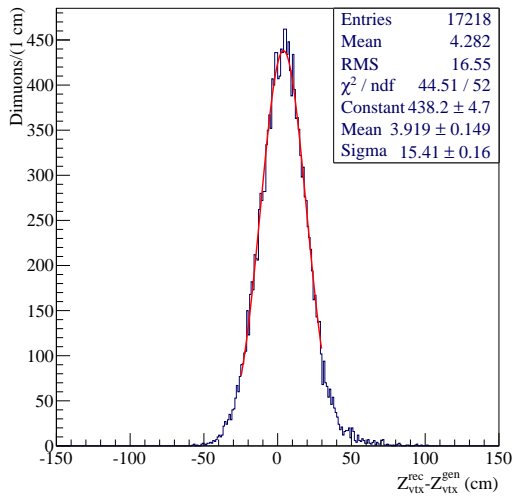


Figure 5.30: Z vertex resolution for the upstream cell.

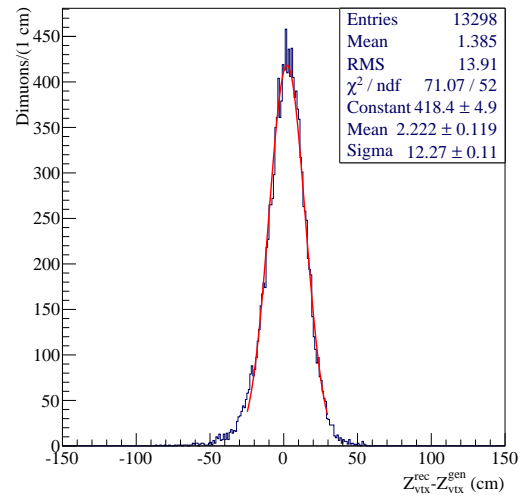


Figure 5.31: Z vertex resolution for the downstream cell.

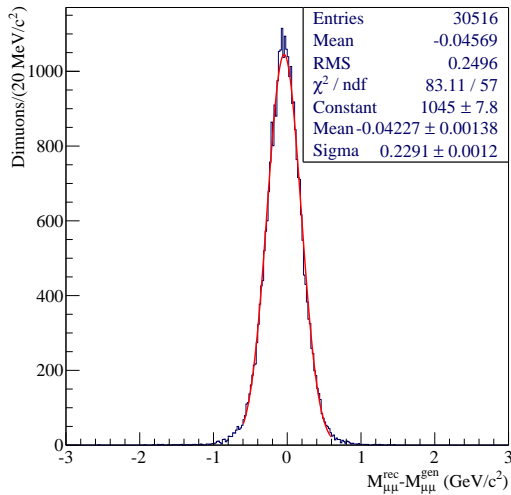


Figure 5.32: Mass resolution.

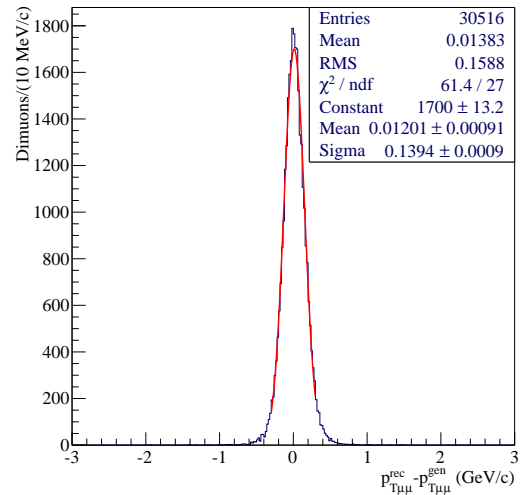


Figure 5.33: Dimuon transverse momentum resolution.

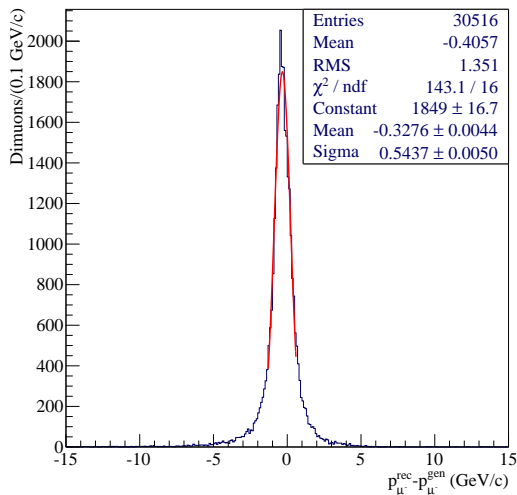


Figure 5.34: Momentum resolution of negative muons.

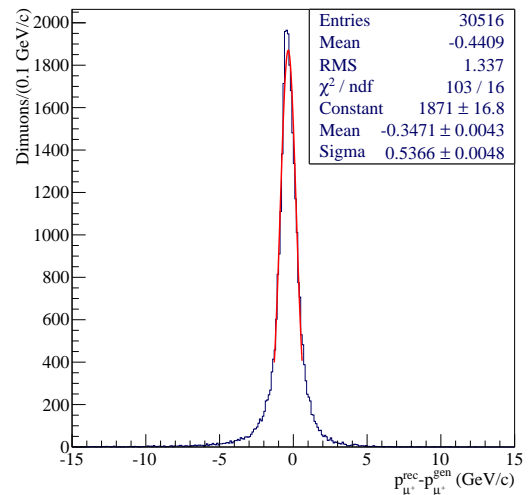


Figure 5.35: Momentum resolution of positive muons.

Fig. 5.35. The RMS of the distributions is around 1.4 GeV/c for both muons. Both show a momentum bias, by more than 300 MeV/c, meaning probably that the energy loss in the extrapolation through the hadron absorber was over-estimated.

5.11.5 Kinematic Distributions

For the selection of the reconstructed muon pairs the following criteria are used:

1. $p_{\mu^-} < 100 \text{ GeV}/c$
2. $-253 < Z_{vtx} < -113 \text{ cm}$
3. $r_{vtx} < 1 \text{ cm}$

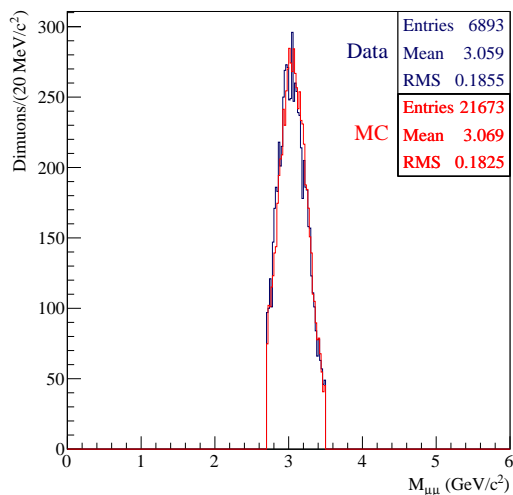


Figure 5.36: Comparison of dimuon masses between data and MC.

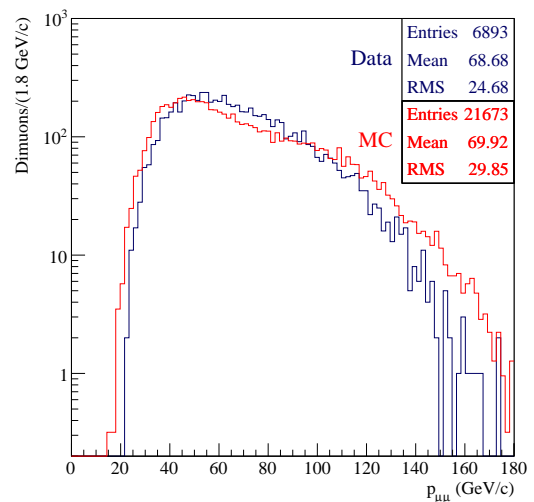


Figure 5.37: Comparison of dimuon momentum between data and MC.

4. $Z_{last} > 1750$ cm for each muon
5. $Z_{first} < 300$ cm for each muon
6. > 4 hits in MA01 for both muons or > 4 hits in MA01 for one muon and hits in one of the SAS hodoscope systems for the other

Since the MC only includes the J/ψ and the beam pileup simulation, to do the comparison between MC and data the mass region from 2.7 to 3.5 GeV/c^2 is selected in both cases. In Fig. 5.36 the dimuon mass distributions are compared and they look similar. This comparison between MC and data was done to see if there was no major differences. The MC was not carefully tuned to match perfectly the data. For the future DY analysis it is mandatory to tune the MC in accordance with the data. One of the major differences is the dimuon trigger, present in data, but not simulated in the MC. Nevertheless, some kinematic distributions are compared between the data and the MC and in fact the comparison is reasonable.

The MC dimuon momentum distribution is in Fig. 5.37, the mean dimuon momentum is 69.9 GeV/c , while for data is 68.7 GeV/c . So it is a bit higher for the MC.

The dimuon transverse momentum distribution is in Fig. 5.38, the mean dimuon transverse momentum is 1.03 GeV/c for data and slightly higher for MC, 1.06 GeV/c .

The x_F distribution is in Fig. 5.39, the mean x_F is 0.25 which compares with 0.25 for MC but, nevertheless, the distributions are different.

The x_2 versus x_1 distribution is in Fig. 5.40 for data, it is similar to the same MC distribution shown in Fig. 5.41.

The momentum distribution for negative muons is in Fig. 5.42, the mean momentum for μ^- is 35.98 GeV/c in data and 33.85 GeV/c in MC. In Fig. 5.43 is the momentum distribution for positive muons, the mean value is 32.77 GeV/c in data and 36.15 GeV/c in MC. In MC there are positive muons with higher momenta, these muons are mainly the ones being accepted with outer trigger hodoscope, which is very inefficient in data. If the outer hodoscope is rejected, from both data and MC, the distributions mean value still differ by more than 2 GeV/c in the case of the negative muon as seen in Fig. 5.44. Here the data sample may have some contamination arising from the decays of pions. In the case of the positive muons the distributions get closer, as seen in Fig. 5.45.

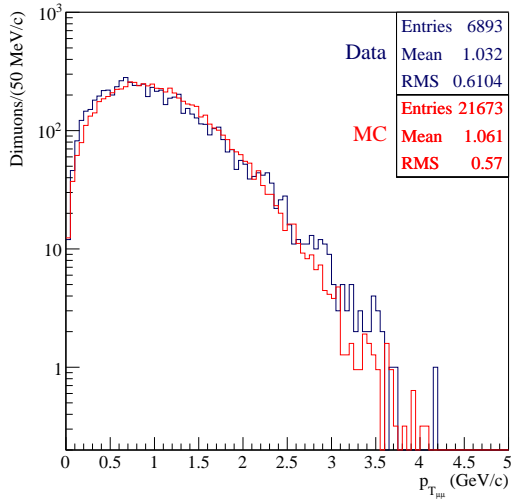


Figure 5.38: Comparison of dimuon transverse momentum distributions between data and MC.

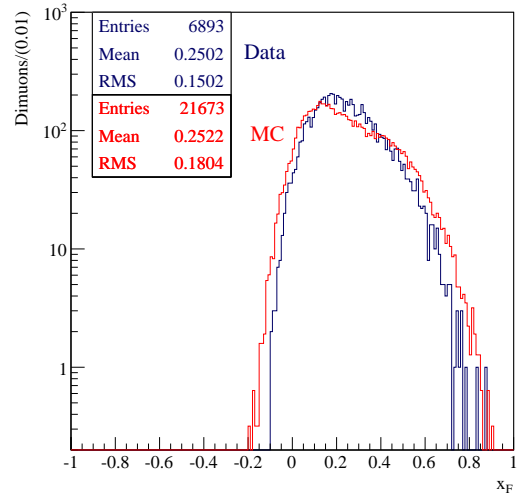


Figure 5.39: Comparison of x_F distributions between data and MC.

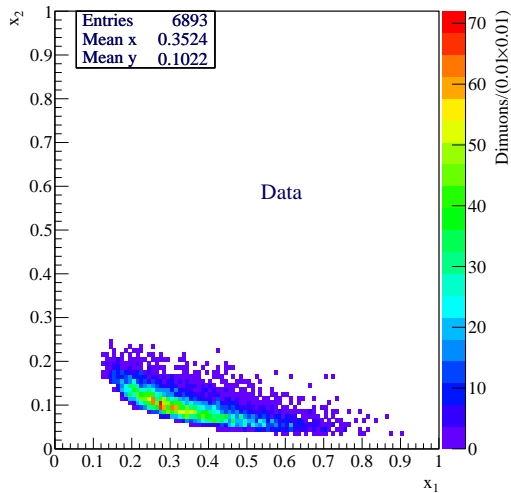


Figure 5.40: x_2 versus x_1 distribution for data.

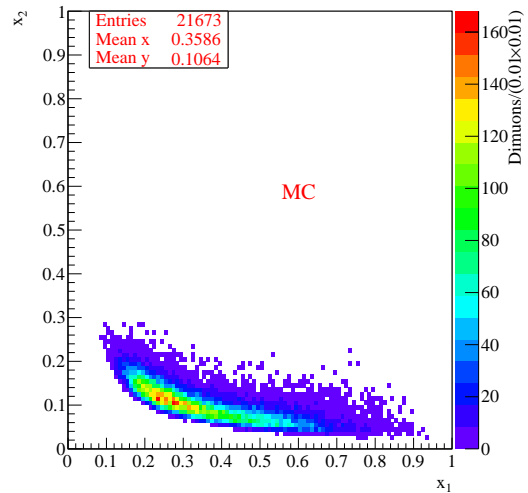


Figure 5.41: x_2 versus x_1 distribution for MC.

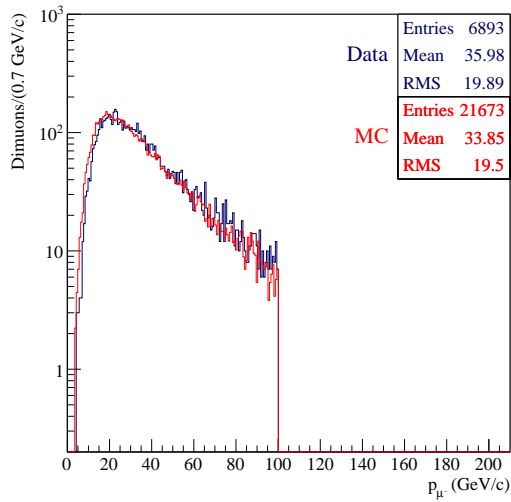


Figure 5.42: Comparison of negative muons momentum distributions between data and MC.

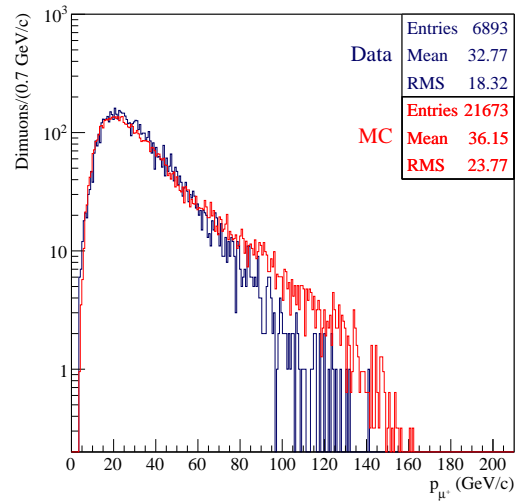


Figure 5.43: Comparison of positive muons momentum distributions between data and MC.

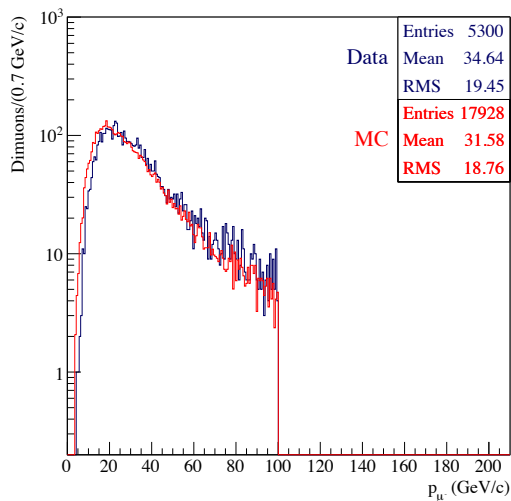


Figure 5.44: Comparison of the μ^- momentum distributions between data and MC, rejecting outer from trigger.

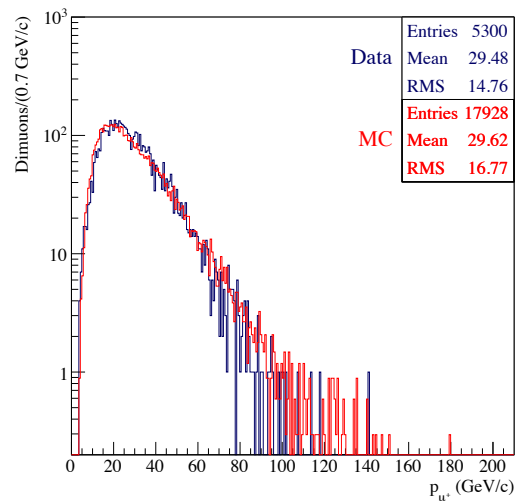


Figure 5.45: Comparison of the μ^+ momentum distributions between data and MC, rejecting outer from trigger.

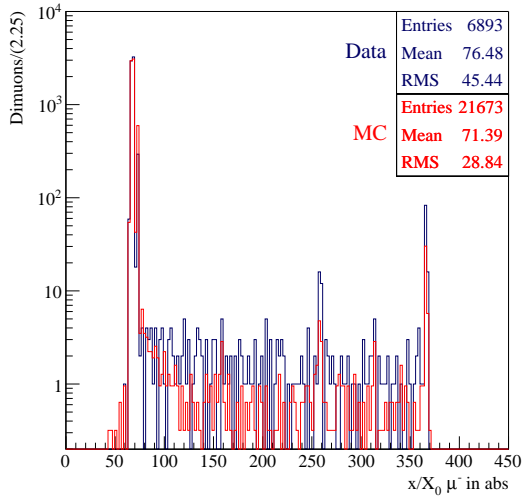


Figure 5.46: Comparison of the radiation lengths crossed by the negative muons in the absorber between data and MC.

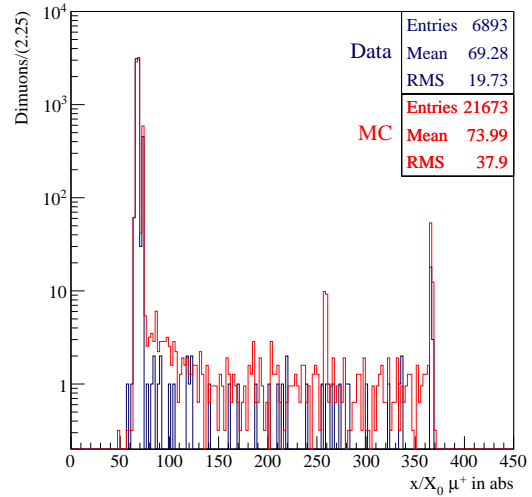


Figure 5.47: Comparison of the radiation lengths crossed by the positive muons in the absorber between data and MC.

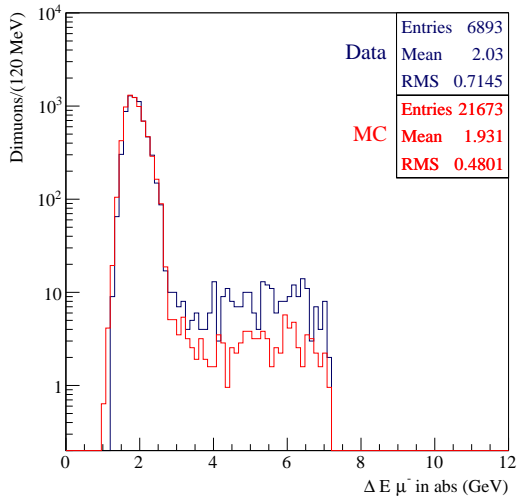


Figure 5.48: Comparison of μ^- energy loss in the absorber between data and MC.

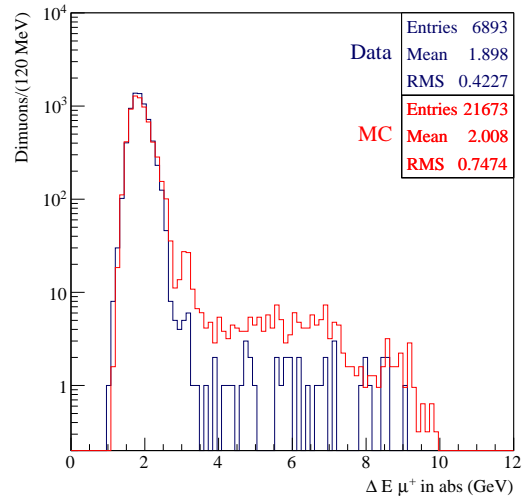


Figure 5.49: Comparison of μ^+ energy loss in the absorber between data and MC.

The comparison between the number of radiation lengths crossed by the muon in the absorber is in Fig. 5.46 for negative muons and in Fig. 5.47 for positive muons. The negative muons cross more the tungsten in data than in MC. For the positive muons it is the opposite. This is in the same direction as the conclusions taken from the momentum of each individual muon.

The comparison between the muons energy loss in the absorber is in Fig. 5.48 for negative muons and in Fig. 5.49 for positive muons. In the case of the energy loss the same conclusions can be taken for both muons.

The comparison between the MC and the data is considered reasonable taking into account the differences between them, mainly the trigger and the fact that the simulation consists of purely J/ψ events. Even though the pile up simulation was included, it is far from describing the combinatorial background as seen in data. For future simulations it would be very useful to describe better the pile-up.

The 2014 Drell-Yan Pilot Run

The 2014 Drell-Yan pilot run preceded the main DY data taking with the ammonia polarised target. This pilot run was very important for the commissioning of the spectrometer and the data acquisition system. The conditions were very similar to the 2015 ones apart from small differences, the target cells were not polarised and the new large area DC5 was not in the spectrometer. These data were useful to evaluate the spectrometer response to the high intensity environment and to test and tune/improve the reconstruction software. After the commissioning, it was possible to collect physics data in stable conditions during 17 days between 28 of November and 14 of December. In this chapter a preliminary analysis of this data is going to be presented, including the selection of the good muon pairs, the impact of the trigger validation requirement and of the image cut for the estimation of the combinatorial background. The division of muon pairs by trigger is also presented and some relevant kinematic distributions are shown.

6.1 Data Taking Conditions

The 2014 data taking took place on the last months of the year. The main differences with respect to the 2009 DY beam test and to the spectrometer configuration for DIS programme were the addition of a completely new hadron absorber with a beam plug in its center, the presence of the new large angle hodoscopes in LAS and the symmetrization of the old SAS hodoscopes.

A negative pion beam was used with an intensity of $6 \times 10^7 \pi/s$, which is around four times higher than the highest intensity in 2009 and it is 0.75 times the intensity in 2015. The target was composed of two cells of ammonia, 55 cm long and with a diameter of 4 cm. The cells were separated by 20 cm. The target was centred at -230 cm. The total cells length corresponds to around 0.57 pion interaction lengths and 1.56 radiation lengths.

The hadron absorber is placed between -132.5 cm and 130 cm. The 262.5 cm long absorber is made of aluminium, alumina and stainless steel. The first 36 cm are of aluminium, followed by a gap of around 6.5 cm to accommodate the vertex detector, the following 200 cm are made of alumina and the last 20 cm of stainless steel. The total length of the absorber was 7.7 pion interaction lengths long and 43.8 radiation lengths long.

The beam plug in the center of the absorber was made by 6 cylinders of tungsten 20 cm long each. The first 60 cm of the central part of the alumina block were empty, followed by the 120 cm of tungsten, 20 cm of alumina and 20 cm of steel. All these materials are 12.1 pion interaction lengths long and 357.3 radiation lengths long.

The beam plug also acts as a nuclear target, and is going to be used for the analysis of the DY dependence with A and the study of the EMC effect. In addition to the ammonia and the tungsten targets, an aluminium target 7 cm long is placed just upstream of the tungsten between -63.5 and -56.5 cm.

The trigger system consisted in three double trigger sub-systems: the so called LAS-LAS, which uses the two large area hodoscopes placed in LAS, and selects events with at least two particles in coincidence originating in the target region, the other two double triggers select one particle in LAS in coincidence with one particle in Outer or in Middle systems. These two smaller trigger hodoscopes were modified to be symmetric and were centred with the MW2 dead zone.

6.2 Data Production

There were 323 runs produced for physics analysis. From the miniDSTs, microDSTs were obtained selecting the events with at least one primary vertex with 2 muons, regardless of the charge, requiring PID 5 or 6 for each. The total number of processed events is 3.8×10^9 and the number of events stored in microDSTs is 1.1×10^8 .

6.3 Event Selection

In order to select the good pair candidates the following cuts were applied to the preselected events stored in microDSTs:

1. All opposite-sign muon pairs from a primary vertex. If the same pair has more than one primary vertex the one with the best χ^2 is chosen.
2. Dimuon trigger (Middle+LAS or Outer+LAS or LAS+LAS).
3. $\theta_{\mu^-} > 12$ mrad OR $p_{\mu^-} < 100$ GeV/c, to reject pairs with a negative muon coming from a pion beam decay. The impact of this selection is visible in Fig. 6.1 and Fig. 6.2. The cut rejects 1.9% of the pairs. It was decided to keep higher momentum muons at angles larger than 12 mrad since the muons coming from the pion decays are mainly at lower angles.
4. $-315 < Z_{vtx} < -145$ cm, to select vertices from the ammonia target cells region. The distribution of the vertices is shown in Fig. 6.3. Around 56% of vertices are rejected when only vertices from ammonia region are selected.
5. $r_{vtx} < 2.5$ cm, to select vertices within the radius ± 0.5 cm of the ammonia cells. In Fig. 6.4 the transverse position of the vertices is shown. The impact of this selection is shown in Fig. 6.5 for the x coordinate and in Fig. 6.6 for the y coordinate. This cut rejects 6.6 % of the pairs.
6. $Z_{last} > 1500$ cm, to select muons with the last measured point after MF1. This selection rejects 0.3% of pairs. The distribution of the last measured point for each muon is in Fig. 6.7.
7. $Z_{first} < 300$ cm, to select muons with the first measured point before SM1. This selection rejects 0.9% of pairs. The distribution of the first measured point for each muon is in Fig. 6.8.

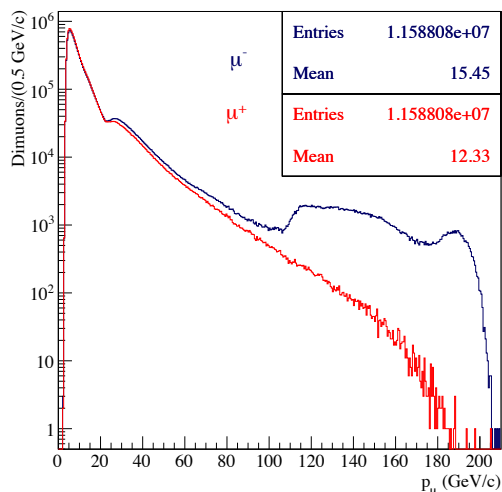


Figure 6.1: Momentum distribution for each muon charge before the selection of negative muons with momentum smaller than 100 GeV/c or angle larger than 12 mrad.

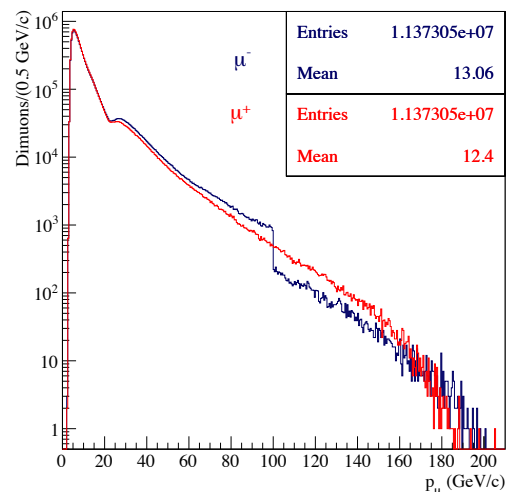


Figure 6.2: Momentum distribution for each muon charge after the selection of negative muons with momentum smaller than 100 GeV/c or angle larger than 12 mrad.

8. t_μ defined, muons with time defined. After all the selections applied this selection only rejects 6 pairs, as expected since now there is hodoscopes in LAS which contribute for the mean time of the tracks. In 2009 around half of the pairs had no time defined.
9. $|t_{\mu_1} - t_{\mu_2}| < 15$ ns, time difference between the two muons lower than 15 ns. The distribution of the mean time difference between the two muons is in Fig 6.9 and the impact of this selection in the individual muons is in Fig.6.10 and Fig.6.11. This selection rejects 4.2% of the pairs.
10. Trigger validation, requiring that the selected muons are in the geometrical acceptance of the hodoscopes of the corresponding fired trigger. The muons were extrapolated to the positions of the hodoscopes corresponding to the fired trigger to check if they fall in their active area.
11. Image cut, requiring that the pair would be geometrically accepted if their muons have the opposite charge. This cut is a requirement to estimate the combinatorial background.

The impact of the cuts is visible in the statistics presented in table 6.1. From all the muon opposite sign pairs with a primary vertex and with masses larger than 4 GeV/c² only around 10 % survive all the cuts. The impact of each cut in the dimuon mass distribution is shown in sequence in Fig. 6.12, where the cleaning effect is evident, the J/ψ peak being more enhanced after the cuts.

6.4 Z vertex distribution

The Z vertex distribution for masses larger than 4.5 GeV/c² with and without the image cut, is shown in Fig. 6.13. The targets are also indicated in green. It is evident a shift in the downstream direction of all the vertices positions, in the case of ammonia, vertex detector and

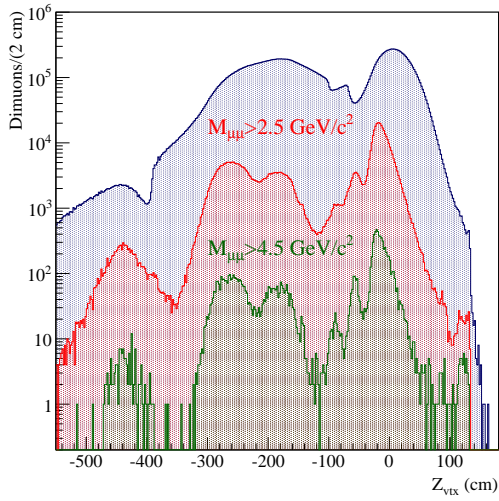


Figure 6.3: Z_{vtx} distributions with the whole selection criteria apart from the Z_{vtx} selection. In blue are the vertices for all masses, in red the vertices for masses larger than $2.5 \text{ GeV}/c^2$ and in green are the vertices for masses larger than $4.5 \text{ GeV}/c^2$.

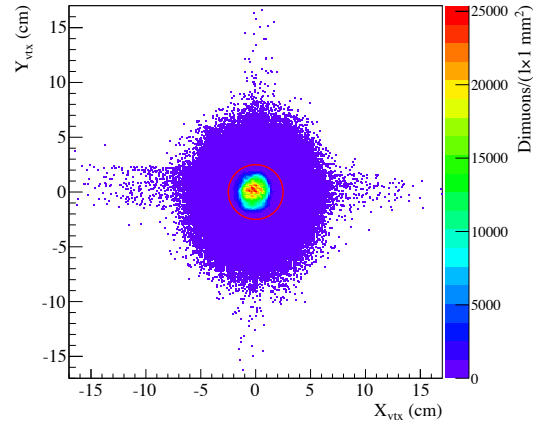


Figure 6.4: Y_{vtx} versus X_{vtx} distribution. The red circumference indicate the cut to be applied.

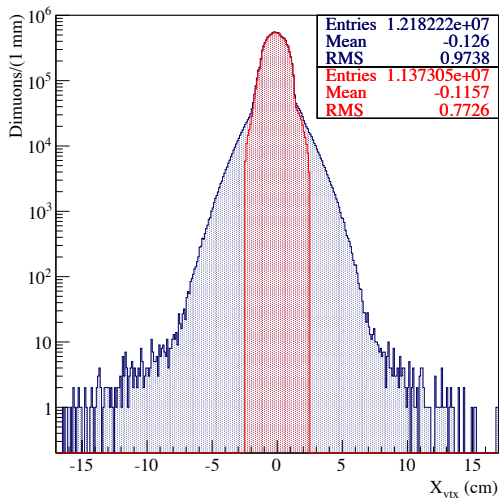


Figure 6.5: X_{vtx} position. In red is the distribution for the selected vertices.

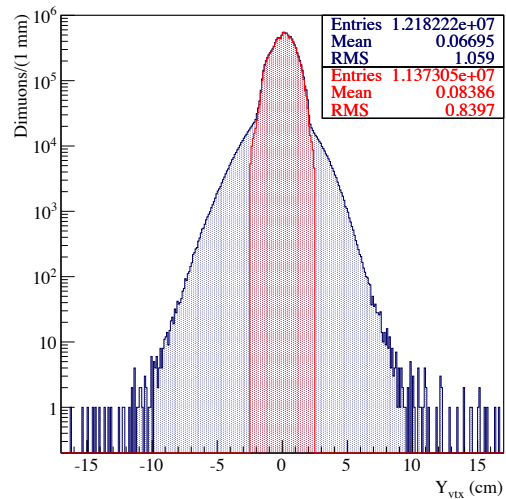


Figure 6.6: Y_{vtx} position. In red is the distribution for the selected vertices.

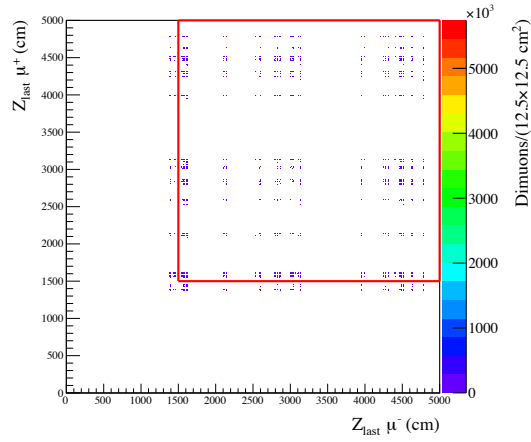


Figure 6.7: Last measured point of each muon. The red square indicates the limit to be selected, only muon with last measured point larger than 1500 cm are accepted.

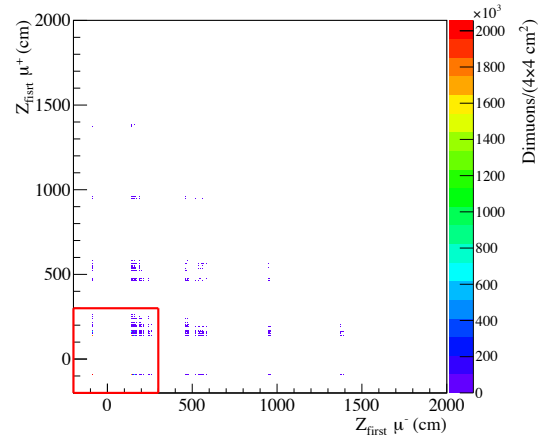


Figure 6.8: First measured point of each muon. The red square indicates the limit to be selected, only muon with first measured point lower than 300 cm are accepted.

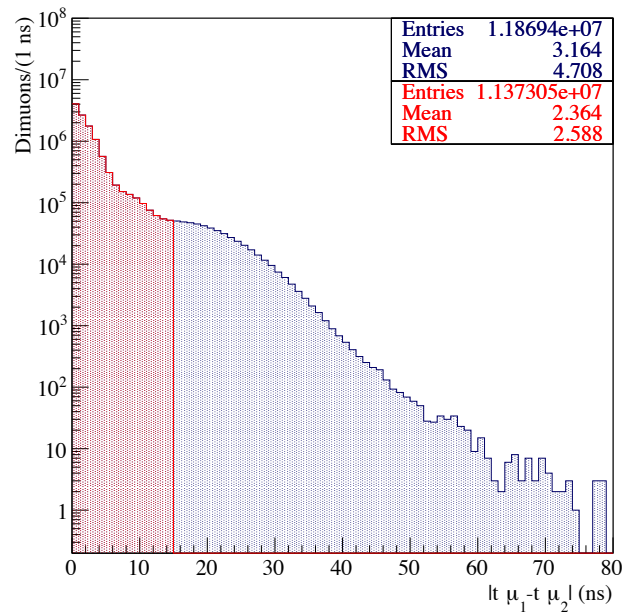


Figure 6.9: Time difference between the muons.

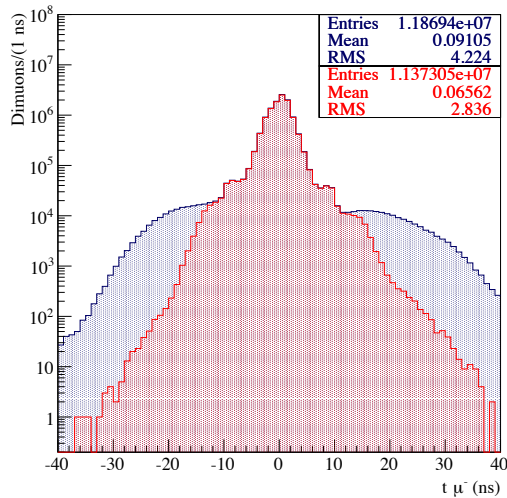


Figure 6.10: Mean time of the negative muons. In red is the distribution after selecting the mean time difference between the two muons to be smaller than 15 ns.

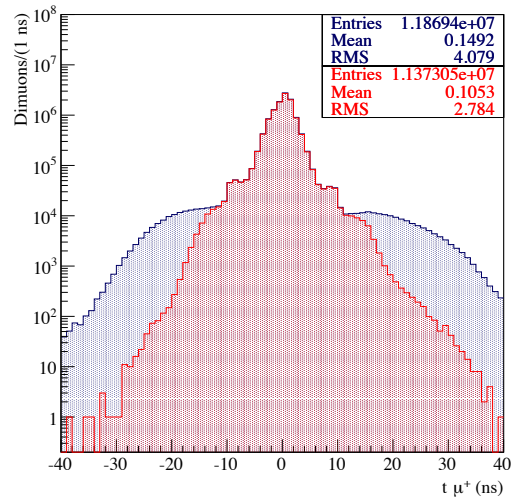


Figure 6.11: Mean time of the positive muons. In red is the distribution after selecting the mean time difference between the two muons to be smaller than 15 ns.

	Selection	#pairs		
		All M	$M_{\mu\mu} > 4 \text{ GeV}/c^2$	
1	Muon opp pairs from primary	83369467	72035	100%
2	Dimuon Trigger	82998266	71448	99.2%
3	$\theta_{\mu^-} > 12 \text{ mrad}$ or $p_{\mu^-} < 100 \text{ GeV}/c$	80951151	31755	44.1%
4	$-315 < Z_{vtx} < -145 \text{ cm}$	34967924	8365	11.6%
5	$r_{vtx} < 2.5 \text{ cm}$	32522910	8127	11.3%
6	$Z_{last} > 1500 \text{ cm}$	32401205	8094	11.2%
7	$Z_{first} < 300 \text{ cm}$	31695712	7979	11.1%
8	t_{μ} defined	31665260	7975	11.1%
9	$ t_{\mu_1} - t_{\mu_2} < 15 \text{ ns}$	30145303	7945	11.0%
10	Trigger Validation	19221234	7446	10.3%
11	Image Cut	11373050	7076	9.8%

Table 6.1: The impact of each selection criterion in the statistics.

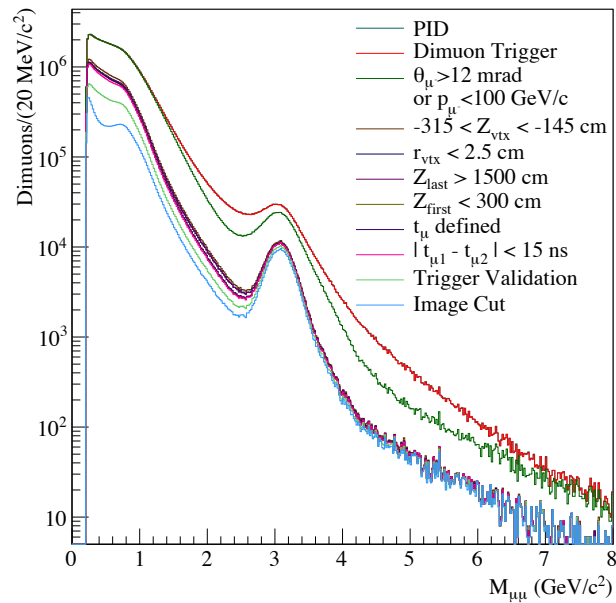


Figure 6.12: The impact of the selection criteria in the dimuon mass distribution.

the aluminium. This shift can be the result of a bias in the vertex reconstruction due to the use of the vertex detector in the reconstruction, which was found to be not working properly. Another hint of such bias comes from the large statistics reconstructed in the vertex detector position if the image cut is not applied. These events are fake dimuons, since the vertex detector dead zone region is made by a very thin plastic material with low interaction probability.

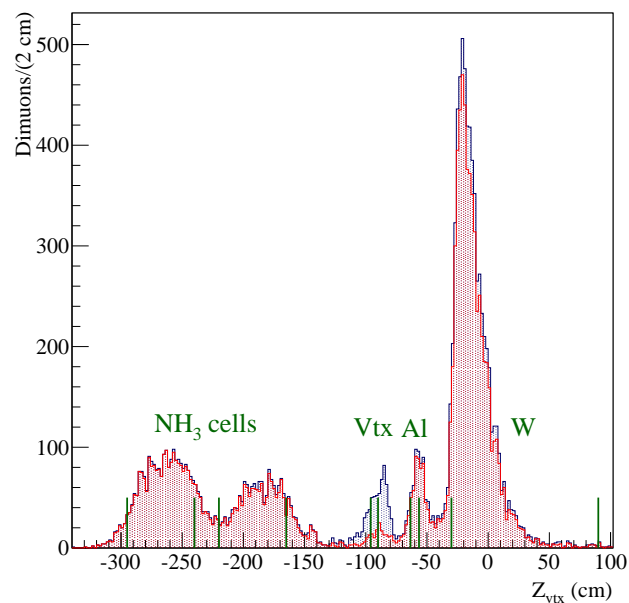


Figure 6.13: Z_{vtx} distributions, with the whole selection criteria apart from the Z_{vtx} selection, for high mass events with and without the image cut. In blue are the vertices distribution without image cut and in red are the vertices after applying the image cut.

6.5 Dimuon Mass Distribution and the Impact of the Trigger Validation

The dimuon mass distribution is produced using the selection criteria described in section 6.3. Fig. 6.14 shows the dimuon mass distribution before the application of the trigger validation and the image cut. In Fig. 6.15 the distribution with trigger validation but without the image cut is shown. The fit function used in both cases is a sum of two Gaussians, one for the J/ψ resonance and the other for the ψ' resonance, and one power law function to fit the continuum under the resonances. The fit is performed in the region from 1.5 to 8 GeV/c^2 .

From the fits the number of J/ψ decreased from 249495 ± 756 to 231978 ± 732 , around 7% of the J/ψ are rejected due to the requirement of trigger validation. This may indicate that in 7% of the cases the event had 3 muons and the trigger was fired from one muon of the J/ψ and one muon from another source or that the reconstruction failed for at least one of the muons. Because of the low redundancy in the limits of the detectors and their dead zones, the reconstructed muon was not propagated up to the hodoscope position and its extrapolation, due to its uncertainty, fall off the active region but close to their limit.

The J/ψ mass extracted from the fits is $3.070 \pm 0.001 \text{ GeV}/c^2$ and $3.072 \pm 0.001 \text{ GeV}/c^2$, which is around 26 MeV/c^2 lower than the PDG mass value, 3.097 GeV/c^2 .

The J/ψ mass resolution is $201.2 \pm 0.7 \text{ MeV}/c^2$ and $200.3 \pm 0.7 \text{ MeV}/c^2$.

The number of ψ' varies from 8470 ± 462 to 8464 ± 472 , which are compatible. The ψ' are around 3.6% of the J/ψ .

The ψ' mass extracted from the fits is $3.618 \pm 0.011 \text{ GeV}/c^2$ and $3.619 \pm 0.012 \text{ GeV}/c^2$. The difference between the fitted ψ' mass and the J/ψ mass is $0.547 \pm 0.011 \text{ GeV}/c^2$, while in the PDG it is $3.686 - 3.097 = 0.589$, which are not compatible.

The ψ' mass resolution is $179.6 \pm 6.5 \text{ MeV}/c^2$ and $188.3 \pm 7.2 \text{ MeV}/c^2$.

As expected, the resolution is better for high masses, $\Delta M_{J/\psi}/M_{J/\psi} \geq \Delta M_{\psi'}/M_{\psi'} \Leftrightarrow 6.5\% \geq 5.2\%$.

The number of DY pairs with $M_{\mu\mu} > 4 \text{ GeV}/c^2$ decreases from 7945 to 7446, which represents a loss of 6.3% when the trigger validation is required. The number of high mass DY pairs is 3.2% with respect to the number of J/ψ dimuons.

6.6 Combinatorial Background Estimation

The estimation of the combinatorial background is done in the same way as for 2009, for more details see Section 5.10.

The dimuon mass distribution as well as the like-sign pairs mass distribution are shown in Fig. 6.16. In order to evaluate the combinatorial background the spectrometer acceptance must be charge symmetric, which is obtained with the image cut. This is applied to the samples in Fig. 6.16 and results in the distributions presented in Fig. 6.17. The impact in the statistics when the image cut is applied is a loss of around 40% for all masses. In 2009 it was slightly higher, around 50%. The number of J/ψ decreases from 231978 ± 732 to 214597 ± 720 , which represents a loss of around 7%, while in 2009 it was 16%. The number of high mass DY events decreases from 7446 to 7076, a loss of 5%. The differences with respect to 2009 are due to the symmetrization of the trigger hodoscopes in SAS.

The combinatorial background is evaluated after the application of the image cut, which is plotted in Fig. 6.18.

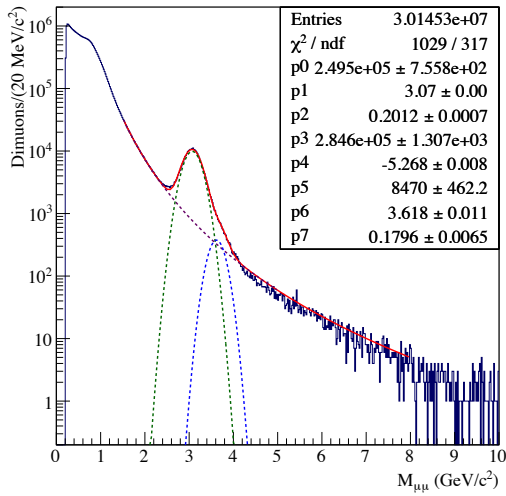


Figure 6.14: Dimuon mass distribution, without the trigger validation and the image cut.

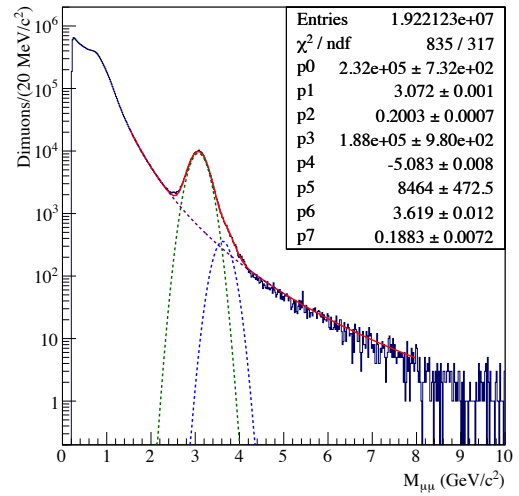


Figure 6.15: Dimuon mass distribution, after the trigger validation is applied, but without the image cut.

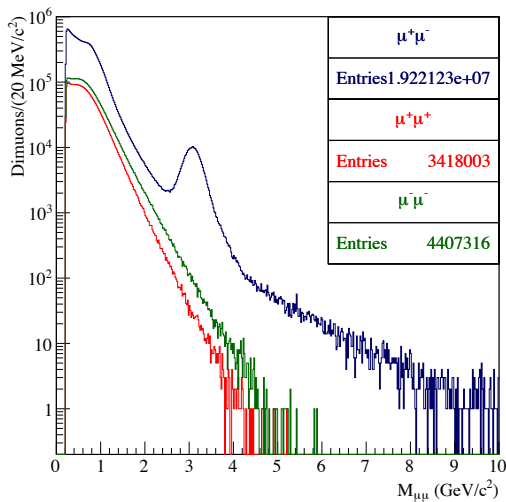


Figure 6.16: Mass distributions. The lines with blue, red, and green colours represent the opposite sign muon pairs, the positive like-sign and the negative like-sign pairs, respectively.

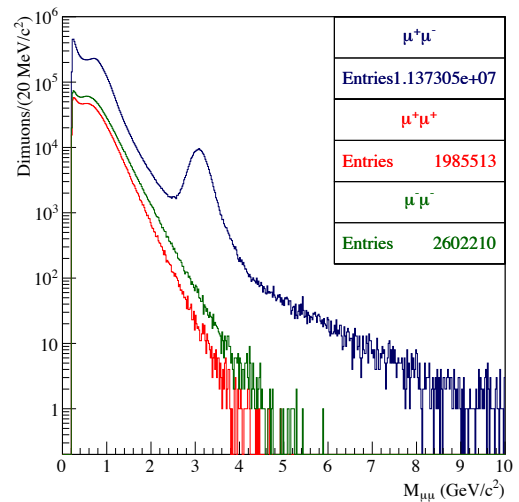


Figure 6.17: Mass distributions. The lines with blue, red, and green colours represent the opposite sign muon pairs, the positive like-sign and the negative like-sign pairs, respectively, after the application of the image cut.

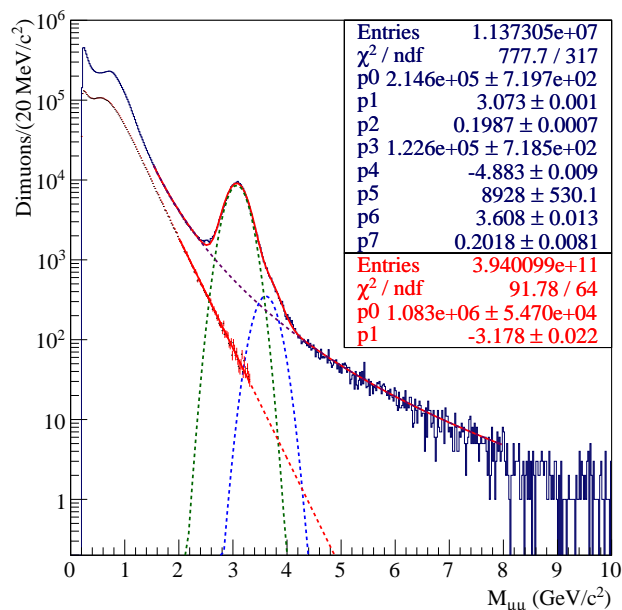


Figure 6.18: In blue is the dimuon mass distribution after the image cut. In red is the combinatorial background calculated after the image cut procedure and using the like-sign pairs.

6.7 Dimuon mass distributions by trigger

The mass distribution of the muon pairs by trigger is presented in Figures 6.20 to 6.22. In Fig. 6.19 the dimuon mass distribution for all the three double triggers is shown, the same distribution as in Fig. 6.18, the difference being in the fit function. It was not possible to fit all the distributions divided by trigger with the previous used function, the fits failed, because one power law function was not enough to describe the continuum under the resonances. Here the same fit function as in 2009 was used (see Eq. 5.1), two Gaussians and two exponential functions. The mass and width of the ψ' were constrained by the mass and width of the J/ψ . The function was found to be reasonable for the fits of the three mass distributions depending on the trigger. A summary of the results for each case is shown in Table 6.2. The pairs with $M_{\mu\mu} > 4 \text{ GeV}/c^2$ are mostly with both muons in LAS, 60.5% of the cases, while 45.5% of cases are in mixed LAS-SAS, thus there is an overlap of 6% of pairs that fired both dimuon trigger systems. The contamination by combinatorial background and by ψ' pairs in the region of $M_{\mu\mu} > 4 \text{ GeV}/c^2$ is around 10%. It is higher in the case of the LAST-MT trigger, and smaller in the case of the LAST-LAST trigger, mainly because of the combinatorial background. The resolution is better for LAS-LAS, as expected since in this case the muons cross the alumina. In the case of the LAS-Middle, the worst case, at least one of the muons cross the tungsten beam plug in most cases.

6.8 Kinematic Distributions

The dimuon momentum distribution is shown in Fig. 6.23. The Feynman x distribution is shown in Fig. 6.24. The dimuon transverse momentum is shown in Fig. 6.25. The distribution of x_2 versus x_1 is shown in Fig. 6.26. The distribution of the cosine of the polar angle of the

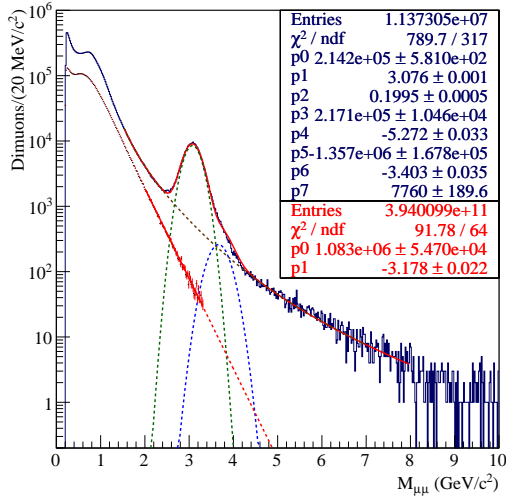


Figure 6.19: Mass distribution for all double triggers.

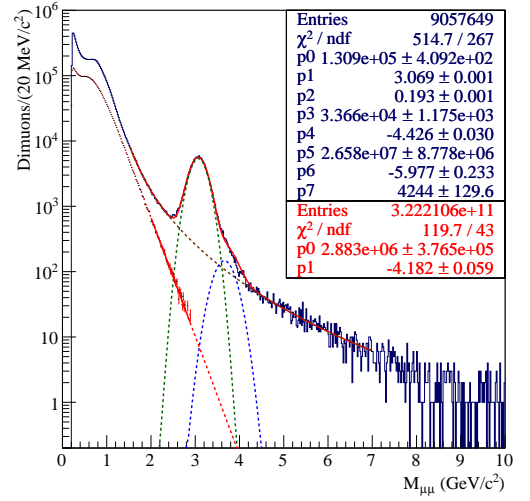


Figure 6.20: Mass distribution for LAS-LAS double trigger.

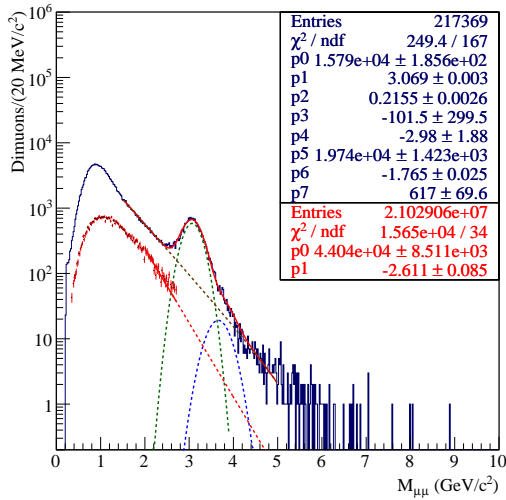


Figure 6.21: Mass distribution for LAS-Middle double trigger.

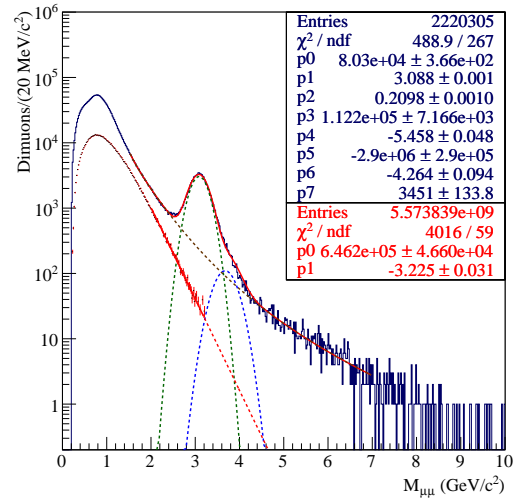


Figure 6.22: Mass distribution for LAS-Outer double trigger.

	Dimuon trig	LAST-LAST	LAST-MT	LAST-OT
$\#J/\psi$	214164±581	130914±409 (61.1%)	15793±186 (7.4%)	80304±366 (37.5%)
$\#\psi'$	7760±190	4244±130 (54.7%)	617±70 (8.0%)	3451±134 (44.5%)
$\#\mu^+\mu^- M > 4$	7076	4283 (60.5%)	462 (6.5%)	2760 (39.0%)
$\#\psi'$ tail $M > 4$	615	291	56	337
$\#\text{Bkg } M > 4$	54	3	30	28
Contamination $M > 4$	9.5%	6.9%	18.6%	13.2%

Table 6.2: Statistics divided by trigger.

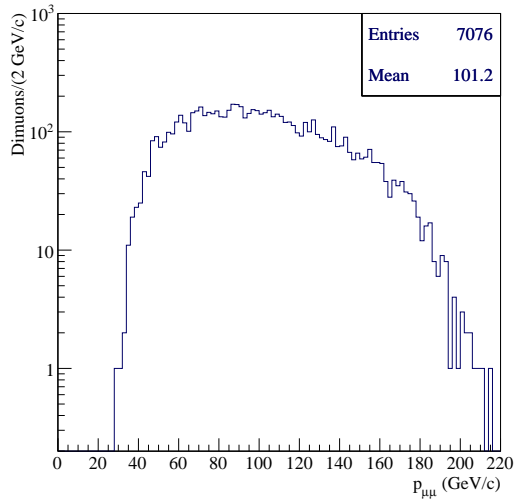


Figure 6.23: Dimuon momentum distribution for $M_{\mu\mu} > 4 \text{ GeV}/c^2$.

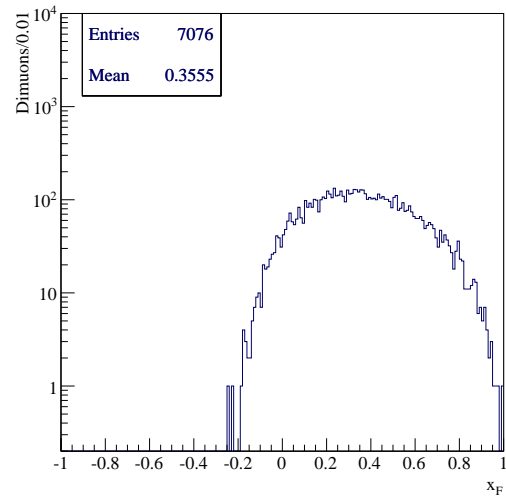


Figure 6.24: Feynman x distribution for $M_{\mu\mu} > 4 \text{ GeV}/c^2$.

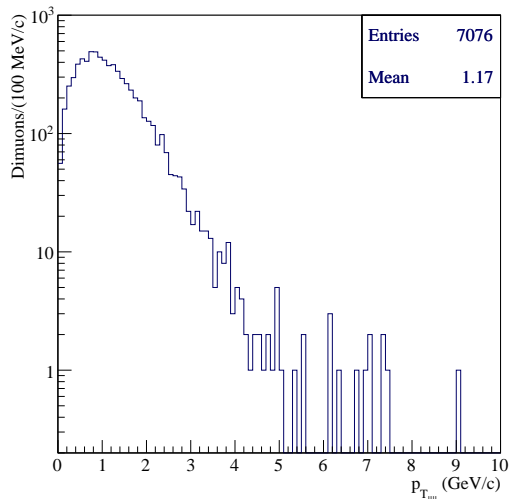


Figure 6.25: Dimuon transverse momentum distribution for $M_{\mu\mu} > 4 \text{ GeV}/c^2$.

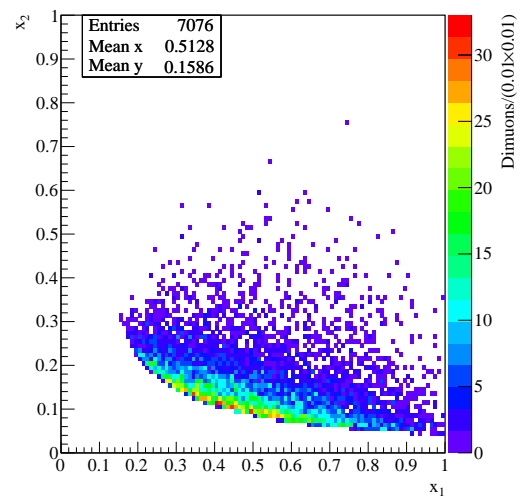
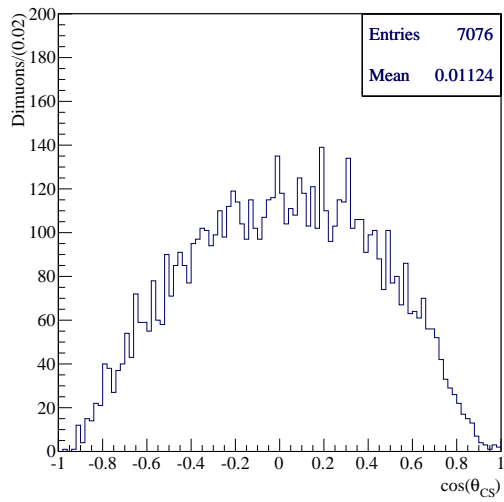
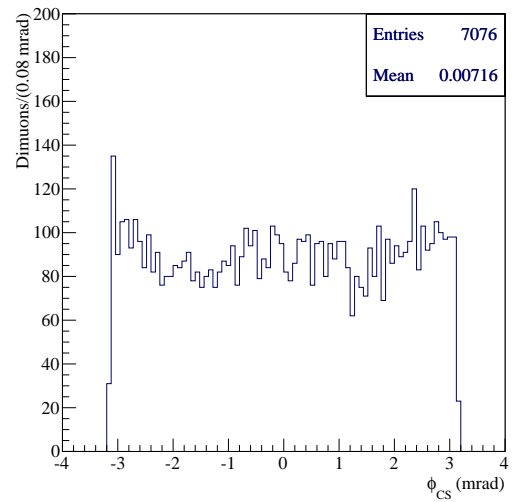


Figure 6.26: x_2 versus x_1 distribution for $M_{\mu\mu} > 4 \text{ GeV}/c^2$.

positive muon in the Collin-Soper frame is shown in Fig. 6.27. The distribution of the azimuthal angle between the hadrons plane and the leptons plane in the CS frame is shown in Fig. 6.28. These distributions are very close to the expected ones from MC, as it can be seen in the COMPASS-II proposal [104], now the MC should be fine tuned in order to exactly describe the kinematics as extracted from the data.

Figure 6.27: Distribution of the $\cos(\theta_{CS})$.Figure 6.28: Distribution of the ϕ_{CS} .

The 2015 Polarised Drell-Yan Run

The COMPASS data taking during the year of 2015 was dedicated to the polarised Drell-Yan measurement. The data taking conditions were very similar to the ones described in the previous Chapter for the 2014 DY pilot run.

The relevant differences are that a negative pion beam with an intensity of $8.1 \times 10^7 \pi^-/\text{s}$ was used, a bit higher than in 2014. Downstream of the absorber a lithium thin absorber foil was added to stop the slow neutrons produced in the interactions along the absorber and causing a high flux in the first spectrometer detectors. The new large area drift chamber detector, DC5, was placed in the spectrometer just downstream of the SM1 and the DC4, which is helpful for the reconstruction in the zone between the SM1 and SM2. The 3 micromegas placed in between the absorber and the SM1 were all modified to include a new pixelized part in their center.

The data taking periods considered good for physics analysis last from 8 of July to 12 of November, each period being divided in two sub-periods. A summary of these periods can be seen in Table 7.1.

Up to now, March 2016, only one period was produced, the so called w10_p4. The reconstruction conditions were different from the ones used in 2014, namely the vertex detector was not used in the reconstruction since it is highly illuminated with time correlated hits. There are suspicious that it induced a bias in the reconstruction of the 2014 data. From the miniDSTs, microDSTs were produced selecting the events with at least one primary vertex with 2 muons, regardless of the charge, requiring PID 5 or 6 for each. The total number of processed events is 3.8×10^9 and the number of events stored in microDSTs is 1.5×10^8 .

7.1 Event Selection

The same event selection as used for the 2014 data is used here. The impact of each cut is presented in Table 7.2. From all the opposite sign muon pairs from a primary vertex with masses larger than $4 \text{ GeV}/c^2$ 11.4% survive all the cuts, a bit more than in 2014 (9.8%), which points to a better data taking and reconstruction conditions in 2015. The impact of each cut in the dimuon mass distribution is shown in sequence in Fig. 7.1, evidencing the cleaning effect.

In Fig. 7.2 and Fig. 7.3 the impact of the selection of pairs with a negative muon with a momentum smaller than $100 \text{ GeV}/c$ or polar angle larger than 12 mrad is clear. This cut rejects 2.0% of pairs, similar to the rejection of 2014, 1.9%. From Fig. 7.3 is evident that this cut is not optimized, the distribution for the negative muons shows a clear loss around $100 \text{ GeV}/c$. Alternative cuts are under study to obtain a better symmetrization between the two distributions.

Period	Sub-period	Runs range	Begin data	End data
w07_p1	↓↑ (+,-)	259360-259677	08 Jul	15 Jul
	↑↓ (-,+)	259744-260024	16 Jul	22 Jul
w08_p2	↑↓ (-,+)	260025-260264	22 Jul	29 Jul
	↓↑ (+,-)	260294-260565	29 Jul	05 Aug
w09_p3	↓↑ (+,-)	260620-260852	05 Aug	12 Aug
	↑↓ (-,+)	260875-261496	12 Aug	26 Aug
w10_p4	↑↓ (-,+)	261501-261760	26 Aug	01 Sep
	↓↑ (+,-)	261970-262221	04 Sep	09 Sep
w11_p5	↓↑ (+,-)	262370-262772	11 Sep	22 Sep
	↑↓ (-,+)	262831-263090	23 Sep	30 Sep
w12_p6	↑↓ (-,+)	263143-263347	30 Sep	07 Oct
	↓↑ (+,-)	263386-263603	08 Oct	14 Oct
w13_p7	↓↑ (+,-)	263655-263853	15 Oct	21 Oct
	↑↓ (-,+)	263926-264134	22 Oct	28 Oct
w14_p8	↑↓ (-,+)	264170-264329	28 Oct	02 Nov
	↓↑ (+,-)	264429-264561	04 Nov	08 Nov
w15_p9	↓↑ (+,-)	264619-264672	09 Nov	11 Nov
	↑↓ (-,+)	264736-264857	12 Nov	16 Nov

Table 7.1: 2015 data taking organization.

	Selection	#pairs		
		All M	$M_{\mu\mu} > 4 \text{ GeV}/c^2$	
1	Muon opp pairs from primary	113762150	80429	100%
2	Dimuon Trigger	112639563	79053	98.3%
3	$\theta_{\mu^-} > 12 \text{ mrad}$ or $p_{\mu^-} < 100 \text{ GeV}/c$	110314209	33430	41.6%
4	$-315 < Z_{vtx} < -145 \text{ cm}$	50100293	11229	14.0%
5	$r_{vtx} < 2.5 \text{ cm}$	45513923	10806	13.4%
6	$Z_{last} > 1500 \text{ cm}$	45344951	10771	13.4%
7	$Z_{first} < 300 \text{ cm}$	45029496	10655	13.2%
8	t_{μ} defined	44957494	10647	13.2%
9	$ t_{\mu_1} - t_{\mu_2} < 15 \text{ ns}$	43678777	10546	13.1%
10	Trigger Validation	27000717	9727	12.1%
11	Image Cut	18065390	9147	11.4%

Table 7.2: The impact of each selection criterion in the statistics.

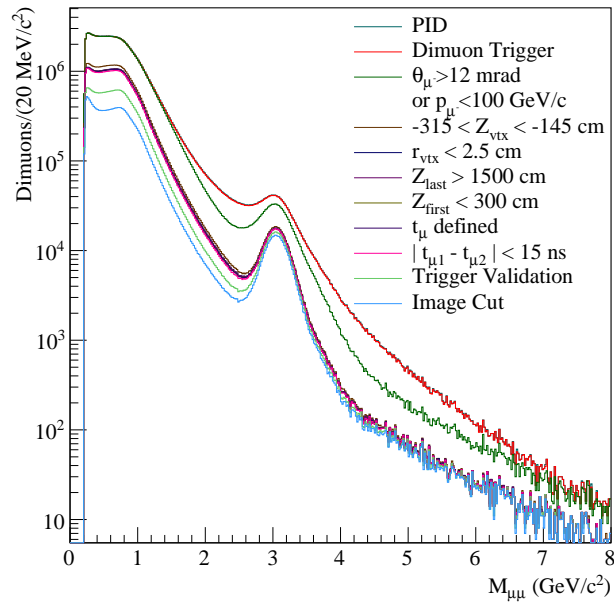


Figure 7.1: The impact of the selection criteria in the dimuon mass distribution.

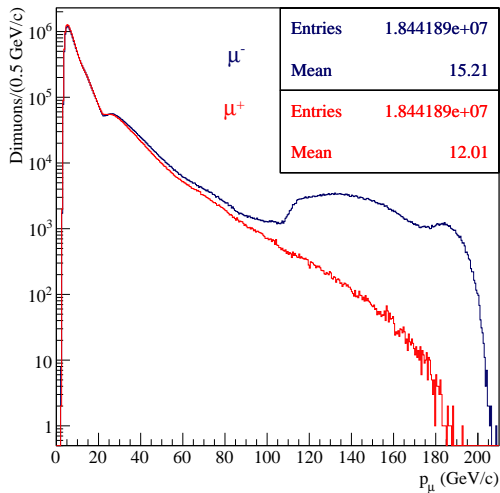


Figure 7.2: Momentum distribution for each muon charge before the selection of negative muons with momentum smaller than 100 GeV/c or angle larger than 12 mrad.

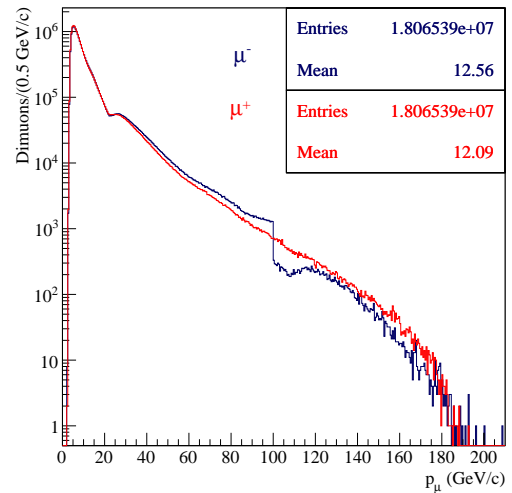


Figure 7.3: Momentum distribution for each muon charge after the selection of negative muons with momentum smaller than 100 GeV/c or angle larger than 12 mrad.

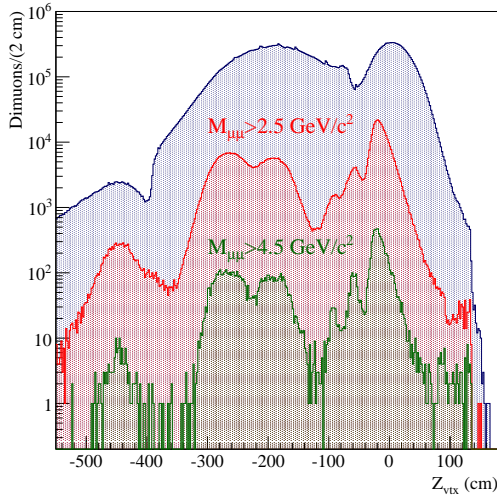


Figure 7.4: Z_{vtx} distributions with the whole selection criteria apart from the Z_{vtx} selection. In blue are the vertices for all masses, in red the vertices for masses larger than $2.5 \text{ GeV}/c^2$ and in green are the vertices for masses larger than $4.5 \text{ GeV}/c^2$.

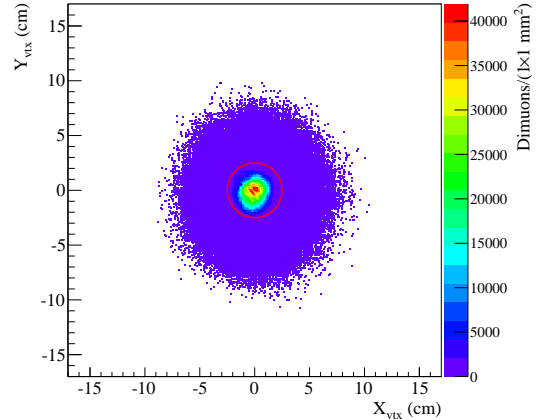


Figure 7.5: Y_{vtx} versus X_{vtx} distribution. The red circumference indicate the cut to be applied.

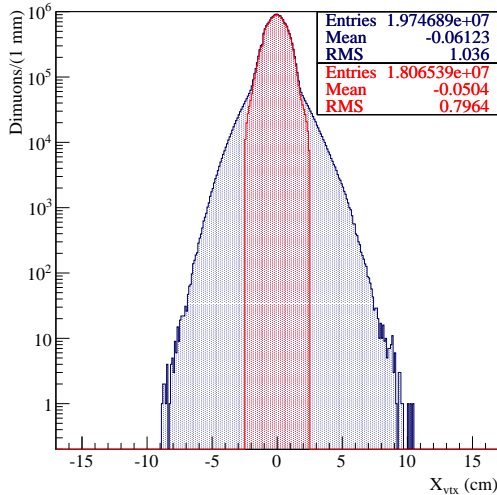


Figure 7.6: X_{vtx} position. In red is the distribution for the selected vertices.

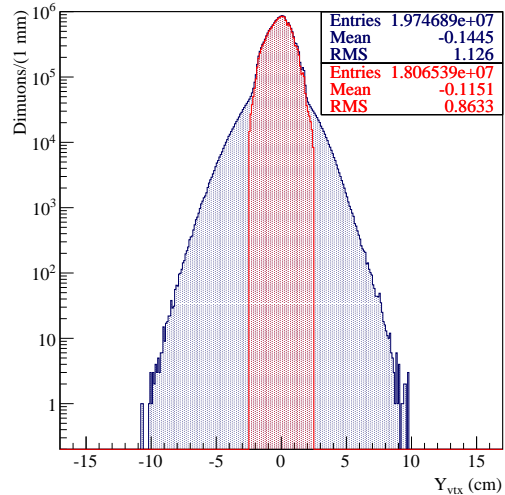


Figure 7.7: Y_{vtx} position. In red is the distribution for the selected vertices.

In Fig.7.4 the vertices distribution for all masses and selecting masses larger than $2.5 \text{ GeV}/c^2$ and larger than $4.5 \text{ GeV}/c^2$ are shown. As the resolution is better for high masses, the target cells separation is also more evident there. The selection of vertices from the ammonia target region, $-315 < Z_{vtx} < -145 \text{ cm}$, rejects around 53% of vertices, slightly less than in 2014, 56%. In Fig. 7.5 is shown the transverse position of the vertices in the ammonia target cells, and the red circle indicates the selection applied. The impact of this selection of $r_{vtx} < 2.5 \text{ cm}$ is shown in Fig. 7.6 for the x coordinate and in Fig. 7.7 for the y coordinate. This selection rejects 8.5% of the pairs, slightly more than in 2014, 6.6%.

The distribution of the Z_{last} of each muon is shown in Fig. 7.8, the selection of Z_{last} larger

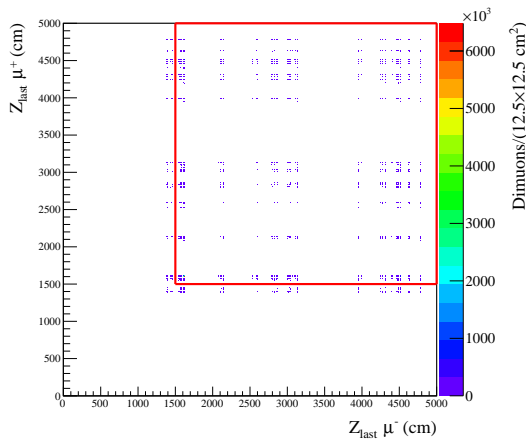


Figure 7.8: Last measured point of each muon. The red indicates the limit to be selected, only muon with last measured point larger than 1500 cm are accepted.

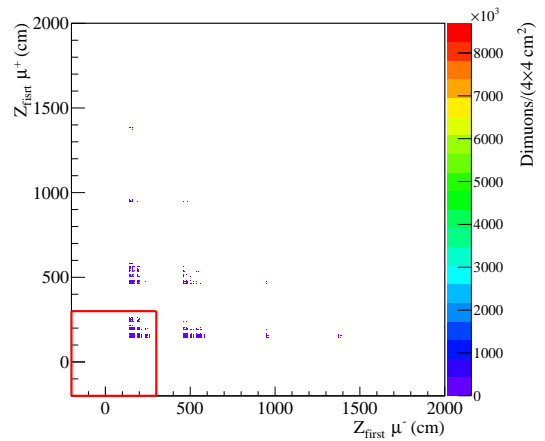


Figure 7.9: First measured point of each muon. The red indicates the limit to be selected, only muon with first measured point lower than 300 cm are accepted.

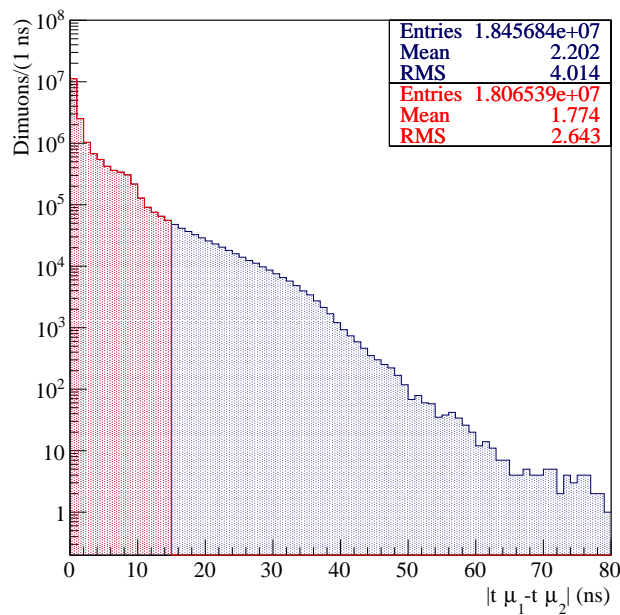


Figure 7.10: Time difference between the muons.

than 1500 cm rejects 0.4% of the pairs, it was 0.3% in 2014. The distribution of the Z_{first} of each muon is shown in Fig.7.9, the selection of the Z_{first} smaller than 300 cm rejects 0.5% of the pairs, it was 0.9% in 2014.

Fig. 7.10 shows the mean time difference between the 2 muons and the selection of pairs with a difference between the 2 muons less than 15 ns. The impact of the selection for each individual muon is shown in Fig.7.11 for the negative muon, and in Fig. 7.12 for the positive one. This selection rejects 2.1% of the pairs, less than in 2014, 4.2%. Comparing the muon time distributions in 2014 and in 2015, the improvement in timing is visible (narrower peaks), this is related with better calibration of the detectors.

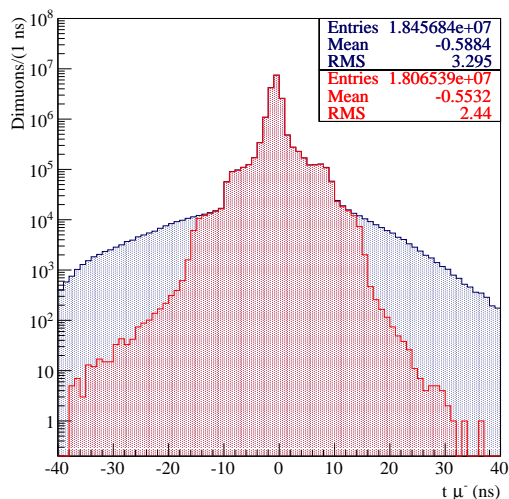


Figure 7.11: Mean time of the negative muons. In red is the distribution after the selection of the mean time difference between the two muons smaller than 15 ns.

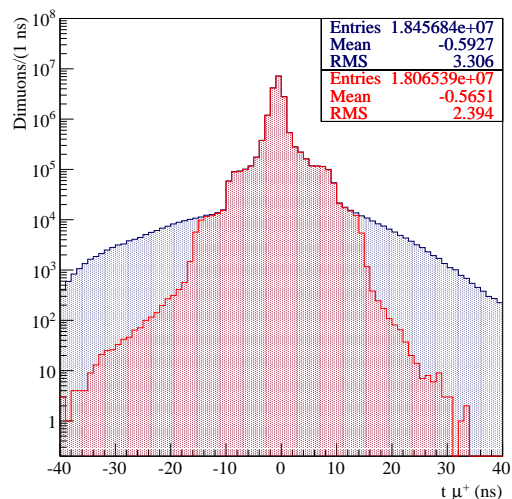


Figure 7.12: Mean time of the positive muons. In red is the distribution after the selection of the mean time difference between the two muons smaller than 15 ns.

7.2 Z Vertex Distribution

The Z vertex distribution for masses larger than $4.5 \text{ GeV}/c^2$ without and with the image cut is shown in Fig. 7.13. Contrary to 2014, here the vertices positions are as expected taking into account the target limits indicated in green. Fig. 7.14 shows the ratio between the two distributions. The image cut has a bigger impact in pairs from tungsten region. The number of reconstructed vertices in vertex detector position is small and it is more or less the same with or without the image cut applied as expected. This result also evidences the problem present in the reconstruction of the 2014 data regarding the use of the vertex detector in the reconstruction.

7.3 Dimuon Mass Distribution and the Impact of the Trigger Validation

In Fig. 7.15 the dimuon mass distribution without the trigger validation and the image cuts applied is shown. Fig. 7.16 shows the dimuon mass distribution with the trigger validation applied, but still without the image cut. The fit function used in both cases is different from the one used in 2014, here was not possible to let the ψ' parameters free and to fit the continuum under the resonances was not possible to use only a power law. The function used was a sum of two Gaussians, a sum of one power law and one exponential to fit the continuum under the resonances. The ψ' mass and width were constrained, as explained in Eq. 5.1. The fit is done in the region from 1.5 to $8 \text{ GeV}/c^2$. The χ^2/ndf of the fits is very high, there are regions where the function is not describing well the distribution. Fig. 7.17 shows the ratio between the fit function and the mass distribution. It is clear the discrepancy in the region of the J/ψ and the ψ' . This indicates that the fit function should be more complex in order to describe all the contributions.

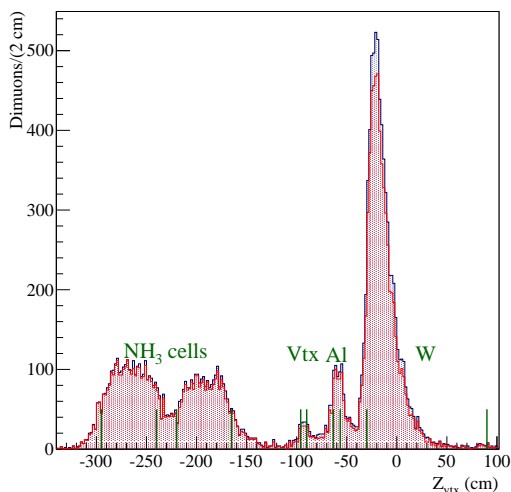


Figure 7.13: Z_{vtx} distributions with the whole selection criteria, apart from the Z_{vtx} selection, for high mass events with and without the image cut. In blue are the vertices distribution without image cut and in red are the vertices after applying the image cut.

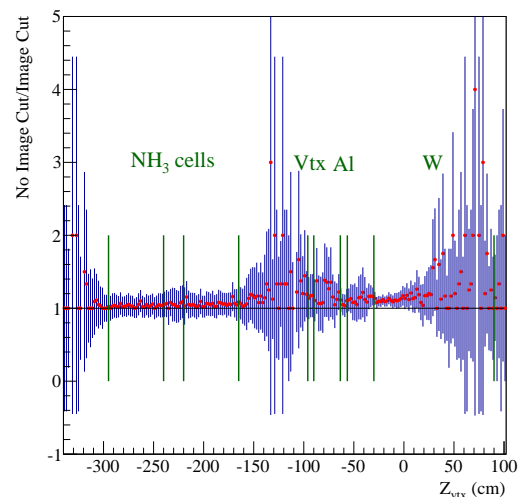


Figure 7.14: Ratio between the Z_{vtx} distributions with and without the image cut for high mass events.

From the fits the number of J/ψ decreased from 362857 ± 789 to 338381 ± 716 6.7%. The loss of J/ψ results from the request of the trigger validation, similar to 2014.

The J/ψ mass in each case is 3.0476 ± 0.0004 and 3.0481 ± 0.0004 , which is $49 \text{ MeV}/c^2$ lower than the PDG mass value. In 2014 it was $26 \text{ MeV}/c^2$ lower than in this case. This difference is believed to be related with the fact that in 2014 the vertex detector was used in the reconstruction and was introducing a bias in the vertices reconstruction. However, the situation will be clarified after the reproduction of the 2014 data without the vertex detector involved in the reconstruction.

The J/ψ mass resolutions are 188.4 ± 0.4 and $188.0 \pm 0.4 \text{ MeV}/c^2$, which are lower than in 2014, $200 \text{ MeV}/c^2$. This reflects a better performance of the reconstruction in 2015.

The number of ψ' are 9868 ± 248 and 9968 ± 228 , around 2.9% of the J/ψ .

The number of pairs with $M_{\mu\mu} > 4 \text{ GeV}/c^2$ decreases from 10546 to 9727, which represents a loss of 7.8% when the trigger validation is required. The high mass pairs is 2.9% of the J/ψ .

7.4 Combinatorial Background Estimation

In Fig. 7.18 the dimuon mass distribution is shown together with the like-sign pairs mass distributions. Fig. 7.19 shows the same distributions after applying the image cut. In Fig. 7.20 the combinatorial background evaluation is shown. The impact in the statistics after applying the image cut is a loss of around 33% for all masses. The number of J/ψ decreases from 338381 ± 716 to 313525 ± 685 , a loss of around 7%. The number of pairs with $M_{\mu\mu} > 4 \text{ GeV}/c^2$ decreases from 9727 to 9147, a loss of 6%.

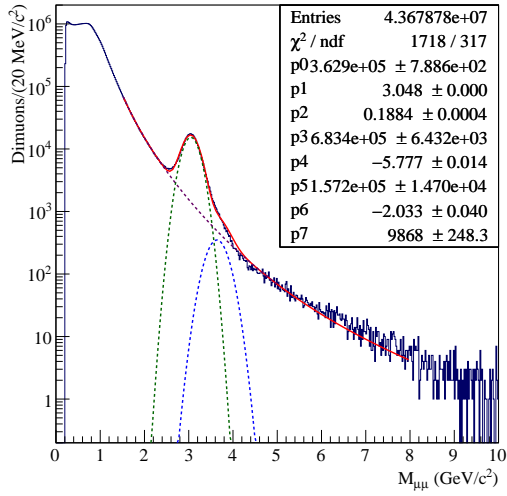


Figure 7.15: Dimuon mass distribution. This distribution is obtained without the trigger validation and the image cut are applied.

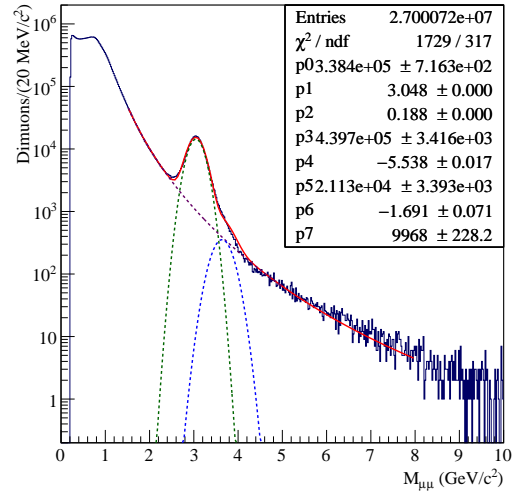


Figure 7.16: Dimuon mass distribution. This distribution is obtained after the trigger validation is applied and without the image cut applied.

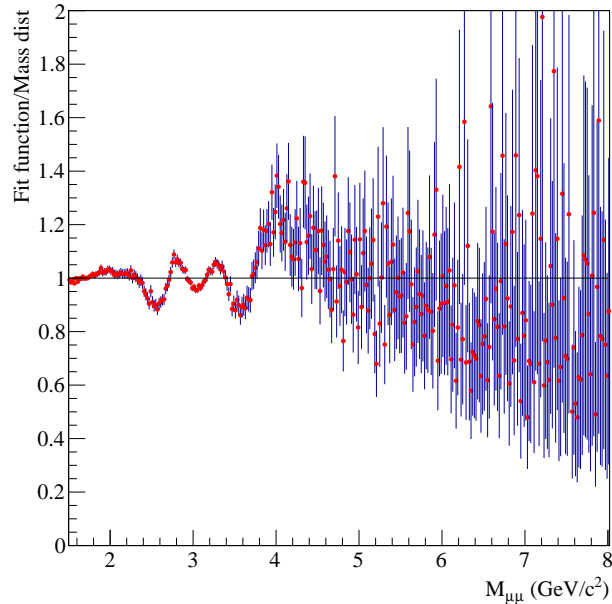


Figure 7.17: Ratio between the fit function and the mass distribution presented in Fig. 7.16.

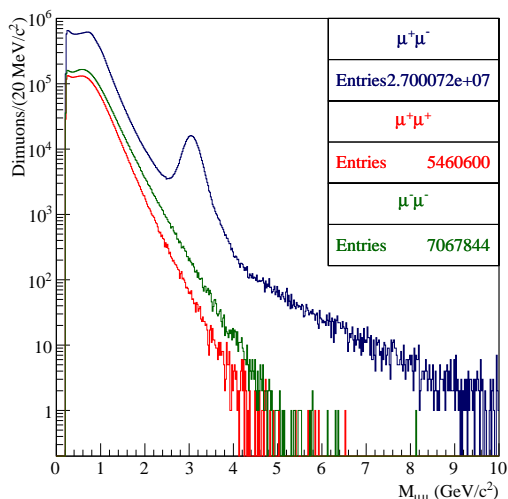


Figure 7.18: Mass distributions. The lines with blue, red, and green colours represent the opposite sign muon pairs, the positive like-sign and the negative like-sign pairs, respectively.

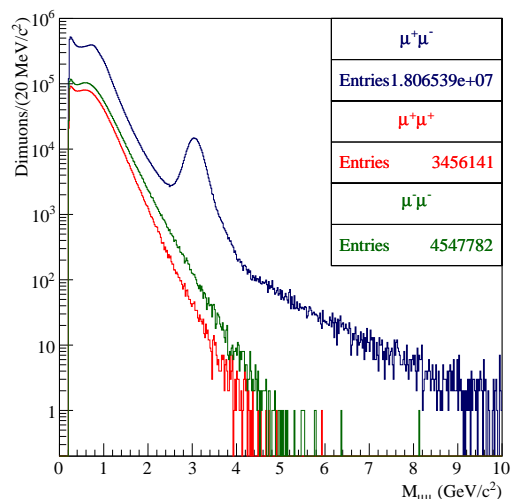


Figure 7.19: Mass distributions after applying the image cut. The lines with blue, red, and green colours represent the opposite sign muon pairs, the positive like-sign and the negative like-sign pairs, respectively.

	Dimuon trig	LAST-LAST	LAST-MT	LAST-OT
$\#J/\psi$	313525±685	188244±478 (60.0%)	22072±242 (7.0%)	119403±448 (38.1%)
$\#\psi'$	9599±228	4903±137 (51.1%)	644±98 (6.7%)	3867±151 (40.3%)
$\#\mu^+\mu^- M > 4$	9147	5432 (59.4%)	688 (7.5%)	3546 (38.8%)
$\#\psi'$ tail $M > 4$	505	196	74	271
$\#\text{Bkg } M > 4$	101	5	85	36
Contamination $M > 4$	6.6%	3.7%	23.1%	8.7%

Table 7.3: Statistics divided by trigger.

7.5 Dimuon Mass Distributions by Trigger

In Fig. 7.21 the dimuon mass distribution selecting only the LAS-LAS double trigger is presented. The spectrum was fitted with the same function as the previous mass distributions. In Fig. 7.22 the dimuon mass distribution selecting only the LAS-Middle double trigger is shown. In this case only an exponential was used to fit the continuum under the resonances. Fig. 7.23 shows the dimuon mass distribution selecting only the LAS-Outer double trigger. It is visible that only LAS-LAS has acceptance at very low masses. The combinatorial background extends to higher masses in the case of the middle trigger. A summary of the results is presented in Table 7.3. The distribution of events per trigger is very similar to the case of 2014 data.

7.6 Kinematic Distributions

All the kinematic distributions were obtained for masses larger than 4 GeV/c^2 , where the DY contribution dominates. They are similar to the ones from 2014 data. In Fig. 7.24 the dimuon momentum distribution is shown, without any trigger separation and also divided by trigger.

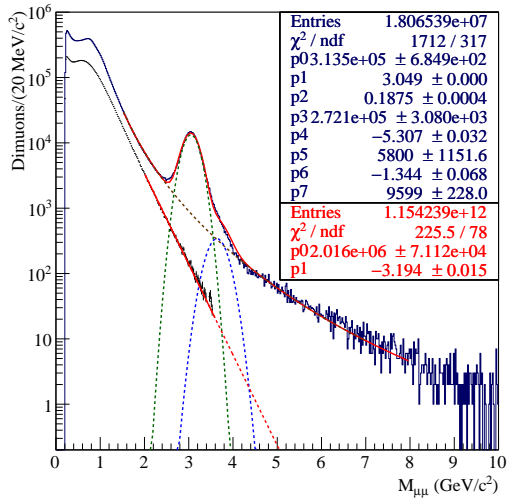


Figure 7.20: In blue is the dimuon mass distribution after the image cut. In red is the combinatorial background calculated after the image cut procedure and using the like-sign pairs.

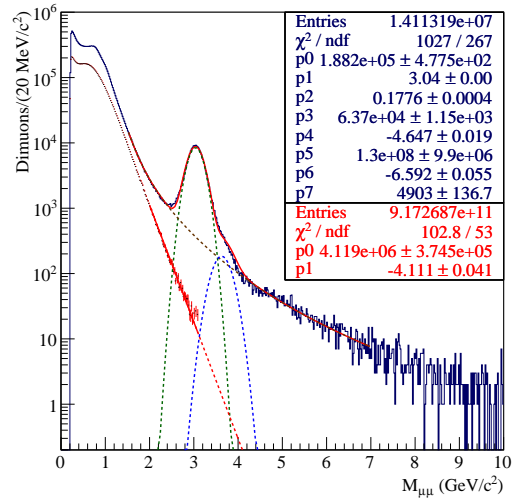


Figure 7.21: Mass distribution for LAS-LAS double trigger.

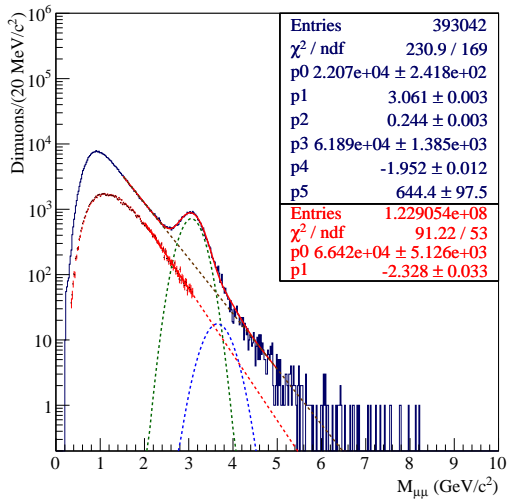


Figure 7.22: Mass distribution for LAS-Middle double trigger.

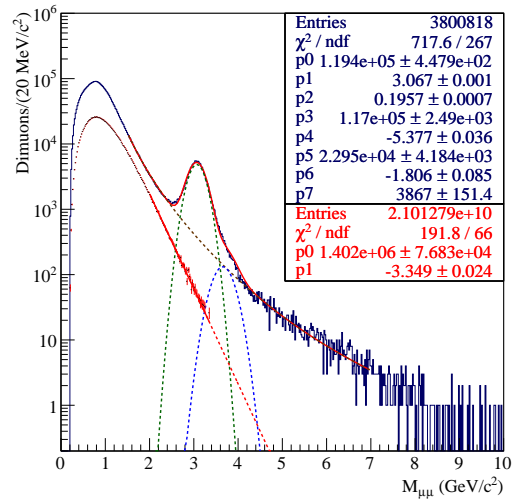


Figure 7.23: Mass distribution for LAS-Outer double trigger.

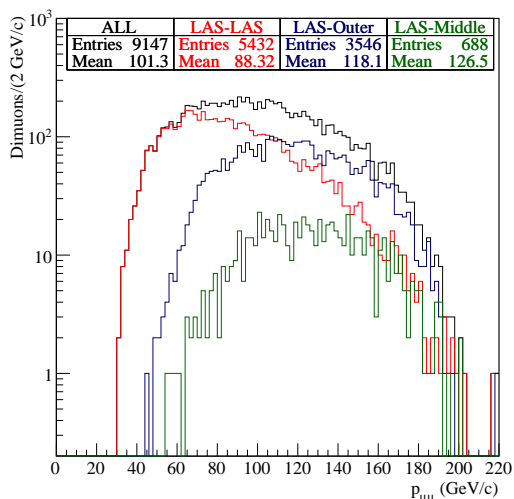


Figure 7.24: Dimuon momentum distribution for $M_{\mu\mu} > 4 \text{ GeV}/c^2$.

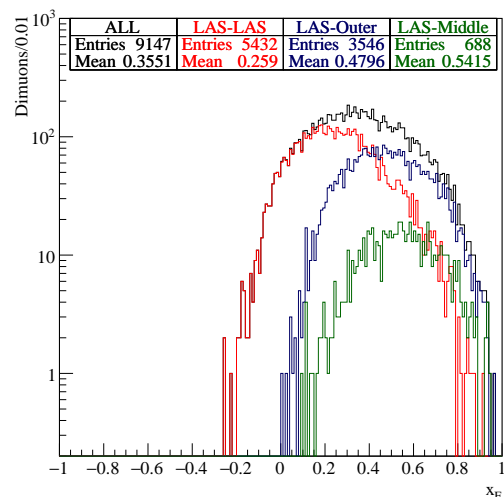


Figure 7.25: Feynman x distribution for $M_{\mu\mu} > 4 \text{ GeV}/c^2$.

The LAS-LAS trigger covers lower momenta than LAS-Outer and LAS-Middle. In Fig. 7.25 the Feynman x distribution is presented, again superimposed with the distributions divided by trigger. The LAS-LAS trigger dominates for low x_F , while SAS triggers cover the higher x_F . Fig. 7.26 shows the dimuon transverse momentum distribution, LAS-LAS events extends to higher p_T . In Fig. 7.27 the x_1 versus x_2 distribution is shown. The individual x_1 distributions divided by trigger are shown in Fig. 7.28, the LAS-LAS events cover the low x_1 region, while the LAS-SAS triggers cover the higher x_1 , which is expected since larger x_1 corresponds to a larger momentum fraction carried by the pion quark. Therefore, the event will be more forward. Fig. 7.29 shows the x_2 distribution divided by trigger, in this case is the opposite to x_1 , LAS-LAS events cover the higher x_2 , while LAS-SAS events cover the lower x_2 . Since the valence region of the proton is more interesting, the LAS-LAS events are more relevant. In Fig. 7.30 is the distribution of the cosine of the polar angle of the positive muon in the Collin-Soper frame. In Fig. 7.31 is the distribution of the azimuthal angle between the hadrons plane and the leptons plane in the CS frame. In Fig. 7.32 is the angle of the target spin in the target rest frame. These angles are going to be used for the extraction of the asymmetries.

7.7 Asymmetries Extraction

An analysis similar to the one done for the SIDIS data, presented in Chapter 4, is going to be done for these polarised DY data. The first step in the analysis chain must be the quality checks, performed in a spill by spill basis. These checks are ongoing for the already produced data as a function of all the relevant variables. An analysis divided by trigger is also being preformed. The outcome of these checks is going to be a list of bad spills to be removed from the analysis. The selection criteria presented here is not the final one, and is also being tuned, testing different cuts and its impact in the final statistics. Nevertheless, the selection presented here can be considered a good approximation to the final sample.

The extracted asymmetries must be corrected by the dilution factor and the target polarisation. The preliminary value for the dilution factor is ≈ 0.22 . The preliminary average target polarisation by configuration and cell is quoted in Table 7.4. It is around 80% and, due to the relaxation time (around 1000 h), there is a loss of 8% after 4 days.

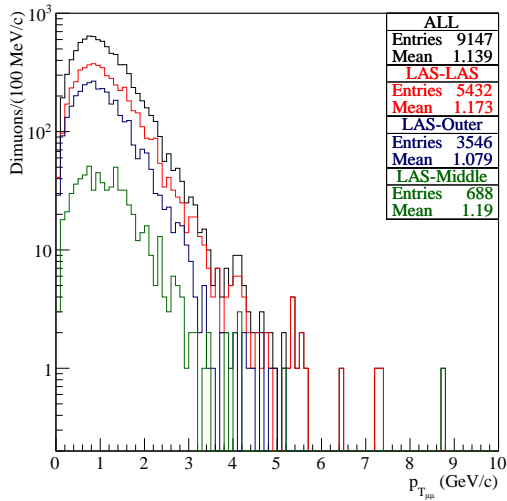


Figure 7.26: Dimuon transverse momentum distribution for $M_{\mu\mu} > 4 \text{ GeV}/c^2$.

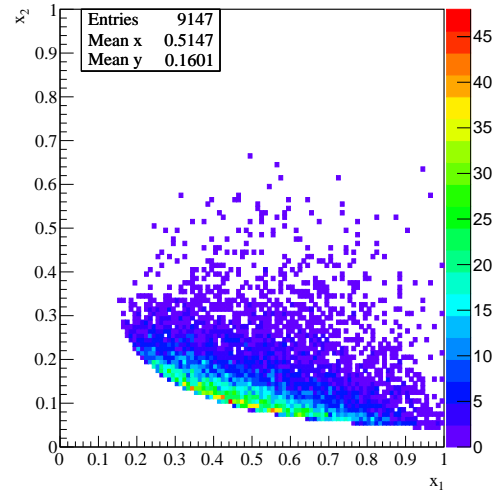


Figure 7.27: x_2 versus x_1 distribution for $M_{\mu\mu} > 4 \text{ GeV}/c^2$.

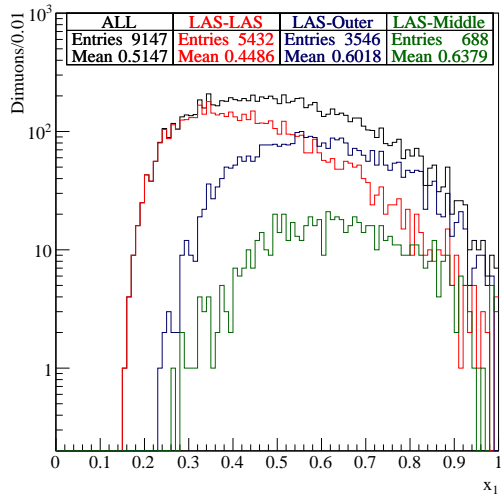


Figure 7.28: x_1 distribution for $M_{\mu\mu} > 4 \text{ GeV}/c^2$.

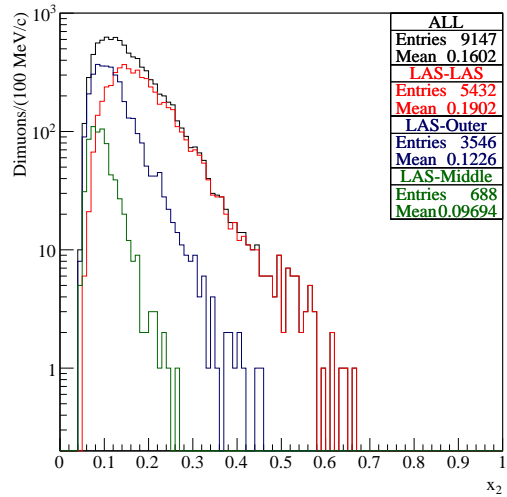
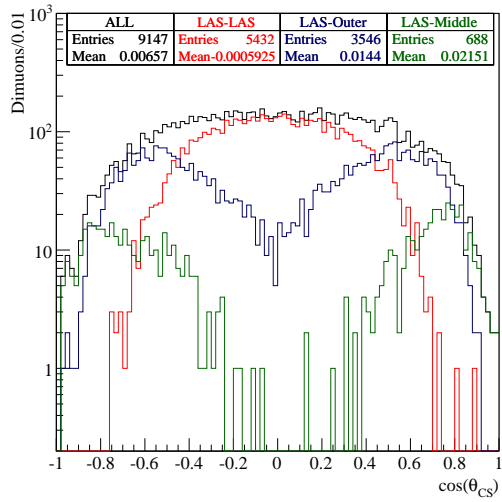
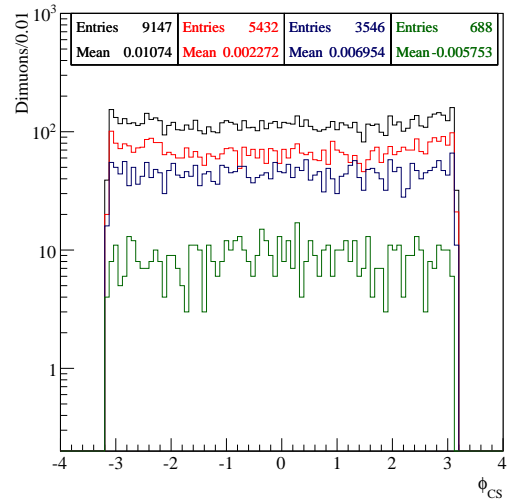
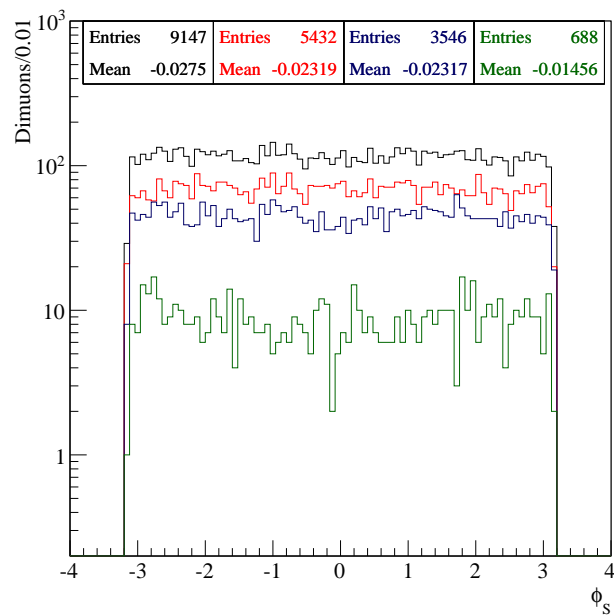


Figure 7.29: x_2 distribution for $M_{\mu\mu} > 4 \text{ GeV}/c^2$.

Figure 7.30: Distribution of the $\cos(\theta_{CS})$.Figure 7.31: Distribution of the ϕ_{CS} .Figure 7.32: Distribution of the ϕ_S .

Configuration	Upstream cell		Downstream cell	
	Pol.	Rel. Time	Pol.	Rel. Time
$\uparrow\downarrow$	82.5	1351 h	-77.7	777 h
$\downarrow\uparrow$	-85.8	1062 h	80.2	969 h

Table 7.4: Preliminary values for the mean target polarisation and relaxation time for each cell. Both spin configurations are shown.

The data taking strategy was decided based on these values. It was decided to reverse the spin configuration and re-polarise fully every two weeks, for 24 h, taking advantage of the Machine Development (MD), which lasts for 10 h without beam. In between the two sequential periods the polarisation is increased, taking advantage again of the MD.

The distribution of ammonia in the two target cells is important to be known with precision. As the cells were empty in the end of the 2014 run and refilled in the beginning of the 2015 run, the packing factor, that is the fraction of material inside the cells which corresponds to ammonia beads (the ammonia granulate being immersed in an helium bath inside each cell) varied from 2014 to 2015 and from upstream to downstream cell. It was 0.52 for upstream cell and 0.46 for the downstream cell in 2014. In 2015 it was slightly higher, 0.57 for the upstream cell and 0.48 for the downstream cell. These factors must be taken into account for the description of the target cells in MC.

Conclusion

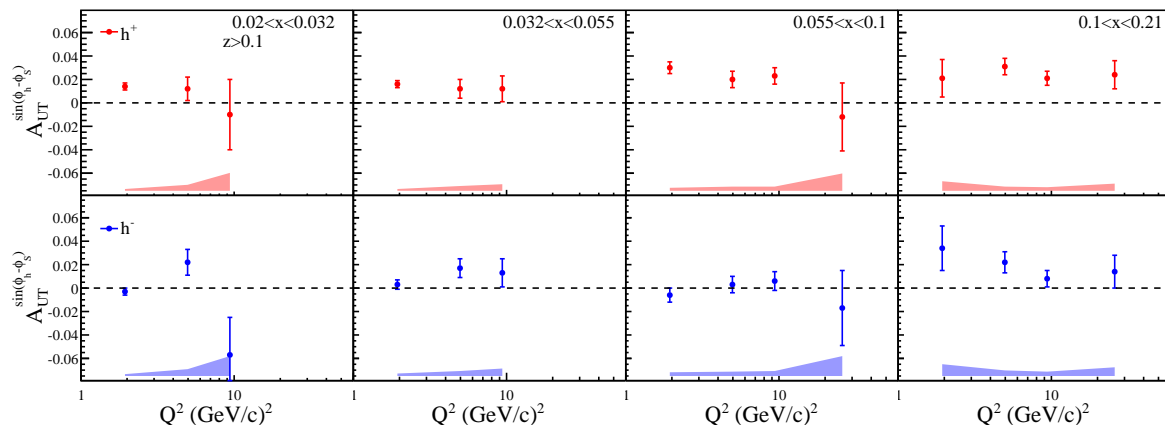
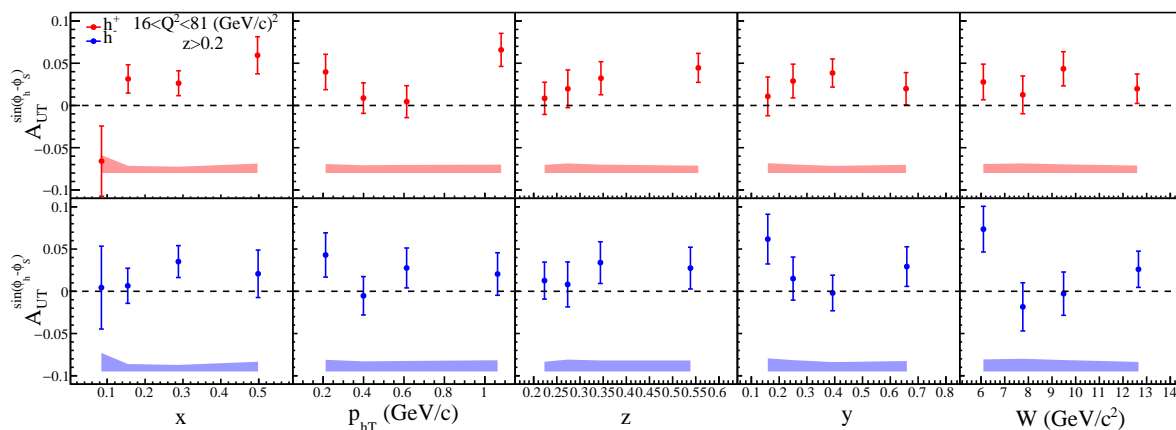
COMPASS has a unique opportunity to access the Transverse Momentum Dependent Parton Distribution Functions through two different processes, SIDIS and DY, in the same kinematic region. In 2010, SIDIS measurements were performed with longitudinally polarised positive muons scattering off a transversely polarised proton (ammonia) target. These data were analysed and lead to the COMPASS results without any direct Q^2 selection, already published [46], [51] and [47]. In this thesis the analysis of these data in different Q^2 ranges is presented, in particular in the overlapping region between SIDIS and high mass DY events, $M_{\mu\mu} > 4 \text{ GeV}/c^2$, where the DY pairs dominate. In 2015, COMPASS took for the first time polarised DY data, using a negative pion beam impinging on a similar transversely polarised ammonia target. These data are now being analysed. The outcome of the analysis are going to be the target spin (in)dependent asymmetries, which are convolutions of two PDFs. The proton PDFs are expected to be the same when extracted through SIDIS or through DY, thus confirming their universality. There are four PDFs that can be extracted from both processes, the transversity, the pretzelosity, the Sivers and the Boer-Mulders. In SIDIS they appear convoluted with a Fragmentation Function, while in DY they are convoluted with a PDF from the pion. COMPASS data should be very useful for the extraction of the TMDs via global fits.

In SIDIS the Sivers asymmetry is positive for positive hadrons and increases with x , for negative hadrons is compatible with zero, apart from some bins. The dependence of the asymmetry with Q^2 is not evident within the statistical accuracy, however there is a hint of a small decrease with Q^2 at the same x for positive hadrons. This dependence is shown in Fig. 8.1. The prediction of the Sivers and Boer-Mulders sign change when accessed from SIDIS or DY should be verified using the COMPASS data.

From SIDIS in $16 < Q^2 < 81 \text{ (GeV}/c^2)^2$ and $z > 0.2$ there are 2M hadrons, 1.2M being positive and 0.8M negative. This gives a statistical error in the Sivers asymmetry of around 0.010 and 0.013. In the case of $z > 0.1$, the errors diminish by around 40% and are 0.007 and 0.009 for the positive and negative hadrons, respectively. The Sivers asymmetry in the overlapping Q^2 region between SIDIS and DY is shown in Fig. 8.2 in bins of x , p_{Th} , z , y and W , the increase with x is visible.

In the highest x the asymmetry is $5.9\% \pm 2.2\%$, 2.7σ from zero. It is also positive for other kinematic bins, in high p_{Th} and in high z for positive hadrons. Nevertheless this is the lowest statistics Q^2 bin from SIDIS data (2.6% of statistics), and the statistical errors here are big. But the trends are similar in all the Q^2 bins.

The Sivers asymmetry, integrated over x , in the four different Q^2 bins and in the three z ranges is shown in Fig. 8.3. It decreases from $z > 0.2$ to $0.1 < z < 0.2$ for positive hadrons in the largest Q^2 bin, being 3.1σ from zero for $z > 0.1$ and $z > 0.2$. For negative hadrons it

Figure 8.1: Sivers asymmetry for different x bins in bins of Q^2 .Figure 8.2: Sivers asymmetry for $16 < Q^2 < 81$ (GeV/c^2)² and in several bins of x , p_{T_h} , z , y and W .

increases with Q^2 . In the largest Q^2 bin it is positive, 1.6σ from zero for $z > 0.2$ and 2.1σ for $z > 0.1$.

The Collins asymmetry is also different from zero, it is positive for negative hadrons and negative for positive hadrons. This asymmetry contains the convolution of the transversity PDF with the Collins FF, the transversity PDF will be also accessible from the DY data.

All the other 6 asymmetries extracted from SIDIS data are compatible with zero, within the statistical accuracy, in the majority of the bins. However, there are some hints of an asymmetry different from zero for the higher twist asymmetry $A_{UT}^{\sin(\phi_S)}$ related to Collins and Sivers effects. Also the asymmetry $A_{LT}^{\cos(\phi_h - \phi_S)}$, which relates with the worm-gear-T PDF, shows a non-zero effect for large x in agreement with some theoretical predictions. There are some hints of an asymmetry different from zero for the asymmetry $A_{UT}^{\sin(3\phi_h - \phi_S)}$, which is related with the Pretzelosity, which will be also accessible from DY, nevertheless there are theoretical predictions [119] pointing for a very small effect in this case.

Concerning the Boer-Mulders asymmetry it is more difficult to be extracted, since it is an unpolarised asymmetry, and the acceptance effects should be considered. Several experiments contributed for its measurement from SIDIS, such as COMPASS [53]. From DY there is already published results from past experiments of a big Boer-Mulders asymmetry (up to 30%). The

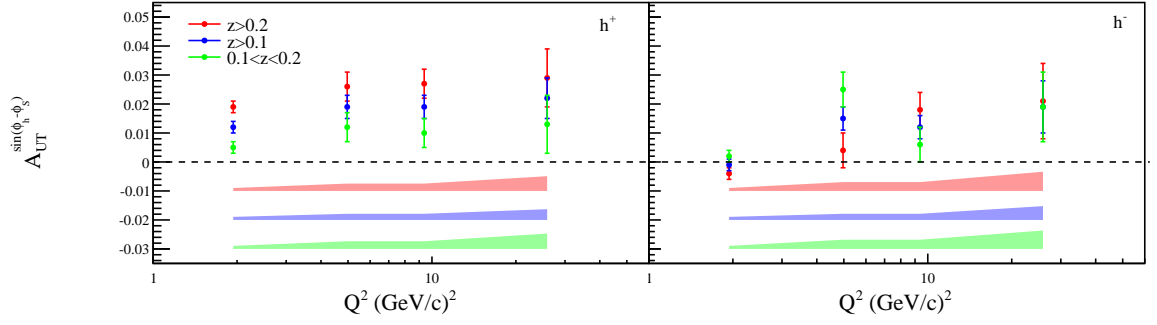


Figure 8.3: Siivers asymmetry for the three different z ranges in bins of Q^2 .

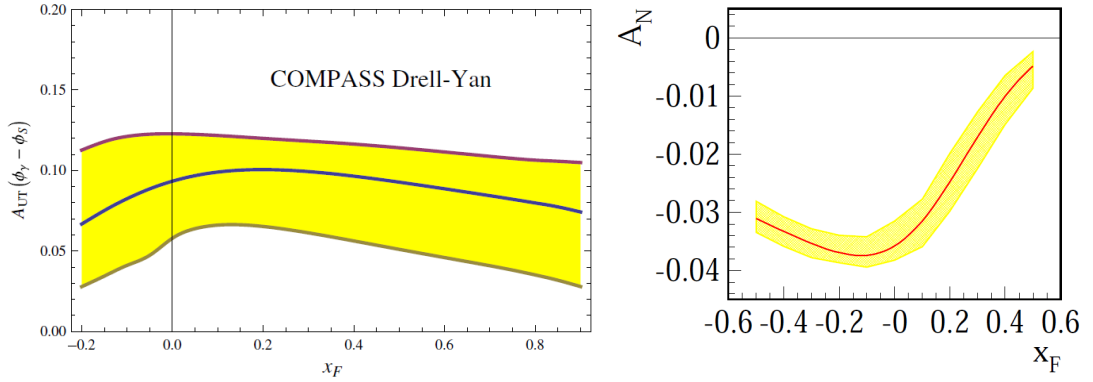


Figure 8.4: Siivers asymmetry predictions. The prediction on the right hand side [72] consider $x_F = x_\pi - x_p$ and has a cut on $p_T < 2 \text{ GeV}/c$. The prediction on the left hand side [73] consider $x_F = x_p - x_\pi$ and has a cut on $p_T < 1 \text{ GeV}/c$.

sign change prediction for the Boer-Mulders PDF can be tested using both the SIDIS and the DY data.

From DY in the high mass region 80000 pairs are expected, which gives a statistical error of 0.028. Some theoretical predictions point to a Siivers asymmetry of up to 10% [72, 73]. These predictions are shown in Figure 8.4, both predictions used the pion PDF [123]. In this scenario the verification of the sign change will be statistically significant.

Combinatorial background evaluation

The combinatorial background is formed by uncorrelated opposite sign muon pairs from pion and kaon decays:

$$\begin{aligned}\pi^+ &\rightarrow \mu^+ \nu_\mu \\ \pi^- &\rightarrow \mu^- \bar{\nu}_\mu \\ K^+ &\rightarrow \mu^+ \nu_\mu \\ K^- &\rightarrow \mu^- \bar{\nu}_\mu\end{aligned}$$

A large amount of mesons, mostly pions (and kaons), is produced in the same event in hadronic cascade interactions in the hadron absorber due to the use of a high intensity beam. So, a large amount of them may decay before the following interaction step, giving rise to a certain number of uncorrelated muons, that can combine to give pairs.

The combinatorial background can be estimated statistically using the like-sign muon pairs detected.

Considering that the produced hadrons multiplicity per event follows a Poisson law, which is true in the case of a high intensity beam, the number of generated meson pairs is:

$$n^+ C_2 = \frac{n^+!}{2(n^+ - 2)!} = \frac{n^+(n^+ - 1)}{2} \quad (\text{A.1})$$

and

$$n^- C_2 = \frac{n^-!}{2(n^- - 2)!} = \frac{n^-(n^- - 1)}{2} \quad (\text{A.2})$$

for a sample of n^+ positive mesons and n^- negative mesons.

If $P(n^+)$ and $P(n^-)$ are the probabilities to produce n^+ mesons and n^- mesons, and ω is the probability of a single meson to decay into $\mu + X$, the numbers of uncorrelated like-sign muon pairs N^{++} and N^{--} produced in N interactions are:

$$N^{++} = NA^{++}\omega^2 \int P(n^+) \frac{n^+(n^+ - 1)}{2} dn^+ = \frac{N}{2} A^{++}\omega^2 (\langle n^{+2} \rangle - \langle n^+ \rangle) \quad (\text{A.3})$$

and

$$N^{--} = NA^{--}\omega^2 \int P(n^-) \frac{n^-(n^- - 1)}{2} dn^- = \frac{N}{2} A^{--}\omega^2 (\langle n^{-2} \rangle - \langle n^- \rangle) \quad (\text{A.4})$$

where A^{++} and A^{--} are the geometrical acceptances of the spectrometer. In the case of N^{+-} , it is given by:

$$N^{+-} = NA^{+-}\omega^2 \int P(n^-)P(n^+)n^+n^- dn^+ dn^- = NA^{+-}\omega^2 (\langle n^+ \rangle \langle n^- \rangle) \quad (\text{A.5})$$

Since $\langle n \rangle = \langle n^2 \rangle - \langle n \rangle^2$ then:

$$N^{+-} = 2\sqrt{N^{++}N^{--}} \frac{A^{+-}}{\sqrt{A^{++}A^{--}}} . \quad (\text{A.6})$$

The image cut explained in section 5.10 is used to ensure that the spectrometer is charge symmetric guaranteeing that the factor $\frac{A^{+-}}{\sqrt{A^{++}A^{--}}}$ is equal to 1.

NOTE:

In the case of limited statistics, or if some bins empty, the expression is generalized to

$$N^{+-} = 2R\sqrt{N^{++}N^{--}},$$

R being slightly > 1 , value that must be evaluated by a dedicated Monte Carlo.

Bibliography

- [1] J. Ashman et al., EMC Collaboration. “A Measurement of the spin asymmetry and determination of the structure function g_1 in deep inelastic muon-proton scattering”. In: *Phys. Lett. B* 206 (1988), p. 364. DOI: 10.1016/0370-2693(88)91523-7.
- [2] V.Yu. Alexakhin et al., COMPASS Collaboration. “The deuteron spin-dependent structure function g_1^d and its first moment”. In: *Phys. Lett. B* 647 (2007), p. 8. DOI: 10.1016/j.physletb.2006.12.076.
- [3] J.P. Ralston and D. E. Soper. “Production of dimuons from high-energy polarized proton-proton collisions”. In: *Nucl. Phys. B* 152 (1979), p. 109. DOI: 10.1016/0550-3213(79)90082-8.
- [4] Robert N. Cahn. “Azimuthal dependence in lepton production: A simple parton model calculation”. In: *Phys. Lett. B* 78 (1978), pp. 269 –273. DOI: 10.1016/0370-2693(78)90020-5.
- [5] John C. Collins and Davison E. Soper. “Back-to-back jets in QCD”. In: *Nuclear Physics B* 193 (1981), pp. 381 –443. DOI: 10.1016/0550-3213(81)90339-4.
- [6] John C. Collins and Davison E. Soper. “Errata - Back-to-back jets in QCD”. In: *Nuclear Physics B* 213 (1983), p. 545. DOI: 10.1016/0550-3213(83)90235-3.
- [7] John C. Collins and Davison E. Soper. “Parton distribution and decay functions”. In: *Nuclear Physics B* 194 (1982), pp. 445 –492. DOI: 10.1016/0550-3213(82)90021-9.
- [8] D. Müller et al. “Wave Functions, Evolution Equations and Evolution Kernels from Light-Ray Operators of QCD”. In: *Fortschr. Phys.* 42 (1994), p. 101. DOI: 10.1002/prop.2190420202.

- [9] R. D. Klem et al. “Measurement of Asymmetries of Inclusive Pion Production in Proton-Proton Interactions at 6 and 11.8 GeV/c”. In: *Phys. Rev. Lett.* 36 (1976), p. 929. DOI: 10.1103/PhysRevLett.36.929.
- [10] W. H. Dragoset et al. “Asymmetries in inclusive proton-nucleon scattering at 11.75 GeV/c”. In: *Phys. Rev. D* 18 (1978), p. 3939. DOI: 10.1103/PhysRevD.18.3939.
- [11] M. J. Alguard et al., E80 Collaboration. “Deep Inelastic Scattering of Polarized Electrons by Polarized Protons”. In: *Phys. Rev. Lett.* 37 (1976), p. 1261. DOI: 10.1103/PhysRevLett.37.1261.
- [12] M. J. Alguard et al., E80 Collaboration. “Deep-Inelastic $e-p$ Asymmetry Measurements and Comparison with the Bjorken Sum Rule and Models of Proton Spin Structure”. In: *Phys. Rev. Lett.* 41 (1978), p. 70. DOI: 10.1103/PhysRevLett.41.70.
- [13] G. Baum et al., E130 Collaboration. “Measurement of Asymmetry in Spin-Dependent $e-p$ Resonance-Region Scattering”. In: *Phys. Rev. Lett.* 45 (1980), p. 2000. DOI: 10.1103/PhysRevLett.45.2000.
- [14] G. Baum et al., E130 Collaboration. “New Measurement of Deep-Inelastic $e-p$ Asymmetries”. In: *Phys. Rev. Lett.* 51 (1983), p. 1135. DOI: 10.1103/PhysRevLett.51.1135.
- [15] P. L. Anthony et al., E142 Collaboration. “Deep inelastic scattering of polarized electrons by polarized ^3He and the study of the neutron spin structure”. In: *Phys. Rev. D* 54 (1996), p. 6620. DOI: 10.1103/PhysRevD.54.6620.
- [16] K. Abe et al., E143 Collaboration. “Measurements of the proton and deuteron spin structure functions g_1 and g_2 ”. In: *Phys. Rev. D* 58 (1998), p. 112003. DOI: 10.1103/PhysRevD.58.112003.
- [17] K. Abe et al., E154 Collaboration. “Precision Determination of the Neutron Spin Structure Function g_1^n ”. In: *Phys. Rev. Lett.* 79 (1997), p. 26. DOI: 10.1103/PhysRevLett.79.26.
- [18] P. L. Anthony et al., E155 Collaboration. “Measurements of the deuteron spin structure function $g_1^d(x)$ for $1 (\text{GeV}/c)^2 < Q^2 < 40 (\text{GeV}/c)^2$ ”. In: *Phys. Lett. B* 463 (1999), p. 339. DOI: 10.1016/S0370-2693(99)00940-5.
- [19] P. L. Anthony et al., E155 Collaboration. “Measurements of the Q^2 -dependence of the proton and neutron spin structure functions g_1^p and g_1^n ”. In: *Phys. Lett. B* 493 (2000), p. 19. DOI: 10.1016/S0370-2693(00)01014-5.

-
- [20] J. Ashman et al., EMC Collaboration. “An investigation of the spin structure of the proton in deep inelastic scattering of polarised muons on polarised protons”. In: *Nucl. Phys. B* 328 (1989), p. 1. DOI: 10.1016/0550-3213(89)90089-8.
- [21] B. Adeva et al., SMC Collaboration. “Polarisation of valence and non-strange sea quarks in the nucleon from semi-inclusive spin asymmetries”. In: *Phys. Lett. B* 369 (1996), p. 93. DOI: 10.1016/0370-2693(95)01584-1.
- [22] B. Adeva et al., SMC Collaboration. “Polarised quark distributions in the nucleon from semi-inclusive spin asymmetries”. In: *Phys. Lett. B* 420 (1998), p. 180. DOI: 10.1016/S0370-2693(97)01546-3.
- [23] A. Airapetian et al., HERMES Collaboration. “Precise determination of the spin structure function g_1 of the proton, deuteron, and neutron”. In: *Phys. Rev. D* 75 (2007), p. 012007. DOI: 10.1103/PhysRevD.75.012007.
- [24] A. Airapetian et al., HERMES Collaboration. “Measurement of parton distributions of strange quarks in the nucleon from charged-kaon production in deep-inelastic scattering on the deuteron”. In: *Phys. Lett. B* 666 (2008), p. 446. DOI: 10.1016/j.physletb.2008.07.090.
- [25] M.G. Alekseev et al., COMPASS Collaboration. “The spin-dependent structure function of the proton and a test of the Bjorken sum rule”. In: *Phys. Lett. B* 690 (2010), p. 466. DOI: 10.1016/j.physletb.2010.05.069.
- [26] M.G. Alekseev et al., COMPASS Collaboration. “Quark helicity distributions from longitudinal spin asymmetries in muon-proton and muon-deuteron scattering”. In: *Phys. Lett. B* 693 (2010), p. 227. DOI: 10.1016/j.physletb.2010.08.034.
- [27] X. Zheng et al., JLab Hall A Collaboration. “Precision Measurement of the Neutron Spin Asymmetry A_1^n and Spin-Flavor Decomposition in the Valence Quark Region”. In: *Phys. Rev. Lett.* 92 (2004), p. 012004. DOI: 10.1103/PhysRevLett.92.012004.
- [28] K.V. Dharmawardane et al., CLAS Collaboration. “Measurement of the x - and Q^2 -dependence of the asymmetry A_1 on the nucleon”. In: *Phys. Lett. B* 641 (2006), p. 11. DOI: 10.1016/j.physletb.2006.08.011.
- [29] A. Airapetian et al., HERMES Collaboration. “Quark helicity distributions in the nucleon for up, down, and strange quarks from semi-inclusive deep-inelastic scattering”. In: *Phys. Rev. D* 71 (2005), p. 012003. DOI: 10.1103/PhysRevD.71.012003.

- [30] Daniel de Florian et al. “Extraction of spin-dependent parton densities and their uncertainties”. In: *Phys. Rev. D* 80 (2009), p. 034030. DOI: 10.1103/PhysRevD.80.034030.
- [31] D. de Florian, R. Sassot, and M. Stratmann, DSS Group. “Global analysis of fragmentation functions for pions and kaons and their uncertainties”. In: *Phys. Rev. D* 75 (2007), p. 114010. DOI: 10.1103/PhysRevD.75.114010.
- [32] D.L. Adams et al., E581/704 Collaboration. “Measurement of the double-spin asymmetry A_{LL} for inclusive multi- γ pair production with 200 GeV/ c polarized proton beam and polarized proton target”. In: *Phys. Lett. B* 336 (1994), p. 269. DOI: 10.1016/0370-2693(94)00998-8.
- [33] A. Airapetian et al., HERMES Collaboration. “Measurement of the Spin Asymmetry in the Photoproduction of Pairs of High- p_T Hadrons at HERMES”. In: *Phys. Rev. Lett.* 84 (2000), p. 2584. DOI: 10.1103/PhysRevLett.84.2584.
- [34] B. Adeva et al., SMC Collaboration. “Spin asymmetries for events with high p_T hadrons in DIS and an evaluation of the gluon polarization”. In: *Phys. Rev. D* 70 (2004), p. 012002. DOI: 10.1103/PhysRevD.70.012002.
- [35] E.S. Ageev et al., COMPASS Collaboration. “Gluon polarization in the nucleon from quasi-real photoproduction of high- p_T hadron pairs”. In: *Phys. Lett. B* 633 (2006), p. 25. DOI: 10.1016/j.physletb.2005.11.049.
- [36] M. Alekseev et al., COMPASS Collaboration. “Gluon polarisation in the nucleon and longitudinal double spin asymmetries from open charm muoproduction”. In: *Phys. Lett. B* 676 (2009), p. 31. DOI: 10.1016/j.physletb.2009.04.059.
- [37] C. Adolph et al., COMPASS Collaboration. “Leading and next-to-leading order gluon polarization in the nucleon and longitudinal double spin asymmetries from open charm muoproduction”. In: *Phys. Rev. D* 87 (2013), p. 052018. DOI: 10.1103/PhysRevD.87.052018.
- [38] Airapetian et al., COMPASS Collaboration. “Leading-order determination of the gluon polarization from high- p_T hadron electroproduction”. In: *Journal of High Energy Physics* 2010 (2010), p. 130. DOI: 10.1007/JHEP08(2010)130.
- [39] C. Adolph et al., COMPASS Collaboration. “Leading order determination of the gluon polarisation from DIS events with high- p_T hadron pairs”. In: *Phys. Lett. B* 718 (2013), p. 922. DOI: 10.1016/j.physletb.2012.11.056.

-
- [40] Daniel de Florian et al. “Evidence for Polarization of Gluons in the Proton”. In: *Phys. Rev. Lett.* 113 (2014), p. 012001. DOI: 10.1103/PhysRevLett.113.012001.
- [41] P.J Mulders and R.D Tangerman. “The complete tree-level result up to order $1/Q$ for polarized deep-inelastic leptonproduction”. In: *Nucl. Phys. B* 461 (1996), p. 197. DOI: 10.1016/0550-3213(95)00632-X.
- [42] Alessandro Bacchetta et al. “Semi-inclusive deep inelastic scattering at small transverse momentum”. In: *Journal of High Energy Physics* 02 (2007), p. 093. DOI: 10.1088/1126-6708/2007/02/093.
- [43] E.S. Ageev et al., COMPASS Collaboration. “A new measurement of the Collins and Sivers asymmetries on a transversely polarised deuteron target”. In: *Nucl. Phys. B* 765 (2007), p. 31. DOI: 10.1016/j.nuclphysb.2006.10.027.
- [44] M. Alekseev et al., COMPASS Collaboration. “Collins and Sivers asymmetries for pions and kaons in muon-deuteron DIS”. In: *Phys. Lett. B* 673 (2009), p. 127. DOI: 10.1016/j.physletb.2009.01.060.
- [45] M.G. Alekseev et al., COMPASS Collaboration. “Measurement of the Collins and Sivers asymmetries on transversely polarised protons”. In: *Phys. Lett. B* 692 (2010), p. 240. DOI: 10.1016/j.physletb.2010.08.001.
- [46] C. Adolph et al., COMPASS Collaboration. “I - Experimental investigation of transverse spin asymmetries in $\mu - p$ SIDIS processes: Collins asymmetries”. In: *Phys. Lett. B* 717 (2012), p. 376. DOI: 10.1016/j.physletb.2012.09.055.
- [47] C. Adolph et al., COMPASS Collaboration. “Collins and Sivers asymmetries in muon-production of pions and kaons off transversely polarised protons”. In: *Phys. Lett. B* 744 (2015), p. 250. DOI: <http://dx.doi.org/10.1016/j.physletb.2015.03.056>.
- [48] A. Airapetian et al., HERMES Collaboration. “Single-Spin Asymmetries in Semi-Inclusive Deep-Inelastic Scattering on a Transversely Polarized Hydrogen Target”. In: *Phys. Rev. Lett.* 94 (2005), p. 012002. DOI: 10.1103/PhysRevLett.94.012002.
- [49] A. Airapetian et al., HERMES Collaboration. “Effects of transversity in deep-inelastic scattering by polarized protons”. In: *Phys. Lett. B* 693 (2010), p. 11. DOI: 10.1016/j.physletb.2010.08.012.

- [50] X. Qian et al., JLab Hall A Collaboration. “Single Spin Asymmetries in Charged Pion Production from Semi-Inclusive Deep Inelastic Scattering on a Transversely Polarized ^3He Target at $Q^2 = 1.4 - 2.7 \text{ GeV}^2$ ”. In: *Phys. Rev. Lett.* 107 (2011), p. 072003. DOI: 10.1103/PhysRevLett.107.072003.
- [51] C. Adolph et al., COMPASS Collaboration. “II - Experimental investigation of transverse spin asymmetries in $\mu - p$ SIDIS processes: Sivers asymmetries”. In: *Phys. Lett. B* 717 (2012), p. 383. DOI: 10.1016/j.physletb.2012.09.056.
- [52] A. Airapetian et al., HERMES Collaboration. “Observation of the Naive- T -Odd Sivers Effect in Deep-Inelastic Scattering”. In: *Phys. Rev. Lett.* 103 (2009), p. 152002. DOI: 10.1103/PhysRevLett.103.152002.
- [53] C. Adolph et al. “Measurement of azimuthal hadron asymmetries in semi-inclusive deep inelastic scattering off unpolarised nucleons”. In: *Nuclear Physics B* 886 (2014), p. 1046. DOI: 10.1016/j.nuclphysb.2014.07.019.
- [54] A. Airapetian et al., HERMES Collaboration. “Azimuthal distributions of charged hadrons, pions, and kaons produced in deep-inelastic scattering off unpolarized protons and deuterons”. In: *Phys. Rev. D* 87 (2013), p. 012010. DOI: 10.1103/PhysRevD.87.012010.
- [55] M. Osipenko et al., CLAS Collaboration. “Measurement of semi-inclusive π^+ electroproduction off the proton”. In: *Phys. Rev. D* 80 (2009), p. 032004. DOI: 10.1103/PhysRevD.80.032004.
- [56] Aram Kotzinian. “Beyond Collins and Sivers: Further measurements of the target transverse spin-dependent azimuthal asymmetries in semi-inclusive DIS from COMPASS”. In: *Proceedings, 15th International Workshop on Deep-inelastic scattering and related subjects (DIS 2007). Vol. 1 and 2.* 2007, p. 647. DOI: 10.3204/proc07-01/107. arXiv: 0705.2402.
- [57] Bakur Parsamyan. “Transverse spin dependent azimuthal asymmetries at COMPASS”. In: vol. 295. 2011, p. 012046. DOI: 10.1088/1742-6596/295/1/012046.
- [58] B. Parsamyan. “Transverse spin asymmetries at COMPASS: beyond Collins and Sivers effects”. In: 2013, p. 231. URL: http://pos.sissa.it/archive/conferences/191/231/DIS%202013_231.pdf.
- [59] L. L. Pappalardo. “Transverse spin dependent azimuthal asymmetries at COMPASS”. In: vol. 125. 2010, p. 51. DOI: 10.1393/ncb/i2010-10827-1.

-
- [60] M.G. Alekseev et al., COMPASS Collaboration. “Azimuthal asymmetries of charged hadrons produced by high-energy muons scattered off longitudinally polarised deuterons”. In: *The European Physical Journal C* 70 (2010), p. 39. DOI: 10.1140/epjc/s10052-010-1461-9.
- [61] A. Airapetian et al., HERMES Collaboration. “Evidence for a Single-Spin Azimuthal Asymmetry in Semi-inclusive Pion Electroproduction”. In: *Phys. Rev. Lett.* 84 (2000), p. 4047. DOI: 10.1103/PhysRevLett.84.4047.
- [62] A. Airapetian et al., HERMES Collaboration. “Single-spin azimuthal asymmetries in electroproduction of neutral pions in semi-inclusive deep-inelastic scattering”. In: *Phys. Rev. D* 64 (2001), p. 097101. DOI: 10.1103/PhysRevD.64.097101.
- [63] A. Airapetian et al., HERMES Collaboration. “Measurement of single-spin azimuthal asymmetries in semi-inclusive electroproduction of pions and kaons on a longitudinally polarised deuterium target”. In: *Phys. Lett. B* 562 (2003), p. 182. DOI: 10.1016/S0370-2693(03)00566-5.
- [64] H. Avakian et al., CLAS Collaboration. “Measurement of Single- and Double-Spin Asymmetries in Deep Inelastic Pion Electroproduction with a Longitudinally Polarized Target”. In: *Phys. Rev. Lett.* 105 (2010), p. 262002. DOI: 10.1103/PhysRevLett.105.262002.
- [65] L. L. Pappalardo and M. Dieffenthaler, HERMES Collaboration. “Measurements of Double-Spin Asymmetries in SIDIS of Longitudinally Polarized Leptons off Transversely Polarized Protons”. In: (2011). arXiv: 1107.4227 [hep-ex].
- [66] J. Huang et al., The Jefferson Lab Hall A Collaboration. “Beam-Target Double-Spin Asymmetry A_{LT} in Charged Pion Production from Deep Inelastic Scattering on a Transversely Polarized ^3He Target at $1.4 < Q^2 < 2.7 \text{ GeV}^2$ ”. In: *Phys. Rev. Lett.* 108 (2012), p. 052001. DOI: 10.1103/PhysRevLett.108.052001.
- [67] D. Sivers. “Single-spin asymmetries from the hard scattering of pointlike constituents”. In: *Phys. Rev. D* 41 (1990), p. 83. DOI: 10.1103/PhysRevD.41.83.
- [68] Stanley J. Brodsky, Dae Sung Hwang, and Ivan Schmidt. “Final-state interactions and single-spin asymmetries in semi-inclusive deep inelastic scattering”. In: *Physics Letters B* 530 (2002), p. 99. DOI: 10.1016/S0370-2693(02)01320-5.
- [69] Stanley J. Brodsky, Dae Sung Hwang, and Ivan Schmidt. “Initial-state interactions and single-spin asymmetries in Drell-Yan processes”. In: *Nucl. Phys. B* 642 (2002), p. 344. DOI: 10.1016/S0550-3213(02)00617-X.

- [70] John C. Collins. “Leading-twist single-transverse-spin asymmetries: Drell-Yan and deep-inelastic scattering”. In: *Phys. Lett. B* 536 (2002), p. 43. DOI: 10.1016/S0370-2693(02)01819-1.
- [71] Zhong-Bo Kang and Alexei Prokudin. “Global fitting of single spin asymmetry: An attempt”. In: *Phys. Rev. D* 85 (2012), p. 074008. DOI: 10.1103/PhysRevD.85.074008.
- [72] Peng Sun and Feng Yuan. “Transverse momentum dependent evolution: Matching semi-inclusive deep inelastic scattering processes to Drell-Yan and W/Z boson production”. In: *Phys. Rev. D* 88 (2013), p. 114012. DOI: 10.1103/PhysRevD.88.114012.
- [73] Miguel G. Echevarria et al. “QCD evolution of the Sivers asymmetry”. In: *Phys. Rev. D* 89 (2014), p. 074013. DOI: 10.1103/PhysRevD.89.074013.
- [74] M. Anselmino, M. Boglione, and S. Melis. “Strategy towards the extraction of the Sivers function with transverse momentum dependent evolution”. In: *Phys. Rev. D* 86 (2012), p. 014028. DOI: 10.1103/PhysRevD.86.014028.
- [75] D. Boer and P. J. Mulders. “Time-reversal odd distribution functions in lepton production”. In: *Phys. Rev. D* 57 (1998), p. 5780. DOI: 10.1103/PhysRevD.57.5780.
- [76] S. Falciano et al., NA10 Collaboration. “Angular distributions of muon pairs produced by 194 GeV/c negative pions”. In: *ZPhys C* 31 (1986), p. 513. DOI: 10.1007/BF01551072.
- [77] M. Guanziroli et al., NA10 Collaboration. “Angular distributions of muon pairs produced by negative pions on deuterium and tungsten”. In: *Zeitschrift für Physik C Particles and Fields* 37 (1988), p. 545. DOI: 10.1007/BF01549713.
- [78] C. S. Lam and Wu-Ki Tung. “Systematic approach to inclusive lepton pair production in hadronic collisions”. In: *Phys. Rev. D* 18 (1978), p. 2447. DOI: 10.1103/PhysRevD.18.2447.
- [79] J. S. Conway et al., FNAL E615 Collaboration. “Experimental study of muon pairs produced by 252-GeV pions on tungsten”. In: *Phys. Rev. D* 39 (1989), p. 92. DOI: 10.1103/PhysRevD.39.92.
- [80] L. Y. Zhu et al., FNAL E866/NuSea Collaboration. “Measurement of Angular Distributions of Drell-Yan Dimuons in $p + d$ Interactions at 800 GeV/c”. In: *Phys. Rev. Lett.* 99 (2007), p. 082301. DOI: 10.1103/PhysRevLett.99.082301.

-
- [81] L. Y. Zhu et al., FNAL E866/NuSea Collaboration. “Measurement of Angular Distributions of Drell-Yan Dimuons in $p + p$ Interactions at 800 GeV/ c ”. In: *Phys. Rev. Lett.* 102 (2009), p. 182001. DOI: 10.1103/PhysRevLett.102.182001.
- [82] Bing Zhang et al. “Extracting Boer-Mulders functions from $p + D$ Drell-Yan processes”. In: *Phys. Rev. D* 77 (2008), p. 054011. DOI: 10.1103/PhysRevD.77.054011.
- [83] Zhun Lu and Ivan Schmidt. “Updating Boer-Mulders functions from unpolarized pd and pp Drell-Yan data”. In: *Phys. Rev. D* 81 (2010), p. 034023. DOI: 10.1103/PhysRevD.81.034023.
- [84] Robert N. Cahn. “Critique of parton-model calculations of azimuthal dependence in lepton production”. In: *Phys. Rev. D* 40 (1989), pp. 3107–3110. DOI: 10.1103/PhysRevD.40.3107.
- [85] Vincenzo Barone, Stefano Melis, and Alexei Prokudin. “Boer-Mulders effect in unpolarized SIDIS: An analysis of the COMPASS and HERMES data on the $\cos 2\phi$ asymmetry”. In: *Phys. Rev. D* 81 (2010), p. 114026. DOI: 10.1103/PhysRevD.81.114026.
- [86] John Collins. “Fragmentation of transversely polarized quarks probed in transverse momentum distributions”. In: *Nucl. Phys. B* 396 (1993), pp. 161–182. DOI: 10.1016/0550-3213(93)90262-N.
- [87] John C. Collins, Steve F. Heppelmann, and Glenn A. Ladinsky. “Measuring transversity densities in singly polarized hadron-hadron and lepton-hadron collisions”. In: *Nucl. Phys. B* 420 (1994), pp. 565–582. DOI: 10.1016/0550-3213(94)90078-7.
- [88] R. Seidl et al., Belle Collaboration. “Measurement of Azimuthal Asymmetries in Inclusive Production of Hadron Pairs in e^+e^- Annihilation at Belle”. In: *Phys. Rev. Lett.* 96 (2006), p. 232002. DOI: 10.1103/PhysRevLett.96.232002.
- [89] R. Seidl et al., Belle Collaboration. “Measurement of azimuthal asymmetries in inclusive production of hadron pairs in e^+e^- annihilation at $\sqrt{s} = 10.58$ GeV”. In: *Phys. Rev. D* 78 (2008), p. 032011. DOI: 10.1103/PhysRevD.78.032011.
- [90] J. P. Lees et al., BABAR Collaboration. “Measurement of Collins asymmetries in inclusive production of charged pion pairs in e^+e^- annihilation at BABAR”. In: *Phys. Rev. D* 90 (2014), p. 052003. DOI: 10.1103/PhysRevD.90.052003.

- [91] M. Anselmino et al. “Simultaneous extraction of transversity and Collins functions from new semi-inclusive deep inelastic scattering and e^+e^- data”. In: *Phys. Rev. D* 87 (2013), p. 094019. DOI: 10.1103/PhysRevD.87.094019.
- [92] S. Mert Aybat and Ted C. Rogers. “Transverse momentum dependent parton distribution and fragmentation functions with QCD evolution”. In: *Phys. Rev. D* 83 (2011), p. 114042. DOI: 10.1103/PhysRevD.83.114042.
- [93] S. M. Aybat et al. “QCD evolution of the Sivers function”. In: *Phys. Rev. D* 85 (2012), p. 034043. DOI: 10.1103/PhysRevD.85.034043.
- [94] S. Mert Aybat, Alexei Prokudin, and Ted C. Rogers. “Calculation of Transverse-Momentum-Dependent Evolution for Sivers Transverse Single Spin Asymmetry Measurements”. In: *Phys. Rev. Lett.* 108 (2012), p. 242003. DOI: 10.1103/PhysRevLett.108.242003.
- [95] S. M. Aybat and T. C. Rogers. “TMD-Factorization, Factorization Breaking and Evolution”. In: *19th International Workshop on Deep-Inelastic Scattering and Related Subjects (DIS 2011) Newport News, Virginia, April 11-15, 2011*. 2011. arXiv: 1107.3973 [hep-ph].
- [96] B. U. Musch et al. “Sivers and Boer-Mulders observables from lattice QCD”. In: *Phys. Rev. D* 85 (2012), p. 094510. DOI: 10.1103/PhysRevD.85.094510.
- [97] Andrea Bianconi. “Inserting Physics Associated with the Transverse Polarization of the Quarks into a Standard Monte Carlo Generator, without Touching the Code Itself”. In: (2011). arXiv: 1109.0688.
- [98] F. Hautmann, M. Hentschinski, and H. Jung. “TMD PDFs: A Monte Carlo implementation for the sea quark distribution”. In: (2012). arXiv: 1205.6358.
- [99] A. Kotzinian. “New quark distributions and semi-inclusive electronproduction on polarized nucleons”. In: *Nucl. Phys. B* 441 (1995), pp. 234–256. DOI: 10.1016/0550-3213(95)00098-D. arXiv: hep-ph/9412283.
- [100] A. Bacchetta et al. “Semi-inclusive deep inelastic scattering at small transverse momentum”. In: *JHEP* 0702 (2007), p. 093. DOI: 10.1088/1126-6708/2007/02/093. arXiv: hep-ph/0611265.
- [101] M. Diehl and S. Sapeta. “On the analysis of lepton scattering on longitudinally or transversely polarised protons”. In: *Eur. Phys. J. C* 41 (2005), p. 515. DOI: 10.1140/epjc/s2005-02242-9. arXiv: hep-ph/0503023.

-
- [102] S. Arnold, A. Metz, and M. Schlegel. “Dilepton production from polarized hadron hadron collisions”. In: *Phys. Rev. D* 79 (2009), p. 034005. DOI: 10.1103/PhysRevD.79.034005.
- [103] A. Kotzinian. “Description of polarized $\pi^- + N$ Drell-Yan processes”. In: *COMPASS note 2* (2010). URL: http://wwwcompass.cern.ch/compass/notes_public/2010-2.pdf.
- [104] F Gautheron et al. *COMPASS-II Proposal*. Tech. rep. CERN-SPSC-2010-014. SPSC-P-340. Geneva: CERN, 2010. URL: <http://cds.cern.ch/record/1265628>.
- [105] P. Abbon et al. “The COMPASS experiment at CERN”. In: *Nuclear Instruments and Methods in Physics Research Section A: Accelerators, Spectrometers, Detectors and Associated Equipment* 577 (2007), p. 455. DOI: 10.1016/j.nima.2007.03.026.
- [106] P. Abbon et al. “The COMPASS setup for physics with hadron beams”. In: *Nuclear Instruments and Methods in Physics Research Section A: Accelerators, Spectrometers, Detectors and Associated Equipment* 779 (2015), p. 69. DOI: 10.1016/j.nima.2015.01.035.
- [107] A Abragam and M Goldman. “Principles of dynamic nuclear polarisation”. In: *Reports on Progress in Physics* 41 (1978), p. 395. URL: <http://stacks.iop.org/0034-4885/41/i=3/a=002>.
- [108] V. Blobel and C. Kleinwort. “A new method for the high precision alignment of track detectors”. In: *Conference on Advanced Statistical Techniques in Particle Physics* (2002). arXiv: [hep-ex/0208021](https://arxiv.org/abs/hep-ex/0208021).
- [109] H. Pereira and J.-M. Le Goff. “Compass Spectrometer Alignment”. In: *COMPASS note 4* (2003).
- [110] Ch. Braun. “Hadron-pair production on transversely polarized targets in semi-inclusive deep inelastic scattering”. PhD thesis. University Erlangen-Nürnberg, July 2014.
- [111] C. Adolph. “One-hadron transverse spin effects on a proton target at COMPASS”. PhD thesis. University Erlangen-Nürnberg, Feb. 2013.
- [112] C. Adolph et al. “Collins, Sivers and two hadron asymmetries from the 2010 transversely polarized proton data”. In: *COMPASS release note* (Aug. 2011).
- [113] R. Barlow. “Extended maximum likelihood”. In: *Nucl. Instrum. Meth. A* 297 (1990), p. 496. DOI: 10.1016/0168-9002(90)91334-8.
- [114] A. Martin et al. “On the role of the acceptance in the Unbinned Maximum Likelihood Method”. In: *COMPASS note 13* (2009).

- [115] A. Martin. “Remarks on the evaluation of systematic errors for transverse spin asymmetries”. In: *COMPASS Analysis meeting* (13 November 1012).
- [116] B. Parsamyan. “Transverse spin asymmetries: Studies on UBL method and systematics”. In: *COMPASS Analysis meeting* (14 March 2013).
- [117] A. Kotzinian, B. Parsamyan, and A. Prokudin. “Predictions for double spin asymmetry A_{LT} in semiinclusive DIS”. In: *Phys. Rev. D* 73 (2006), p. 114017. DOI: 10.1103/PhysRevD.73.114017.
- [118] Aram Kotzinian. “SIDIS Asymmetries in Quark-Diquark Model”. In: *Transversity 2008: 2nd International Workshop on Transverse Polarization Phenomena in Hard Processes Ferrara, Italy, May 28-31, 2008*. 2008. arXiv: 0806.3804 [hep-ph]. URL: <https://inspirehep.net/record/788980/files/arXiv:0806.3804.pdf>.
- [119] S. Boffi et al. “Azimuthal spin asymmetries in light-cone constituent quark models”. In: *Phys. Rev. D* 79 (2009), p. 094012. DOI: 10.1103/PhysRevD.79.094012.
- [120] J. Badier et al. “Experimental J/ψ hadronic production from 150 to 280 GeV/ c ”. In: *Z. Phys. C Particles and Fields* 20 (1983), p. 101. DOI: 10.1007/BF01573213.
- [121] B. Alessandro et al. “ J/ψ and ψ' production and their normal nuclear absorption in proton-nucleus collisions at 400 GeV”. In: *European Physical Journal C* 48 (2006), p. 329. URL: <http://pythia6.hepforge.org>.
- [122] Torbjörn Sjöstrand, Stephen Mrenna, and Peter Skands. “PYTHIA 6.4 physics and manual”. In: *Journal of High Energy Physics* 2006.05 (2006), p. 026. URL: <http://stacks.iop.org/1126-6708/2006/i=05/a=026>.
- [123] P. J. Sutton et al. “Parton distributions for the pion extracted from Drell-Yan and prompt photon experiments”. In: *Phys. Rev. D* 45 (1992), pp. 2349–2359. DOI: 10.1103/PhysRevD.45.2349.